Structure and Property Correlations in Heavy Atom Radicals

by

Alicea Anne Leitch

A thesis
presented to the University of Waterloo
in fulfillment of the
thesis requirement for the degree of
Doctor of Philosophy
in
Chemistry

Waterloo, Ontario, Canada, 2009

Author's Declaration

I hereby declare that I am the sole author of this thesis. This is a true copy of the thesis, including any required final revisions, as accepted by my examiners.

I understand that my thesis may be made electronically available to the public.

Abstract

Neutral radicals represent versatile building blocks for the design of new conductive and magnetic molecular materials. In order to obtain good electron transport, materials displaying a high bandwidth *W* and a low on-site Coulomb repulsion energy *U* must be generated, and to this end, the pyridine-bridged bisdithiazolyl radicals were developed. As a result of resonance stabilization, these materials possessed a low *U*, a high thermal stability, and did not dimerize in the solid state. Their heterocyclic framework carried R_1 and R_2 groups that provided the necessary steric protection, but also caused plate slippage in the π-stack arrays, limiting the overall bandwidth. Although the bisdithiazolyls exhibited relatively high conductivity values, these materials were Mott insulators.

With the view of extending the beneficial features of the bisdithiazolyl radicals to a new building block, the resonance stabilized bisthiadiazinyl radicals were developed. Two derivatives were generated, and although these compounds exhibited the desired properties (low *U*, good thermal stability, suppression of dimerization), the R_3 groups on the periphery of the framework behaved as buffers to isolate the radicals from one another. This limited the number of close S-N and S-S intermolecular contacts in the solid state, thereby shutting down overall bandwidth. As a result, these compounds had very low conductivity values. Nonetheless, the low-dimensionality enabled the study of the magnetic properties and subsequent modeling of one compound as a 1D Heisenberg antiferromagnetic S = ½ chain. Substituent modification has been explored and may afford other interesting properties.

An alternative strategy in developing neutral radical conductors involved improving the known bisdithiazolyl framework to increase the orbital overlap between radicals, and thus *W*. This could be achieved by (i) removing some of the steric bulk to allow for more superimposed π-stacking in the solid state, or (ii) incorporating the heavier, more spatially diffuse selenium atom into the framework. This thesis encompassed both of these strategies. To remove one of the R substituents, a pyrazine ring was used to replace the pyridine bridge of the bisdithiazolyl framework, a design modification that could potentially afford a superimposed π-stacked structure and large *W*. Two derivatives were obtained, and the first (R = Et) formed two types of σ-bonded dimers in the solid state, demonstrating the importance of steric protection in preventing association in these types of systems. The second derivative (R = Me) however, crystallized in the desired structural arrangement as vertically aligned alternating radical stacks. The bandwidth afforded by the multitude of close intermolecular contacts (*W* = 1.5 eV) suggested a metallic

ground state, although the conductivity and magnetic properties did not support this prediction. Variable temperature crystallography studies discovered a gradual phase transition to a dimer state at low temperatures, and the transport properties are consistent with those of a small band gap semiconductor.

The second approach to improving the bandwidth in the bisdithiazolyl radicals was to incorporate selenium into the framework. There are three selenium-containing variants possible, and in order to generate them, lengthy and difficult synthetic methods were developed. These synthetic routes include selenium insertion reactions, R_1/R_2 modification procedures, purification steps, and reduction and crystal growth techniques. Many R_1/R_2 derivatives have been produced by these methods, and their properties and structures have been examined.

When selenium occupies the center position of the heterocycle, lateral σ-dimerization is especially prevalent, although it can be avoided with certain combinations of R_1/R_2 substituents. The σ-dimers are semiconductors and exhibit high conductivity values, particularly under mild applied pressure ($\leq$5 GPa). To study the effects of pressure on the crystal structures of these compounds, and to investigate the causes behind the conductive behaviour, two other isostructural σ-dimers were developed and their conductive properties were measured under increasing pressure. A preliminary high pressure crystal structure of one derivative was also obtained. Although the mechanism for conductivity remains elusive, the results suggest that the molecular geometry is maintained upon pressurization up to 5 GPa and that the closure of the electronic band gap may be the cause of the increase in conductivity in these systems. The differences in pressure response between compounds was attributed to the compressibility of each crystal structure, with a greater response observed for small R substituents. The conductivity of one derivative (R_1 = Me, R_2 = H) increased by five orders of magnitude to 0.5 x 10^1 S cm^{-1} at 5 GPa, with the activation energy (E_{act}) dropping to near 0.10 eV.

An entire group of four S/Se radicals with R_1 = Me, R_2 = Cl was developed that did not dimerize in the solid state, and unlike previously studied R_1/R_2 families, did not form an isostructural set. Instead, two types of crystallographic space groups were observed, the radicals separated according to the chalcogen atom in the center position of the heterocycle. When sulfur occupied that site, the orthorhombic space group $P2_12_12_1$ was preferred, but when selenium occupied the center position the monoclinic space group $P2_1/n$ was adopted. This structural dichotomy allowed, for the first time, the opportunity to investigate the effects of crystal structure on the transport properties. It was found that the structural arrangement afforded

in the monoclinic space group provided much stronger interactions between radicals. The magnetic exchange interactions were more strongly antiferromagnetic for this set of compounds, and the conductivity was two orders of magnitude higher. The all-selenium derivative displayed the highest conductivity we have observed, with a σ_{RT} value of 4 x 10^{-3} S cm^{-1} and E_{act} of 0.17 eV. Under an applied pressure of 5 GPa the conductivity increased to 0.2 x 10^{1} S cm^{-1} and E_{act} dropped to 0.10 eV, nearly reaching a metallic ground state. The differences in the transport properties between the two structures, that is, the orthorhombic and monoclinic packing arrangements, have been analyzed using EHT bandwidth calculations and DFT magnetic exchange energy calculations as a function of the degree and direction of plate slippage along the π-stack. It was found that in the monoclinic structures there is greater orbital overlap along the stacks, which affords stronger magnetic interactions and higher conductivity values for these compounds.

Acknowledgments

I'd like to take this opportunity to acknowledge all of the people who have helped me get to where I am today. First and foremost I would like to thank my supervisor Prof. Rich Oakley. You have not only been a mentor to me, but also a dear friend. The long conversations about both chemistry and life have meant a great deal to me. Thank you so much for your patience, your support and your example.

I would like to thank my coworkers Dr. Leanne Beer, Dr. Jaclyn Brusso, Dr. Owen Clements, Kristina Cvrkalj, Doug MacGregor, Kristin Matkovich, Dr. Daniel Myles, Dr. Rob Reed, Maarit Risto, Dr. Craig Robertson, Lenora Sawyer and Stephen Winters. Thank you for making the *every day* so great and the experience so memorable.

Thank you to my supervisory committee, Prof. Holger Kleinke, Prof. Sonny Lee and Prof. Kathryn Preuss for being a part of this journey with me. Your advice and guidance is greatly appreciated.

I would like to acknowledge our collaborators Prof. Robert Haddon and Dr. Mikhail Itkis (UC Riverside), Dr. Paul Dube (Brockhouse), Dr. Laurie Thompson (MUN), Prof. Natia Frank (Victoria), Prof. Rick Secco and Xueyang Yu (Western Ontario), and Prof. John Tse (Saskatoon) for transport property measurements, and Dr. Jim Britten (McMaster) and Prof. John Richardson (Louisville) for crystallography. Thank you for your support and contributions.

I would like to thank all of my family and friends for their support throughout my degree and in my life. Thank you for caring enough to ask "so what is it that you're trying to do?" I'd like to mention my sister Amanda in particular, who is my dearest friend and confidant. Thank you for your unlimited support and encouragement. And finally, to my husband Randy, I can not thank you enough for all that you do. I am grateful for your unwavering confidence in me.

In memory of my mother.

Table of Contents

Chapter 4: The Synthetic Methodology to Selenium-Containing Bisdithiazolyls

Chapter 5: Pressure Response of Selenium σ-Dimers

References:

List of Tables

List of Captioned Figures

List of Uncaptioned Figures

Figures are numbered sequentially in each chapter. The numerical prefix in the figure label corresponds to the chapter in which the figure may be found. For example, a figure in Chapter 1 will be assigned the prefix **1-**. The same figure may appear in multiple chapters, having the appropriate prefix.

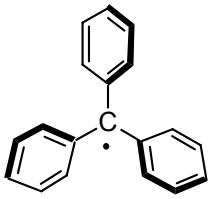

1-1

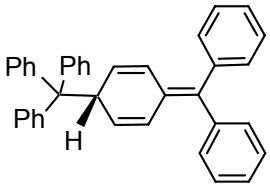

[1-1]$_2$

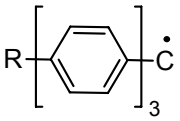

1-2

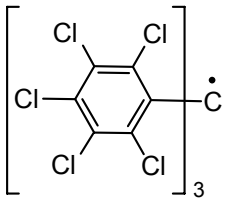

1-3

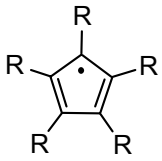

1-4

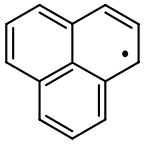

1-5

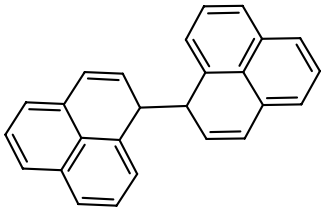

[1-5]$_2$

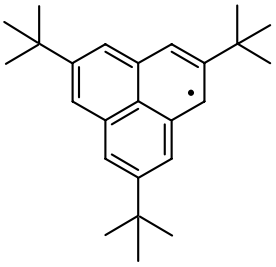

1-6

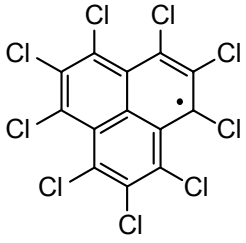

1-7

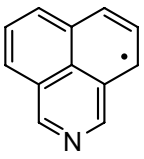

1-8

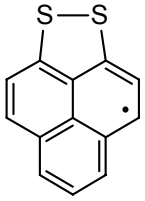

1-9

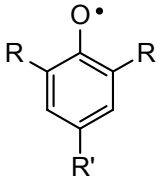

1-10

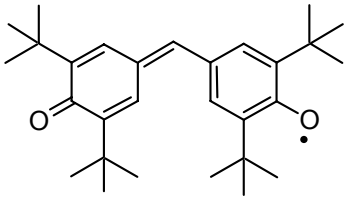

1-11

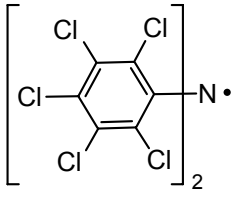

1-12

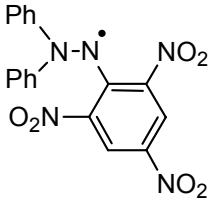

1-13

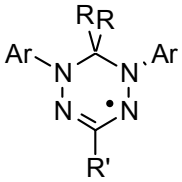

1-14

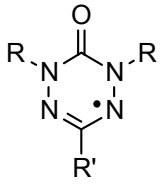

1-15

1-16

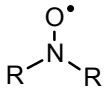

1-17

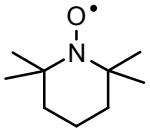

1-18

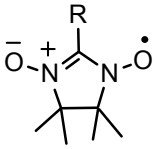

1-19

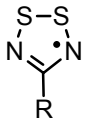

1-20

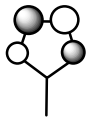

1-21

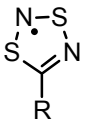

1-22

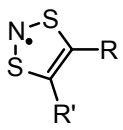

1-23

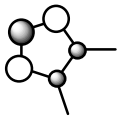

1-24

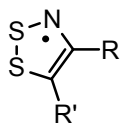

1-25

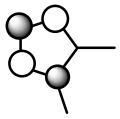

1-26

1-27

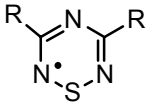

1-28

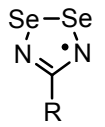

1-29

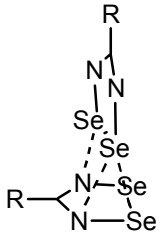

1-30

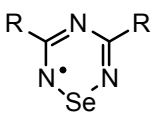

1-31

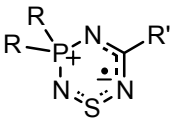

1-32

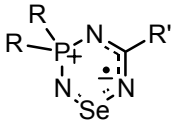

1-33

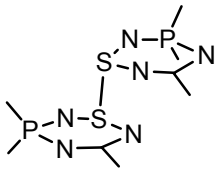

[**1-32**]$_2$

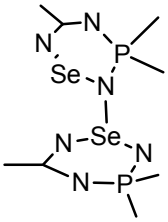

[**1-33**]$_2$

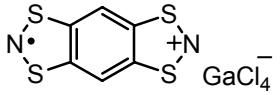

1-34

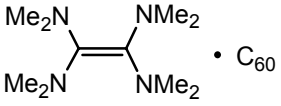

1-35

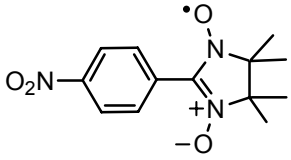

1-36

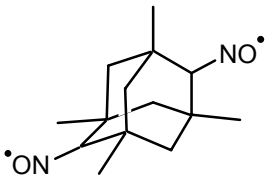

1-37

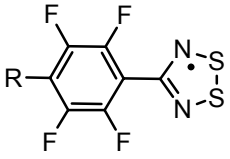

1-38

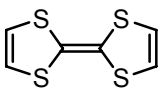

1-39

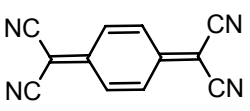

1-40

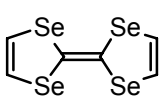

1-41

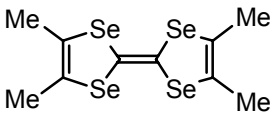

1-42

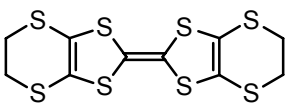

1-43

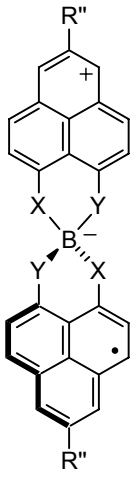

1-45

a X = NR, Y = NR', R'' = H
b X = NR, Y = O, R'' = H
c X = O, Y = O, R'' = Me, H

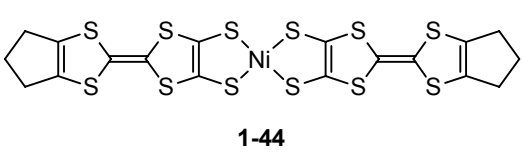

1-44

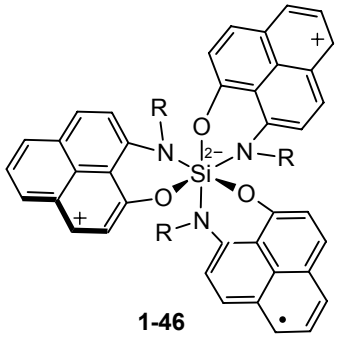

1-46

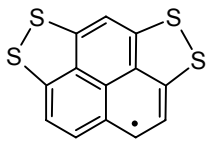

1-47

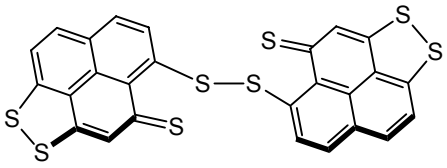

[**1-47**]$_2$

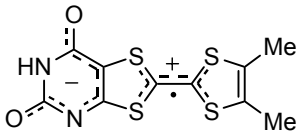

1-48

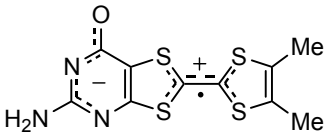

1-49

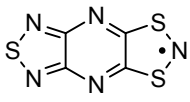

1-50

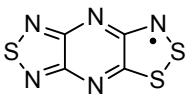

1-51

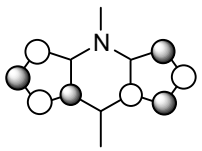

1-52

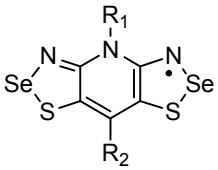

1-53

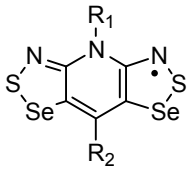

1-54

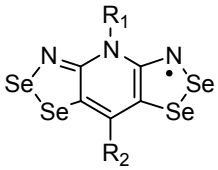

1-55

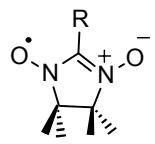

2-1

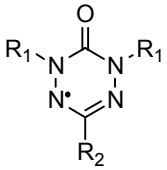

2-2

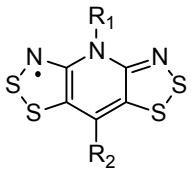

2-3

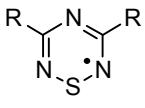

2-4

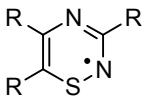

2-5

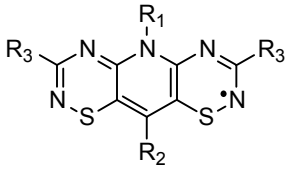

2-6

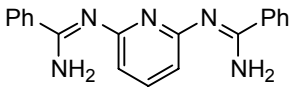

2-7

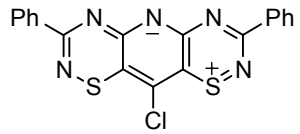

2-8

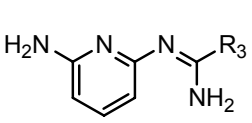

2-9

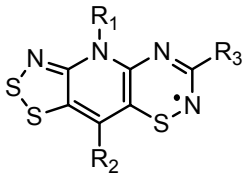

2-10

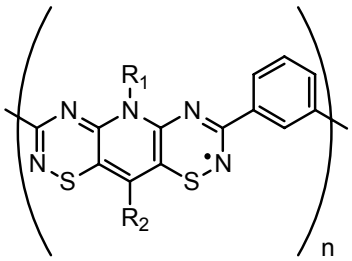

2-11

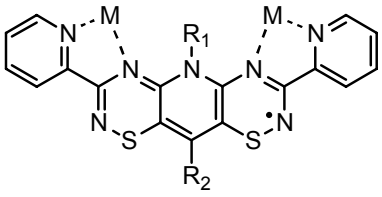

2-12

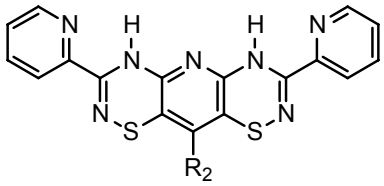

2-13

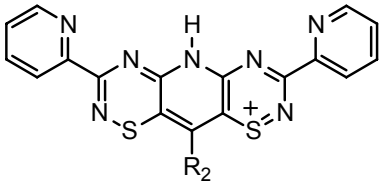

2-14

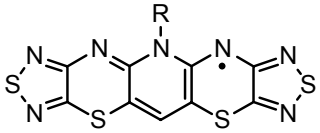

2-15

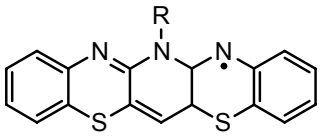

2-16

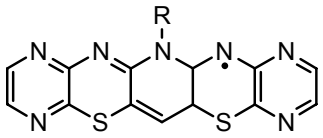

2-17

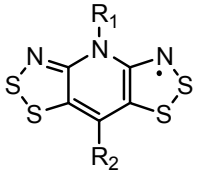

3-1

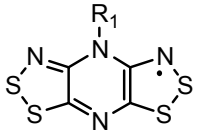

3-2

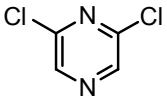

3-3

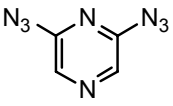

3-4

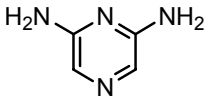

3-5

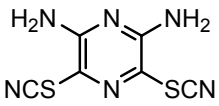

3-6

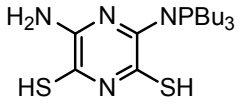

3-7

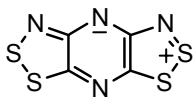

3-8

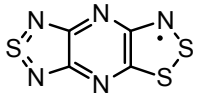

3-9

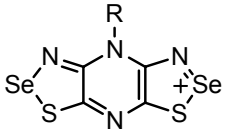

[3-10]$^+$

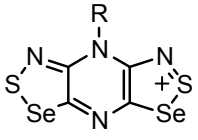

[3-11]$^+$

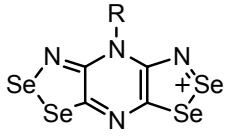

[3-12]$^+$

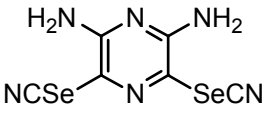

3-13

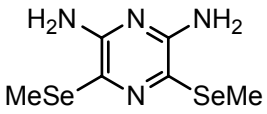

3-14

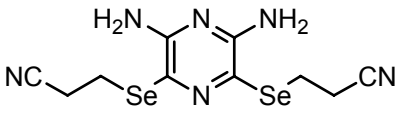

3-15

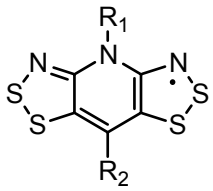

4-1

4-2

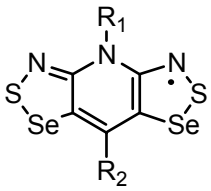

4-3

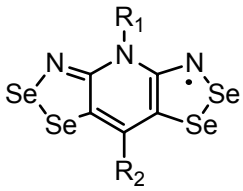

4-4

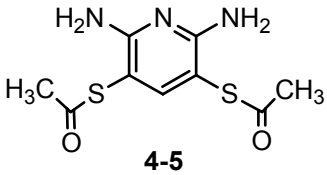

4-5

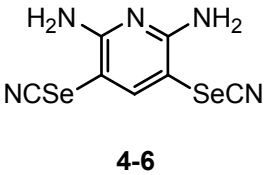

4-6

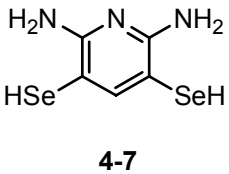

4-7

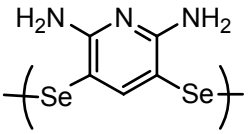

4-8

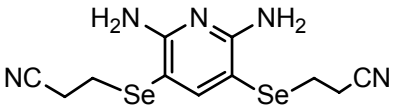

4-9

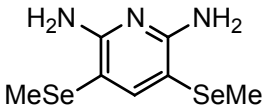

4-10

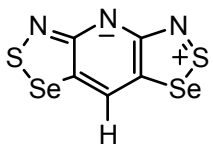

4-11

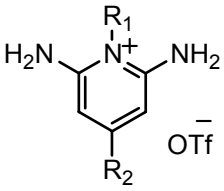

[**4-12**][OTf

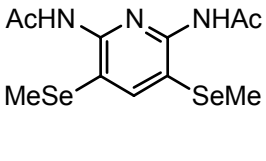

4-13

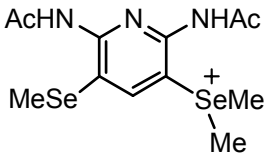

4-14

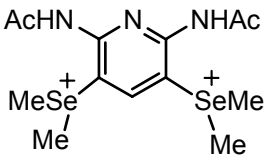

4-15

[**4-16**][Cl]

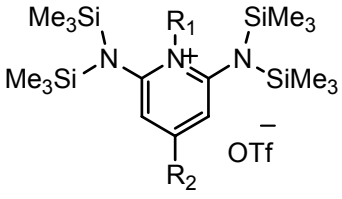

[**4-17**][OTf]

5-1

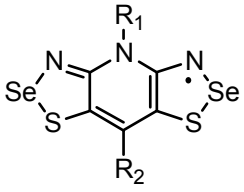

5-2

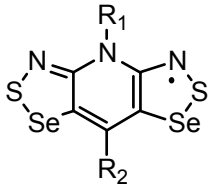

5-3

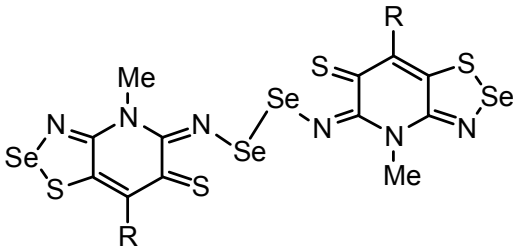

[**5-2a,b,c**]$_2$

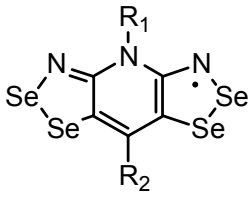

5-4

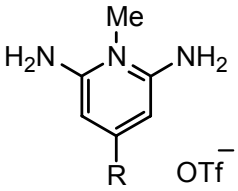

[**5-5a,b,c**][OTf]

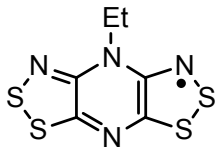

5-6

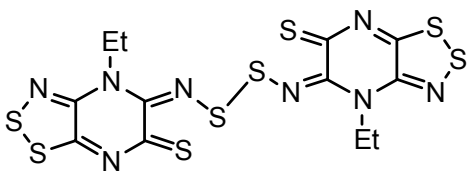

[**5-6**]$_2$

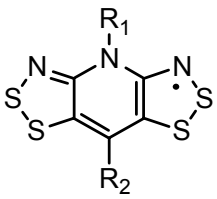

6-1

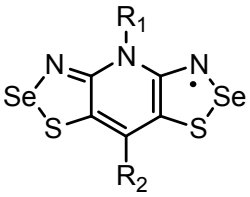

6-2

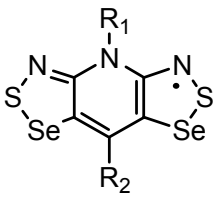

6-3

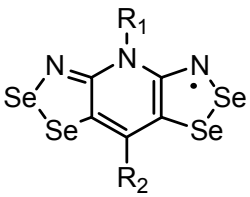

6-4

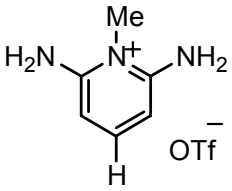

[**6-5**][OTf]

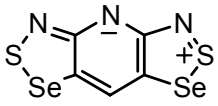

6-6

List of Abbreviations

6-31G(d,p)	a split valence plus polarization basis set
a	crystallographic unit cell axis; hyperfine coupling constatnts
AFM	antiferromagnetism
Å	Angstrom
Anal.	analysis
b	crystallographic unit cell axis
B3LYP	hybrid B3 including an HF exchange term and the LYP correlation functional
BEDT	*bis*(ethlenedithio)
br	broad (IR peak descriptor)
BSS	broken symmetry singlet
C	Curie constant
ºC	degree centigrade
c	crystallographic unit cell axis
calcd.	calculated
cm^{-1}	reciprocal centimeters
CO	crystal orbital
CT	charge transfer
CV	cyclic voltammetry
d	doublet (NMR peak descriptor)
D	dimensionality, as in 1D or 3D
DCE	dichloroethane
DCM	dichloromethane
dec.	decomposition
deg	degrees
DFT	Density Functional Theory
DMFc	*bis*(pentamethylcyclopentadienyl)iron
DTA	dithiazolyl

DTDA	dithiadiazolyl
E	chalcogen, either sulfur or selenium
E_1	chalcogen in the 1-position of the bisdithiazolyl framework, sulfur or selenium
E_2	chalcogen in the 2-position of the bisdithiazolyl framework, sulfur or selenium
E	energy
ΔE	change in energy
$E_{1/2}$	half-wave potential
E_{act}	activation energy
EA	electron affinity
E_{cell}	peak to peak potential separation
EHT	Extended Hückel Theory
EI	electron impact
emu	electromagnetic unit
E_{pa}	anodic peak potential
E_{pc}	cathodic peak potential
EPR	electron paramagnetic resonance
ET	*bis*(ethlenedithio) tetrathiafulvalene
ESI	electrospray ionization
Et	ethyl
EtOH	ethanol
eV	electron volt
f	fraction of band filled
FM	ferromagnetism
g	gram
g	Landé factor
GPa	gigapascal, unit of pressure
$\mathbf{H}'$	effective Hamiltonian
^{1}H	proton

h	hour
H	magnetic field
H_c	coercive field
ΔH_{disp}	disproportionation enthalpy
ΔH_{diss}	bond dissociation enthalpy
HMFc	*bis*(trimethylcyclopentadienyl)iron
HOAc	acetic acid
HOMO	highest occupied molecular orbital
Hz	Hertz
IP	ionization potential
IR	infrared
J	exchange energy
J	valence bond exchange integral
j, j'	electrostatic terms of the valence bond exchange integral
J_π	exchange energy along the π-stack direction
J_{12}	Coulomb integral
k	a quantum number, direction in reciprocal space
k_B	Boltzmann constant
K	Kelvin
kHz	kilohertz
kJ	kilojoule
L	litre
LT	low temperature
LUMO	lowest unoccupied molecular orbital
LW	linewidth
M	molarity
M^+	base peak (mass spectrometry)
m	minute; medium (IR peak descriptor); multiplet (NMR descriptor)

m/e	mass to charge ratio
min	minute
Me	methyl
MeCN	acetonitrile
MeOH	methanol
mL	millilitre
mmol	millimole
MO	molecular orbital
mol	mole
mp	melting point
MS	mass spectrometry
mT	millitesla
NMR	nuclear magnetic resonance
NTf	nonaflate (nonafluorobutanesulfonate) anion
NRC	neutral radical conductor
OAH	odd alternative hydrocarbon
Oe	Oersted
OMFc	*bis*(tetramethylcyclopentadienyl)iron
OTf	triflate (trifluoromethanesulfonate) anion
ORTEP	Oak Ridge thermal ellipsoid parameter
param.	parameters
Ph	phenyl group
PLY	phenalenyl radical
ppm	parts per million
Pr	propyl group
PXRD	powder X-ray diffraction
Q	valence bond Coulomb integral
R	general substituent group

R	agreement index (crystallography)
ref.	referenced
restr.	restraints
RIC	radical ion conductor
ROTf	alkyl triflate
R_p	agreement index- profile (crystallography)
RT	room temperature
RVB	resonance valence bond
R_w	weighted agreement index
s	strong (IR peak descriptor); singlet (NMR peak descriptor); second
S	Siemens ($1S = 1\Omega^{-1}$); singlet state
S	spin
S^2	overlap density integral
$\langle S \rangle^2$	expectation value
SCE	saturated calomel electrode
SCF	self consistent field
SHMO	Simple Hückel Molecular Orbital Theory
SOMO	singly occupied molecular orbital
SW	sweep width
t	triplet (NMR peak descriptor)
T	temperature; triplet state
T_c	Curie temperature
TCNQ	tetracyano-*p*-diquinomethane
TDAE	tetrakisdimethyl-aminoethylene
temp	temperature
TM	transition metal
TMPDA	N,N,N′,N′-tetramethyl-*p*-phenylenediamine
T_N	Néel temperature

Torr	unit of pressure = 133.32 Pa
tmdt	trimethylenetetrathiafulvalenedithiolate
TMS	trimethylsilyl group
TMTSF	tetramethyltetraselenafulvalene
TTF	1,1′,3,3′-tetrathiafulvalene
U	on-site Coulomb repulsion energy
V	Volt
V	volume
VB	valence bond
vs	very strong (IR peak descriptor)
vs	versus
vw	very weak (IR peak descriptor)
w	weak (IR peak descriptor)
W	bandwidth
wR_p	weighted agreement index - profile (powder crystallography)
X	halogen group
x	Cartesian coordinate
y	Cartesian coordinate
Z	number of asymmetric units per unit cell
z	Cartesian coordinate
ZFC	zero field cooled
º	degree
α	crystallographic axis angle; coulombic parameter
β	crystallographic axis angle; resonance parameter
γ	crystallographic axis angle
δ	chemical shift in ppm; mean separation of molecules in a slipped stack
ε	orbital energy
μ	absorption correction

μA	microamps
π	orbital symmetry
τ	angle between the mean plane of the heterocyclic backbone and the stacking axis
υ	frequence
ρ	electrical resistivity; spin density
σ	electric conductivity; orbital symmetry
σ_{RT}	room temperature conductivity
λ	wavelength
ϕ	atomic orbital
χ	magnetic susceptibility
ψ	wavefunction

Chapter 1

Neutral Radicals as Functional Materials

1.1 Molecular Radicals

Generally, non-metal based molecules have paired electrons and are closed shell. However, by virtue of the number or types of atoms present, systems with unpaired electrons can also exist.[1] These molecules, usually referred to as radicals,[2] are often thought of as highly reactive and even transient in nature, as many rapidly decompose *via* dimerization, hydrogen or alkyl abstraction, hydrolysis or redox reaction pathways. However, many radicals are considered stable, that is, they are thermodynamically favoured with respect to specific reactions like those mentioned above, and are observable and even isolable. The degree of stability is an important feature when comparing radicals, although unfortunately the definition of a stable radical is a subjective term, as there is no universal convention used. Therefore the terms "persistent" and "stable" must be defined before any particular examples are described. Thus, for present purposes, the definitions provided by Ingold,[3] and used by others,[4] will be employed. When a radical is described as persistent it survives long enough to be observed by conventional spectroscopic methods, but can not be isolated. This suggests compounds with half-lives on the order of minutes.[5] By contrast, radicals that are considered stable are those that can be isolated and stored as a pure substance, with *no more precautions than would be used for the majority of commercially available organic chemicals*,[3] and exist for prolonged periods of time.

In general, four design strategies are used in generating stable radicals and often a combination of these are utilized. The first is to position bulky substituents around the periphery of the molecule to impede

close contact with other molecules, and the second is to block reactive sites and inhibit certain decomposition pathways. A third strategy is to incorporate resonance within the framework to delocalize the electron and distribute spin density, and the fourth method is to include electron-rich heteroatoms that, due to electron pair repulsion, inhibit association (the so-called alpha-effect).[6,7] Many different types of molecular radicals have been developed, and a range of reactivities have been observed. Several classes will be described here, ranging from radicals that have an entirely organic backbone to those that consist predominately of heteroatoms. The design strategies used to increase the stability in these compounds are also discussed.

1.1.1 Organic Carbon-Centered Radicals

Gomberg's report of the triphenylmethyl radical **1-1** marked the beginning of organic free radical chemistry in 1900.[8] He discovered this unusual carbon-based radical while attempting to prepare the sterically encumbered hexaphenylethane molecule.[9] The triphenylmethyl radical can not be isolated and is present in solution along with its σ-dimer [**1-1**]$_2$, which is bonded through a central carbon atom on one molecule and a carbon atom at the *para* position of a phenyl ring on another. The σ-bond is weak, as a bond dissociation energy of ~ 11 kcal mol^{-1} was reported.[10] When the *para* positions are blocked with substituents, as in **1-2**, the radicals are monomeric in solution and deemed kinetically stable.[11] When all positions are substituted, as the perchlorinated compound **1-3**, the molecule is so severely obstructed that it is considered chemically inert, being monomeric in the solid state, as well as in solution.[12]

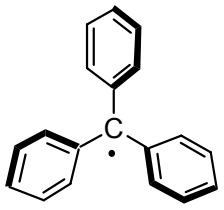

1-1

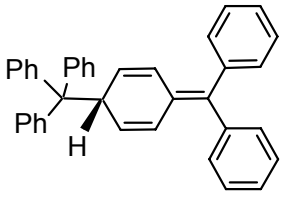

[**1-1**]$_2$

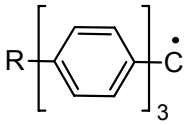

1-2

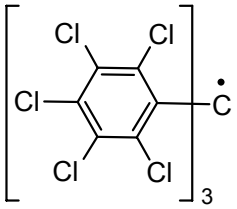

1-3

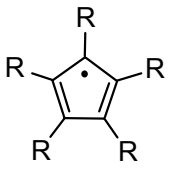

1-4

Another class of carbon-based radical comprises the substituted cyclopentadienyls **1-4**, which can be monomeric or dimeric depending on the R substituent. For example, the pentamethyl derivative (R = Me) forms σ-dimers in solution and requires temperatures > 360 K for dissociation into discrete radicals. A carbon-carbon bond enthalpy of ~19 kcal mol^{-1} was reported.[13] By contrast, the pentaisopropyl compound (R = *i*-Pr) can be isolated in the solid state and forms evenly spaced stacks, with molecules being 5.82 Å apart.[14]

Phenalenyl **1-5** and its derivatives also possess a carbon backbone. Like triphenylmethyl, phenalenyl is in thermodynamic equilibrium with its σ-bonded dimer [**1-5**]$_2$ in solution.[15] σ-Dimerization is avoided in **1-6**, which has *t*-butyl groups positioned at the *β*-carbon sites.[16] In the solid state, this compound forms stacks of π-dimers, in which the molecules are eclipsed so as to minimize steric repulsion between the substituents. When chlorine atoms are placed around the periphery of the molecule, as in the perchlorophenalenyl radical **1-7**, the molecules are monomeric.[17] In the solid state, the molecules are well separated, but are nonplanar as a result of the steric interaction between the chlorine atoms on neighbouring molecules. Dimerization through carbon-carbon bond formation has also been avoided without the use of steric protection through the incorporation of nitrogen (**1-8**)[18] or sulfur (**1-9**).[19]

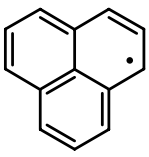

1-5

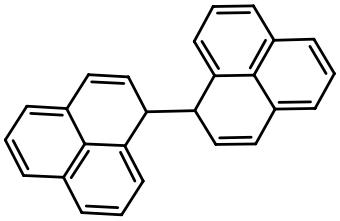

[**1-5**]$_2$

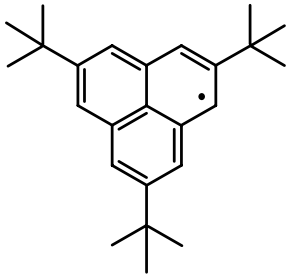

1-6

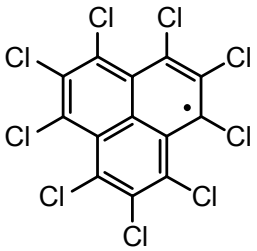

1-7

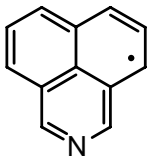

1-8

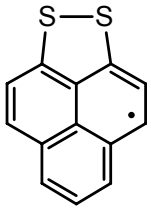

1-9

The behaviour of these organic open-shell compounds demonstrates that generating stable carbon-centered radicals requires a combination of resonance delocalization, steric bulk and strategic placement of substituents. The incorporation of other elements into the organic framework, where the unpaired electron is centered on an atom other than carbon, specifically oxygen, nitrogen and sulfur, has been shown to provide additional stability.

1.1.2 Organic Heteroatom Radicals

Carboxyl radicals, such as the phenoxyls **1-10**,[20] are a well-known example of an organic radical that has the electron centered on a heteroatom. These molecules are studied as models of tyrosyl radicals in living systems, and also as antioxidants.[21] The unpaired electron is delocalized over the aromatic ring, and for a phenoxyl to be more than a transient intermediate the *ortho* and *para* positions must be blocked by groups that give steric protection. The resonance delocalized galvinoxyl radical **1-11** for example, can be isolated in pure form as a monomeric species that is stable in the solid state.[22] This radical is unreactive towards oxygen, even in solution, and is commercially available.[23]

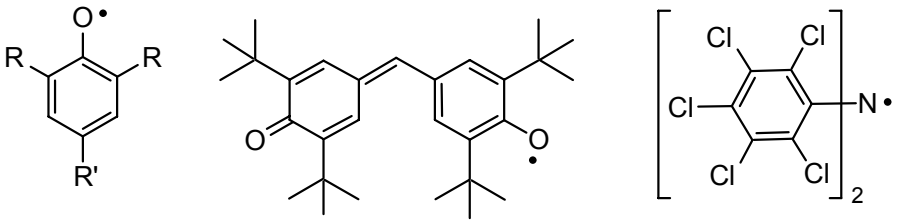

1-10 **1-11** **1-12**

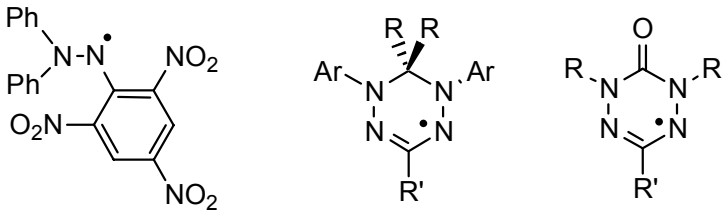

1-13 **1-14** **1-15**

Aminyls, organic radicals that contain the CN unit, also require steric bulk for stability. For example, perchlorodiphenylaminyl **1-12** can be stored indefinitely in air.[24] Its stability is attributed to the shielding of the nitrogen atom by the four *ortho* chlorine atoms on the phenyl substituents. This molecule has a half-life of about two months in carbon tetrachloride (in air at room temperature), but it reacts rapidly with toluene, undergoing hydrogen abstraction and disproportionation. Hydrazyls [RNNR]· are generally only persistent in solution, although 2,2-diphenyl-1-picrylhydrazyl (DPPH) **1-13** has been known for several decades as a stable radical, as it does not dimerize or react with oxygen.[25] Consequently, DPPH is commonly used as a reference compound in EPR (electron paramagnetic resonance) spectroscopy. Resonance delocalized hydrazyls are among the most stable class of radicals and include the verdazyls **1-14**, which were reported over forty years ago by Kuhn and Trischmann,[26] and the related oxoverdazyls **1-15**, reported more recently in the 1980's by Neugebauer.[27] These radicals are generally stable to air and water, and do not require bulky substituents for stability.

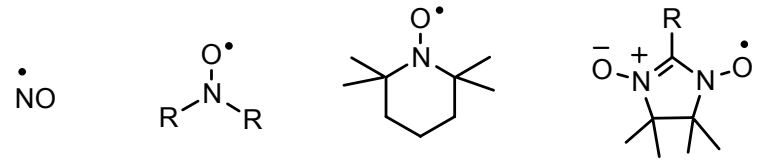

1-16 **1-17** **1-18** **1-19**

Combining nitrogen and oxygen provides a range of nitroxyl radicals, the simplest being nitric oxide **1-16**. This compound is indefinitely stable in the absence of oxygen, and does not rely on steric protection to avoid dimerization. Instead, the alpha-effect,[6,7] that is, the repulsion between lone pairs on neighbouring molecules, is sufficient to prevent σ-bond formation. The NO unit has been incorporated into carbon frameworks to afford a host of organic nitroxyl derivatives **1-17** with a range of stabilities that depend primarily on the R substituents.[28] To avoid disproportionation reactions for these compounds, quaternary carbon-based substituents are used, as hydrogen atoms situated on the α-carbons are particularly sensitive to H· abstraction. For example, TEMPO (2,2,6,6-tetramethylpiperidine-N-oxyl) **1-18** is very stable and is used as a building block for spin labeling studies.[29] Incorporating resonance delocalization into the framework affords the nitronyl nitroxide radicals **1-19**, in which the spin density is dispersed

evenly on both NO units.[30] These compounds also require the absence of α-hydrogens, but once this condition is met, these radicals are considered highly stable.

1.1.3 Inorganic Heteroatom Radicals

Replacing oxygen in the nitroxyl radicals with the heavier chalcogen sulfur leads to what is considered to be a more inorganic class of radicals, the thiazyls. Although oxygen and sulfur are both in Group 16 of the periodic table, the thiazyl radicals are quite different from their nitroxyl analogues. This results from the fact that the sulfur atom is larger and more polarizable than oxygen, and that the S-N bond is oppositely polarized to that of N-O.[31] The thiazyl radicals are inherently stable, as they do not require steric bulk for their stability. Several acyclic thioaminyls [RSNR]· have been reported,[32] but the bulk of the stable thiazyls are ring systems,[33] many including conjugation to carbon. The 1,2,3,5-dithiadiazolyls **1-20** include a single carbon atom to make a 5-membered ring. The R substituent is situated on the nodal plane of the π-SOMO (singly occupied molecular orbital) **1-21**, and therefore has little effect on the electronic properties of the system, although it does influence solid state packing. Most derivatives form π-dimers in the solid state,[34] displaying a range of association modes (Figure 1.1),[35] although there are several examples that remain as discrete radicals.[36] The related isomer 1,3,2,5-dithiadiazolyl **1-22** is also known, however, it is less thermodynamically stable and readily converts into **1-20** both in solution and in the solid state.[37]

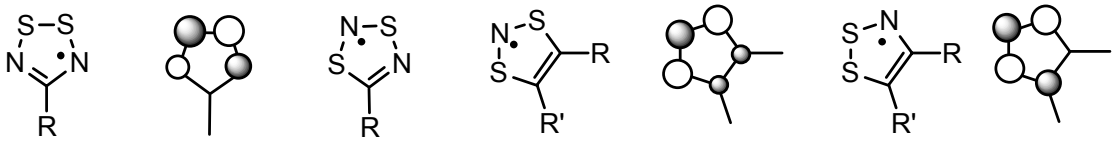

1-20 **1-21** **1-22** **1-23** **1-24** **1-25** **1-26**

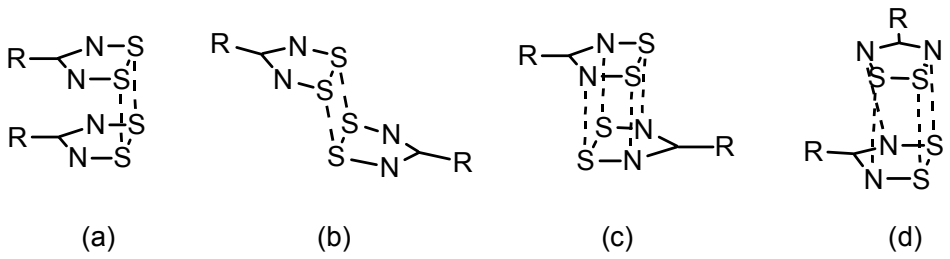

Figure 1.1 Modes of association demonstrated by **1-20** in the solid state, including the (a) *cis*-cofacial, (b) *trans*-antarafacial, (c) *trans*-cofacial, and (d) twisted conformations.

Compounds **1-23** and **1-25** are also 5-membered rings, but have one of the nitrogen atoms in the dithiadiazolyl ring replaced with a carbon atom. The π-SOMOs of both compounds, **1-24** and **1-26** respectively, have spin density on the carbon atoms, allowing for the fine-tuning of their redox properties through variations in the R substituent. The 1,3,2-dithiazolyls **1-23** are air sensitive in solution, but are indefinitely stable in the solid state. Many examples exist as π-dimers,[38] although the quinoxaline and naphthalene fused compounds are monomeric.[39] Some derivatives undergo a reversible phase change between a structure of π-dimer stacks and a structure of π-radical stacks with change in temperature.[40,41] For a few examples this transition is hysteretic, and can be observed in both magnetic and structural measurements. In 2004, Oakley outlined the structural mechanisms that afford the cooperative effects, and resulting magnetic bistability, for several of these systems.[41] Materials that exhibit this type of behaviour are pursued for potential applications in magnetic switching devices.[42]

The other isomer, the 1,2,3-dithiazolyl **1-25**, has also been explored, although only a few examples of the monofunctional radicals have been stable enough to be structurally characterized. Of these, three consist of π-dimers,[43] where only one is monomeric as a result of its strongly electron-withdrawing substituents ($R_1 = Cl_2C_3SN$, $R_2 = Cl$).[44] More recently, the 1,2,3-dithiazolyl unit has been extended to the bifunctional system **1-27**, in which two rings are in resonance across a bridging pyridine moiety.[45] These derivatives are highly stable and consist of discrete radicals both in solution and the solid state. The structures and properties of these compounds are further described in Section 1.4.1.

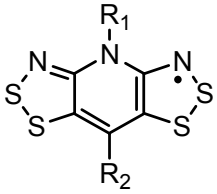

1-27

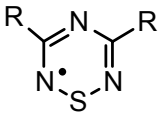

1-28

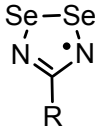

1-29

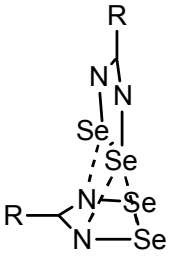

1-30

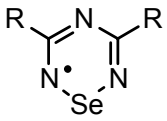

1-31

Another monofunctional thiazyl radical is the 6-membered compound, the 1,2,4,6-thiatriazinyl **1-28**. Many derivatives have been studied in solution,[46] although only one has been characterized in the solid state. This derivative (R = Ph) forms cofacial π-dimers, with an S---S′ contact of 2.66 Å.[47] Selenazyls are also known, although all of the monofunctional derivatives form dimers in the solid state. The 1,2,3,5-diselenadiazolyls **1-29** generally align cofacially,[48] although there are a couple of examples (R = Cl, Br) that dimerize *via* a unique T-shaped mode **1-30**.[49] Like its sulfur analogue **1-28**, the only known 1,2,4,6-selenatriazinyl **1-31** forms cofacial dimers, with a Se---Se′ distance of 2.79 Å.[50] In contrast to these carbon-containing thiazyls, when phosphorus is incorporated into the framework, as in **1-32** and **1-33**, new modes of association are observed. While the thiaphosphatriazinyl dimerizes *via* a S---S′ contact in the solid state [**1-32**]$_2$, the selenium derivative associates through a heteronuclear linkage [**1-33**]$_2$, an association mode that has been observed only for this system.[51]

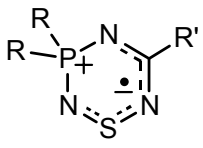

1-32

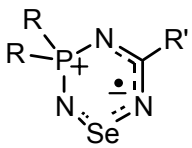

1-33

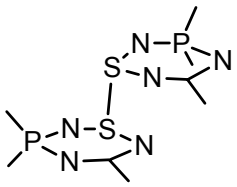

[**1-32**]$_2$

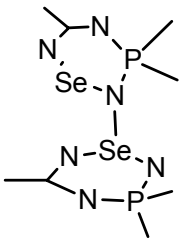

[**1-33**]$_2$

In summary, several different classes of molecular radicals are known, both based on organic and inorganic frameworks, and while some species are only persistent and observed for short periods in solution, others are quite stable and long lived. Typically, steric protection is necessary to inhibit decomposition pathways and prevent dimerization in many of the radicals, although the incorporation of heteroatoms (O, N, S, Se) can increase stability without the use of bulky substituents. Since radicals

possess an unpaired electron, they have found use in a variety of biological, chemical and physical applications, and the ability to alter the molecular framework and thus modify the structure or reactivity of the species makes these open-shell molecules ideal candidates for many areas of research.

1.1.4 Applications of Molecular Radicals

Open-shell molecules are actively studied and used in a range of disciplines and research topics, from biological processes to functional materials. Radicals are commonly involved in chemical reactions as reactive intermediates, although some are used specifically as either nucleophiles or electrophiles.[52] Certain radicals are used as oxidizing agents,[53] while others are employed for their ability to act as *anti*oxidants.[54] Radicals also have a variety of roles in living free-radical polymerization since radical species act as initiators, transfer agents and terminators in polymer chain reactions.[55] The ability to observe and monitor radicals by EPR spectroscopy has provided insight into biological[56] and chemical[1] systems that contain radicals, or ones in which radicals are introduced, using EPR imaging,[57] spin labeling,[58] and spin trapping[59] techniques.

Radicals are not only used in chemical processes, they are also studied for potential use in applications where the conductive and/or magnetic properties afforded by the unpaired electron are exploited. In liquid crystalline materials, a radical species is incorporated into a rigid organic backbone that can be manipulated with the application of a magnetic field.[60] Some molecular radicals are used as spin-bearing ligands that are coordinated to paramagnetic transition metals to allow for possible ferrimagnetic effects,[61,62] while others exhibit magnetic behaviour without the presence of a transition metal, and both ferromagnetic[63,64] and canted antiferromagnetic[65,66,67] ordering has been observed. For use in magneto-thermal switching[42] and information storage devices,[68] radicals that exhibit bistability in which two crystallographic phases (dimers or radicals) can coexist and be interconverted by an external perturbation, are pursued.[69] Also, molecular radicals are explored for use as organic semiconductors, metals and superconductors,[70] and systems in which both conductive and magnetic behaviour are displayed, that is,

those that exhibit magnetoresistance, have the potential to be used in spintronic applications.[71] As the work described in this thesis focuses on the conductive and magnetic properties of neutral radicals, the following sections will provide a more detailed overview of materials that exhibit these properties, as well as a theoretical background behind the behaviour.

1.2 Molecular Magnetic Materials

Both chemists and physicists have been looking to extend the well-known magnetic behaviour of transition metal (TM) alloys,[72] that is, their bulk ferromagnetism at high ordering temperatures with large coercivities, to molecular materials. The flexibility and versatility of organic compounds has the potential of providing a wealth of new and exciting magnetic behaviour. Consequently, molecular magnetism has a long history, and there have been several approaches taken towards generating systems in which the spins associated with molecular units, and not atomic units, order in the solid state.[73] Some strategies rely on the use of TMs to provide the necessary unpaired electrons, and these include the areas of single-molecule magnets (SMMs),[74] organometallic charge transfer salts,[75] and TM complexes that can be linked together to form single chain magnets (SCMs).[76] The SMMs consist of clusters of TMs in which the spins couple through ligand atoms, allowing for high cumulative spin values. A primary example is the 'Mn_{12}'compound, $[Mn^{III}_8Mn^{IV}_4O_{12}(O_2CMe)_{16}(H_2O)_4]\cdot 4H_2O\cdot 2MeCO_2H$, with S = 10.[77] A higher dimensionality is achieved for the TM complexes that are linked together through diamagnetic or paramagnetic ligands in 1-3 dimensions. Gatteschi's $[Mn(hfac)_2NIT]$ (hfac = hexafluoroacetylacetonate, NIT = nitronyl nitroxide with R = *i*-Pr) complex for example, is a SCM where molecular radicals are used as spin-bearing ligands that link the metal centers into 1D chains.[78] By contrast, the charge transfer salts rely on charge transfer to generate spin couplers, with examples including Millers's V[TCNE] and $[Fe(C_5Me_5)_2][TCNE]$ (TCNE = tetracyanoethylene) salts.[79] The known TM-containing molecular magnetic materials display 1D or 3D magnetic ordering at temperatures that range from below 10 K to above 300 K, with only a few examples exhibiting large coercive fields.[80] Although there have been some major discoveries in this area, the design of materials with predictable properties continues to be a challenge.

Other strategies of preparing molecular magnets do not contain TMs and consist entirely of organo-main group elements. However, there are only a few examples that actually exhibit bulk magnetic ordering. These non-metal containing magnets fall into two groups, those based on radical ion salts,[81] and those based on neutral radicals.[82] The radical ion salts require charge transfer for generating the necessary spins, and therefore are composed of two components. One example, [BBDTA][$GaCl_4$] **1-34**, displays bulk ferromagnetism at temperatures below 6.7 K when all of the solvent molecules have been removed from the crystalline lattice.[83] Another example is Wudl's C_{60}[TDAE] (TDAE = tetrakisdimethylaminoethylene) salt **1-35** which also undergoes a transition to a ferromagnetic state, but at the record high Curie temperature (T_C) of 16.1 K.[84] Unlike the salts, molecular magnets based on neutral radicals, which naturally possess unpaired electrons, are single-component. The first reported example was in 1991, in which the onset of ferromagnetic ordering was observed in the β-phase of the *p*-nitrophenyl nitronyl nitroxide radical **1-36** at 0.65 K.[85] A few years later a ferromagnetic transition was reported for the adamantane biradical **1-37** at a slightly higher T_C of 1.48 K.[86] Ferromagnetism has also been observed for a dithiadiazolyl radical **1-38** (R = NO_2) below 1.32 K.[87] When the substituent in **1-38** is changed to a nitrile group (R = CN), the β-phase of this material displays weak ferromagnetism (or canted antiferromagnetism) at an unprecedented temperature of 36 K.[65] Under an applied pressure of 16 kbar the Néel temperature (T_N) of this material increases to 65 K.[88] Some verdazyl radicals also exhibit weak ferromagnetism, but at much lower temperatures.[89] It is important to note that all of the above materials, both the radical ion salts and the neutral radical materials, possess negligibly small coercive fields. In order to be a practical alternative to the TM-based molecular magnets, higher ordering temperatures and coercivity values are required.

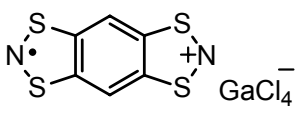

1-34

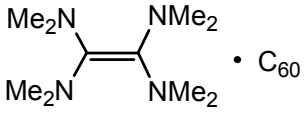

1-35

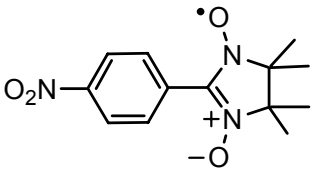

1-36

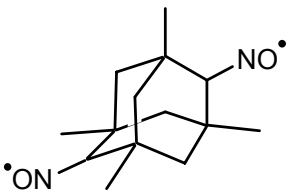

1-37

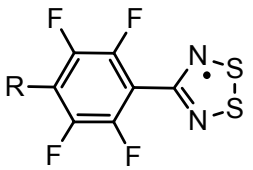

1-38

Oakley has recently discovered magnetic ordering in several bisthiaselenazolyls, and these materials are discussed later in Section 1.4.1. At this time, it is prudent to introduce some of the theory behind molecular magnetism and the computational methods used to examine the behaviour, as this has now become one of the research directions of work in the Oakley group. It is well known that the development of long range order of the electron spins in radical-based systems relies on the packing arrangements of the molecules and the way in which they interact with one another in the solid state.[90] For these materials, a quantum mechanical approach may be used to derive the relationship between the magnetic ground state of the system, with the type and degree of intermolecular orbital overlap.

1.2.1 Magnetism in Neutral Radicals - Theory and Computation

If we consider two molecules A and B, each with one unpaired electron, that are weakly interacting, the two associated spins can be aligned either parallel ($\uparrow\uparrow$) or antiparallel ($\uparrow\downarrow$) to one another. When the spins are aligned parallel, the system has a triplet ground state and the coupling is ferromagnetic (FM). Alternatively, when the spins are aligned antiparallel, the singlet state is the ground state and the system has antiferromagnetic (AFM) exchange. Most organic radicals have spins that are randomly oriented at ambient temperature and are paramagnetic, although at lower temperatures, the spins may show some alignment and FM or AFM coupling may be observed. For the magnetic radicals mentioned in Section 1.2, there is long range order of the spins in three dimensions, which occurs at a particular transition temperature T_C (FM) or T_N (AFM).

The multiplicity of the ground state, whether it is a triplet (T) or a singlet (S), depends, to a large extent, on the type and degree of orbital overlap between the two molecules. An expression relating the relative energies of the two states to the orbital overlap may be obtained using quantum mechanics,[91] and both Molecular Orbital (MO)[92] or Valence Bond (VB)[6,93] methods can be employed. A VB approach is taken here, in which Heitler-London theory is used to describe the electronic structure of a homonuclear, two orbital (ϕ_A, ϕ_B), two electron (1, 2) system. Applying the Variation Method provides the triplet and

singlet wavefunctions ψ_T and ψ_S , as well as their respective energies E_T and E_S. These are defined in Figure 1.2, where S is the overlap density integral, Q is the VB Coulomb integral and J is the VB exchange integral. For two weakly interacting radicals, the orbital overlap is small ($S^2 << 1$) and the energy difference between the singlet and the triplet states, ΔE_{ST}, is approximately equal to -2J.

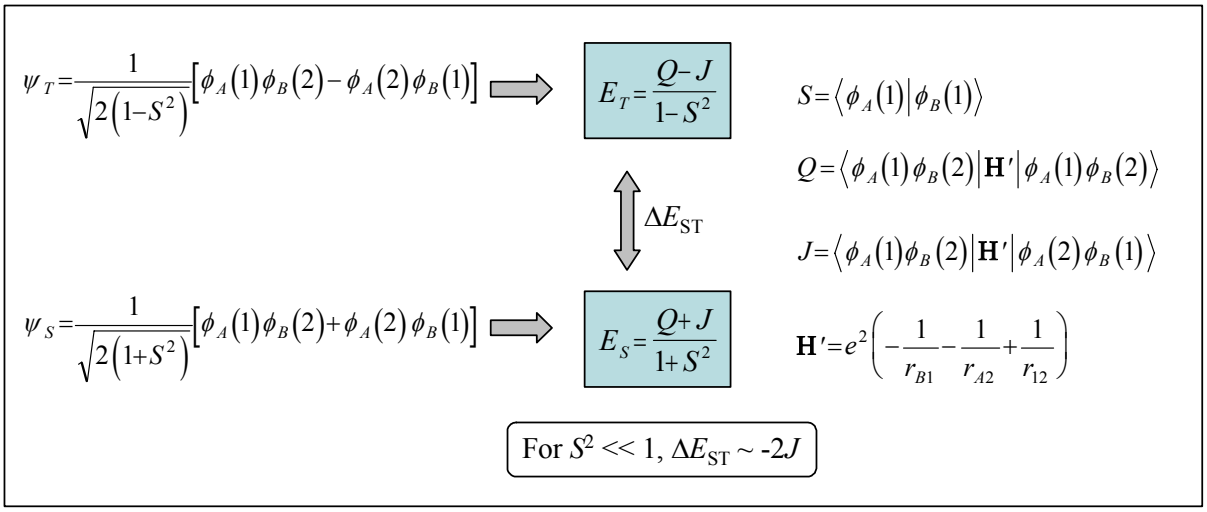

Figure 1.2 The energy difference between the singlet and triplet states, ΔE_{ST}, of two weakly interacting radicals.

The exchange integral J is expanded into its three terms in Figure 1.3, two of which are equivalent. The $j'|S|$ term is the integral that involves the attraction of the overlap density with the two nuclei, and j is the integral that corresponds to the repulsion of the overlap density with itself.[94] Since the energy difference between the singlet and triplet states is equal to 2J, the ground state, and thus the type of magnetic interaction in a particular system, is governed by the sign and magnitude of the exchange interaction J. For $J > 0$, the triplet state (FM) is the ground state, but for $J < 0$, the singlet state (AFM) is the ground state. Therefore, in the 2J expression, +2j is considered the FM term because it stabilizes the triplet state, whereas $-4j'|S|$ is the AFM term as it stabilizes the singlet state.

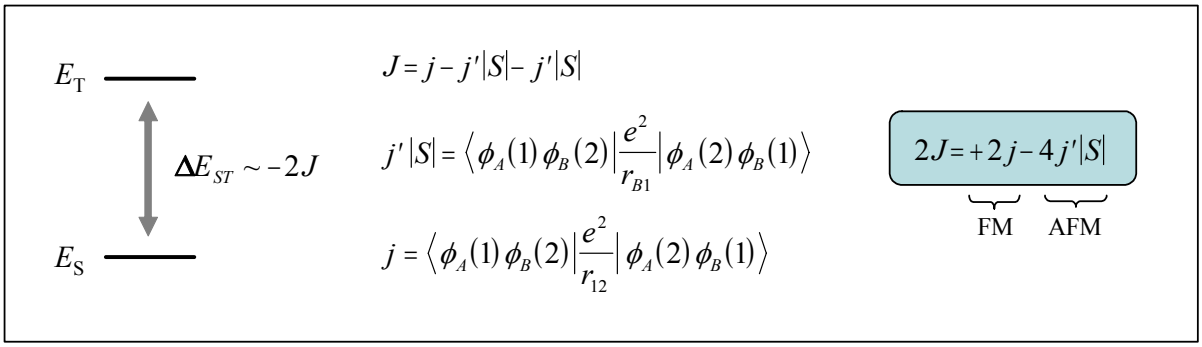

Figure 1.3 The energy difference, ΔE_{ST}, as a function of the exchange integral J.

The magnitude of the overlap integral S, has a significant effect on the sign and magnitude of $2J$, and therefore the ground state of the system. When $|S| >> 0$, the AFM term dominates the $2J$ expression so that $J < 0$, and the singlet state is favoured. However, when $|S| \sim 0$, the AFM term diminishes, allowing for the equation to be controlled by the FM term, with $J > 0$. Therefore, ferromagnetism in molecular materials is favoured by orthogonal, yet strongly interpenetrating overlap between magnetically active orbitals.

The extent of orbital overlap between molecules in a particular lattice can be studied using Extended Hückel (tight-binding) Theory (EHT) band structure calculations. The results are plotted as the energy as a function of direction in k-space and consist of the crystal orbitals (COs) that arise from the radical SOMOs in the unit cell.[‡] The behaviour of the dispersion curves indicates the degree and type of interaction between molecules in the lattice. An example of this is illustrated in Figure 1.4 for a model system consisting of a 1D-array of π-stacked thiazyl radicals, each possessing a simple two-site antibonding π* SOMO. When the radicals are directly superimposed (Figure 1.4a), intermolecular overlap S is large and antibonding (at $k = 0$), and the dispersion curve is characteristic of a 1D-string of σ-bonded p-orbitals, that is, dE_k/dk is negative and the electronic bandwidth W is large. As the radical stacks slip progressively away from a directly superimposed arrangement, the phase difference between the two atomic orbitals of

[‡] In a simple Hückel description of the electronic band structures of radicals, the SOMO constitutes the single basis set function. In the extended Hückel description, a full valence shell atomic orbital basis set is used.

the SOMO on each radical give rise to destructive interference in the intermolecular interactions, so that overall both S and W decrease. At some point along the slippage coordinate perfectly orthogonal overlap is encountered (Figure 1.4b), a condition that nullifies CO dispersion and affords a zero bandwidth. Beyond this null point orbital overlap re-emerges and W increases, but now the net intermolecular overlap (at $k = 0$) is bonding, and the dispersion curve is characterized by a positive dE_k/dk (Figure 1.4c). For the arrangements where $|S|$ is large (Figure 1.4a and c), AFM exchange interactions are anticipated, but when S is small (Figure 1.4b), it is possible that FM exchange will be observed.

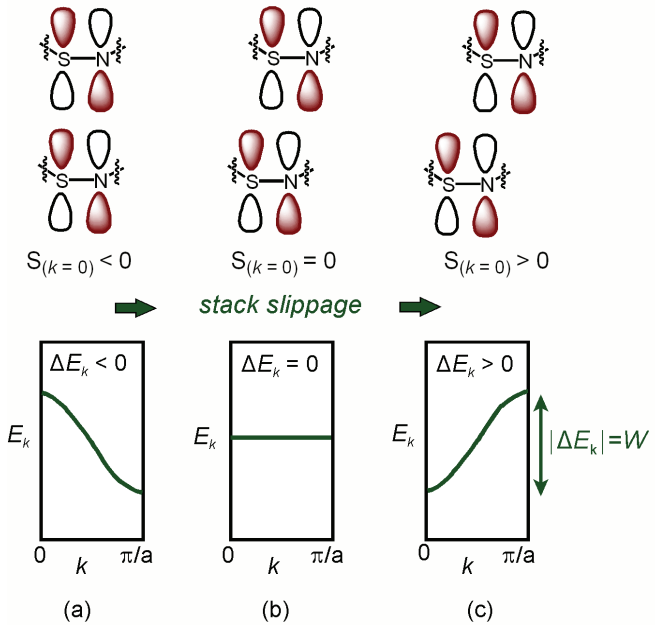

Figure 1.4 Dispersion curves of a model 1D π-stack of thiazyl radicals as a function of stack slippage.

It has been shown above that the sign and magnitude of the exchange energy J indicates the type (FM or AFM) and strength of the magnetic exchange between two interacting molecules. This value can be estimated for a radical and each of its nearest neighbours in a lattice using Density Functional Theory (DFT) methods, where the experimental magnetic properties are considered to be a composite of all of the individual interactions.[95] Typically, the broken symmetry method is employed,[96] which bypasses the difficult-to-compute open-shell singlet state (E_S) by calculating the energy of the hypothetical broken

symmetry singlet state (E_{BSS}). These energies, along with that of the triplet state (E_T), are shown in Figure 1.5, where the energy difference between E_{BSS} and E_T is J, and ΔE_{ST} is equal to $2J$. With reference to the Heisenberg Hamiltonian, $H_{ex} = -2J\{S_1 \bullet S_2\}$,[97] where J is the magnetic coupling constant between two centers and S is the total spin operator, the exchange energy (J) for any pair of interacting radicals can be estimated according to the J expression in Figure 1.5. In this equation, E_{BSS} and E_T are the single point energies of the broken-symmetry singlet and triplet states, and $\langle S^2 \rangle$ is the respective expectation value. This approach has been applied to several radical-based systems, including nitrogen-centered radicals,[98] heterocyclic thiazyls[99,100] and selenazyls,[101] and also phenalenyls,[102] to determine the dominant magnetic exchange interactions between molecules and to elucidate the magnetic exchange pathways within the system.

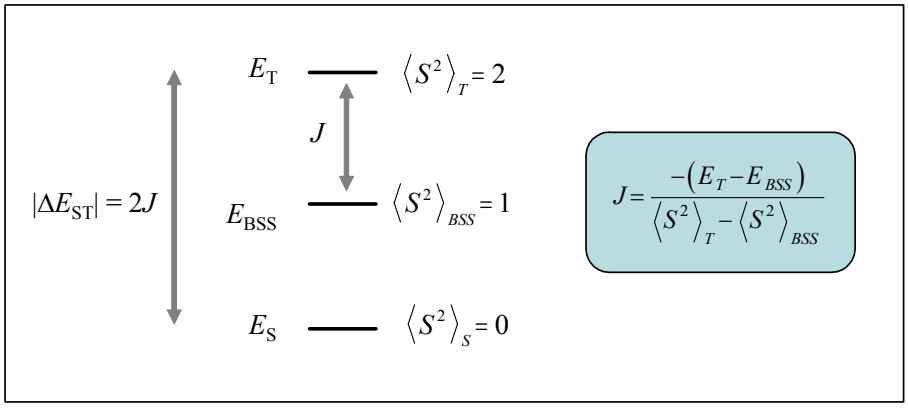

Figure 1.5 The relative energies of the singlet (E_S), broken symmetry singlet (E_{BSS}) and triplet (E_T) states, along with the expression for the exchange energy J, using the broken symmetry method.

1.3 Molecular Conductive Materials

Similar to the field of molecular magnetism, the development of organic metals and superconductors without the use of metallic elements,[‡] is also a very active field of research. As conductivity in neutral radicals is one of the primary goals in the Oakley group, a more extensive discussion

[‡] See Appendix A.4 for a range of conductivity behaviour in selected elemental and synthetic compounds.

of molecular conductors is presented. For electrical conductivity to occur in any system, there are two features that are required. The first is the presence of charge carriers and the second is the existence of a pathway by which the carriers can move through the material. As organic materials usually exhibit filled valence bands and vacant conduction bands, molecular conductors have traditionally relied on charge transfer to generate charge carriers. This approach has led to the field of charge transfer salts, radical ion conductors, and conducting polymers, and typically required the use of two components. Alternatively, neutral radicals have been used as building blocks for molecular conductors, and unlike the previous systems, these materials naturally possess partially filled energy bands and therefore do not require a second component.

1.3.1 Charge Transfer Salts

The field of charge transfer (CT) salts began for the most part with the report of the π-molecular acceptor TCNQ (tetracyano-*p*-quinodimethane) in 1962,[103] and the discovery of the high conductivity of its salts.[104] Conductivity is possible in these TCNQ salts because (i) the crystal structures consist of segregated π-stacks of cation and anion molecules, allowing for good orbital overlap along the stacks and the development of an energy band, and (ii) charge transfer from the donor to acceptor species which generates the charge carriers. With strong interactions between molecules the electrons are partially delocalized and able to migrate along the π-stacking direction. It was not until a large number of TCNQ salts were prepared, with both organic and inorganic cations, that it was understood that partial charge transfer was necessary for high conductivity.[105]

When charge transfer is complete, there is one electron per site giving a half filled energy band (f = ½) and a situation in which the on-site Coulomb repulsion energy U is the largest. This energy is large because the repulsion between two electrons on the same site must be overcome for charge transport to occur (Figure 1.6a). Its effect on conductivity is demonstrated by the insulating [Na][TCNQ] salt, which has complete charge transfer and exhibits a room temperature conductivity $\sigma_{RT} \sim 10^{-5}$ S cm^{-1}.[106] Conversely,

when there is partial charge transfer ($f \neq ½$), there is no longer one electron per site (Figure 1.6b). Instead, in the case of TCNQ, there are empty sites and the movement of an electron into one of these sites requires much less energy than the previous arrangement. Obtaining a level of band filling other than $f = ½$ can be achieved by either partial charge transfer, as in the N-methylphenazinium salt, [NMP][TCNQ] ($\sigma_{RT} \sim 10^2$ S cm^{-1}),[107] or by using mixed ratios as for the 1:2 acridinium salt, [Ac][TCNQ]$_2$ ($\sigma_{RT} \sim 10^2$ S cm^{-1}).[108]

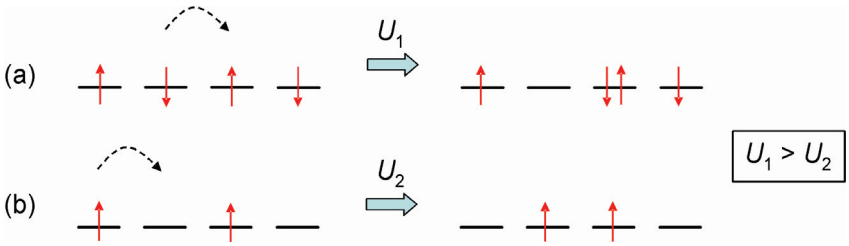

Figure 1.6 The on-site Coulomb repulsion energies (U) of systems with (a) $f = ½$ and (b) $f \neq ½$.

When the good π-donor TTF (tetrathiafulvalene) **1-39** was combined with the good π-acceptor TCNQ **1-40**, the first organic metal was discovered (Figure 1.7).[109] The TTF-TCNQ salt has a crystal structure consisting of independent TTF and TCNQ π-stacks, with partial charge transfer from the valence band of the donor to the conduction band of the acceptor, leading to partially filled energy bands. The TTF-TCNQ salt has a σ_{RT} value of ~ 4 x 10^2 S cm^{-1}, with conductivity increasing when temperature is decreased, reaching a maximum conductivity of ~10^4 S cm^{-1} at 60 K.[105] To improve the transport properties of TTF-TCNQ, both the donor and acceptor molecules have been modified, leading to an immense number of CT salts.[110] Of particular interest is the incorporation of selenium into TTF, to give TSF (tetraselenafulvalene) **1-41**. When co-crystallized with TCNQ, the resulting 1:1 CT salt was isomorphous to that of TTF-TCNQ and the presence of selenium afforded a doubling of the σ_{RT} value.[111]

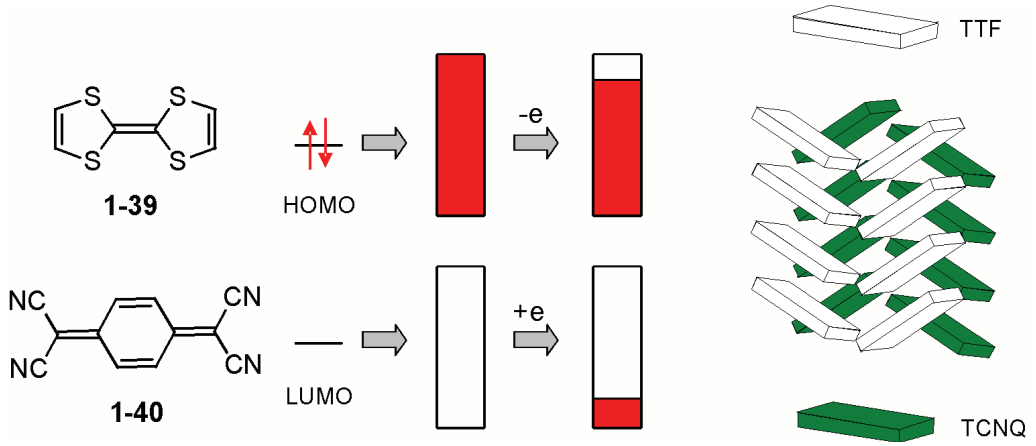

Figure 1.7 The charge transfer salt TTF-TCNQ, with packing motif (right). HOMO is the highest occupied molecular orbital, and LUMO is the lowest unoccupied molecular orbital.

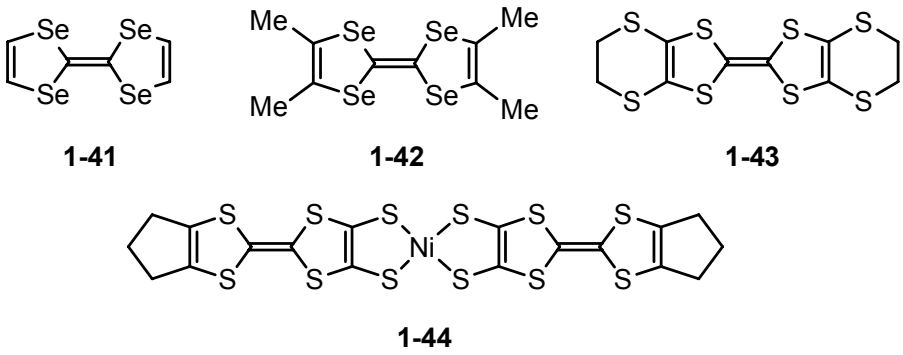

With a view to simplifying the CT salts and controlling the degree of charge transfer, systems referred to as the radical ion conductors (RICs) were produced. These materials typically employed organic π-molecular donors with inorganic counterions, where the charge of the anion fixed the degree of CT. Two principle donors have been studied, both modified versions of TTF, and a vast array of radical cation salts have been generated.[112] The first group were termed the Bechgaard salts, which used TMTSF (tetramethyl-tetraselenafulvalene) **1-42** as the π-donor, with salts of the form $[TMTSF]_2[X]$, where, for example, X = PF_6^-, AsF_6^-, NO_3^-.[113] The other group used BEDT-TTF (bis(ethylenedithio)tetrathiafulvalene or ET) **1-43** as the electron donor, to give the $[ET]_2X$ salts, with X being a monovalent anion such as I_3^-.[114] These 2:1

compounds were obtained by electrochemical oxidation of the donor species in the presence on the anion, which serves only to balance the charge. By virtue of their mixed valency, the donor molecules have a band filling of $f = ¾$, allowing for metallic behaviour in several systems. Superconductivity has also been observed for a few examples at low temperatures.[115,116]

As an alternative approach, the donor and acceptor species have been incorporated into a single molecule, thereby alleviating the difficulties associated with two component systems. These closed-shell materials consist of neutral transition metal complexes that have extended TTF ligands, and the first reported example was $[Ni(tmdt)_2]$ (tmdt = trimethylenetetrathiafulvalenedithiolate) **1-44**.[117] This material exhibits a room temperature conductivity of 400 S cm^{-1} and is metallic down to 0.6 K. Other derivatives have been developed, with variations in both the ligand and the transition metal.[118] These materials are conductive because the separation of their HOMO and LUMO energy levels are sufficiently small that in the solid state the valence and conduction bands overlap and allow for internal charge transfer.

The CT strategy has also been applied to the development of multifunctional materials in which the molecular crystal is composed of two sub-lattices, each exhibiting a distinct property. Typically, this involves the co-crystallization of highly conducting organic π-electron donors, such as TTF derivatives, with magnetically active inorganic anions.[119] For example, Coronado has reported the bifunctional $[BEDT\text{-}TTF]_3[MnCr(C_2O_4)_3]$ complex, in which the crystal structure consists of alternating columns of organic cations with layers of the bimetallic anions.[120] This material is both ferromagnetic at 5.5 K and metallic down to 2 K ($\sigma_{RT} = 250$ S cm^{-1}), although the authors report no indication of an interaction between the two sublattices, a requirement for use in spintronic applications.[71]

1.3.2 Conductive Polymers

The discovery that an organic polymer could be made metallic, with certain modifications, led to the 2000 Nobel Prize being awarded to Shirakawa, Heeger and MacDiarmid for the report of the conductive

properties of doped polyacetylene. Polyacetylene itself, $(CH)_x$, is a carbon chain with alternating single and double bonds, and is insulating. The *trans* isomer has a room temperature conductivity of 10^{-5} S cm^{-1}, where the *cis* conformation has a much lower value of 10^{-10} S cm^{-1}. However, the conductivity of polyacetylene can be increased by approximately 13 orders of magnitude by simply doping it.[121] Partial oxidation or partial reduction of $(CH)_x$ by a variety of dopants has provided a range of materials and properties,[122,104] although the highest conductivity is observed for the AsF_5 doped species, $[(CH)(AsF_5)_{0.14}]_x$, which exhibits a σ_{RT} of 560 S cm^{-1}.[123] Variations to the $(CH)_x$ backbone have been pursued by replacing hydrogen with other substituents, as in $(CHCR)_x$ where R = C_6H_5, CN, CF_3.[124] However, when doped, none of these materials reach the high σ_{RT} values of doped polyacetylene. Other polymers have been explored, including poly(pyrrole),[125] poly(thiophene)[126] and poly(selenophene),[127] and all require doping to achieve their conductive properties, with none reaching the high conductivity of doped $(CH)_x$.

Unlike polyacetylene, the inorganic compound poly(sulfur nitride) $(SN)_x$ does not require doping to display metallic behaviour. This material exhibits a conductivity of 2 x 10^3 S cm^{-1} at 300 K, with conductivity increasing with decreasing temperature.[128] Not only was poly(sulfur nitride) the first metallic polymer to be reported, it was also the first nonmetal-containing, single component material to exhibit superconductivity, with a critical temperature of 0.3 K.[129] It is synthesized *via* the solid state polymerization of molecular S_2N_2,[130] and is isolated as fibrous bundles that consist of parallel chains of covalently linked SN units tightly packed to allow for close interchain interactions.[131] This material has one unpaired π-electron per SN repeat unit and has a partially filled energy band (f = ½),[132] enabling metallic conductivity. Poly(sulfur nitride) has been doped with both donors and acceptors, and the largest improvement in conductivity is by an order of magnitude, which is observed for the bromine-doped material, written as $(SNBr_{0.4})_x$.[130] Attempts to incorporate selenium into the framework have failed,[133] limiting any potential modifications to the framework. Since the precursors used in generating polysulfur nitride are potentially dangerous (explosive), this material is not widely used.

1.3.3 Neutral Radical Conductors

As an alternative to the CT paradigm, Haddon suggested the use of neutral radicals as the building blocks of molecular metals and superconductors.[70] In neutral radical conductors (NRCs), the unpaired electron serves as the charge carrier, thereby obviating the need for two components. This approach requires the use of planar molecules that would form 1D π-stacked arrays in the solid state with strong orbital overlap between SOMOs, similar to that exhibited by TTF-TCNQ. This allows for the development of a half filled energy band ($f = ½$) and inherent metallic conductivity (Figure 1.8b), similar to an elemental metal.[134] Haddon has argued in favour of odd alternant hydrocarbons (OAHs) as ideal candidates for NRCs, specifcally phenalenyl (**1-5**), as it has a non-bonding SOMO and a triad of stable oxidation states (cation, radical and anion). As a consequence, the migration of an electron to and from this molecular orbital would require minimal structural reorganization.

There are, however, several design challenges associated with this model. Firstly, any 1D system with a partially filled energy band is vulnerable to a Peierls distortion.[135] For $f = ½$ materials dimerization can occur, accompanied by the opening of a band gap at the Fermi level (Figure 1.8c). Secondly, $f = ½$ systems have very large on-site Coulomb repulsion energies U (see Section 1.3.1), and this, coupled with a low bandwidth W, results in the localization of the charge carriers and a Mott insulating ground state (Figure 1.8d). Neither of these states exhibit metallic behaviour and therefore must be avoided. As described in Section 1.1, there are ways of suppressing dimerization in molecular radicals, but what is potentially more challenging is overcoming the Mott insulating state that results from the large U. For systems in which the on-site Coulomb repulsion energy U is greater than the bandwidth ($U > W$), a Mott insulating state will result. However, for systems in which W is greater than U ($U < W$), a metallic ground state will prevail. Since these issues are at the forefront of NRC chemistry, a more thorough explanation of the relationships between U and W, and insulators and metals, will now be described.

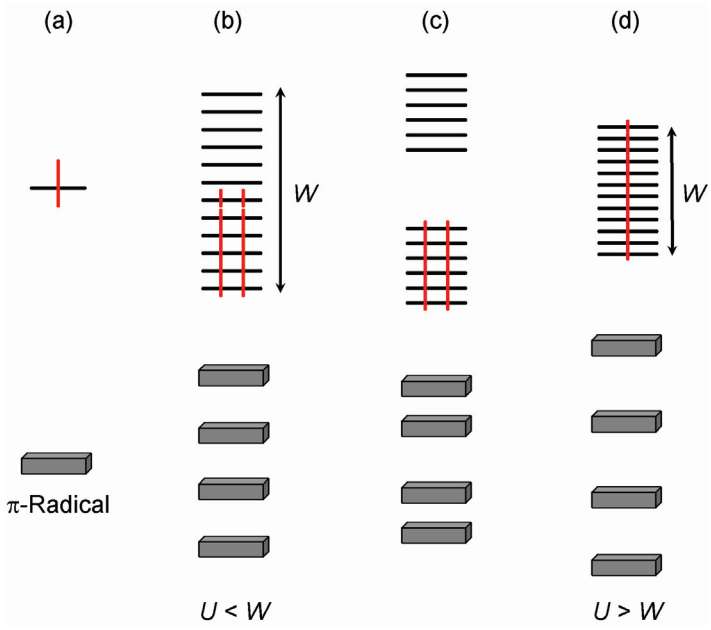

Figure 1.8 Idealized energy levels and packing arrangements associated with (a) a single π-radical, (b) a strongly interacting π-stack with a metallic ground state, (c) a Peierls distorted π-dimer stack with an insulating or semiconducting ground state, and (d) a strongly correlated π-stack with a Mott insulating ground state.

1.3.3.1 Electron Correlation and Mott Insulating States

Not all materials with partially filled energy bands are metallic, they can also be insulators. The difference between the two is the way in which the bands are occupied, and this is shown in Figure 1.9. In the metallic state, the electrons are delocalized and able to move freely from one site to another. In contrast, electrons in the insulating state are localized and there is an energy barrier to charge transport. This electron correlation occurs when the orbital overlap between molecules is weak and the repulsion between electrons is large. Insulating states are particularly prevalent in $f = ½$ systems where the movement of an electron to a neighbouring site must overcome the high on-site Coulomb repulsion energy U. The one-electron band theory that is used to describe these systems is associated with a 1D chain with one atomic orbital ϕ_i and one electron on each lattice site i, as shown in Figure 1.9. Whether the ground state is

metallic or insulating depends on the relationship between the repulsion energy U and the bandwidth W, and this can be obtained using molecular orbital theory. To examine the relative energies of the two states, the system is first simplified to a molecular dimer, in which the metal and insulator states of the chain are equivalent to the low-spin and high-spin states of the dimer, respectively (Figure 1.9).[136]

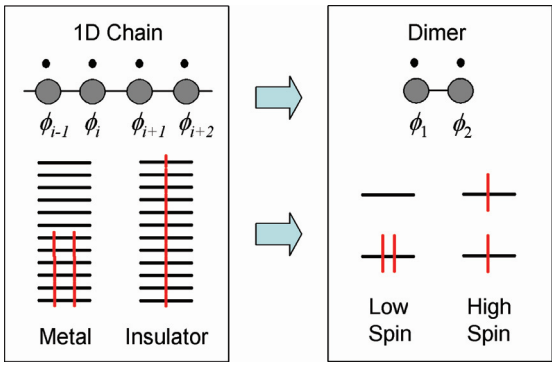

Figure 1.9 The metal and insulator states of a 1D chain and the low-spin and high-spin states of a dimer.

In Simple Hückel molecular orbital (SHMO) theory, when the two orbitals (ϕ_1, ϕ_2) within the dimer overlap, two molecular orbitals are formed, ψ_1 and ψ_2, with energies ε_1 and ε_2, as shown to Figure 1.10. At the SHMO level, the difference between the two energies (ε_1 - ε_2) is equal to 2β, where β is the resonance integral. For this two electron system, the levels can be occupied to give either a high-spin state (a triplet) or a low-spin state (a singlet).

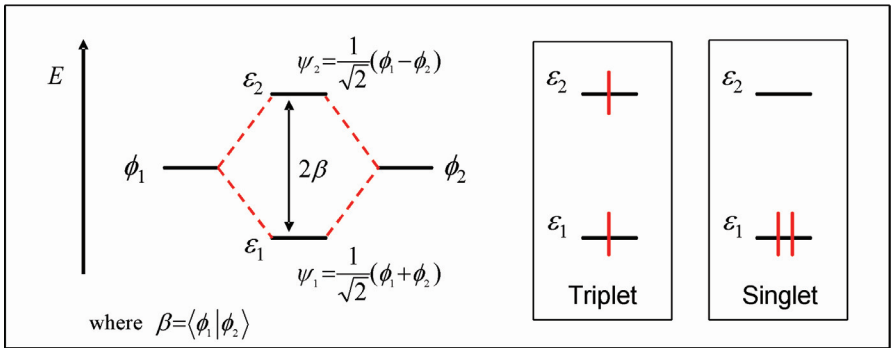

Figure 1.10 The energy level diagram of a dimer using SHMO theory, with triplet and singlet energy states.

If the SHMO effective Hamiltonian is replaced by one in which electron repulsion is explicitly included, and the antisymmetrized versions of ϕ_1 and ϕ_2 are employed, the singlet and triplet energy states, E_S and E_T respectively, can be obtained. These energies are expressed in Figure 1.11,[136] in terms of the orbital energies ε_1 and ε_2 and the Coulomb integral J_{ij}. The energy difference, ΔE_{ST}, is a function of the ε_1 and ε_2 energies and the repulsion integral J_{12}.

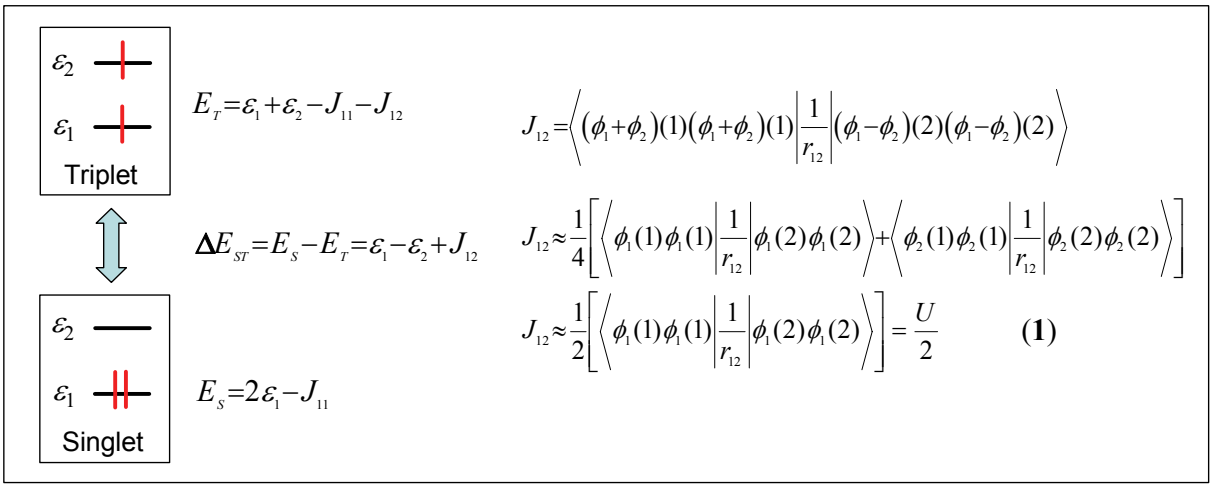

Figure 1.11 The energy difference between singlet (low-spin) and triplet (high-spin) energy states, along with the definition of the Coulomb integral J_{12}.

The J_{12} term can be simplified by expanding it and keeping only the on-site ($\phi_i\phi_i$, not $\phi_i\phi_j$) Coulomb repulsion integrals, according to equation (**1**) in Figure 1.11. Since $J_{12} = U/2$ and $\varepsilon_1 - \varepsilon_2 = 2\beta$ from Figure 1.10, the energy difference between the singlet state and the triplet state has been reduced to an expression consisting of the repulsion energy U and the orbital overlap β, as shown in Figure 1.12. Keeping in mind that $\beta < 0$ and $U > 0$, the ground state can be determined by the sign of ΔE_{ST}. Therefore, if $\Delta E_{ST} < 0$, then $2\beta > U/2$ and the singlet (low-spin) energy state is the ground state. Alternatively, if $\Delta E_{ST} > 0$, then $2\beta < U/2$ and the ground state is the triplet (high-spin) state. Extending this two-site system to a 1D chain in the solid state, and developing the low-spin and high-spin states into energy bands as shown in Figure 1.12, the energy difference between a Mott insulating ground state and a metallic ground state is obtained.

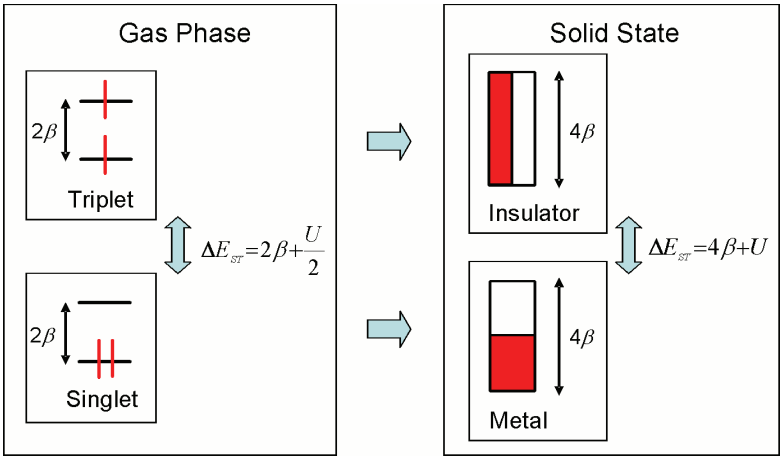

Figure 1.12 Extension of the singlet and triplet states of a dimer to the metal and insulator states of a solid.

For systems with Mott insulating ground states, $U > W$ (where $W = 4\beta$), and the metallic state is higher in energy, as illustrated in Figure 1.13. As W is increased, however, there becomes a point when $U \sim W$ and the two states are approximately equal in energy. As W is increased further, so that $W > U$, there is a state crossover and the metallic state is now lower in energy, making it the ground state. Essentially, systems with partially filled energy bands can be made metallic if the bandwidth is large enough to overcome the on-site Coulomb repulsion energy, and this is the strategy used in developing molecular metals from neutral radicals.

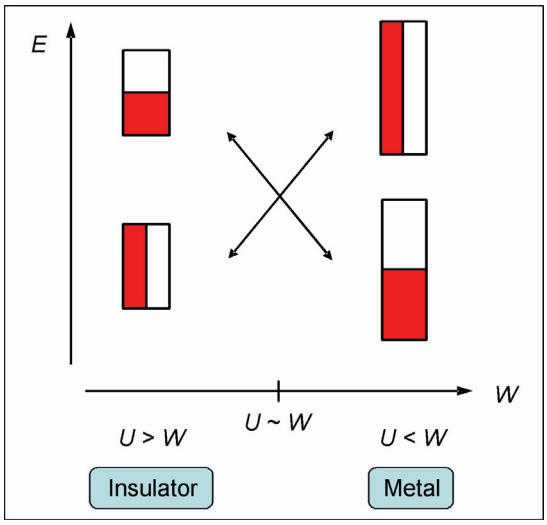

Figure 1.13 Crossover between a Mott insulating ground state and a metallic ground state for a 1D chain.

For any system, the solid state bandwidth W can be approximated using, for example, Extended Hückel Theory, but the Coulomb energy U is more difficult to assess. For a neutral radical (R·) system, the movement of an electron from one molecule to the next generates a cationic (R^+) and anionic (R^-) species as shown in Figure 1.14. This process is associated with the loss of an electron from one molecule (the ionization potential, IP) and the gain of an electron to another molecule (the electron affinity, EA). The energy needed to move the electron can be interpreted as the repulsion energy between two electrons on the same site, that is, U.[137]

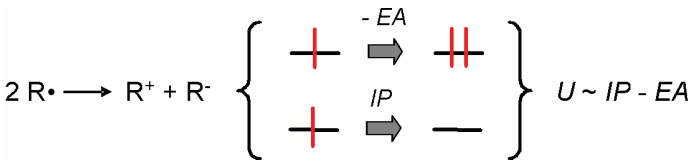

Figure 1.14 Relating U to the ionization potential (IP) and electron affinity (EA) of a radical (R·) system.

In the gas phase, U is equal to the disproportionation enthalpy ΔH_{disp} (= IP - EA), which can be calculated using computational methods. In solution, the reaction in Figure 1.14 corresponds to the electrochemical half-wave potentials of the oxidation ($E_{1/2}^{(0/+1)}$) and reduction ($E_{1/2}^{(-1/0)}$) processes of the radical. Therefore, U can be related to the electrochemical window E_{cell} (= $E_{1/2}^{(0/+1)}$ - $E_{1/2}^{(-1/0)}$) of a particular system. In the solid state however, U is not so easily obtained, and is instead determined indirectly. It has been well established that the trends in ΔH_{disp} and E_{cell} of a series of related compounds mimic the trends in U.[138] Therefore, neutral radicals with lower ΔH_{disp} and E_{cell} values have lower on-site Coulomb repulsion energies U, and it is these materials that are better suited for use as neutral radical conductors.

1.3.3.2 Examples of Neutral Radical Conductors

In order to obtain neutral radical conductors, systems with low on-site Coulomb repulsion energies U and large bandwidths W are needed, with $\sigma \sim W/U$. High conductivity can be achieved either by reducing U, through the use of polarizable molecular frameworks, or by maximizing orbital overlap to enlarge W.

Oftentimes a combination of strategies are used in developing conductive materials, and although metallic behaviour has not yet been observed, great strides have been made towards realizing this goal.

Haddon's approach to overcoming *U* and obtaining neutral radical conductors based on the phenalenyl (PLY) skeleton follows two separate pathways. The first is by combining two or three PLY units into a single molecule to move away from a half filled energy band entirely, and the second is by incorporating heavy elements into the framework, to make PLY more polarizable and increase orbital overlap between molecules. The first strategy involved the bis- and tris-spiro-phenalenyl compounds **1-45** and **1-46** in which a band filling of 1/4 and 1/6 is achieved in the solid state, respectively. Many substituent modifications have been made to the **1-45** compounds, affording several different structural motifs and a rich array of electronic behaviour.[139] The room temperature conductivity values ranged between 10^{-7} and 10^{-2} S cm^{-1} depending on the compound, with a σ_{RT} value of 0.05 S cm^{-1} observed for **1-45b** (R = hexyl).[140] Some derivatives exhibit a reversible phase transition between a diamagnetic state and a paramagnetic state with changes in temperature. For one derivative, this transition is hysteretic allowing for bistability in three physical channels (magnetic, electrical and optical).[141] The high conductivity and Pauli-paramagnetism exhibited by other derivatives, including **1-45b** (R = cyclohexyl) with σ_{RT} reaching 0.3 S cm^{-1}, has been rationalized using Anderson's Resonating Valence Bond (RVB) model.[142] The recently reported tris-phenalenyl molecule **1-46**, has a complex structural arrangement with some electronic communication between species, although the conductivity is low ($\sigma_{RT} \sim 10^{-6}$ S cm^{-1}).[143]

The second approach taken by Haddon was to incorporate sulfur into the PLY framework, and so far two derivatives have been isolated, **1-9** and **1-47**. Dithiophenalenyl **1-9** was first reported in 1978, at which time it was demonstrated that the radical was monomeric in solution.[144] However, it took nearly thirty years before the compound was fully characterized in the solid state.[19] Unlike all other reported PLY-based derivatives, its crystal structure did not involve σ-dimers, representing the first example to be stabilized against σ-dimerization without the use of bulky substituents. However, the structure of **1-9** does consist of π-dimers and the material exhibits insulating behaviour with $\sigma_{RT} < 10^{-6}$ S cm^{-1}. Continued

positioning of sulfur around the phenalenyl core afforded tetrathiophenalenyl **1-47**.[145] Like **1-9**, this compound did not form C-C σ-bonded dimers in the solid state, although the crystal structure reveals a rupture of one of the dithiole rings and the formation of a S-S σ-bonded dimer [**1-47**]$_2$.

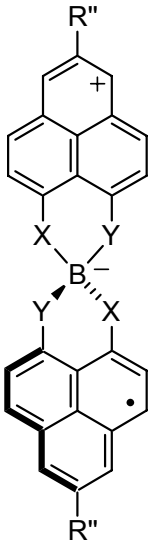

1-45

a X = NR, Y = NR', R" = H
b X = NR, Y = O, R" = H
c X = O, Y = O, R" = Me, H

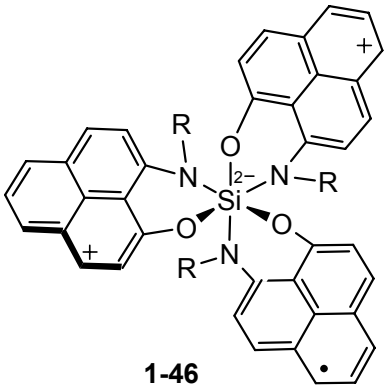

1-46

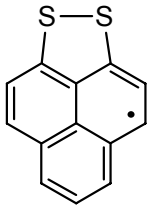

1-9

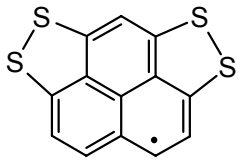

1-47

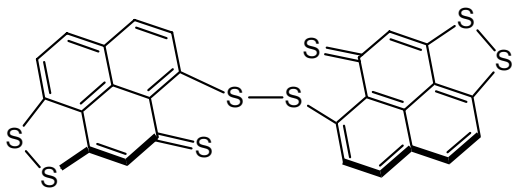

[**1-47**]$_2$

Betainic radicals, specifically the pyrimido-fused TTF derivatives **1-48** and **1-49** developed by Neilands, also show potential for use as single component conductors.[146] These materials have an unpaired electron and a charge separation with the positive charge localized on the TTF portion of the molecule, and the negative charge centered on the more electronegative pyrimidine moiety. The betainic radicals have half filled energy bands, but as a result of their highly polarizable nature, *U* is reduced. The pyrimido-fused TTF derivatives are able to form multiple intermolecular hydrogen bonds in the solid state similar to nucleic acids, however, these systems are hindered by spin-quenching dimerization. Magnetic measurements indicate the presence of less than 3 % free Curie spins for all reported compounds. Nonetheless, several derivatives exhibit semiconducting behaviour with σ_{RT} reaching 10^{-1} S cm^{-1}.

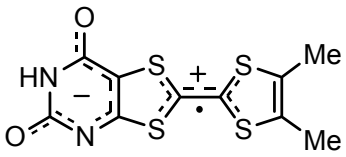

1-48

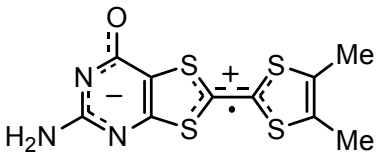

1-49

An alternative approach is taken by Oakley who pursues thiazyls and selenazyls as neutral radical conductors. The presence of the large S/Se atoms within the molecular framework should provide good orbital overlap and a bandwidth large enough to overcome *U*. His work was initiated by the combined discoveries of the metallic polymer $(SN)_x$[130] and the π-stacking motif observed for a cyclic thiazyl radical.[147] Many sulfur-nitrogen and selenium-nitrogen radicals have been developed by Oakley and a great deal of progress has been made towards obtaining a neutral radical conductor. This work is discussed in the following section.

1.4 Thiazyls as Neutral Radical Conductors

An important design criterion for developing NRCs is the need for systems with low *U* values, and this has been an ongoing challenge in the Oakley group. Several thiazyl and selenazyl radicals have been explored over the years (Section 1.1), and the gas-phase ion energetics and the experimental cell potentials for several of these (Scheme 1) are listed in Table 1.1. The trends in these two parameters provide a handle on the more elusive *U*, with low values of ΔH_{disp} and E_{cell} indicating a low *U*. As described earlier, many of the monofunctional derivatives **1-20**, **1-23** and **1-25**, when isolated, formed π-dimers in the solid state, thereby quenching any potential charge carriers and opening up a band gap at the Fermi level. Even when dimerization could be suppressed, either by incorporating steric bulk or by increasing temperature, conductivity did not improve, demonstrating that these materials were Mott insulators. Attaching strong electron withdrawing groups, such as in **1-50** or **1-51**, was able to lower both ΔH_{disp} and E_{cell}, but this was insufficient to overcome the Mott insulating condition where $U > W$. For the monomeric compounds, the room temperature conductivity values were less than 10^{-6} S cm^{-1}, although when converted into charge transfer salts these values were improved.[148]

Table 1.1 Computed Gas-Phase Ion Energetics[a] and Cell Potentials[b] for Radicals in Scheme 1.

Compound	*IP*	*EA*	ΔH_{disp} [c]	$E_{1/2}^{(-1/0)}$	$E_{1/2}^{(0/+1)}$	E_{cell} [d]
1-20	7.82	1.02	6.81	-0.94	0.59	1.53[e]
1-23	6.77	-0.41	7.18	---	---	---
1-25	7.01	0.34	6.67	-1.1[f]	0.38	1.48[g,h]
1-50	7.60	2.14	5.46	-0.06	1.00	1.06
1-51	7.81	2.57	5.23	0.15[f]	1.14	0.99[g]
1-27	6.16	1.39	4.77	-0.95	-0.130	0.77[i]

[a] Adiabatic ΔSCF values at the B3LYP/6-31G(d,p) level, R = H for all systems, values in eV. [b] In MeCN, ref. SCE, values in V. [c] $\Delta H_{disp} = IP - EA$. [d] $E_{cell} = E_{1/2}^{(0/+1)} - E_{1/2}^{(-1/0)}$. [e] R = Me.[149] [f] Irreversible behaviour, E_{pc} value quoted. [g] E_{cell} estimated as $E_{pc}^{(0/+1)} - E_{pc}^{(-1/0)}$. [h] R = Cl, R′ = C_6F_5.[43c] [i] R = Me.[45a]

Scheme 1

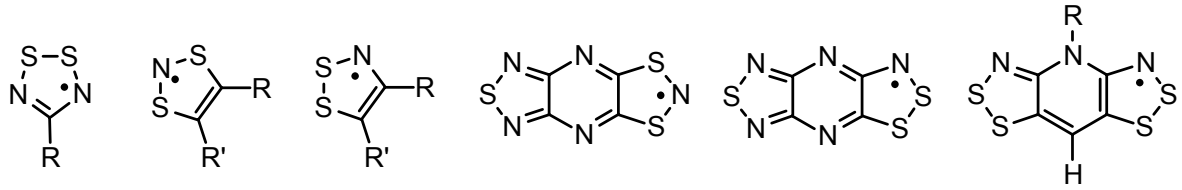

1-20 **1-23** **1-25** **1-50** **1-51** **1-27**

It became apparent that the on-site Coulomb repulsion energy *U* would have to be drastically reduced in order to offset the *W*/*U* ratio and enable thiazyls to be effective as single-component molecular metals. Therefore, a new class of radicals was developed in which a closed-shell 1,2,3-dithiazole ring was in resonance with an open-shell 1,2,3-dithiazolyl across a pyridine bridging unit, to give the bisdithiazolyls **1-27**. The inclusion of resonance not only decreased the ΔH_{disp} and E_{cell} parameters, but also suppressed π-dimerization entirely. The π-SOMO (**1-52**) demonstrates that the electron is delocalized over the tricyclic framework, and that the R_1/R_2 substituents lie on a nodal plane, thereby inhibiting any influence they may have on the electronic properties of the compound. The substituents do however, have an effect on solid state packing. These belt-line ligands provide the steric bulk necessary to suppress dimerization, as well as cause the slippage of the radical π-stacks. Although the bisdithiazolyls possess very low *U* values, all

derivatives exhibit activated conductivity and are Mott insulators. In hindsight, this is a result of the stack slippage, and reduction in overall bandwidth, observed for these materials. The behaviour of some of the first reported bisdithiazolyl compounds will be described further, as it was the conclusions drawn from these systems that directed my research goals.

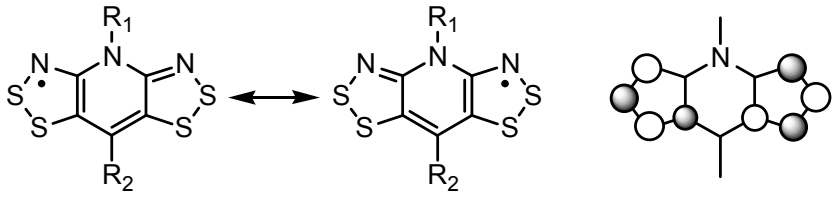

1-27 **1-52**

1.4.1 The Bisdithiazolyls

Many derivatives of **1-27** have been developed, with the R_1/R_2 groups varying in both size and shape.[45] For the most part, the R_2 = Cl compounds effectively represent the behaviour of this class of radicals, and the discussion will be limited to this group, which includes the R_1 = Me, Et, Pr derivatives.[45b] In the solid state, radicals of the methyl compound pack in the orthorhombic space group $P2_12_12_1$, while the ethyl and propyl derivatives form an isomorphous set and arrange in the tetragonal space group $P\bar{4}2_1m$. The magnetic properties of all three compounds are shown in Figure 1.15 in the form of the product χT, where χ is the magnetic susceptiblity, as a function of temperature. These plots indicate that above 100 K the three derivatives are all Curie paramagnets, however, at lower temperatures their behaviour diverges. The methyl compound undergoes a phase change below 95 K that is accompanied by a surge in the magnetic susceptibility with decreasing temperature, indicating the onset of FM exchange. A phase transition is not observed for the ethyl and propyl derivatives, and their low temperature data suggests weak FM and AFM coupling, respectively. Their conductive behaviour is also shown in Figure 1.15, as a log plot of σ as a function of inverse temperature. In all cases the conductivity is activated, with room temperature values between 10^{-5} and 10^{-6} S cm^{-1} and activation energies between 0.4 and 0.5 eV. Although these values are an improvement over previously studied thiazyl radicals, the behaviour of the **1-27** compounds was at first surprising, as the on-site Coulomb repulsion energy *U* was so dramatically reduced.

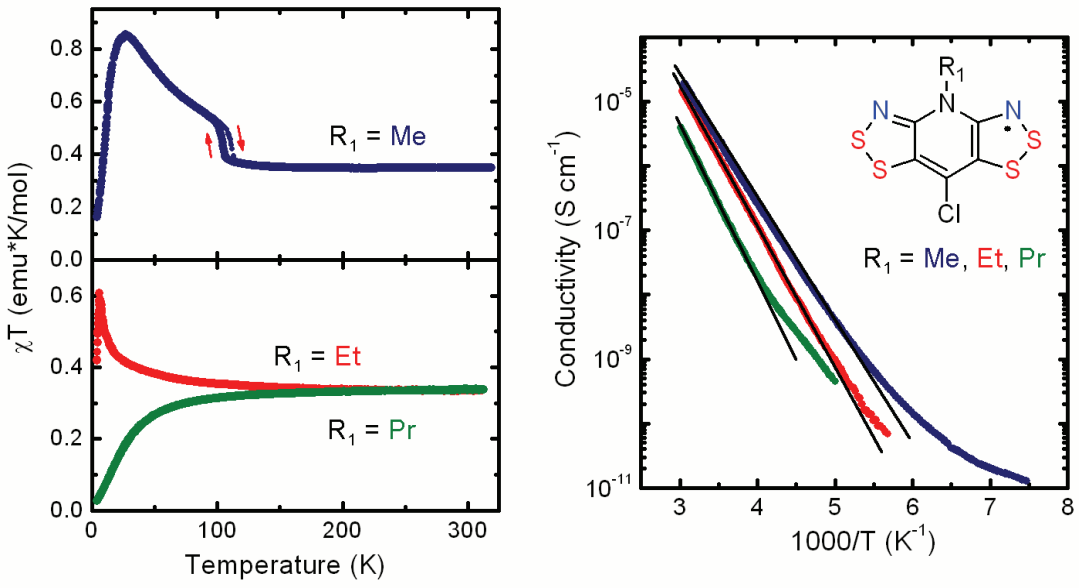

Figure 1.15 Plots of χT vs T (left) and conductivity vs 1/T (right) for compounds **1-27** (R_1 = Me, Et, Pr; R_2 = Cl).

Since conductivity is a function of both *U* and *W* ($\sigma \sim W/U$), the individual packing arrangements were examined in order to determine the degree of orbital overlap between radical SOMOs along the π-stacks, and thus the 1D bandwidth *W*. Although all three compounds, **1-27** (R_1 = Me, Et, Pr; R_2 = Cl), have crystal structures that consist of radical π-stacks, each has a very different direction and degree of plate slippage. Figure 1.16 shows the packing arrangement of a pair of radicals along the stacking direction for the methyl and ethyl compounds. Radicals of the methyl derivative slip primarily along the long axis of the molecule, or the *x* direction, while molecules of the ethyl compound slip predominantly along the short axis, or *y* direction, of the molecule.[‡] Since the structural arrangements of each compound are different, the interactions between the radical SOMOs along the stacks must vary, and it is therefore not surprising that these materials exhibit different properties.

[‡] These *x* and *y* axes are directions of plate slippage along the π-stacks that have been arbitrarily set according to the stacking direction. They are defined in Figure 1.16, and are not related to the crystallographic axes.

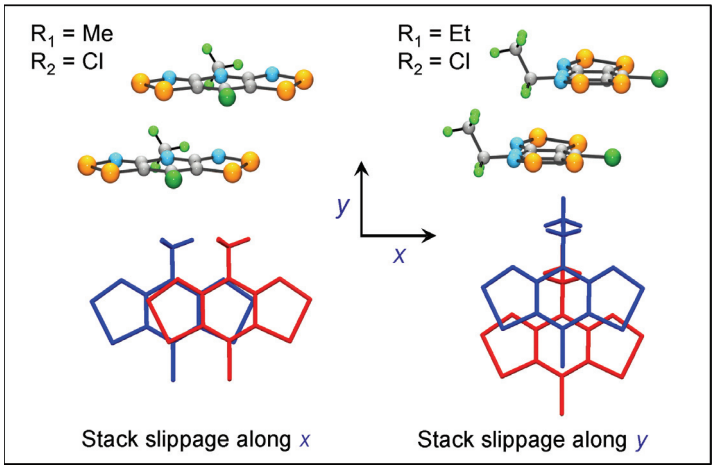

Figure 1.16 Pairs of radicals in π-stacks of **1-27** (R_1 = Me, Et; R_2 = Cl) showing slippage along *x* and *y*.

In order to get a better sense of the interactions along the π-stacks of these compounds, we have performed a series of calculations to probe both the conductive and magnetic behaviour as a function of the direction and degree of plate slippage. A model radical of **1-27** ($R_1 = R_2$ = H) was employed, with an idealized molecular geometry taken from a C_{2v} optimized B3LYP/6-31G(d,p) calculation. We used this model as the building block for a series of (i) EHT calculations of the 1D π-SOMO dispersion energy ΔE_k (where $|\Delta E_k| = W$) and (ii) DFT (B3LYP/6-31G(d,p)) calculations of the pairwise intrastack exchange energy J_π. Both series of calculations considered the effects of all possible translations (slippage) along *x* and *y*, with individual radicals separated by 3.5 Å. The results of the calculations are summarized in Figure 1.17 in the form of surface plots of the EHT 1D dispersion energy ΔE_k and the magnetic exchange energy J_π for the model radical stack of **1-27** ($R_1 = R_2$ = H) as a function of *x* and *y*. Due to the symmetry of the molecular framework, only the [+*x*, +*y*] coordinates are shown.

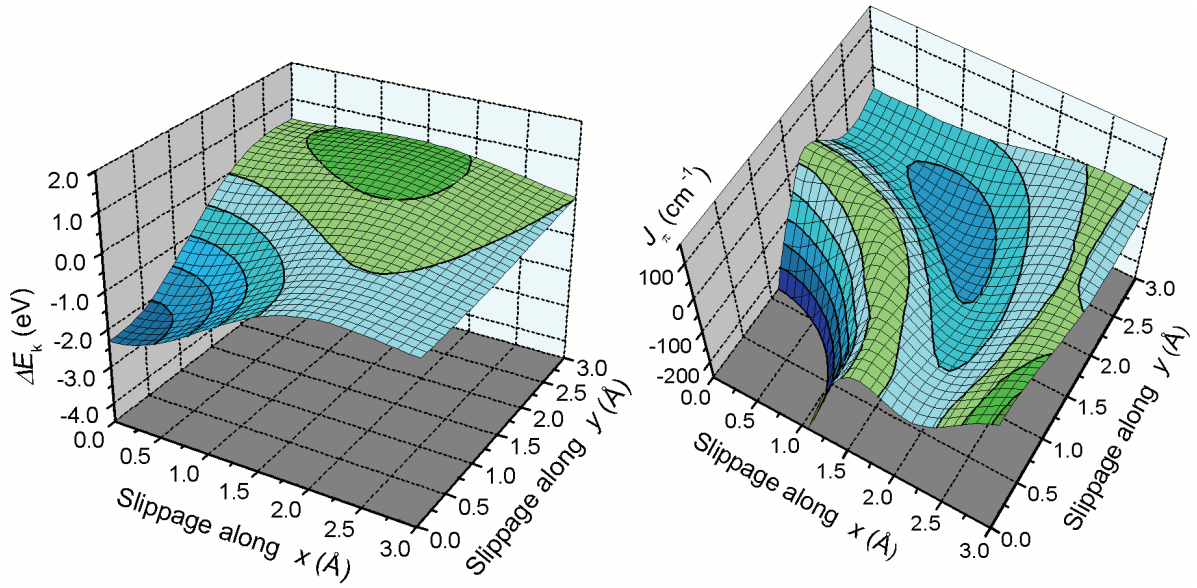

Figure 1.17 The 1D dispersion energy ΔE_k (in eV) (left) and the exchange energy J_π (in cm^{-1}) as a function of x and y for model **1-27** ($R_1 = R_2 = H$). Contour lines are drawn at 0.5 eV (left) and 50 cm^{-1} (right) intervals.

According to the dispersion energy plot (Figure 1.17, left), the suggested region of largest $|\Delta E_k|$ is for direct superposition at [0.0,0.0] where a $|\Delta E_k|$ value greater than 2.0 eV is reached. Another area of relatively high dispersion is near the middle of the map at approximately [1.5, 2.5] where $|\Delta E_k| \sim 0.7$ eV. All other translations along x and y suggest weak, or even orthogonal (at the boundary between green and blue), orbital overlap between radical SOMOs in the π-stack. The surface plot for the magnetic exchange energy J_π (Figure 1.17, right) corresponds quite well to the dispersion energy map, particularly in the light of the well-established relationship between the overlap of magnetically active orbitals and magnetic exchange, as described earlier in Section 1.2.1. Accordingly, the regions of large $|\Delta E_k|$ map onto areas of $J_\pi < 0$ and AFM exchange, while regions with $|\Delta E_k| \sim 0$, correspond to areas where $J_\pi > 0$ and FM behaviour is suggested.

The actual solid state slippage coordinates of **1-27** (R_1 = Me, Et, Pr; R_2 = Cl) were used to test the predictive value of the calculations. Keeping in mind that the surface maps were generated using a model radical **1-27** ($R_1 = R_2$ = H) and a particular interplanar separation (3.5 Å), the results nonetheless translate well to the experimental properties. The room temperature structure of the methyl derivative has slippage coordinates [2.45, 0.07], which places it in a region of low $|\Delta E_k|$ and small negative J_π. The phase transition that occurs below 95 K involves further plate slippage only in the *x* direction giving new coordinates [2.99, 0.03]. This change pushes the structure into the positive J_π region of the map, a change which is consistent with the observation of FM behaviour at low temperature. The R_1 = Et and Pr compounds have coordinates [0.0, 2.15] and [0.0, 2.79], respectively. Both compounds slip exclusively along the *y* direction, but to varying degrees. The R_1 = Et derivative is situated in a region of low $|\Delta E_k|$ and small positive J_π (FM exchange), where the R_1 = Pr compound, also with a low $|\Delta E_k|$, has a small negative J_π value (AFM exchange). Since all three derivatives have small $|\Delta E_k|$ it is not surprising that the conductivity values are low. Also, the small J_π values are consistent with Curie paramagnetism, and the sign of J_π matches the low temperature behaviour of all three compounds.

Overall, the calculations are in agreement with the experimental properties exhibited by the bisdithiazolyl radicals **1-27** (R_1 = Me, Et, Pr; R_2 = Cl). This exercise has provided us with the capability to predict qualitatively the conductive and magnetic behaviour of new structures, as well as to highlight packing arrangements with potentially desirable properties. For example, high conductivity is expected for systems with large $|\Delta E_k|$ values, and therefore compounds that have superimposed π-stacks are potentially good targets. Alternatively, diagonal slippage along *x* and *y* may also provide a structure with high conductivity.

Another way of improving bandwidth is to incorporate the larger selenium atom into the molecular framework. The more spatially extensive orbitals of this chalcogen should provide better orbital overlap between radical SOMOs, and this approach has been used to increase conductivity in charge transfer salts (Section 1.3.1).[111] To probe the influence of the incorporation of selenium, we have repeated the EHT

dispersion energy ΔE_k and DFT magnetic exchange energy J_π calculations on a 1D stack of model radicals **1-55** ($R_1 = R_2 = H$), which has all of the sulfur atoms replaced with selenium. The 3D surface plots are shown in Figure 1.18, and it is readily apparent that the general trends in ΔE_k and J_π are identical to those established for the all-sulfur derivative **1-27** ($R_1 = R_2 = H$) in Figure 1.17. However, for the all-selenium compound, the maxima and minima are more extreme, and interestingly, at direct superposition [0.0, 0.0], a bandwidth ($W = |\Delta E_k|$) of over 3.5 eV is suggested. If compound **1-55** can be prepared, and directly superimposed π-stacks can be obtained, it may be possible to achieve a bandwidth that will overcome U and produce a neutral radical conductor with metallic behaviour.

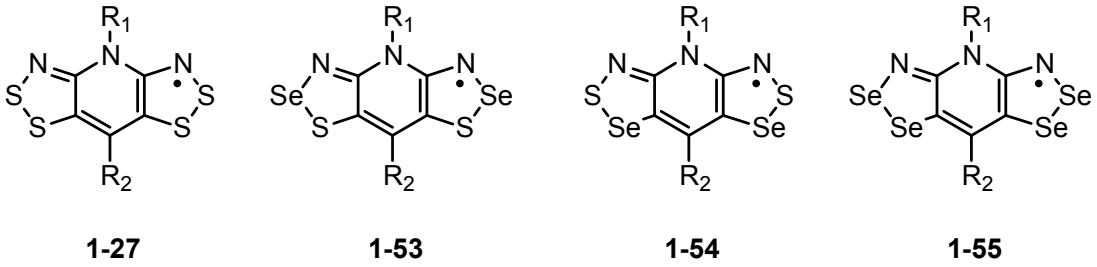

1-27 **1-53** **1-54** **1-55**

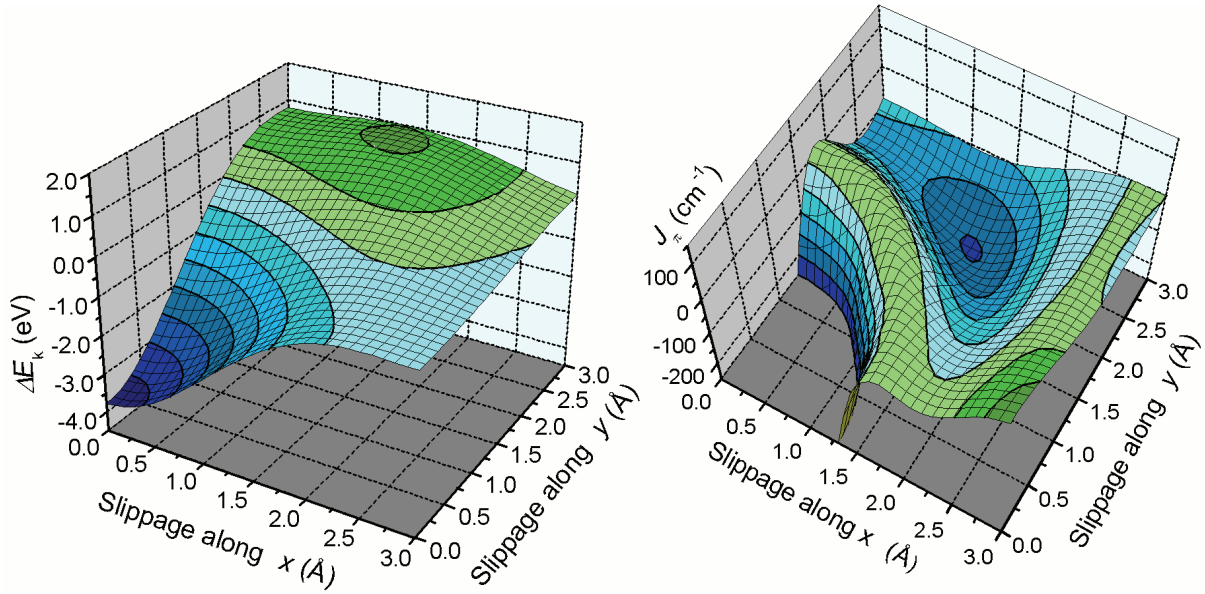

Figure 1.18 The 1D dispersion energy ΔE_k (in eV) (left) and the exchange energy J_π (in cm^{-1}) as a function of x and y for model **1-55** ($R_1 = R_2 = H$). Contour lines are drawn at 0.5 eV (left) and 50 cm^{-1} (right) intervals.

The inclusion of selenium into the bisdithiazolyl framework **1-27** affords three possible isomers, the two mixed S/Se variants **1-53** and **1-54** and the previously mentioned all-selenium compound **1-55**. A large portion of my research has involved the development of these selenium-containing derivatives, and the preparation and transport properties of a selection of these are described in this thesis. However, the discovery of magnetic ordering in several of the compounds is not presented, and will instead be mentioned here. Canted AFM is observed in compounds **1-53** and **1-55** (R_1 = Et, R_2 = H), with Néel temperatures of 18 and 27 K, respectively.[150] These ordering temperatures are not far from Rawson's dithiadiazolyl radical that exhibits a transition to a canted antiferromagnet at 36 K.[65] Several other derivatives have now been found to exhibit FM ordering at low temperatures, and these include **1-53** and **1-55** (R_1 = Et, R_2 = Cl).[151] Curie temperatures of 12.8 and 17.0 K are observed, values that outperform all other molecular non-metal containing ferromagnets reported to date (Section 1.2). The ferromagnetic ordering expressed by derivatives of **1-53** (R_1 = Et R_2 = Me, Br) have also been recently reported.[152] In addition to the high T_C values demonstrated by these materials, large coercive fields reaching 1370 Oe (at 2 K) are observed, establishing that these compounds are relatively hard magnets. The incorporation of selenium demonstrates the importance of the heavy atom effect, and the resulting spin-orbit coupling and magnetic anisotropy, in developing magnetic ordering in molecular compounds.

Not only do several examples exhibit interesting magnetic behaviour, but the selenium-containing radicals **1-53**, **1-54**, **1-55** also possess some of the highest room temperature conductivity values for any thiazyl or selenazyl radical so far. The potential for multifunctional behaviour in neutral radicals, that is, those that display both conductive and magnetic properties, is also now within reach. A great deal has been learned about neutral radical chemistry in the past five years, with the development of many interesting solid state properties and structural motifs. The following section outlines the work presented in this thesis and the contributions that I have made towards the advancement of neutral radicals in materials science.

1.5 Thesis Scope

At the beginning of my graduate work in 2004, the bisdithiazolyls **1-27** had just recently been reported and the properties and behaviours demonstrated by these compounds were used as a starting point for the directions of my own research goals. As resonance delocalization in **1-27** had provided low ΔH_{disp} and E_{cell} values (low U), suppressed dimerization and increased thermal stability, it seemed reasonable to extend this to a new molecular framework. This lead to the development of the bisthiadiazinyls as a new class of resonance-stabilized radical, and their potential as NRCs are discussed in **Chapter 2**. Another research focus was the improvement of the bandwidth in the bisdithiazolyls **1-27**, with the intention of increasing the W/U ratio, and two strategies were followed. The first was to alter the crystal packing so as to obtain direct superposition, an arrangement that is suggested in Figure 1.17 to reach a bandwidth of over 2.0 eV. This was pursued through the replacement of the pyridine ring with a pyrazine ring, and the removal of one of the belt-line ligands. These radicals are presented in **Chapter 3**. The second strategy of improving bandwidth in **1-27** was to incorporate selenium, as it was established by computational studies in Figure 1.18 that this increases W for all slipped π-stack structures. **Chapter 4** describes the development of the synthetic methodologies used to generate the three selenium-containing radicals **1-53**, **1-54** and **1-55**. Several R_1/R_2 derivatives have stemmed from this work, and I have been involved with a number of them. Within the size constraints of this dissertation, I have confined the presentation to only a selection of these. A series of uniquely bonded σ-dimers based on the **1-53** framework are presented in **Chapter 5**, along with their dramatic increases in conductivity with the application of pressure. An entire set of four S/Se radicals **1-27**, **1-53**, **1-54** and **1-55**, that do not dimerize, are described in **Chapter 6**. These materials represent the only complete family that does not show isostructural replacement of selenium for sulfur, and their behaviour has demonstrated the importance of the packing arrangement on transport properties. Two of the set exhibit the highest room temperature conductivity values ever reported for a selenazyl radical, and applying pressure improves this behaviour, nearly reaching the metallic ground state.

Chapter 2

Bisthiadiazinyls as a New Class of Resonance Stabilized Radical

2.1 Introduction

As discussed in Chapter 1, the incorporation of resonance into a molecular radical and the concomitant delocalization of spin density is a typical method of increasing stability. The benefits of resonance are demonstrated by the highly robust nitronyl nitroxides **2-1** and verdazyls **2-2**, examples of which are stable in the presence of both moisture and oxygen.[1,2] It was also established in the previous chapter that the bisdithiazolyls **2-3**, in which the unpaired electron is delocalized across the tricyclic system, are stable in solution and exist as monomers in the solid state.[3] Not only did the incorporation of resonance suppress dimerization in these radicals, it also increased thermal stability and lowered the gas phase disporportionation enthalpy ΔH_{disp} and the electrochemical cell potential E_{cell}, parameters that indicate a lower on-site Coulomb repulsion energy U than the monofunctional thiazyl radicals.[4] A low U is paramount for the use of thiazyls as neutral radical conductors (NRCs), where the bandwidth W must overcome the high U associated with systems having half-filled energy bands. Although the bisdithiazolyls did not achieve a bandwidth greater than U ($W < U$) and were Mott insulators, they did possess features that were superior to all previously studied thiazyls.

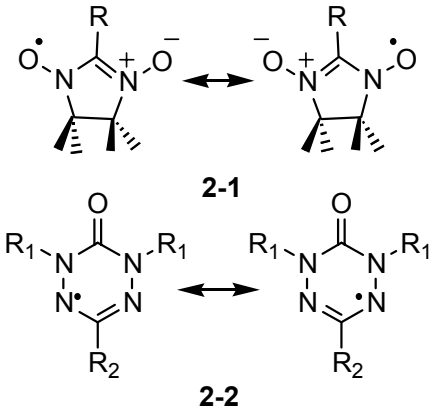

2-1

2-2

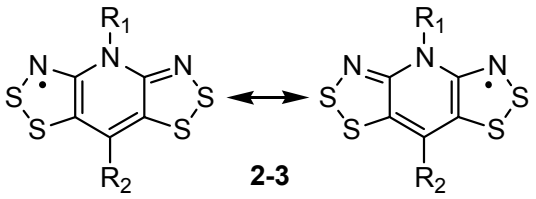

2-3

In the development of NRCs, we wanted to incorporate the positive attributes provided by resonance delocalization to a new molecular framework. We used the same strategy as used for the bisdithiazolyls, where a closed-shell thiazole was linked to an open-shell thiazyl through a pyridine bridging unit. In this case however, the sulfur-nitrogen ring system was based on the thiatriazinyl **2-4**. Several examples of this radical are known,[5] although only one has been characterized in the solid state.[6] In order to incorporate resonance and attach a pyridine ring, the thiadiazinyl framework **2-5** was examined. Only the condensed ring variants of this radical are known, and the per-halogenated compounds are the only examples that are stable enough to be isolated in the solid state.[7] These annelated thiadiazinyls were explored for potential use in liquid crystalline materials.

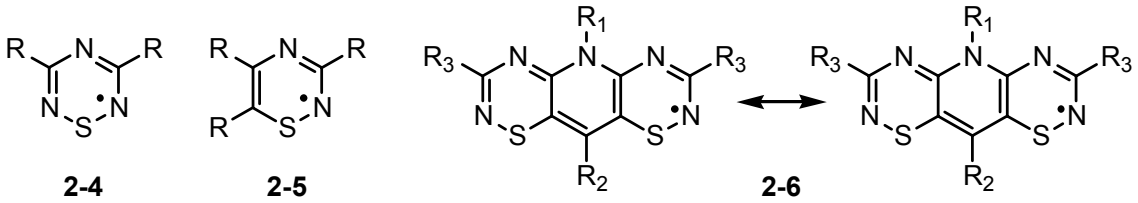

2-4 **2-5** **2-6**

Extending the thiadiazine unit to the desired tricyclic framework affords the bisthiadiazinyls **2-6**. To test if this target radical is suitable for use in NRCs, the ion energetics, that is, the ionization potential (*IP*) and the electron affinity (*EA*), were determined *via* a B3LYP/6-31G(d,p) calculation on a model radical **2-6** ($R_1 = R_2 = R_3 = H$) using the ΔSCF single point energies of the cation, radical and anion species. These, along with the values calculated for the other thiazyl radicals **2-3**, **2-4** and **2-5**, are listed in Table 2.1. The monofunctional radicals **2-4** and **2-5** have relatively high ΔH_{disp} values as a result of their compact electronegative cores. However, when resonance is included, the disproportionation enthalpy drops and the bisthiadiazinyl radical **2-6** has a value comparable to that calculated for the bisdithiazolyl framework **2-3**. This suggests that, like **2-3**, the bisthiadiazinyl has a relatively low value of *U*.

Table 2.1 Computed Gas-Phase Ion Energetics[a] of Selected Thiazyl Radicals

Compound	*IP*	*EA*	ΔH_{disp} [b]
2-3[c]	6.16	1.39	4.77
2-4[d]	8.18	1.36	6.81
2-5[d]	7.09	1.38	5.71
2-6[d]	6.56	1.84	4.72

[a] Adiabatic ΔSCF values at the B3LYP/6-31G(d,p) level, R = H for all systems, values in eV. [b] $\Delta H_{disp} = IP - EA$, where *IP* is the ionization potential and *EA* the electron affinity. [c] Reference 3a. [d] From this work.

The singly occupied molecular orbital (SOMO) and spin distribution of **2-6** ($R_1 = R_2 = R_3 = H$) were also obtained from these DFT calculations, and they are illustrated in Figure 2.1. The SOMO is antibonding and has a_2 symmetry, and may be considered as an out-of-phase combination of the SOMOs of two monofunctional thiadiazines. Similar to the bisdithiazolyls **2-3**, there is a nodal plane down the short axis of the molecule, indicating that the R_1 and R_2 substituents will have, to first order, little effect on the electronic properties of the system. The calculated spin density is also shown in Figure 2.1, and demonstrates that the unpaired electron is delocalized across the entire framework. Not only is this important for lowering the ΔH_{disp} value, it also increases the stability of the system. A closer look at the spin distribution reveals heavy spin concentration on the two thiadiazine rings, with relatively low negative spin density along the central axis of the molecule, corresponding to the nodal plane of the SOMO.

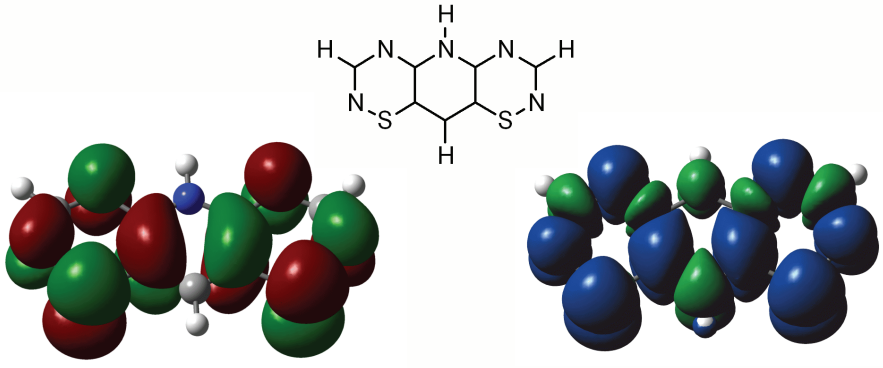

Figure 2.1 B3LYP/6-31G(d,p) SOMO (left) and spin density (right) of **2-6** ($R_1 = R_2 = R_3 = H$).

Overall, the DFT (Density Functional Theory) studies on the model bisdithiadiazinyl **2-6** ($R_1 = R_2 = R_3 = H$) demonstrate that the framework has a relatively low *U* and a delocalized spin distribution. These features, in conjunction with the synthetic flexibility afforded by the R_1, R_2 and R_3 substituents, make the **2-6** radical an attractive framework in the development of NRCs. This chapter encompasses the development of the first family of radicals of this type, **2-6** with R_1 = Me, Et, Pr; R_2 = Cl and R_3 = Ph, and includes synthesis, electrochemistry, crystallography and transport property measurements. In addition to a preliminary communication,[8] a full report was published on this work.[9] The latter part of this chapter includes attempts at substituent modification, as well as suggestions for future work on the bisthiadiazinyl framework.

2.2 Synthesis

Monofunctional thiadiazines have been studied for a number of years, and there are several methods which can be used to form the thiadiazine ring.[10] Of these, the favoured route has involved the cyclization of an amidine with a sulfur halide.[10a] The amidine can be prepared from the reaction of an aryl amine with $AlCl_3$ and the appropriate nitrile,[11] or by the reaction of an amine and an orthoester.[12] We have found, however, that the latter method is not conducive to bifunctional amines, as it leads to polymerization. Another route to the amidine involves the reaction between an *o*-aminothiol and hydroximoyl chloride.[13] Extending the synthetic work just described to the bifunctional framework, we utilized the condensation reaction of a diamine with two equivalents of a nitrile to obtain the bisamidine, and then followed the general procedure[3b] established in the Oakley group for the bisdithiazolyl radicals **2-3** to prepare the bisthiadiazinyls **2-6** (Scheme 1).

Scheme 1

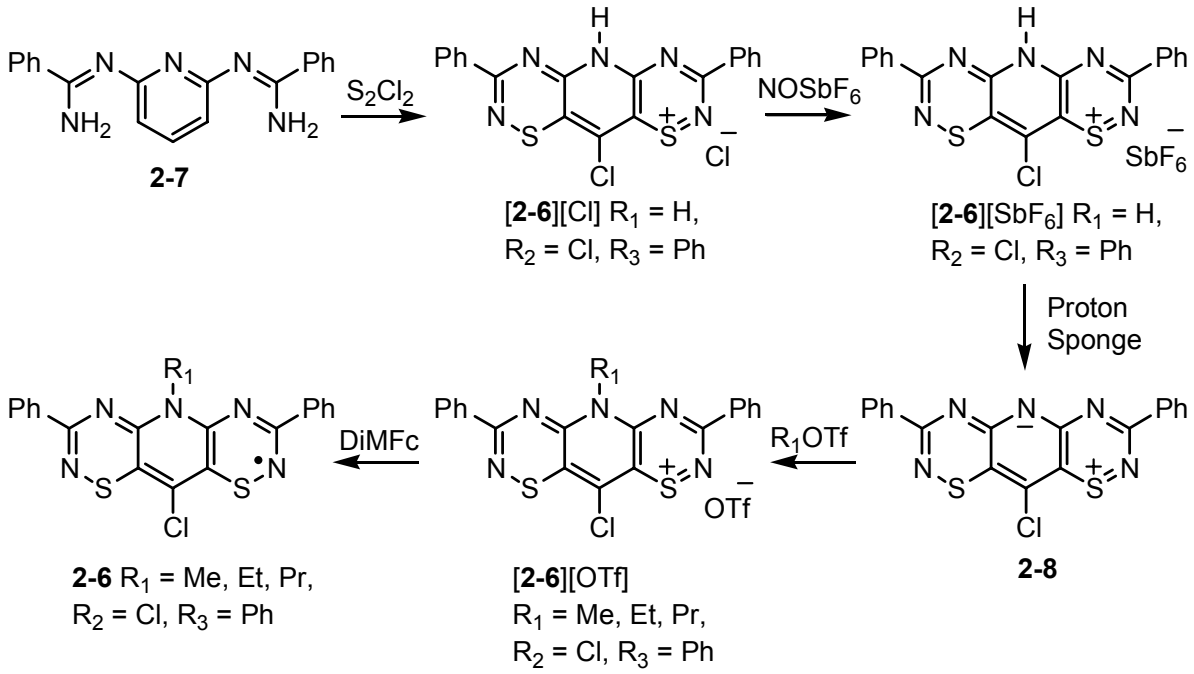

In our pursuit of the bisthiadiazinyl system we obtained the desired bisamidine **2-7** by condensing 2,6-diaminopyridine with benzonitrile at the melt and in the presence of $AlCl_3$. The bisthiadiazine framework was achieved by the reaction of **2-7** with sulfur monochloride in refluxing chlorobenzene, isolating the chloride salt [**2-6**][Cl] (R_1 = H, R_2 = Cl, R_3=Ph) as a green insoluble powder. The chloride anion was replaced with SbF_6 by methathesis with nitrosonium hexafluoroantimonate to facilitate purification through recrystallization. This material was deprotonated with Proton Sponge to afford the thermally robust zwitterion **2-8**, that could then be reacted with an alkyl (methyl, ethyl and propyl) triflate (trifluoromethansulfonate, OTf^-) to yield the bisthiadiazinium triflates [**2-6**][OTf] (R_1 = Me, Et, Pr; R_2 = Cl, R_3=Ph). These salts are highly coloured (λ_{max} = 6.2 x 10^2 nm, log ε = 4.7), as expected from their antiaromatic 16π-electron count. In the solid state the salts have an iridescent red/green hue, while in solution they are deep blue with a strong red fluorescence (Figure 2.2), similar to that found in other heterocyclic zwitterionic dyes.[14] From the electrochemical behaviour of these materials we determined that dimethylferrocene ($E_{½}^{(0/+1)}$ = 0.263 V vs SCE in MeCN) could be used as reducing agent to afford the desired radicals, single crystals of which were grown by vacuum sublimation at 200°C/10^{-4} Torr. Crystals

of the R_1 = Pr derivative were malformed and unfit for structural determination, but fortunately the crystals of the R_1 = Me, Et compounds were suitable for X-ray work and were fully characterized.

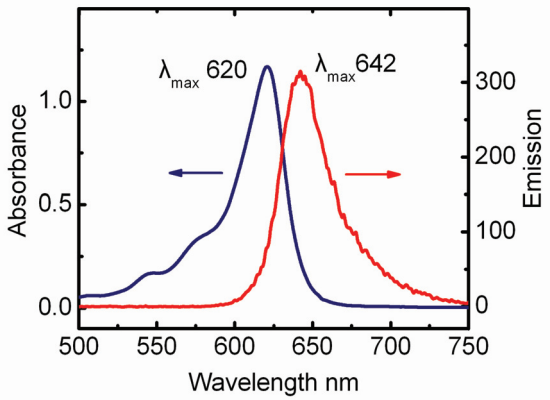

Figure 2.2 Absorption and fluorescence spectra of [**2-6**][OTf] (R_1 = Me, R_2 = Cl, R_3 = Ph). (Intensity units are arbitrary).

2.3 Electrochemistry

The electrochemical behaviour of the bisthiadiazinyl framework was probed by cyclic voltammetry on the salts dissolved in MeCN (with 0.1 M *n*-Bu_4NPF_6 supporting electrolyte) and the voltammogram for the methyl compound is illustrated in Figure 2.3. The cell potentials for the bisthiadiazinyls **2-6**, as well as the related bisdithiazolyls **2-3**, are listed in Table 2.2. For compounds **2-6** (R_1 = Me, Et; R_2 = Cl, R_3 = Ph), both variants show three waves corresponding to the -1/0, 0/+1 and +1/+2 processes, two of which (-1/0 and 0/+1) show reversible behaviour. Unlike the bisdithiazolyls **2-3**, the third wave, or the +1/+2 redox couple, is irreversible. The half-wave potentials are shifted anodically by about 300 mV with respect to the bisdithiazolyls, demonstrating that the bisthiadiazinyl framework is more electronegative. The electrochemical window E_{cell} obtained from the half-wave potentials ($E_{½}^{(0/+1)}$ - $E_{½}^{(-1/0)}$) is similar to that found for the bisdithiazolyl radicals, though considerably smaller than those found for monofunctional benzo-fused thiadiazinyls.[7] This shows, experimentally, that resonance stabilization has the effect of lowering the energetics of charge transfer in solution, and by doing so affords a lower value of *U*.

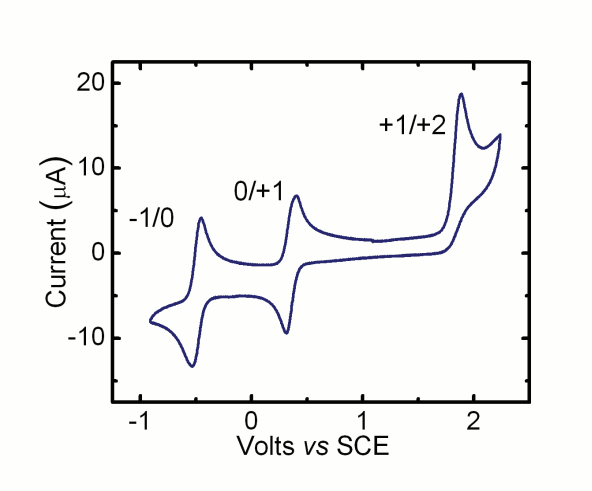

Figure 2.3 Cyclic voltammetry of [**2-6**][OTf] (R_1= Me, R_2 = Cl, R_3 = Ph) in MeCN.

Table 2.2 Electrochemical Potentials[a] and EPR Data[b]

	2-6[c]		**2-3**[c,d]	
	R_1 = Me	R_1 = Et	R_1 = Me	R_1 = Et
$E_{½}^{(+1/+2)}$	1.88[e]	1.88[e]	1.415	1.39
$E_{½}^{(0/+1)}$	0.355	0.339	0.005	-0.018
$E_{½}^{(-1/0)}$	-0.476	-0.486	-0.835	-0.845
E_{cell}	0.831	0.825	0.840	0.827
g	2.0059	2.0059	2.0083	2.0082
a_N (NR$_1$)[f]	0.069 (-0.097)	0.070 (-0.097)	0.060 (-0.069)	0.060 (-0.069)
a_N (CNC)[f]	0.268 (0.327)	0.271 (0.327)	---	---
a_N (CNS)[f]	0.184 (0.238)	0.187 (0.238)	0.310 (0.357)[g]	0.310 (0.357)[g]

[a] $E_{½}$ values (V) in MeCN, reference SCE; $E_{cell} = E_{½}^{(0/+1)} - E_{½}^{(-1/0)}$. [b] Coupling constants, a_N, in mT, experimental values are absolute. [c] R_2= Cl for both **2-6** and **2-3**; R_3 = Ph for **2-6**. [d] Data from reference 3b. [e] Irreversible wave, E_{pa} value cited. [f] B3LYP/6-31G(d,p) values in parenthesis for a model with all R = H. [g] Coupling only possible to the CNS nitrogens of **2-3**.

2.4 EPR Spectroscopy

Electron paramagnetic resonance (EPR) spectra were obtained for both radicals **2-6** (R_1 = Me, Et; R_2 = Cl, R_3 = Ph). The experiments were carried out at ambient temperature on samples dissolved in methylene chloride. The plots of both the methyl and ethyl compounds are shown in Figure 2.4, and the spectral data is listed in Table 2.2. In both compounds the *g* values are slightly larger than that of the free electron value, an effect attributed to spin-orbit coupling on sulfur. The spectra display a complex hyperfine multiplet pattern dominated by the four ^{14}N nuclei within the thiadiazine rings, and smaller couplings to ^{35}Cl and ^{37}Cl, to the pyridine nitrogen, and to the alkyl and aryl protons lead to a general line broadening.[‡] In the case of the methyl derivative, the appearance of the spectrum was sharpened by deuteration of the phenyl rings (prepared by the use of d^5-benzonitrile as starting material), whereas the spectrum of the ethyl radical was reasonably well resolved without such measures. The hyperfine coupling constants were extracted by spectral simulation and assignments were confirmed by comparison to values predicted from B3LYP/6-31G(d,p) calculations on a model **2-6** (R_1 = R_2 = R_3 = H). The spectra are consistent with a highly delocalized spin distribution, with approximately equal spin densities on the two chemically distinct nitrogens within the thiadiazine rings. The a_N coupling constants and the calculated spin densities on these nitrogens are about one-half the values of those found in monofunctional thiadiazinyls and thiatriazinyls, as would be expected given that the unpaired spin distribution is delocalized over two rings rather than one. A similar effect has been noted in bisdithiazolyls.[3] The discrepancy between the observed a_N values for **2-6** (R_1 = Me, Et; R_2 = Cl, R_3 = Ph) and those calculated for the model with R_1 = R_2 = R_3 = H reflect the effects of spin delocalization onto the ligands, particularly the phenyl groups.

[‡] The smaller hyperfine couplings were also obtained from the simulations. For R_1 = Me, a_H (CH_3) 0.033, a_{Cl} 0.029/0.024 ($^{35}Cl/^{37}Cl$) mT. For R_1 = Et, a_H (CH_2) 0.022, a_{Cl} 0.027/0.023 ($^{35}Cl/^{37}Cl$) mT.

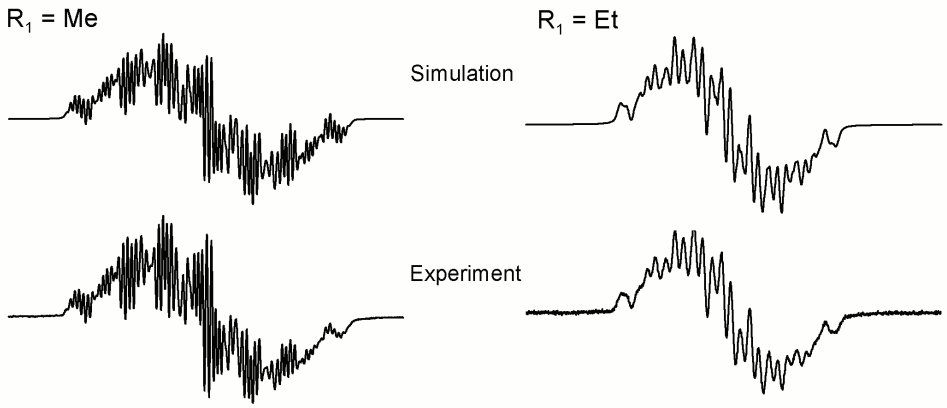

Figure 2.4 X-Band EPR spectrum of **2-6** (R_1 = Me, R_2 = Cl, R_3 = C_6D_5) on left, and **2-6** (R_1 = Et, R_2 = Cl, R_3 = C_6H_5) on right (in CH_2Cl_2, for R_1 = Me: SW = 3 mT, LW = 0.016 mT, and for R_1 = Et: SW = 4 mT, LW = 0.032 mT).

From the solution based experiments, the bisthiadiazinyl framework **2-6** has been shown to exhibit a delocalized spin distribution, reversible redox processes and low ion energetics, all attributes which favour its use as a neutral radical conductor. Now, focusing on the solid state, it is necessary for these materials to remain as discrete radicals, rather than dimers, in order to be of any use as an NRC.

2.5 Crystal Structures

Three crystal structures were determined in the course of this work, that of the salt [**2-6**][OTf] (R_1 = Me, R_2 = Cl, R_3 = Ph) and the two radicals **2-6** (R_1 = Me, Et; R_2 = Cl, R_3 = Ph). The crystallographic data for all three structures are presented in Table 2.3. The crystal of the salt [**2-6**][OTf] (R_1 = Me, R_2 = Cl, R_3 = Ph) was grown by careful recrystallization from MeCN, and the molecular framework and packing arrangement are shown in Figure 2.5. The salt crystallizes in the orthorhombic space group *Pbca*, and consists of stacks of alternating cations and anions, as depicted in Figure 2.5C. Pairs of stacks, related by the *a* glide, are dovetailed together to allow for direct overlap of the phenyl rings (Figure 2.5B). The anions are sandwiched between cation plates, as well as in the pocket created between the N-methyl and phenyl

moieties (Figure 2.5A). The structure of [**2-6**][OTf] (R_1 = Me, R_2 = Cl, R_3 = Ph) confirmed the identity of the desired framework and was an important step towards isolating the radical species.

Table 2.3 Crystallographic Data

	[**2-6**][OTf] (R_1 = Me)	**2-6** (R_1 = Me)	**2-6** (R_1 = Et)
M, g mol^{-1}	571.99	422.92	436.95
a, Å	8.4474(6)	3.9232(8)	5.6870(2)
b, Å	13.9712(10)	27.527(6)	25.3004(8)
c, Å	40.105(3)	16.378(3)	13.5877(4)
β, deg	---	90.17(3)	91.742(2)
V, Å^3	4733.2(6)	1768.7(6)	1954.14(11)
ρ(calcd), g cm^{-1}	1.605	1.588	1.485
space group	*Pbca*	$P2_1/c$	$P2_1/n$
Z	8	4	4
temp, K	295(2)	173(2)	298(2)
μ, mm^{-1}	0.486	0.470	3.877
λ, Å	0.71073	0.71073	1.54178
θ_{full}, deg	27.50	26.3714	65.05
data/restr/param	5591/0/326	3516/0/253	3242/0/323
solution method	direct methods	direct methods	direct methods
R, R_w (on F^2)	0.0587, 0.1615	0.0983, 0.2159	0.0350, 0.0914
ϕ1, deg	11.8(4)	-2.1(1)	12.3(3)
ϕ2, deg	-7.5(4)	-3.7(7)	20.95(3)
δ, Å	---	3.436(4)	3.559(2)
τ, deg	---	61.18(6)	38.74(1)

ϕ is the twist angle of the phenyl ring with respect to the plane of the heterocycle, in a counterclockwise rotation. δ is the plate-to-plate separation between neighbouring radicals. τ is the angle of inclination of the mean heterocyclic plane to the stacking axis.

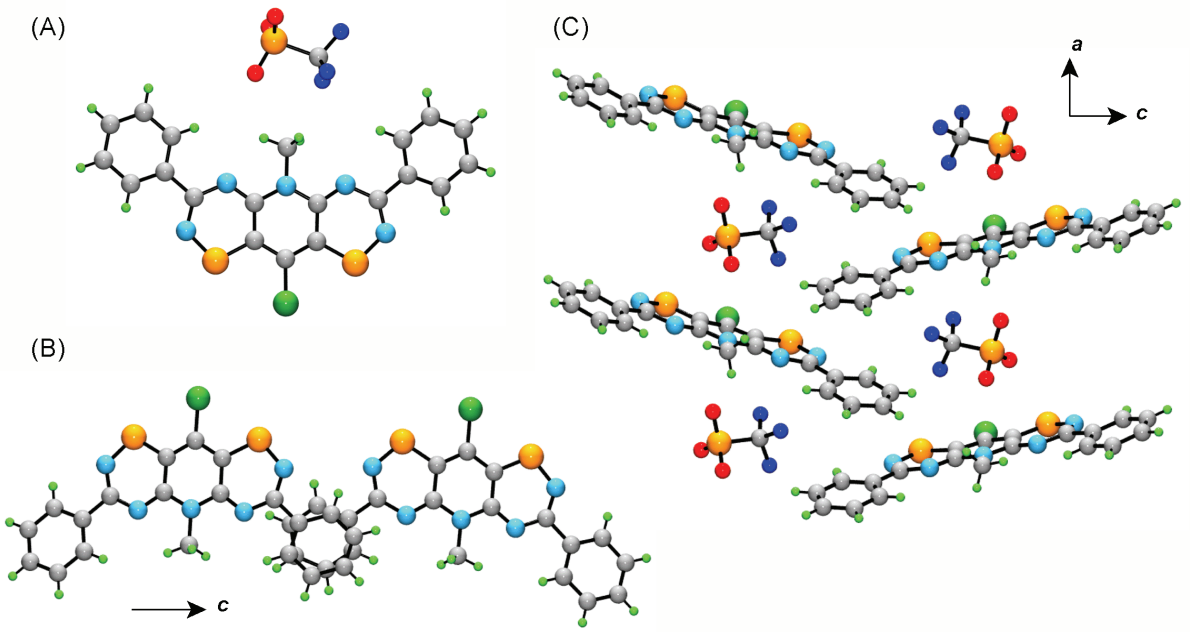

Figure 2.5 Crystal structure of [**2-6**][OTf] (R_1 = Me, R_2 = Cl, R_3 = Ph) with asymmetric unit (A), overlapping cations (B) and stacks of alternating cations and anions (C).

Crystals of the methyl radical **2-6** (R_1 = Me, R_2 = Cl, R_3 = Ph) were grown by vacuum sublimation and were extremely fibrous needles. As a result, the data collection was performed at 173 K and the refinement was less than ideal, although sufficient to elucidate the molecular framework and packing arrangement. The radicals do not dimerize, but form slipped π-stacks in the solid state as shown in Figure 2.6. The molecular structure of the radical shows a lengthening of the bonds to S1/S2 and N1/N4 and a concomitant shortening of the central C-C and C-N bonds compared to that of the cation, a feature attributed to the occupation of the antibonding SOMO. The central heterocycle is essentially planar (to within 0.042(2) Å), with the phenyl rings twisting only slightly away from the plane of the heterocycle. The radicals pack in the monoclinic space group $P2_1/c$, and the structure consists of cross braced π-stacks that are severely slipped by τ = 61.16(6)° away from the stacking direction. The separation between heterocycles along the π-stack (δ) is 3.436(4) Å, a value similar to that seen for the bisdithiazolyls **2-3**.[3] The phenyl groups on the periphery of the heterocycle serve as buffers to isolate the radical from its neighbours, and there are no close S---S′ or S---N′ intermolecular contacts.

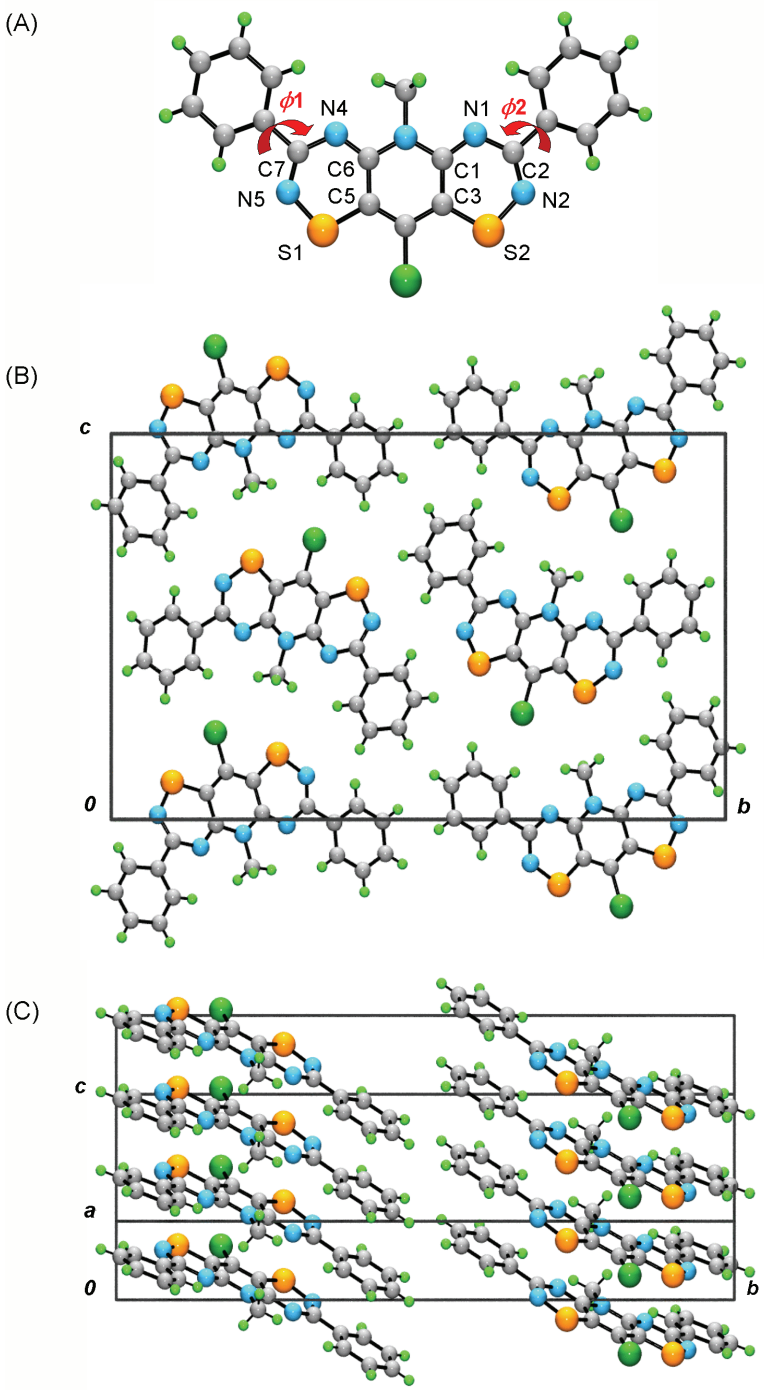

Figure 2.6 Crystal structure of **2-6** (R_1= Me, R_2 = Cl, R_3 = Ph) with a single molecule from above (A), with atom numbering, and unit cell drawings looking down the stacking axis (B) and perpendicular to it (C) illustrating the slipped π-stacks.

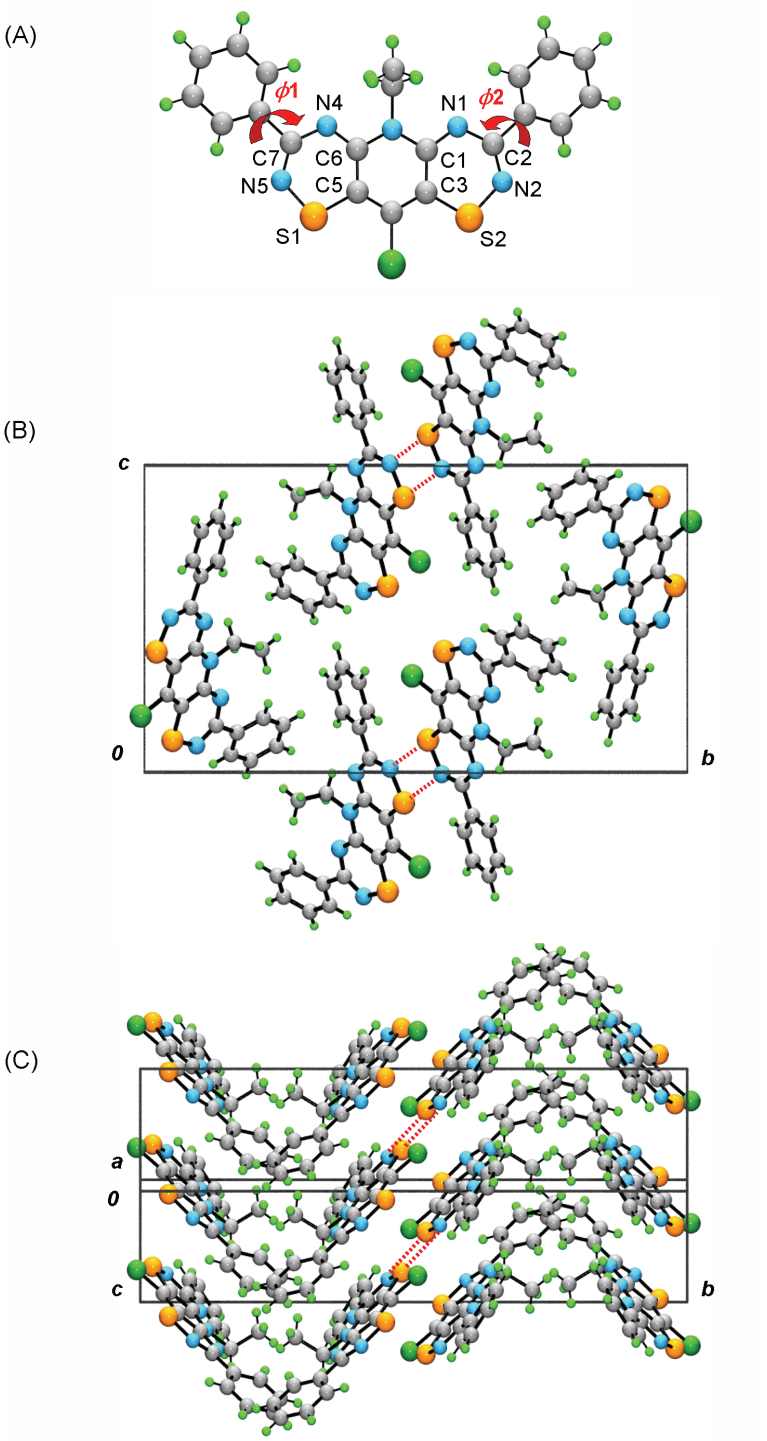

Figure 2.7 Crystal structure of **2-6** (R_1= Et, R_2 = Cl, R_3 = Ph) with a single molecule from above (A), showing atom numbering, and unit cell drawings looking down the stacking axis (B) and perpendicular to it (C) illustrating the slipped π-stacks. Close S---N′ contacts are shown as dotted red lines.

Crystals of the ethyl compound **2-6** (R_1= Et, R_2 = Cl, R_3= Ph) were also grown by vacuum sublimation, but the needles were thicker than the methyl derivative and good X-ray data could be collected at ambient temperature. As with the methyl radical, the ethyl compound does not dimerize, and forms slipped π-stacks in the solid state as shown in Figure 2.7, with radicals arranged in the monoclinic space group $P2_1/n$. The heterocyclic core is close to planarity (to within 0.42(2) Å), but in this case the ethyl groups cause the phenyl substituents to tip more severely away from the plane of the heterocycle, with torsion angles ϕ1 and ϕ2 of 12.3(3) and 20.95(3)°, respectively. The molecules along the π-stacks are less severely slipped than the methyl derivative, with a slippage angle τ of 38.74(1)°, although the plates are more widely spaced with a separation distance δ of 3.559(2) Å. The bulky R groups, particularly the phenyl substituents, keep the radicals apart from one another as in the methyl compound, but here the radicals are arranged so as to allow a single set of lateral intermolecular contacts between thiadiazine rings (S1---N5′at 3.406(2) Å).

Within the π-stacks the plate-to-plate separation of neighbouring heterocycles (δ) is significantly smaller for the methyl derivative but, as demonstrated below, this closer spacing of the plates does not lead to enhanced electronic or magnetic interactions along the stacks. This can be appreciated upon inspection of the heterocycle overlaps shown in Figure 2.8. In the methyl derivative, the closest interannular contacts involving sulfur are to carbon atoms C3, C4 and C5. One of these, C4 lies on a node in the SOMO, and the other two are outside the normal van der Waals range.[15] By contrast, in the ethyl derivative, the radicals slip in such a way that only a few close interannular contacts are possible. Only three involve sulfur atoms, but one of these (S1---C1′ = 3.486(2) Å) is aligned so as to afford directly superimposed overlap of the pπ-orbitals on sulfur and carbon. The role of this particular interaction on the electronic and magnetic structure of the ethyl radical is described below.

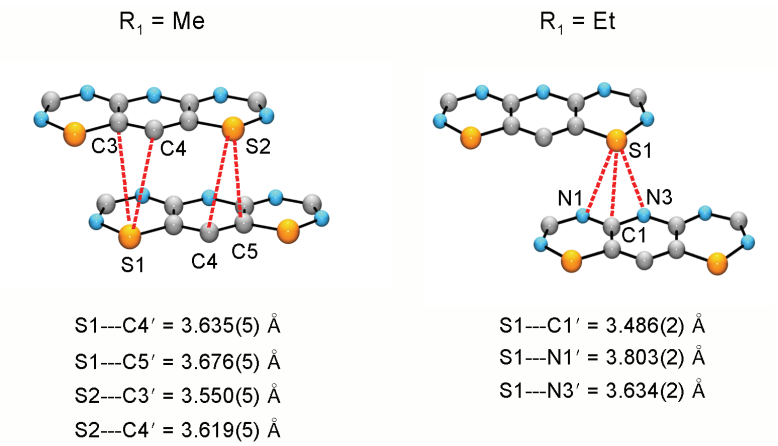

Figure 2.8 Intermolecular contacts within π-stacks of **2-6** (R_1= Me, Et; R_2 = Cl, R_3 = Ph).

2.6 Electronic Band Structures

The electronic structure of the two radicals were investigated by means of EHT (Extended Hückel Theory) band calculations, and the results are shown in Figure 2.9. Each plot consists of the four crystal orbitals (COs) arising from the four radical SOMOs of each unit cell. The dispersion curves associated with these COs are tracked from Γ (0, 0, 0) to B (½, 0,0), a direction closely related to the orbital interactions along the stacking axis of the real space lattice. Both the magnitude and overall appearance of the dispersion curves provide some insight into the degree of orbital overlap along the π-stacks, as well as between them. For comparison purposes, the analogous plots for the four SOMOs of the bisdithiazolyls **2-3** are also shown,[3b] plotted along the k-vector that corresponds to their stacking direction in real space.[‡]

[‡] In the monoclinic structures (**2-6**) the directions of the real unit cell vectors can be approximated to the reciprocal unit cell vectors, as the β angle is such that the correspondence is nearly exact. In the case of orthorhombic (**2-3**, R_1 = Me) and tetragonal (**2-3**, R_1 = Et) structures, there is direct correspondence between the directions of the real and reciprocal unit cell vectors.

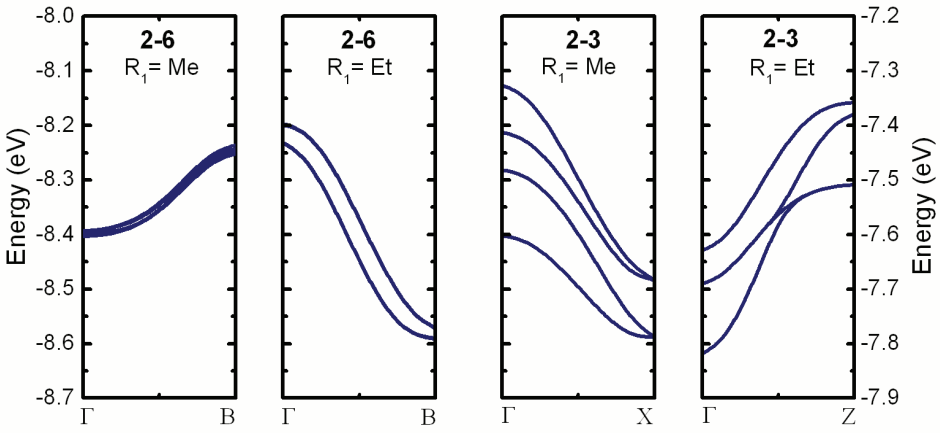

Figure 2.9 Dispersion energy curves for **2-6** (R_1 = Me, Et; R_2 = Cl, R_3 = Ph) and **2-3** (R_1 = Me, Et; R_2 = Cl).

The slope of the curves (or the sign of dE_k/dk) of these plots can be associated with the orbital overlap properties between the radicals along the π-stack. For the methyl derivative, the positive slope seen as energy changes with k-space vector indicates a net bonding interaction between radical SOMOs at k = 0, where for the ethyl compound the negative slope suggests a net antibonding overlap (at k = 0) along the stacks. A similar feature is seen for the **2-3** radicals, although opposite in nature, as the energy increases for the ethyl variant and decreases for the methyl-substituted compound along the k-space direction corresponding to their stacking axes. The overall dispersion of the ethyl derivative (W ~ 0.4 eV) is comparable to that of the **2-3** radicals, and much larger than that of the methyl compound, a feature resulting from the shorter S---C′ contacts, and thus stronger interaction, along the π-stacks. Not only does the methyl derivative have a lower energy dispersion along the stacking direction, the four COs are nearly coincident, demonstrating that the radicals are non-interacting between the stacks and that the material is essentially 1-dimensional. This conclusion can also be reached for the ethyl compound, although the presence of the lateral S1---N5′ interactions cause the four COs to separate into closely spaced pairs. In general the radicals are isolated from one another as a result of the blocking affect of the phenyl groups, in stark contrast to the bisdithiazolyls **2-3** which are much more multidimensional due to their essentially naked periphery and ability to form close lateral S---S′ and S---N′ contacts.

2.7 Transport Property Measurements

The lack of communication between radicals within the stacks, as well as between them, greatly restricts the bandwidths for these systems, and as a result, these radicals are Mott insulators with conductivity values σ(300K) less than 10^{-7} S cm^{-1} for both compounds. However, the limited number of intermolecular interactions enable the magnetic properties to be more easily studied. The results of variable temperature magnetic susceptibility measurements on **2-6** (R_1 = Me, Et; R_2 = Cl, R_3 = Ph) are summarized in Figure 2.10, which shows plots of the paramagnetic susceptibility χ_P and $\chi_P T$ as a function of temperature for the two compounds. The methyl derivative behaves as a Curie-Weiss paramagnet with a $\chi_P T$ value reaching 0.350 emu K mol^{-1} at 300 K, a number close to that expected (0.375 emu K mol^{-1}) for an S = ½ system of undimerized radicals (assuming $g = 2$). A fit to the high temperature data gives a Curie constant C = 0.360 emu K mol^{-1} and θ-value of -11.9 K, suggesting the possibility of weak antiferromagnetic behaviour. In contrast, the magnetic susceptibility of the ethyl-substituted compound shows a pronounced maximum in χ_P near 90 K indicating the presence of significant antiferromagnetic (AFM) exchange coupling. The $\chi_P T$ versus T plot shows a gradual increase in $\chi_P T$ with increasing temperature, reaching a maximum of 0.355 emu K mol^{-1} at 300 K.

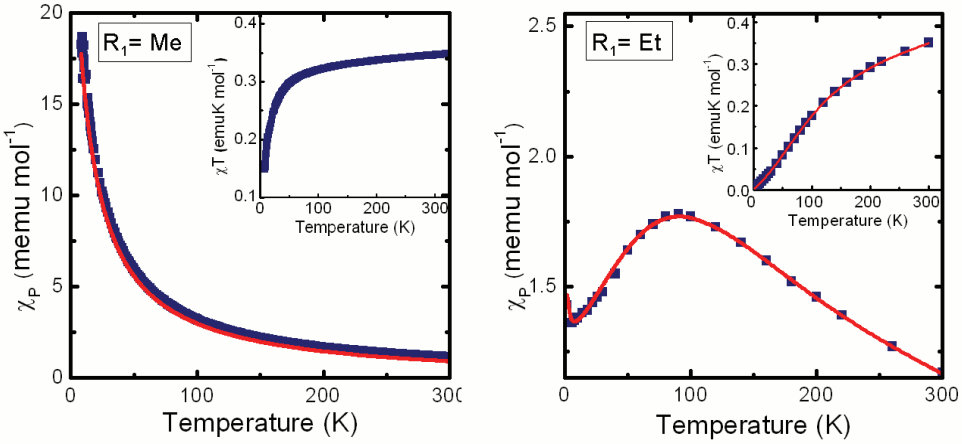

Figure 2.10 Magnetic susceptibility, χ_P, versus T plots for **2-6** (R_1 = Me, Et; R_2 = Cl, R_3 = Ph). Insert shows plots of $\chi_P T$ versus temperature, and red lines indicate the derived fits to experimental data.

We have seen strong AFM coupling effects in π-stacked bisdithiazolyls **2-3**,[3d] but in those cases the electronic interactions were numerous and the potential exchange pathways more complex. It was therefore not possible to model the magnetic data in those cases. Given the more 1D nature of the electronic structure of **2-6** (R_1 = Et), with a single strong S1---C1′ interaction linking radicals along the π-stack and a much weaker lateral S1---N5′ interaction linking the stacks into pairs, we decided to model the temperature dependence of the χ_P data to a 1D Heisenberg chain of AFM coupled S = ½ centers. Based on a Bonner-Fischer approach[16] and an $H_{ex} = -2J\{S_1 \bullet S_2\}$ Hamiltonian,[17] the derived fit (shown in Figure 2.10) was obtained using the following parameters: J = -49 cm^{-1}, zJ = -3 cm^{-1}, g = 2.007, θ = 0 cm^{-1}, α = 0.001, TIP = 2.2 × 10^{-4} emu mol^{-1}, and R(χ) = 0.0157.‡ The exchange equation was modified to include a molecular field correction, which suggested a small long range AFM component.

In order to explore the origins of the magnetic properties of the two bisthiadiazinyls, we have performed a series of DFT calculations in an attempt to characterize the individual exchange interactions involved. We have used broken symmetry methods[18] to estimate the singlet-triplet exchange energies for closely interacting radical pairs, an approach which was described in Chapter 1, and has been successfully applied to a variety of nitrogen centered radicals[19] and heterocyclic thiazyl radicals.[20,21] Accordingly, and with reference to the Hamiltonian $H_{ex} = -2J\{S_1 \bullet S_2\}$, the exchange energy J for any pair of interacting radicals can be estimated from the total energies of the triplet (E_T) and broken symmetry singlet (E_{BSS}) states and the respective expectation values $< S^2 >$ of the two states, according to equation (**1**).

$$J = \frac{-(E_T - E_{BSS})}{<S^2>_T - <S^2>_{BSS}} \qquad (\mathbf{1})$$

Exchange energies were calculated with a simple dinuclear nearest neighbour exchange model using a variety of pairwise combinations of radicals, with atomic coordinates taken from crystallographic data. For the methyl-substituted compound only one possible exchange pathway J_A was considered, namely

‡ $R(\chi) = [\Sigma(\chi_{obs} - \chi_{calc})^2/\Sigma(\chi_{obs})^2]^{½}$, α = fraction of monomeric paramagnetic impurity, TIP = temperature independent paramagnetism.

that involving the interaction of nearest neighbour radicals along the π-stack. For the ethyl derivative, the lateral interactions noted above give rise to a ladder-like structure (Figure 2.11) in which there are three possible exchange couplings J_A , J_B and J_C . As in the methyl compound, the J_A pathway involves radical-radical interactions along the π-stacks, while J_B is associated with the lateral S1---N5′ contacts noted above. The potential third coupling J_C arises from the head-over-tail pairing of radicals in adjacent π-stacks. Single point total energies were calculated using the hybrid exchange correlation functional B3LYP and a series of polarized, split-valence basis sets with double-zeta (6-31G(d,p)), triple-zeta (6-311G(d,p)) and triple-zeta plus diffuse (6-311+G(d,p)) functions.

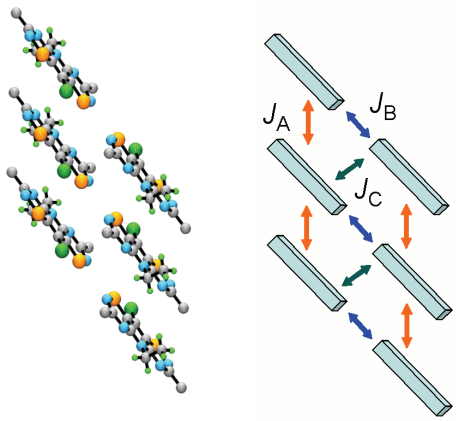

Figure 2.11 Magnetic exchange pathways J_A, J_B and J_C in **2-6** (R_1 = Et, R_2 = Cl, R_3 = Ph).

The results are summarized in Table 2.4, which shows individual exchange energies as a function of basis set. Overall there is a fair consistency across the basis sets, certainly sufficient for a qualitative evaluation of the relative importance of the various pathways. In both cases (R_1 = Me, Et) the calculations predict an antiferromagnetic exchange interaction J_A along the stacking axis, that of the ethyl compound being substantially larger, as anticipated from the structural features noted above. Within a mean field model the 6-311+G(d,p) J_A exchange energy for R_1 = Me translates (with two equivalent neighbours) into a predicted[22] Curie Weiss θ-value of -5.4 K,‡ a value comparable to that observed from the Curie-Weiss

‡ According to reference 22, $\theta = \dfrac{\xi JS(S+1)}{3k}$ where ξ is the number of equivalent neighbours.

fit of the experimental data. There are similarly small discrepancies between the 6-311+G(d,p) J_A, and $J_{B,C}$ energies and those derived from the 1D Heisenberg chain model with the molecular field term included, but given the size of the radicals the correspondence between DFT calculations and the modified chain model is reasonable.

Table 2.4 Calculated Exchange Coupling Constants (in cm^{-1}) of **2-6** (R_2 = Cl, R_3 = Ph)

R_1	J	6-31G(d,p)	6-311G(d,p)	6-311+G(d,p)
Me	J_A	-14.4	-9.3	-7.5
Et	J_A	-32.2	-32.7	-32.9
Et	J_B	-5.6	-7.8	-8.5
Et	J_C	-3.5	-4.3	-4.6

2.8 Conclusions

The bisthiadiazinyl radicals **2-6** are a new class of heterocyclic neutral radical and the first systems of this type (R_1= Me, Et; R_2 = Cl, R_3 = Ph) exhibited low ion energetics (a low *U*), high thermal stability and a solid state packing arrangement consisting of discrete radicals. All of the these attributes are in favour of these materials being radical conductors. Unique to these systems, over the bisdithiazolyls **2-3**, are the R_3 groups on the outer ends of the heterocyclic core, and although these substituents offer another mode for design modification, they also isolate the radicals from one another. For the R_3 = Ph compounds, there were either no (R_1 = Me) or few (R_1 = Et) lateral intermolecular interactions within the crystal structure, which are critical for a bandwidth *W* that is sufficiently large to overcome *U*. As a result, these materials are Mott insulators with low conductivity values. Nonetheless, due to the limited number of close intermolecular contacts in the solid state, these materials provided a unique opportunity to model their magnetic properties.

2.9 Future Work

There are several ways in which the bisthiadiazinyl framework can be modified through variations in the R_1, R_2 and R_3 substituents to alter both the conductive and magnetic properties of the system. To improve the bandwidth, and thus conductivity, one obvious strategy is to change the R_3 group to something much smaller than phenyl, such as methyl or proto, to allow for the radicals to pack closer together. Unfortunately, early work along this avenue has been thwarted by (i) the oxidation of the methyl group during the closure reaction with S_2Cl_2, and (ii) the hydrolysis of the amidine of the R_3 = H derivative during the basic work up. Other R_3 substitents, those capable of S---S′ and S---N′ contacts, such as dithiazoles or thiatriazines, could be used to increase the number and strength of intermolecular contacts in the solid state. In addition, the replacement of sulfur by selenium, or even tellurium, can also increase bandwidth, a strategy implemented in improving the bandwidth of the bisdithiazolyls **2-3**.[23] Synthetic work into these areas has not yet been approached.

Alternatively, one could focus on lowering the *U* parameter in conjunction with improving *W*, to obtain a higher conductivity. Variation of the redox properties, and therefore *U*, can be achieved through the development of a 'push-pull' system in which the R_3 groups are replaced by an electron-withdrawing group (e.g., CF_3) and an electron-donating group (e.g., NR_2). These hetero-substituted frameworks could show interesting structures and electronic behaviour, and DFT calculations show ΔH_{disp} values lower than that of the R_3 = H framework. With this goal in mind, our work on 'one-armed' amidines **2-9** has shown partial success. For the case of R_3 = pyridyl and phenyl derivatives, the one-armed species is more activated to a second substitution than the diamine and gives the bisamidine compounds in almost 100 % yield. In contrast, when R_3 = trifluoromethyl and pyrimidyl, we can isolate the one-armed species through the alkylation of the center nitrogen, but have difficulty placing a second arm. Nonetheless, with **2-9** in hand, it is possible, upon reaction with sulfur halides, to obtain the hybrid species **2-10**, with one 5-membered ring and one 6-membered ring in resonance across the pyridine bridge. The precursors to this framework have been isolated, and work on these systems is ongoing.

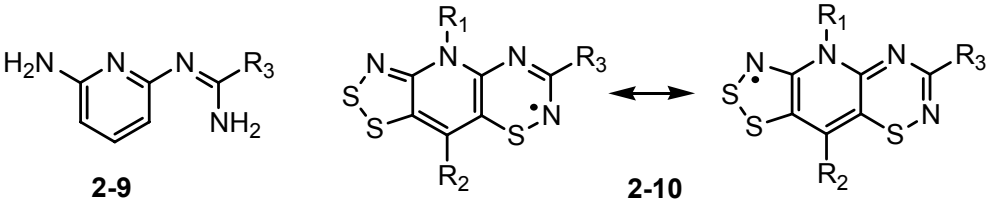

2-9 **2-10**

Properties other than conductivity can also be envisaged, as R_3 groups capable of polymerization (**2-11**) or metal (M) coordination (**2-12**) could be developed. Our work towards **2-12**, with the R_3 = pyridyl derivative, has been restricted by the oxidation state of the isolated compound on ring closure. We obtain the bisthiadiazine framework in the fully reduced form **2-13**, and we are as yet unable to successfully oxidize the compound to the monocation **2-14**. We were initially surprised to find this synthetic obstacle following a minor modification in the R_3 group (from phenyl to pyridyl), but we believe that the protons are strongly held in the pocket created by the thiadiazine nitrogen and the pyridine nitrogen, an arrangement similar to that of **2-12** but with a proton instead of a metal atom. We realized from this work that we must further explore the redox chemistry of each bisthiadiazine system before we can make any progress on a general synthetic route to substituent modification.

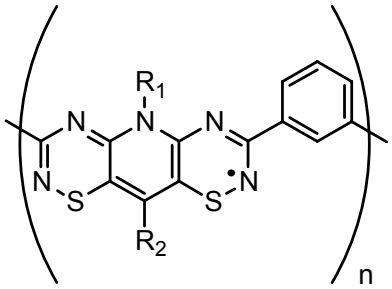

2-11

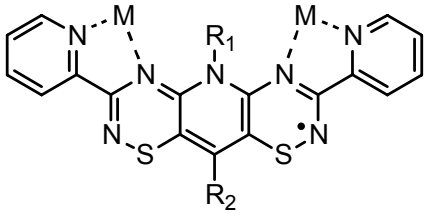

2-12

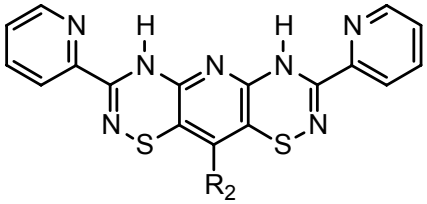

2-13

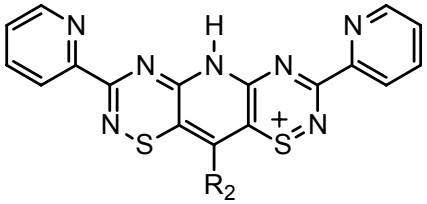

2-14

Another area for investigation is the development of extended ring systems such as **2-15**, **2-16** and **2-17**. Similar polycyclic systems have been studied for use as field effect and thin film transistors,[24] liquid crystalline materials,[25] zwitterionic cyanine dyes[14] and organic electronic materials.[26] Our preliminary calculations on these radicals indicate lower ΔH_{disp} values than the three ring systems **2-3** and **2-6**, making them potential targets for NRCs. Possible synthetic pathways to these five ringed compounds have been investigated for future work.[27]

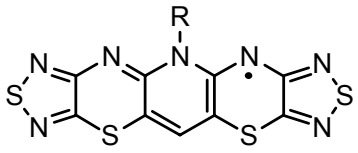

2-15

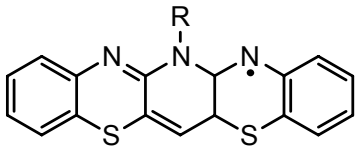

2-16

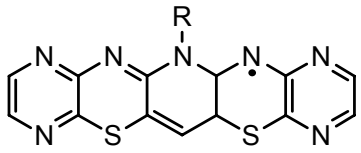

2-17

In summary, the bisthiadiazinyl framework shows much potential for use as functional materials with a variety of options available and modes of modification seemingly endless. Work in this area has demonstrated however, that a greater understanding into the redox chemistry and intermediate reaction pathways must be achieved in order for the bisthiadiazinyl system to be widely applicable.

2.10 Experimental Section

Preparation of N, N -pyridine-2,6-diyldibenzenecarboximidamide 2-7 Aluminum chloride (12.2 g, 0.0916 mol), benzonitrile (9.50 mL, 0.0921 mol) and 2,6-diaminopyridine (5.00 g, 0.0458 mol) were combined and melted together at 200 °C for 15 min. The hard glassy solid was heated into 50 mL 10 % aqueous HCl solution, which turned over to a brown crystalline solid that was filtered and washed with 20 mL 20 % aqueous HCl solution. This hydrochloride salt (14.5 g, 0.0412 mol) was dissolved in 100 mL boiling water and, on cooling, 100 mL aqueous sodium carbonate monohydrate solution (35.3 g, 0.284 mol) was added to afford a light brown solid, that was filtered off and washed with water. The bisamidine **2-7** was recrystallized from MeCN as light brown flakes, yield 9.48 g (0.0301 mol, 73 %); mp 177.5-180.5 °C. IR: 3421 (m), 3274 (m), 1622 (s), 1584 (s), 1527 (s), 1492 (m), 1432 (w), 1320 (m), 1244 (m), 1182

(w), 1153 (m), 1078 (w),1028 (m), 969 (w), 826 (m), 795 (m), 787 (m), 698 (s), 522 (w), 485 (w) cm^{-1}. ^1H NMR (δ , CD_3CN): 7.97 (m, 2H), 7.68 (t, 1H, J = 7.7 Hz), 7.49 (m, 3H), 6.76 (d, 2H, J = 7.7 Hz). Anal. Calcd for $C_{19}H_{17}N_5$: C, 72.36; H, 5.43; N, 22.21 %. Found: C, 72.21; H, 5.61; N, 21.99 %.

Preparation of 10-chloro-3,7-diphenyl-5H-[1,2,4]thiadiazino[6',5':5,6]pyrido[2,3-e][1,2,4]-thiadiazin-1-ium hexafluoroantimonate [2-6][SbF_6], R_1 = H, R_2 = Cl, R_3 = Ph Sulfur monochloride (10.1 g, 0.0747 mol) was added to a slurry of **2-7** (3.92 g, 0.0124 mol) in 125 mL chlorobenzene. The reaction mixture was set to reflux for 16 h and the resulting precipitate was collected by filtration and washed with 2 x 60 mL chlorobenzene. Crude [**2-6**][Cl] (R_1 = H, R_2 = Cl, R_3 = Ph) was obtained as a green-brown powder, yield 5.09 g (0.0114 mol, 93 %). IR: 1885 (m), 1631 (w), 1596 (w), 1583 (w), 1556 (w), 1362 (s), 1233 (s), 1176 (w), 1043 (m), 1073 (m), 1064 (m), 1027 (m), 1000 (w), 972 (w), 845 (w), 829 (w), 775 (s), 789 (m), 696 (s), 664 (m), 624 (w), 585 (m), 535 (w), 472 (m), 453 (w) cm^{-1}. A sample of [**2-6**][Cl] (R_1 = H, R_2 = Cl, R_3 = Ph) (5.09 g, 0.0114 mol) was added to a colourless solution of nitrosonium hexafluoro-antimonate (3.67 g, 0.0138 mol) in 70 mL MeCN to give a dark blue solution with lustrous red precipitate. After 1 h, the solvent was removed by flash distillation and the residue was filtered using 60 mL HOAc. The product, [**2-6**][SbF_6] (R_1 = H, R_2 = Cl, R_3 = Ph) was washed 2 × 50 mL HOAc to afford a dark green crystalline solid, yield 4.03 g (0.00633 mol, 55 %); dec > 255 °C. IR: 3224 (w), 1586 (m), 1561 (m), 1531 (m), 1407 (w), 1322 (s), 1237 (s), 1178 (m), 1149 (w), 1073 (w), 1061 (s), 1027 (m), 1000 (w), 938 (w), 821 (w), 788 (w), 774 (s), 725 (w), 695 (s), 664 (s), 652 (s), 643 (m), 581 (s), 564 (w), 460 (w) cm^{-1}. ^1H NMR (δ , CD_3CN): 7.65 (m, 3H), 8.20 (m, 2H). Anal. Calcd for $C_{19}H_{11}ClF_6N_5S_2Sb$: C, 35.40; H, 1.72; N, 10.86 %. Found: C, 35.41; H, 2.00; N, 10.63 %.

Preparation of 10-chloro-3,7-diphenyl[1,2,4]thiadiazino[6',5':5,6]pyrido[2,3-e][1,2,4]thiadiazin-1-ium-5-ide, 2-8, R_2 = Cl, R_3 = Ph Proton sponge (1.61 g, 7.54 mmol) was added to a slurry of [**2-6**][SbF_6] (R_1 = H, R_2 = Cl, R_3 = Ph) (4.01 g, 3.21 mmol) in 125 mL MeCN to give a purple precipitate of **2-8** (R_2 = Cl, R_3 = Ph) that was collected by filtration and washed 2 × 50 mL MeCN, yield 2.28 g (5.59 mmol, 90 %); dec > 320 °C. IR: 1627 (w), 1584 (w), 1507 (w), 1489 (w), 1432 (s), 1410 (w), 1343 (w), 1313 (m),

1302 (m), 1179 (s), 1070 (w), 1053 (w), 1028 (m), 9321 (w), 866 (w), 847 (w), 779 (s), 764 (s), 722 (w), 708 (s), 693 (w), 627 (s), 597 (m), 553 (w), cm^{-1}. Anal. Calcd. for $C_{19}H_{10}ClN_5S_2$: C, 55.95; H, 2.47; N, 17.17 %. Found: C, 55.81; H, 2.25; N, 17.36 %.

Preparation of 10-chloro-5-methyl-3,7-diphenyl-5H-[1,2,4]thiadiazino[6',5':5,6]pyrido[2,3-e][1,2,4] thiadiazin-1-ium trifluoromethanesulfonate [2-6][OTf], R_1 = Me, R_2 = Cl, R_3 = Ph Methyl trifluoromethanesulfonate (0.340 mL, 3.00 mmol) was added to a slurry of **2-8** (R_2 = Cl, R_3 = Ph) (1.00 g, 2.45 mmol) in 8 mL DCE to give a turquoise slurry that was stirred for 16 h. The brown precipitate of [**2-6**][OTf] (R_1 = Me, R_2 = Cl, R_3 = Ph) was filtered off and washed with 2 × 10 mL DCE. The crude product was recrystallized in MeCN to afford a mixture of red rhombohedral plates and needles, yield 0.970 g (1.70 mmol, 69 %); dec > 248 °C for rhombohedral plates. IR of rhombohedral plates: 1583 (w), 1530 (m), 1335 (s), 1314 (w), 1272 (m), 1263 (s), 1223 (w), 1158 (m), 1136 (m), 1039 (w), 1030 (m), 1022 (w), 966 (m), 838 (w), 809 (w), 794 (w), 775 (s), 750 (m), 722 (w), 722 (s), 701 (m), 692 (m), 680 (s), 636 (w), 621 (w), 573 (w), 559 (w), 520 (w), 498 (w) cm^{-1}. IR for needles: 1583 (m), 1530 (m), 1414 (s), 1337 (s), 1312 (w), 1264 (s), 1223 (w), 1179 (w), 1148 (s), 1097 (w), 1032 (s), 1023 (s), 966 (m), 840 (w), 814 (w), 779 (s), 749 (s), 697 (s), 680 (m), 637 (s), 621 (m), 573 (w), 559 (w), 517 (m), 500 (w) cm^{-1}. ^1H NMR of rhombohedral plates (δ, CD_3CN): 3.90 (s, 3H, CH3), 7.64 (m, 3H), 8.26 (m, 2H). UV-vis: λ_{max} 622 nm, log ε = 4.7. Anal. Calcd. for rhombohedral plates, $C_{21}H_{13}ClF_3N_5O_3S_3$: C, 44.09; H, 2.29; N, 12.24 %. Found: C, 44.25; H, 2.40; N, 11.99 %.

Preparation of 10-chloro-5-ethyl-3,7-diphenyl-5H-[1,2,4]thiadiazino[6',5':5,6]pyrido[2,3-e][1,2,4]-thiadiazin-1-ium trifluoromethanesulfonate [2-6][OTf], R_1 = Et, R_2 = Cl, R_3 = Ph A slurry of **2-8** (R_2 = Cl, R_3 = Ph) (1.00 g, 2.45 mmol) and ethyl trifluoromethanesulfonate (0.380 mL, 2.93 mmol) in 8 mL DCE was stirred for 32 h. The brown precipitate of [**2-11**][OTf] (R_1 = Et, R_2 = Cl, R_3 = Ph) was filtered off and washed with 2 × 10 mL DCE. The crude product was recrystallized from MeCN as bronze needles, yield 0.638 g (1.09 mmol, 45 %); dec > 278 °C. IR: 1595 (w), 1582 (m), 1529 (m), 1337 (s), 1263 (s), 1234 (w), 1176 (w), 1145 (s), 1111 (w), 1069 (s), 1048 (s), 1031 (s), 932 (w), 787 (m), 774 (s), 753 (s), 698

(s), 678 (m), 636 (s), 619 (m), 571 (m), 517 (m) cm^{-1}. ^1H NMR (δ, CD_3CN): 1.45 (t, 3H, CH_2CH_3, J = 7.0 Hz), 4.67 (m, 2H, CH_2CH_3, J = 7.0 Hz), 7.65 (m, 3H), 8.26 (m, 2H). UV-vis: λ_{max} 619 nm, log ε = 4.8. Anal. Calcd. for $C_{22}H_{15}ClF_3N_5O_3S_3$: C, 45.09; H, 2.58; N, 11.95 %. Found: C, 45.17; H, 2.43; N, 11.99 %.

Preparation of 10-chloro-5-propyl-3,7-diphenyl-5H-[1,2,4]thiadiazino[6',5':5,6]pyrido[2,3-e][1,2,4]-thiadiazin-1-ium trifluoromethanesulfonate [2-6][OTf], R_1 = Pr, R_2 = Cl, R_3 = Ph Propyl trifluoromethanesulfonate (0.860 g, 4.48 mmol) was added to a slurry of **2-8** (1.50 g, 3.68 mmol) in 15 mL DCE and the reaction mixture was set to reflux for 16 h. At this time the heat was removed and the slurry cooled to room temperature and then at -20 °C for 2 h. The coppery precipitate was collected by filtration and washed 2 x 10 mL DCE. Recrystallization from MeCN afforded [**2-6**][OTf] (R_1 = Pr, R_2 = Cl, R_3 = Ph), yield 1.28 g (2.13 mmol, 58 %); dec > 255 °C. IR: 1529 (w), 1424 (w), 1337 (s), 1265 (s), 1235 (w), 1224 (w), 1152 (m), 1096 (w), 1071 (w), 1051 (m), 1033 (m), 1025 (m), 967 (w), 801 (s), 774 (s), 753 (w), 698 (s), 674 (w), 638 (s), 617 (w), 568 (w), 517 (w) cm^{-1}. UV-vis: λ_{max} 620 nm, log ε = 4.7. Anal. Calcd. for $C_{23}H_{17}ClF_3N_5O_3S_3$: C, 46.04; H, 2.86; N, 11.67 %. Found: C, 46.72; H, 3.00; N, 10.54 %.

Preparation of 10-chloro-5-methyl-3,7-diphenyl-2H,5H-[1,2,4]thiadiazino-[6',5':5,6]pyrido[2,3-e] [1,2,4]thiadiazin-2-yl, 2-6, R_1 = Me, R_2 = Cl, R_3 = Ph Dimethylferrocene (0.443 g, 2.07 mmol) was added to a solution of [**2-6**][OTf] (R_1 = Me, R_2 = Cl, R_3 = Ph) (0.970 g,1.70 mmol) in 100 mL degassed MeCN. The maroon microcrystalline material was filtered after 1 h and washed with 2 × 50 mL MeCN, yield 0.630 g (1.49 mmol, 88%); mp 228 - 230 °C. IR: 1583 (m), 1536 (s), 1500 (m), 1444 (s), 1403 (w), 1336 (w), 1308 (s), 1277 (s), 1246 (w), 1177 (s), 1116 (w), 1069 (w), 1030 (s), 1018 (w), 1000 (m), 953 (m), 921 (m), 852 (w), 785 (m), 760 (s), 728 (s), 693 (s), 677 (m), 672 (m), 621 (m), 616 (m), 543 (w), 486 (w), 451 (w) cm^{-1}. Anal. Calcd. for $C_{20}H_{13}ClN_5S_2$: C, 56.80; H, 3.10; N, 16.56 %. Found: C, 56.68; H, 3.30; N, 16.38 %. Crystals suitable for structure analysis were grown by vacuum sublimation at 10^{-4} Torr down a temperature gradient of 210 °C to 100 °C.

Preparation of 10-chloro-5-ethyl-3,7-diphenyl-2H,5H-[1,2,4]thiadiazino-[6',5':5,6]pyrido[2,3-e][1,2,4]thiadiazin-2-yl, 2-6, R_1 = Et, R_2 = Cl, R_3 = Ph Dimethylferrocene (0.230 g, 1.07 mmol) was added to a degassed solution of [**2-6**][OTf] (R_1 = Et, R_2 = Cl, R_3 = Ph) (0.513 g, 0.088 mmol) in 40 mL MeCN. After 30 min the maroon microcrystalline material was filtered off and washed with 2 × 30 mL MeCN, yield 0.323 g (0.739 mmol, 84 %); dec > 200 °C. IR: 1583 (w), 1545 (m), 1521 (w), 1499 (s), 1347 (w), 1312 (s), 1299 (w), 1277 (s), 1219 (m), 1181 (m), 1090 (w), 1037 (m), 1023 (s), 993 (s), 931 (w), 920 (w), 780 (m), 755 (s), 736 (s), 705 (w), 695 (s), 691 (s), 678 (w), 667 (m), 616 (m), 559 (w), 484 (w) cm^{-1}. Anal. Calcd. for $C_{21}H_{15}ClN_5S_2$: C, 57.72; H, 3.46; N, 16.03 %. Found: C, 58.12; H, 3.62; N, 16.24 %. Crystals suitable for X-ray work were grown by vacuum sublimation at 10^{-4} Torr down a temperature gradient of 200 °C to 100 °C.

Preparation of 10-chloro-5-propyl-3,7-diphenyl-2H,5H-[1,2,4]thiadiazino-[6',5':5,6]pyrido[2,3-e][1,2,4]thiadiazin-2-yl, 2-6, R_1 = Pr, R_2 = Cl, R_3 = Ph Dimethylferrocene (0.442 g, 2.07 mmol) was added to a degassed solution of [**2-6**][OTf] (R_1 = Pr, R_2 = Cl, R_3 = Ph) (1.00 g, 1.67 mmol) in 50 mL MeCN. After 1 h the maroon microcrystalline material was filtered off and washed with 2 × 20 mL MeCN, yield 0.626 g (1.39 mmol, 83 %); dec > 200 °C. IR: 1584 (w), 1535 (s), 1499 (s), 1442 (s), 1367 (w), 1316 (s), 1276 (s), 1207 (s), 1175 (s), 1116 (w), 1069 (w), 1038 (s), 1022 (s), 961 (m), 937 (w), 929 (w), 919 (w), 901 (w), 871 (w), 844 (w), 778 (m), 759 (s), 734 (s), 691 (s), 677 (m), 667 (w), 620 (m), 616 (m), 556 (w), 478 (w) cm^{-1}. Anal. Calcd. for $C_{22}H_{17}ClN_5S_2$: C, 58.59; H, 3.80; N, 15.53 %. Found: C, 58.39; H, 4.00; N, 15.63 %. Crystals suitable for X-ray work could not be grown by either recrystallization or vacuum sublimation.

Chapter 3

Pursuing Superimposed π-Stacks in Pyrazine-Bridged Bisdithiazolyls

3.1 Introduction

As demonstrated in Chapter 1, the development of the bisdithiazolyl radicals **3-1** was a major step forward in the pursuit of stable radicals as building blocks for single-component conductors. The resonance stabilization achieved by this framework lowered the on-site Coulomb repulsion energy *U*, increased thermal stability and suppressed dimerization in comparison to the monofunctional dithiazolyls. The belt-line ligands R_1 and R_2 contributed to the prevention of association by providing the necessary steric bulk, but they also caused the radicals to form slipped π-stacks in the solid state (Chart 1), a feature that limited overall bandwidth *W*. The necessary requirement for a metallic ground state is $W > U$, and in all examples of **3-1**, *W* was insufficient to overcome *U*, and these materials were Mott insulators.

Chart 1

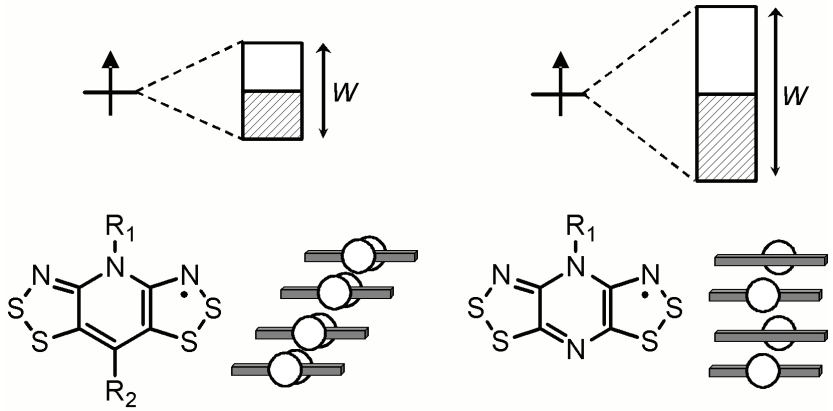

3-1 **3-2**

The Extended Hückel Theory (EHT) calculations shown in Chapter 1 on a model π-stack consisting of perfectly superimposed radicals of **3-1** suggest that bandwidths near 2 eV are possible, a value surely

to rival the relatively low *U* value for resonance stabilized systems. In order to achieve these vertically aligned π-stacks, a design strategy was developed to remove some of the steric bulk, while still maintaining resonance delocalization. An obvious molecular modification is the replacement of the pyridine ring in **3-1**, with a pyrazine bridge, as in **3-2**. Ideally, this would afford alternating, but superimposed π-stacks in the solid state as shown in Chart 1, an arrangement that should provide maximum orbital overlap.

Two derivatives of **3-2** were examined (R = Me and Et), and although they behave similarly in solution, their solid state structures and properties are very different. The ethyl-substituted compound forms two phases in which both consist of unique σ-bonded dimers. The methyl variant on the other hand, crystallizes in the desired manner with vertically aligned ABABAB π-stacked arrays. However, the transport properties seemed to contradict this high bandwidth structure, and an in depth structural investigation was undertaken. Within this chapter, the two derivatives (R = Me, Et) are combined for the solution based experiments (cyclic voltammetry (CV) and electron paramagnetic resonance (EPR) spectroscopy), but are described separately for their solid state structures and properties. Two reports have been published on the pyrazine-bridged bisdithiazolyls **3-2**, the first an initial communication on the ethyl compound,[1] and the second a full paper describing the methyl radical.[2]

3.2 Synthesis

Construction of the pyrazine-bridged bisdithiazolyl framework **3-2** required a lengthy synthetic sequence (Scheme 1), the first step of which was the preparation of 2,6-diaminopyrazine **3-5**. This latter compound can be generated in small quantities by the hydrogenation of the corresponding diazide **3-4**, which is itself readily prepared from dichloropyrazine **3-3**.[3] With more convenient reagents, such as sodium borohydride, only one azide is fully reduced while the other is trapped as a tetrazole.[3] We have found, however, that complete reduction of both azides can be achieved using iron in aqueous acetic acid,[4] and after an alkaline work-up the diamino compound **3-5** can be extracted in 70 % yield (from **3-3**). Previous studies have shown that the pyridine-bridged bisdithiazolyl framework **3-1** can be made, in a

single step, *via* a double Herz cyclization of diaminopyridine with sulfur monochloride.[5,6,7] Unfortunately, the 3,5-positions of diaminopyrazine are less susceptible to electrophilic substitution than are the corresponding sites in diaminopyridine, as a result of which double Herz cyclization of **3-5** with sulfur monochloride fails. Assembly of the desired tricyclic skeleton of **3-2** therefore required, as a first step, the conversion of the diaminopyrazine **3-5** to its bisthiocyanate derivative **3-6**. Reductive deprotection of thiocyanates has typically been achieved with aqueous sodium sulfide, followed by acidification to afford the diamino-dithiol.[8] However, the use of this approach on **3-6** afforded, after an acidic work-up, an intractable brown solid that did not undergo a cyclization reaction with thionyl chloride or sulfur monochloride. We therefore turned to the use of tributylphosphine, a reagent commonly employed in the reductive deprotection of thiocyanates.[9] Accordingly the reaction of **3-6** with Bu_3P in anhydrous MeCN afforded a deep orange solution, and addition of small amounts of water to this mixture led to the precipitation of the mono-substituted aminophosphiniminodithiol **3-7** as an orange microcrystalline solid, the identity of which was confirmed by X-ray crystallography.[‡]

Reaction of **3-7** with thionyl chloride in the presence of pyridine afforded the desired bisdithiazolylium framework in the form of the protonated salt [**3-2**][Cl] (R = H). The crude insoluble chloride was purified by conversion to a tetrachlorogallate salt, [**3-2**][$GaCl_4$] (R = H), which could be deprotonated with Proton-Sponge to afford the zwitterion **3-8**. Alkylation of this free base with Meerwein salts R_3OBF_4 (R = Me, Et) caused some initial difficulties, as the product was invariably contaminated by protonated material. However, when the alkylation was performed in the presence of Proton Sponge, protonation was effectively suppressed, and the desired *N*-alkylated salts [**3-2**][BF_4] (R = Me, Et) were obtained in good yield. Chemical reduction of [**3-2**][BF_4] (R = Me, Et) was achieved using decamethylferrocene (DMFc) in MeCN.

[‡] The structural constitution of compound **3-7** has been confirmed by single crystal X-ray diffraction. The crystals belong to the trigonal space group $P3_12_1$, with $a = b = 12.0557(4)$, $c = 55.325(4)$ Å, $Z = 12$ (at T = 200 K). There are two hydrogen-bonded molecules in the asymmetric unit, each with the formula shown in Scheme 1.

Scheme 1

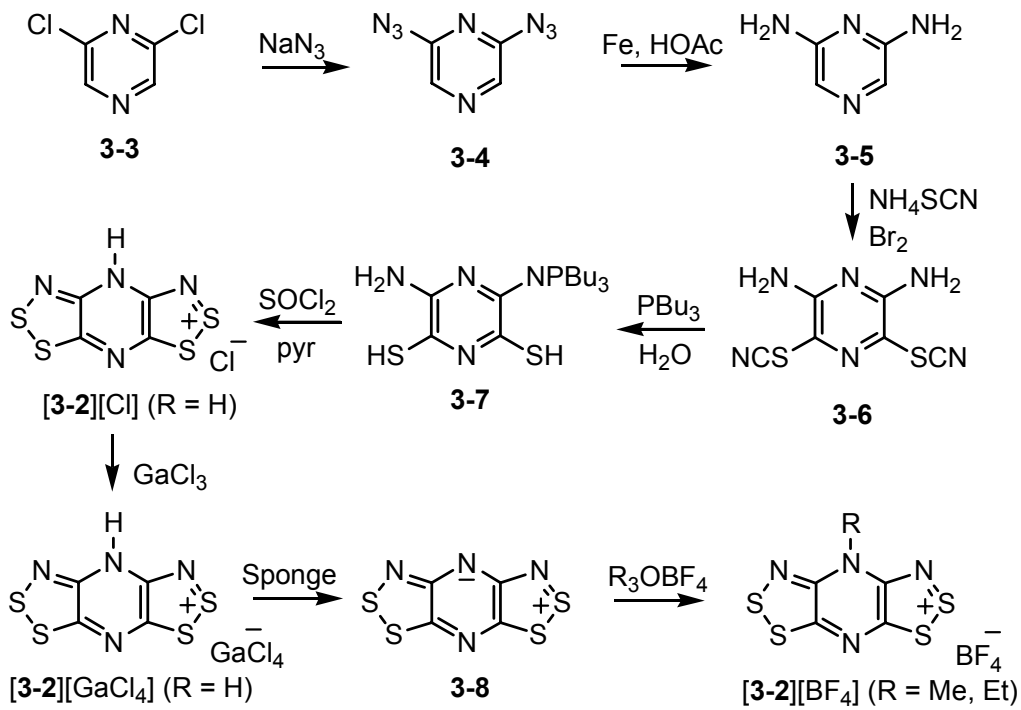

Single crystals of **3-2** (R = Me) were grown by slow diffusion of degassed solutions of DMFc and [**3-2**][BF_4] (R = Me) using H-cell techniques. Crystals of **3-2** (R = Et) could not be obtained by this method, and were instead grown by vacuum sublimation at 10^{-4} Torr down a temperature gradient from 100 °C to 50 °C. We were surprised to find that the sublimation of the light brown microcrystalline solid of **3-2** (R = Et) from the chemical reduction afforded a mixture of two different crystals, amber blocks (the α-phase) and black needles (the β-phase). The two phases display similar behaviour when dissolved in solution, but possess very different structures in the solid state.

3.3 Solution-Based Experiments

3.3.1 Cyclic Voltammetry

The electrochemical behaviour of the pyrazine-bridged bisdithiazolyl framework was probed by cyclic voltammetry on samples of [**3-2**][BF_4] (R = Me, Et) in MeCN with 0.1 M *n*-Bu_4NPF_6 as supporting electrolyte. A representative plot for the ethyl-substituted compound is shown in Figure 3.1 and the cell potentials for both derivatives of **3-2**, as well as the related pyridine-bridged compounds **3-1**, are listed in Table 3.1. For the **3-2** framework, there is a reversible wave for the 0/+1 process, with an anodic shift of the individual half wave potentials by about 120 mV with respect to the analogous pyridine compounds **3-1** (R_1 = Me, Et; R_2 = H), as a result of the more electronegative pyrazine core. The +1/+2 process is also reversible, although the reduction of the radical to the anion (-1/0) is not, a feature also seen for **3-1** (R_1 = Me, Et; R_2 = H). This irreversible process is attributed to the cleavage of the S-S[10] (or S-N)[11] bonds upon reduction of the radical. The electrochemical window E_{cell} for the pyrazine framework **3-2**, estimated in this case by the difference in the cathodic peak potentials ($E_{pc}^{(0/+1)}$ - $E_{pc}^{(-1/0)}$), is slightly larger than that of **3-1**, and suggests a low *U* value.

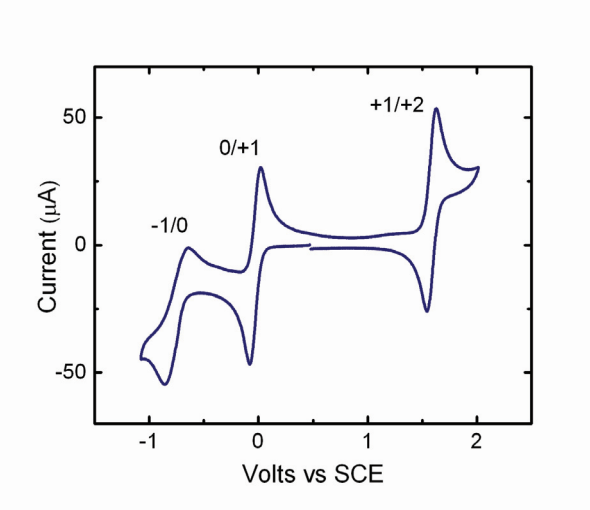

Figure 3.1 Cyclic voltammetry of [**3-2**][BF_4] (R = Et) in MeCN.

3.3.2 EPR Spectroscopy

The X-band EPR spectra of **3-2** (R = Me, Et) were obtained on samples dissolved in methylene chloride at ambient temperatures. The spectra for both samples are shown in Figure 3.2, along with the simulations in which the ^{14}N and ^{1}H hyperfine coupling constants were extracted. The coupling constants are presented in Table 3.1, along with those for radicals **3-1** (R_1 = Me, Et; R_2 = H). The spectral patterns are dominated by coupling to two equivalent dithiazolyl nitrogens, the value of a_N being approximately one-half of that observed in monofunctional 1,2,3-dithiazolyl radicals.[12] There is a weaker coupling to the N-alkyl nitrogen and to the protons of the alkyl (Me or Et) substituent, as well as a relatively large hyperfine interaction with the basal nitrogen of the pyrazine ring. In the pyridine-bridged systems **3-1**, this is replaced by coupling to the CH proton. The complex hyperfine coupling pattern exhibited by the pyrazine-bridged radicals **3-2**, is evidence of a delocalized spin distribution.

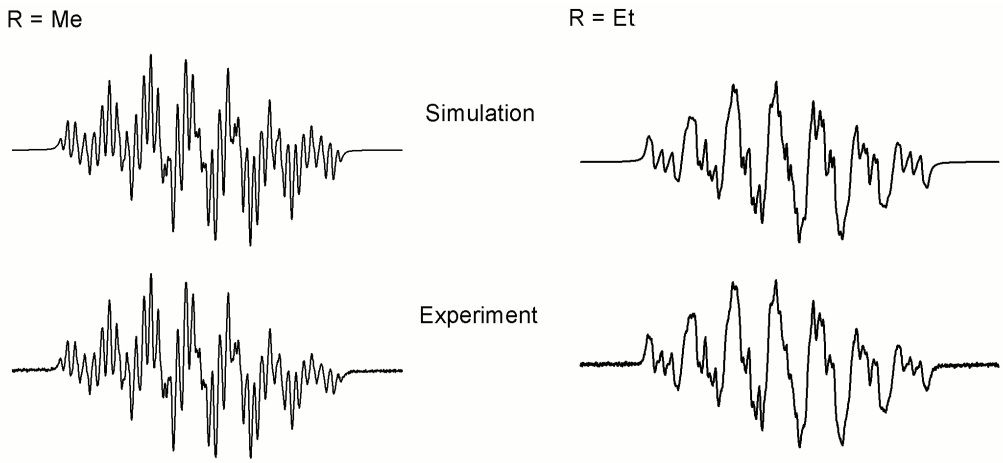

Figure 3.2 X-band EPR spectra of **3-2** (R = Me, Et) in CH_2Cl_2, SW = 3 mT. For R = Me, L/G = 0.01 and LW = 0.024 mT. For R = Et, L/G = 0.10 and LW = 0.029 mT.

Table 3.1 Hyperfine Coupling Constants (mT), *g*-Values, and Half-Wave Potentials[a]

	3-1[b] (R_1 = Me, R_2 = H)	**3-1**[b] (R_1 = Et, R_2 = H)	**3-2** (R = Me)	**3-2** (R = Et)
a_N	0.313 (2N)	0.318 (2N)	0.309 (2N)	0.313 (2N)
	0.062 (1N)	0.061 (1N)	0.073 (1N)	0.073 (1N)
	---	---	0.266 (1N)	0.266 (1N)
a_H (CH)	0.230 (1H)	0.228 (1H)	---	---
a_H (NR)	0.034 (NCH_3)	<0.02 (NCH_2CH$_3$)	0.053 (NCH_3)	0.025 (NCH_2CH$_3$)
g-value	2.0082	2.0082	2.0087	2.0087
$E_{1/2}^{-1/0}$	-0.95[d]	-0.95[d]	-0.870[d]	-0.853[d]
$E_{1/2}^{0/+1}$	-0.130	-0.146	-0.0104	-0.0291
$E_{1/2}^{+1/+2}$	1.294	1.272	1.610	1.585
E_{cell}[c]	0.77[e]	0.76[e]	0.82[e]	0.85[e]

[a] $E_{1/2}$ values (volts) in MeCN, referenced to saturated calomel electrode (SCE). [b] Data from reference 6b. [c] $E_{cell} = E_{1/2}^{(0/+1)} - E_{1/2}^{(-1/0)}$. [d] Irreversible behaviour; E_{pc} value quoted. [e] E_{cell} estimated as $E_{pc}^{(0/+1)} - E_{pc}^{(-1/0)}$.

The EPR spectrum of **3-2** (R = Et) shown in Figure 3.2 is obtained for both the α-phase (amber blocks) and the β-phase (black needles) when samples of each are dissolved in methylene chloride. In both cases, the measured signals are strong and persistent. However, in the solid state, both phases are EPR silent and suggest a diamagnetic ground state.

3.4 Solid State Properties of the Ethyl-Substituted Radical

Upon chemical reduction of [**3-2**][BF_4] (R = Et) with DMFc, the light brown microcrystalline solid of the α-phase was isolated. Vacuum sublimation of this material down a temperature gradient of 100 °C to 50 °C afforded a mixture of amber blocks (α-[**3-2**]$_2$) and black needles (β-[**3-2**]$_2$) that were manually separated from one another and analyzed by X-ray crystallography. The relative proportions of the two phases are sensitive to temperature, as at elevated temperatures (110 °C to 60 °C) the formation of the β-

phase is favoured. Also, when a mixture of the two phases are re-sublimed, the β-phase is formed exclusively. Since both the α-phase and β-phase are EPR silent in the solid state, we expected their structures to consist of dimers.

3.4.1 Crystal Structure

The crystal structure of the α-phase of **3-2** (R = Et) consists of centrosymmetric dimers arranged in the monoclinic space group $P2_1/n$. The dimer, and its packing arrangement, are shown in Figure 3.3, and the crystallographic data are listed in Table 3.2. The dimers are linked cofacially by a long C3-C3′ σ-bond (1.607 Å), which is significantly longer than a standard sp^3–sp^3 C–C linkage (1.54 Å),[13] and comparable to those found in other strained systems in which a σ-bond forms at the expense of a π-system.[14] The rehybridization at C3 causes the otherwise planar molecules to distort into a butterfly-like conformation, and the bond lengths are localized into a pattern consistent with the valence bond (VB) formulation shown in Figure 3.3A. Each individual dimer is surrounded by a web of close S---S′ and S---N′ intermolecular contacts d1-d5, which are listed in Table 3.3. We believe this extensive network of interactions stabilizes the dimers with respect to dissociation.

Table 3.2 Crystallographic Data for **3-2** (R = Et)

	α-[**3-2**]$_2$ (R = Et)	β-[**3-2**]$_2$ (R = Et)
a, Å	9.332(2)	4.5411(15)
b, Å	7.4076(16)	7.583(2)
c, Å	14.207(3)	27.391(9)
β, deg	100.594(3)	94.050(5)
V, Å^3	965.4(4)	940.9(5)
ρ(calcd), g cm^{-1}	1.798	1.845
space group	$P2_1/n$	$P2_1/c$
Z	2	2
temp, K	298(2)	298(2)
μ, mm^{-1}	0.944	0.969
λ, Å	0.71073	0.71073
θ_{full}, deg	27.50	25.00
data/restr/param	2203/0/128	2000/0/128
solution method	direct methods	direct methods
R, R_w (on F^2)	0.0382, 0.0899	0.0782, 0.1725

Table 3.3 Summary of Intra- and Intermolecular Distances (in Å) in **3-2** (R = Et)

	α-[**3-2**]$_2$ (R = Et)	β-[**3-2**]$_2$ (R = Et)
	C3–C3′, 1.607(4)	S4–S4′, 2.168(4)
	N2–C1, 1.289(3)	S3···S4, 2.817(4)
	N4–C4, 1.276(3)	C3–S3, 1.641(7)
d1	S---S′, 3.432(1)	S---N′, 2.862(6)
d2	S---N′, 3.140(2)	S---N′, 3.011(6)
d3	S---N′, 2.959(2)	S---S′, 3.226(3)
d4	S---S′, 3.534(1)	S---C′, 3.435(6)
d5	S---S′, 3.317(1)	--

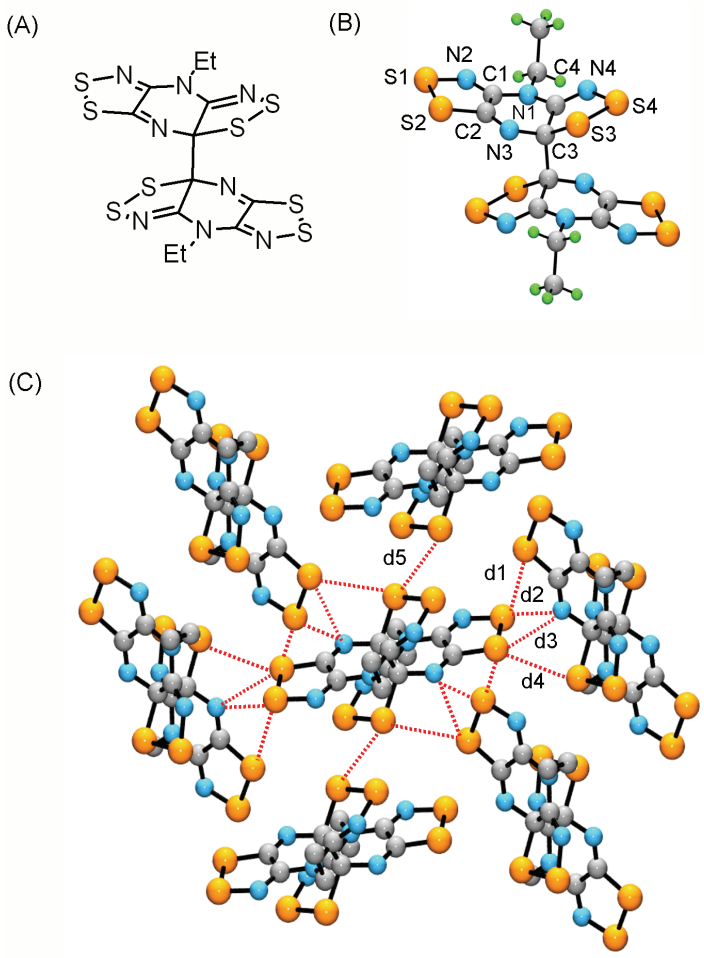

Figure 3.3 Crystal structure of the α-phase of **3-2** (R = Et), with (A) the valence bond formulation, (B) the C-C σ-dimer, and (C) the web of close S---S′ and S---N′ contacts d1-d5 (hydrogens are removed for clarity).

Crystals of the β-phase of **3-2** (R = Et) belong to the monoclinic space group $P2_1/c$ and also consist of centrosymmetric dimers. However, in this case the radicals are bonded through a lateral S4-S4′ σ-bond that is 2.168(4) Å in length. The structure is illustrated in Figure 3.4, with crystallographic data listed in Table 3.2. The nearly coplanar association of radicals is accompanied by ring opening and formation of an exocyclic thione group, the sulfur atom (S3) of which develops a long range (2.817(4) Å) hypervalent interaction with S4. The resulting localization of bond lengths is consistent with the VB formulation shown

in Figure 3.4A. This mode of dimerization has been observed for 1,2,3-thiaselenazolyls, in which the molecules are bonded at selenium,[15] but it has never before been seen for 1,2,3-dithiazolyls.[16] The dimers are tightly packed into intersecting π-stacked arrays that are linked into ribbons by short S---S′ and S---N′ contacts d1-d3 (Table 3.3). These intermolecular interactions are limited to the outer edges of each dimer, as their inner cores are far removed from neighbouring molecules. There is also a set of S---C′ contacts (d4) that run up and down the slipped π-stacks

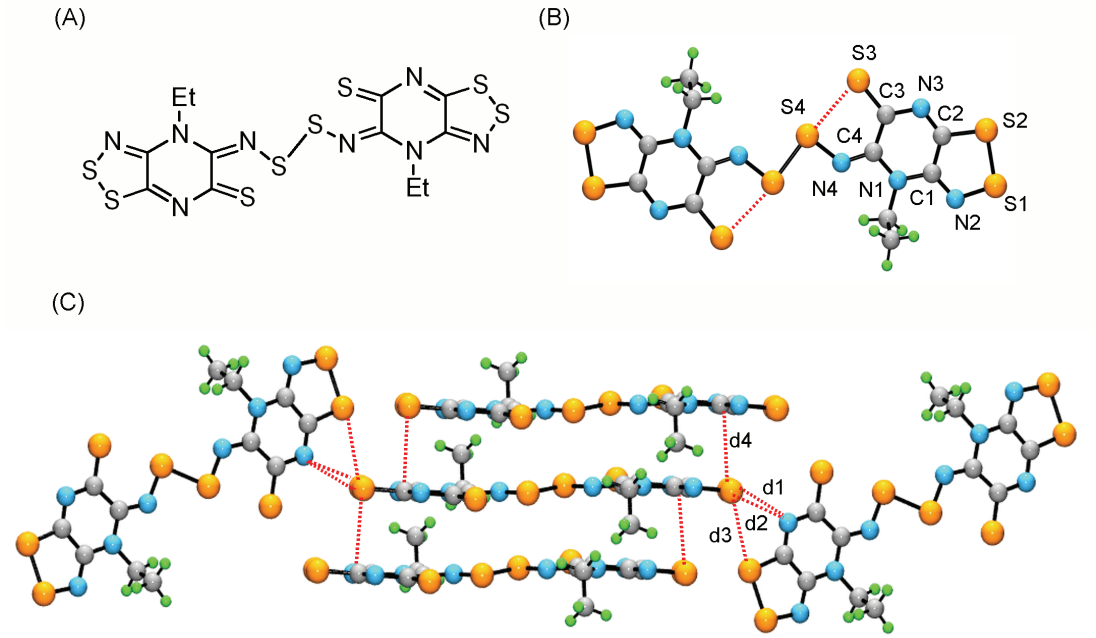

Figure 3.4 Crystal structure of the β-phase of **3-2** (R = Et), with (A) the valence bond formulation, (B) the S-S σ-bonded dimer, and (C) the ribbons of slipped π-stacks with close intermolecular contacts d1-d4.

To date the known examples of 1,2,3-dithiazoyl dimers associate cofacially through their π-systems, and are linked *via* long (> 3.0 Å) transannular S---S′ contacts.[17] The observation of these new modes of dimerization is therefore unusual, but the occurrence of two different modes for the same radical has never before been seen for a thiazyl radical.[18] In the present case the C-C bonded α-dimer appears to be the kinetically favoured product, as it readily crystallizes on chemical reduction in MeCN at room temperature. Vaporization and recondensation of the radical leads to partial or complete conversion (depending on the landing zone temperature) to the more thermodynamically favored β-dimer. This interpretation is supported by the results of B3LYP/6-31G(d,p) calculations (performed with full geometry optimization) on **3-2**, α-[**3-2**]$_2$ and β-[**3-2**]$_2$ (R = Et), which predict that association of the radical to the C-C dimer is, at the molecular level, an endothermic process (Figure 3.5). Presumably the high lattice energy of the crystal structure, resulting from the network of close S---S' and S---N' contacts, stabilizes the dimer in the solid state. By contrast, radical association to the S-S bonded β-dimer is exothermic, but the process requires thermal activation, as might be expected from a reaction that involves an electronic configurational (σ → π) change and is nominally symmetry forbidden.[19] However, the fact that **3-2** is readily detected by EPR when β-[**3-2**]$_2$ is dissolved in methylene chloride suggests that the interconversion barrier is not great.

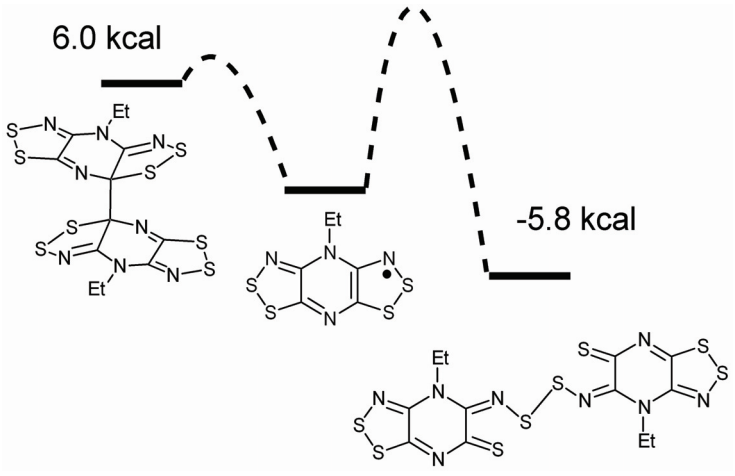

Figure 3.5 B3LYP/6-31G(d,p) enthalpies of dimerization (per mole of dimer) for **3-2** (R = Et).

3.4.2 Transport Properties

Since both phases of **3-2** (R = Et) consist of diamagnetic dimers, the magnetic properties were not pursued. The two-probe conductivity measurements demonstrated that the α-phase is an insulator, while the β-dimer behaves as a semiconductor with $\sigma_{RT} \sim 10^{-7}$ S cm^{-1}.

3.5 Solid State Properties of the Methyl-Substituted Radical

Crystals of **3-2** (R = Me) could not be grown by vacuum sublimation, and were instead obtained chemically through the careful diffusion of solutions of [**3-2**][BF_4] (R = Me) with DMFc using H-cell techniques. Material used for bulk measurements was made by large scale chemical reduction to afford **3-2** (R = Me) as a golden powder. Single crystal structural work at ambient temperature showed a high symmetry space group with vertically aligned ABABAB π-stacks as anticipated. However, the transport properties seemed to contradict this seemingly perfect packing arrangement (vide infra), and a low temperature structural investigation was undertaken. The crystallographic work performed at 295, 123 and 88 K showed subtle structural changes with decreasing temperature, which accounted for the observed transport properties.

3.5.1 Crystal Structure

At 295 K, the copper-coloured needles of **3-2** (R = Me) belong to the high symmetry orthorhombic space group *Cmca*, and consist of vertically aligned π-stacks of evenly spaced radicals. There are eight molecules in the unit cell as illustrated in Figure 3.6, with views down the stacking direction and perpendicular to it. The crystallographic data is listed in Table 3.4. Each radical is situated on a mirror plane at $x = 0$ and ½, with consecutive plates along the z direction related by an a glide, so as to form not superimposed, but alternating ABABAB π-stacks.

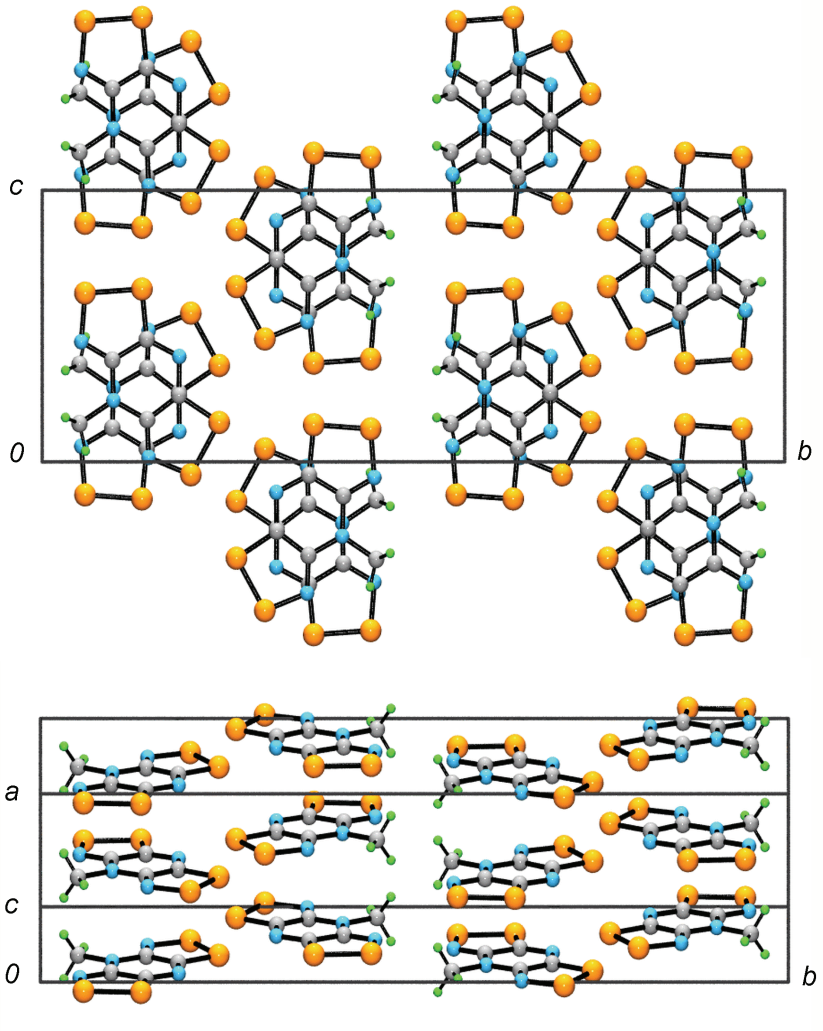

Figure 3.6 Two views of the *Cmca* unit cell of **3-2** (R = Me) at 295 K, down the stacking direction (above) and perpendicular to it (below).

Table 3.4 Crystallographic Data for **3-2** (R = Me) at 88, 123 and 295 K

	88 K	123 K	295 K
a, Å	9.244(2)	6.5456(6)	6.6488(2)
b, Å	6.5344(17)	9.2558(8)	27.2177(5)
c, Å	27.035(7)	27.040(2)	9.2797(2)
β	90.004(4)	–	–
V, Å^3	1633.0(7)	1638.2(2)	1679.30(7)
ρ(calcd), g cm^{-3}	2.012	2.006	1.957
Space group	$P2_1/c$	*Pccn*	*Cmca*
Z	8	8	8
μ, mm^{-1}	1.11	10.266	10.015
λ, Å	0.71073	1.54178	1.54178
θ_{full}, deg	28.29	65.04	68.22
Data/restraints/parameters	4040/182/236	1399/0/130	829/0/79
Solution method	Direct methods	Direct methods	Direct methods
R, Rw (on F^2)[a]	0.0720, 0.1398	0.0570, 0.1617	0.0387, 0.1105

[a] $R = [\Sigma||F_o| - |F_c||]/[\Sigma|F_o|]$ for $I > 2\sigma(I)$; $R_w = \{[\Sigma w||F_o|^2 - |F_c|^2|^2]/[\Sigma(w|F_o|^4)]\}^{½}$

This packing arrangement allows for the generation of several close intermolecular interactions and these are shown in Figure 3.7. In addition to the lateral S---S′ and S---N′ contacts (which range in distance from 3.059(3) - 3.466(1) Å) , there are many S---S′ contacts within and between the π-stacks that lace the radicals together in both the *x* and *z* directions. Although these contacts (at 3.831(1) - 3.865(1) Å) are outside the van der Waals distance for two sulfur atoms (3.6 Å),[20] they are well oriented for good pπ-overlap. The inter-columnar contacts form a ladder-like appearance between the stacks, while the intra-stack interactions appear to zigzag between molecules as a result of the twisted nature of the radicals in this direction.

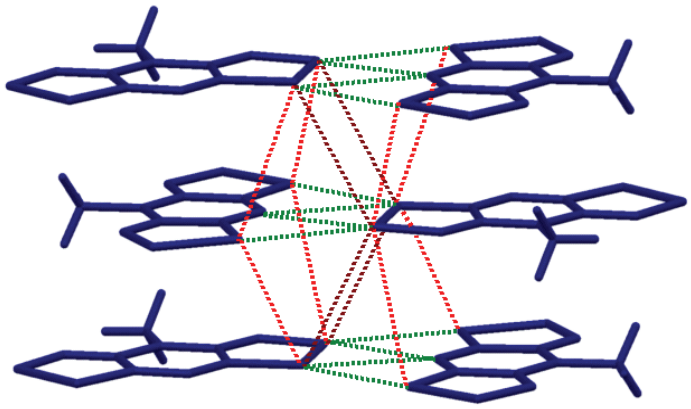

Figure 3.7 Packing of the π-stacks, showing intermolecular S---N′ (< 3.19 Å) and S---S′ (< 3.87 Å) contacts between the stacks.

An isolated π-stack taken from the structures obtained at 295, 123 and 88 K is presented in Figure 3.8, with the ORTEP drawings showing the size and shape of the thermal ellipsoids at each temperature. At 295 K the molecules are evenly spaced, and the thermal ellipsoids are large, but evenly distributed, as one would expect from a high temperature data collection. Upon cooling to 123 K, the crystal structure could again be solved in the high symmetry space group *Cmca* and refined to afford an R-factor of ~5 %. However, there were two features that suggested that there was a problem with this assignment, (i) the transport properties of the material did not show metallic behaviour, which would be a natural consequence of the *Cmca* structure suggested (vide infra), and (ii) the thermal ellipsoids of the sulfur atoms in the *Cmca* structure became more elongated along the stacking direction at the lower temperature, as shown in Figure 3.8. This prompted a careful examination of the weak reflections and systematic absences for the 123 K data set, and it was found that there were several violations of the C-centering. A primitive orthorhombic cell was more appropriate, and the assignment of the *Pccn* space group included the weak data and consisted of reasonably shaped thermal ellipsoids.

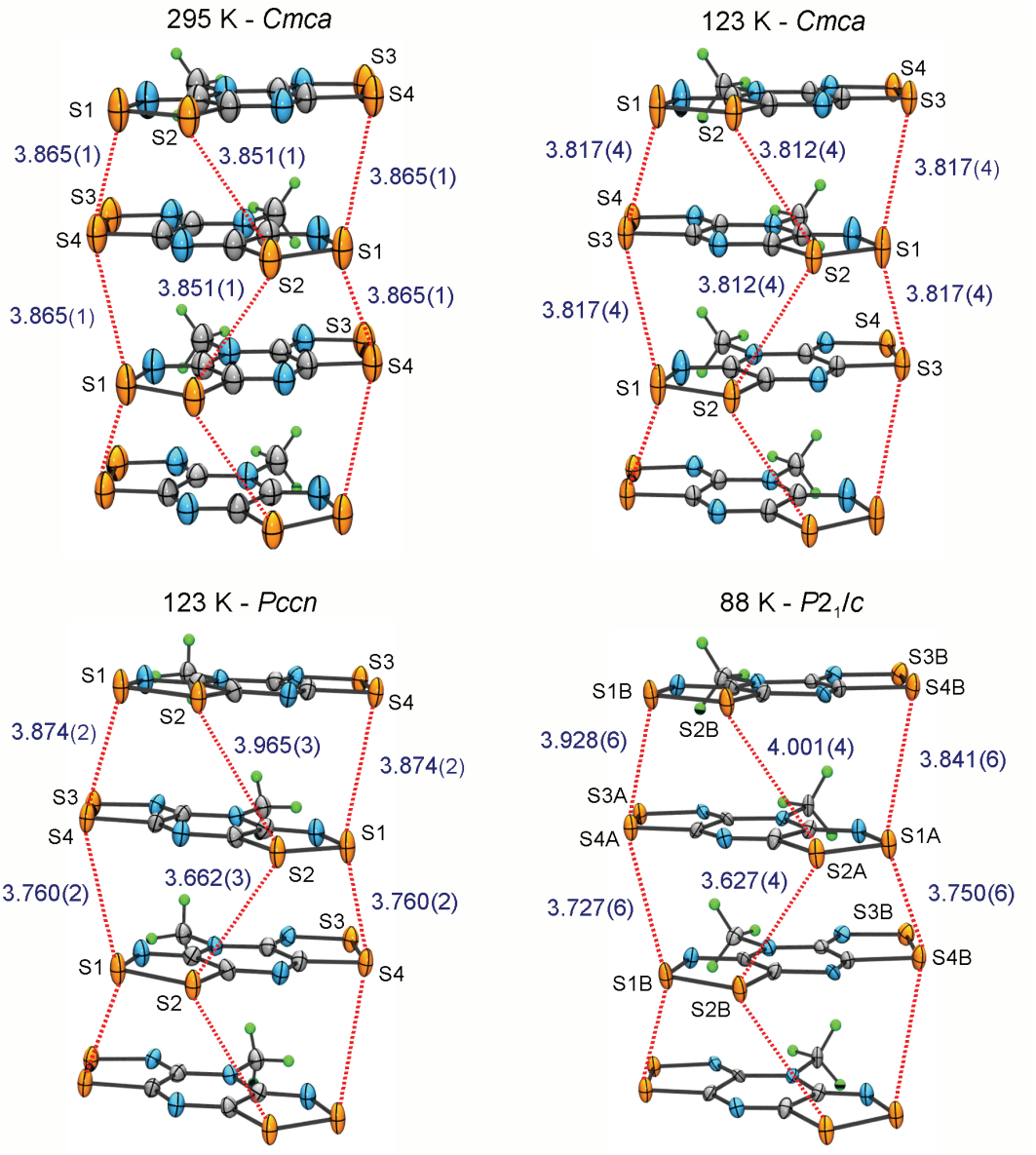

Figure 3.8 Alternating π-stacks of **3-2** (R = Me) at 295, 123 and 88 K, showing ORTEP drawings (50% thermal ellipsoids), short S---S′ contacts (in Å), and atom numbering.

As a result of the change in space group to *Pccn*, there is a crossover in the definition of the *b* and *c* axes, as may be seen in Table 3.4. Also evident in Table 3.4 is the contraction in the unit cell parameters typical of a lower temperature experiment. Within this new space group, the mirror plane is no longer present and the radicals along the π-stacks are free to move away from the otherwise fixed positions of *x*

= 0 and ½. Although the molecules remain essentially planar (deviation from the plane $\delta = 0.018$ Å), there is a subtle rocking of the plates, with a tilt angle of 2.2° away from perpendicularity with respect to the stacking direction. Radicals between the stacks are now related by a 2-fold rotation axis, and are no longer evenly spaced within each column. Instead there is an alternation in the plate-to-plate separation, with intra-stack S---S′ contacts interchanging between long and short distances as demonstrated in Figure 3.8.

A third data set was collected at 88 K, and a close examination of the systematic absences revealed a loss of two of the three glide planes of *Pccn* and a further reduction of space group symmetry to primitive monoclinic. The structure was assigned to the $P2_1/c$ space group. As before, there is a crossover in the unit cell axes ($a \leftrightarrow b$), although the cell parameters remain very similar to those seen in the 123 K structure (Table 3.4). As a result of the symmetry lowering, there are now two molecules in the asymmetric unit so that consecutive plates along the ABABAB π-stacks are no longer equivalent. The two molecules (A and B) are essentially planar ($\delta = 0.026$ and 0.24 Å) and are slightly more tilted (2.6 and 2.8°) relative to the 123 K structure. The 88 K π-stack presented in Figure 3.8 shows that the differing amounts of rocking for each radical cause the once alternating set of S---S′ distances to be dissimilar on either side of the stack.

3.5.2 Magnetic Susceptibility Measurements

The magnetic susceptibility measurements on **3-2** (R = Me) were performed on a Faraday balance over the temperature range 9-300 K, and the results are shown in Figure 3.9. The paramagnetic susceptibility, χ_P, has been corrected for diamagnetic contributions ($\chi_D = 117.29 \times 10^{-6}$ emu mol^{-1}), which were estimated using Pascal's constants.[21] The χ_P versus T plot shows that at ambient temperature, the material is weakly paramagnetic, with $\chi_P = 277 \times 10^{-6}$ emu mol^{-1} at 300 K. With decreasing temperature the χ_P value decreases to a minimum (at 101×10^{-6} emu mol^{-1}) near 100 K, and then rapidly increases as a result of paramagnetic defects in the lattice. This paramagnetic behaviour has been fit to the Curie-Weiss expression (red, solid line in Figure 3.9) between 12 and 81 K, and values of $C = 0.0091$ emu K mol^{-1} and

θ = - 5.2 K have been extracted. The temperatures at which the crystal structures were determined are indicated by green arrows in Figure 3.9 to show the relationship between the magnetic susceptibility and crystal structure at each temperature.

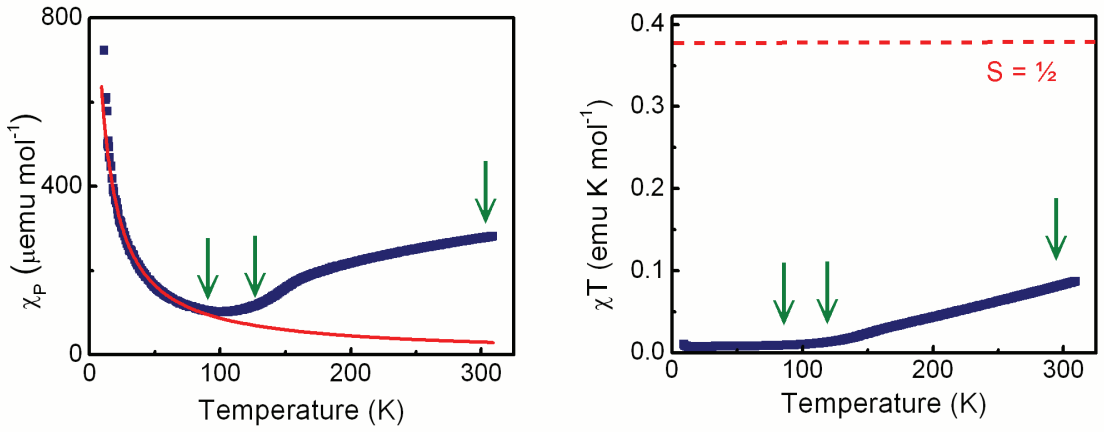

Figure 3.9 Magnetic susceptibility of **3-2** (R= Me), with plots of χ_P and χ_PT as a function of temperature. The red line on the χ_P versus T plot shows the Curie-Weiss fit, and dashed red line on the χ_PT versus T plot is the expected χ_PT value for an S = ½ system. The arrows indicate temperatures at which crystal structures were obtained (at 88, 123 and 295 K).

Also shown in Figure 3.9 is a plot of χ_PT as a function of temperature. Below 100 K, χ_PT remains approximately constant, with a value of 2% of that expected (0.375 emu K mol^{-1}) for a Curie paramagnet with S = ½. This residual paramagnetism amounts to the contribution of the defect electrons to the total moment. Above 120 K, the value of χ_PT begins to increase steadily from its threshold value, reaching a value of 0.09 emu K mol^{-1} at 300 K, which corresponds to a spin defect concentration of approximately 25%. Similar paramagnetic enhancements of otherwise diamagnetic π-dimer stacks have been observed elsewhere,[22,23] and these have been attributed to the uncoupling of weak intra-dimer bonds and the generation of additional spin defects.

3.5.3 Conductivity Measurements

Four-probe conductivity (σ) measurements were carried out on both pressed pellet and single crystal samples of **3-2** (R = Me). The results are self-consistent, as the conductivity at 295 K from a pressed pellet sample is 6.4×10^{-4} S cm^{-1}, while for a single crystal the conductivity increases to 9.7×10^{-4} S cm^{-1}. These values constitute the highest conductivity values ever observed for a thiazyl radical. The temperature dependence of the single crystal conductivity over the range 73 K - 295 K, shown in Figure 3.10, confirms that the conductivity is activated. It is also apparent that the thermal activation energy E_{act} is itself temperature dependent, with two distinct and approximately linear conductivity vs 1/T regimes, one spanning the range 295 K - 120 K, the other 120 K - 80 K. In the high temperature range the derived E_{act} is 0.19 eV, while in the low temperature region it is 0.12 eV. Below 80 K, the activation energy appears to drop even further, but there is insufficient data to warrant a numerical analysis.

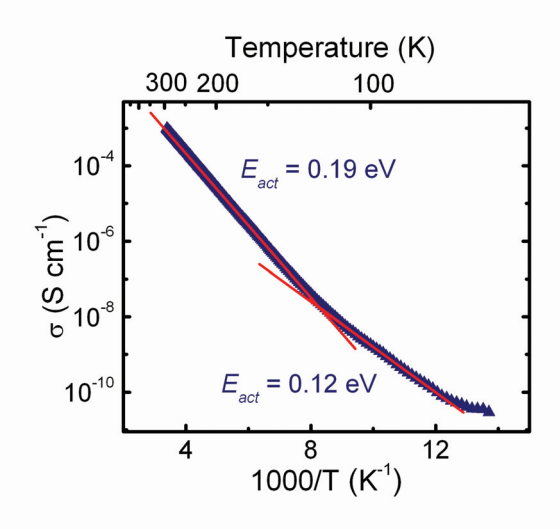

Figure 3.10 Single crystal conductivity of **3-2** (R = Me) at ambient pressure.

The pressure dependence of the conductivity of **3-2** (R = Me) has also been probed using a cubic anvil press. As illustrated in Figure 3.11, σ (at 294 K) increases steadily with applied pressure, reaching a value near 0.2 S cm^{-1} at 5 GPa. Analysis of the temperature dependence (from 20 °C to 90 °C) of the conductivity indicates that it remains activated over the entire pressure range studied. From a series of plots

of log σ *vs* 1/T, the activation energies E_{act} have been derived as a function of pressure, and these results are also plotted in Figure 3.11. Initially the value of E_{act} decreases steadily to a plateau value near 0.13 eV between 3 and 4 GPa. It then begins to decrease more rapidly around 5 GPa, reaching a value of 0.11 eV at 5.5 GPa, the limiting pressure of the apparatus. Comparison of these results with those obtained from the slipped π-stack bisdithiazolyl **3-1** (R_1 = Me, R_2 = Ph)[24] reveals that the pressure responses of the conductivity for the two compounds are similar, that is, both show an increase in conductivity of about three orders of magnitude over a 5 GPa range. However, for the present compound the decrease in the activation energy with increasing pressure is somewhat smaller.

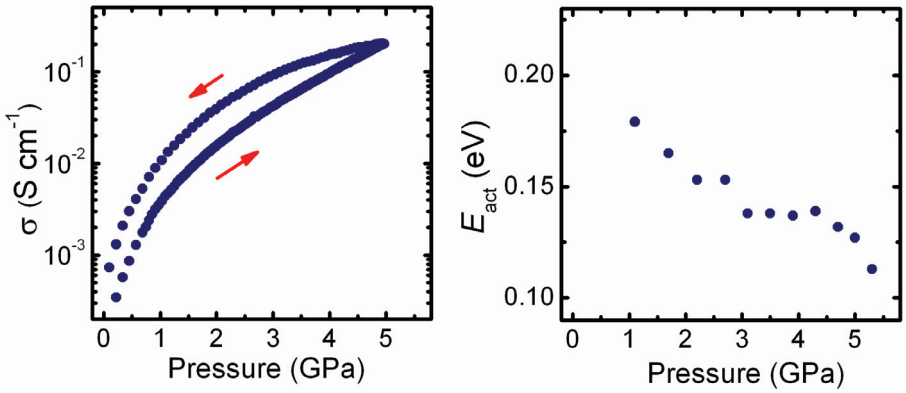

Figure 3.11 Pressure dependence of σ (at 294 K) (left) and E_{act} (right) of **3-2** (R = Me).

3.5.4 Near-Infrared Spectrum

As a complement to the conductivity measurements, and the activation energies derived therefrom, the near-infrared spectrum of a single crystal sample of **3-2** (R = Me) has been examined at ambient temperature. Figure 3.12 shows the IR transmittance over the range 650 - 11000 cm^{-1}. In the mid-IR region, between 650 and 3100 cm^{-1}, there is a series of absorptions arising from molecular vibrations of the molecule. Underlying these modes, however, is a strong background absorption, which, we believe, arises from solid state processes (vide infra). In addition, there is a strong, well-developed, low lying absorption cutoff beyond 3000 cm^{-1} which, as will be described below, corresponds to the valence to conduction band

excitation of a semiconductor. The optical energy gap E_g has a threshold value near 0.48 eV, increasing to near 0.75 eV at the transmission cutoff.

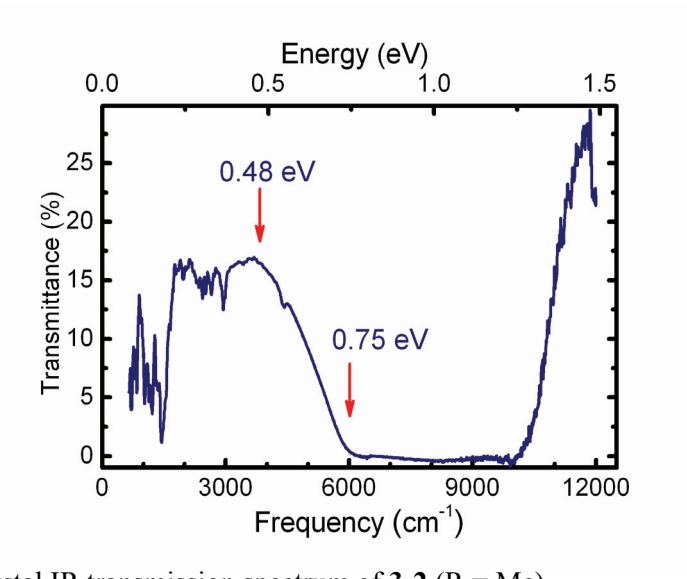

Figure 3.12 Single crystal IR transmission spectrum of **3-2** (R = Me).

3.5.5 Electronic Band Structures

In order to develop an understanding of the electronic structure of **3-2** (R = Me), and to rationalize the results of the crystallographic, magnetic, conductivity and optical measurements, Extended Hückel Theory (EHT) band structure calculations have been carried out on the three crystal structures of **3-2** (R = Me) reported in Section 3.5.1. The results are shown in Figure 3.13 in the form of dispersion curves for the crystal orbitals (COs) arising from the eight radical SOMOs (singly occupied molecular orbitals) in the unit cell, as tracked along the reciprocal space direction that corresponds to the π-stacking direction of each cell.[‡] At 295 K, in the *Cmca* structure, the alternating orientation of radicals along the π-stack produced by the *a*-glide precludes perfect superposition and reduces orbital interactions along the stack, that is, those

[‡] In the two orthorhombic structures (*Cmca* and *Pccn*) there is an absolute correspondence between the directions of the real and reciprocal unit cell vectors, and in the 88 K ($P2_1/c$) structure the β angle is such that the correspondence is very nearly exact. The COs are plotted from Γ (0, 0, 0) to X (½, 0, 0) for the two orthorhombic structures, and from Γ (0, 0, 0) to Y (0, ½, 0) for the monoclinic cell. For the calculations on the 295 K structure we used the special position of the primitive cell rather than that of the full C-centered version so as to allow for a more direct comparison of the three band structures.

associated with the S1---S4′ and S2---S2′ contacts (Figure 3.8). However, the same feature also allows for increased interactions between the stacks, that is, through the S---S′contacts shown in Figure 3.7, so that significant bandwidth can still be obtained. Based on the energetic spread of the eight COs, the estimated bandwidth W is close to 1.5 eV, approaching that predicted for a perfectly superimposed π-stacked structure.[25] On the basis of this description, such a bandwidth might well be expected to give rise to an f = ½ metal.

The loss of C-centering occasioned by cooling crystals of **3-2** (R = Me) to 123 K, and the associated onset of an alternation in the plate-to-plate separation along the π-stack, should lead to the opening of an energy gap at the Fermi level and the creation of a semiconducting state. The band structure calculations on the *Pccn* cell support this conclusion, although the observed band gap E_g is only 0.09 eV. However, upon further cooling, and transformation to the monoclinic $P2_1/c$ cell, the magnitude of the band gap increases quite dramatically to 0.42 eV, in spite of the fact that the structural changes between the *Pccn* and $P2_1/c$ structures appear to be extremely small.

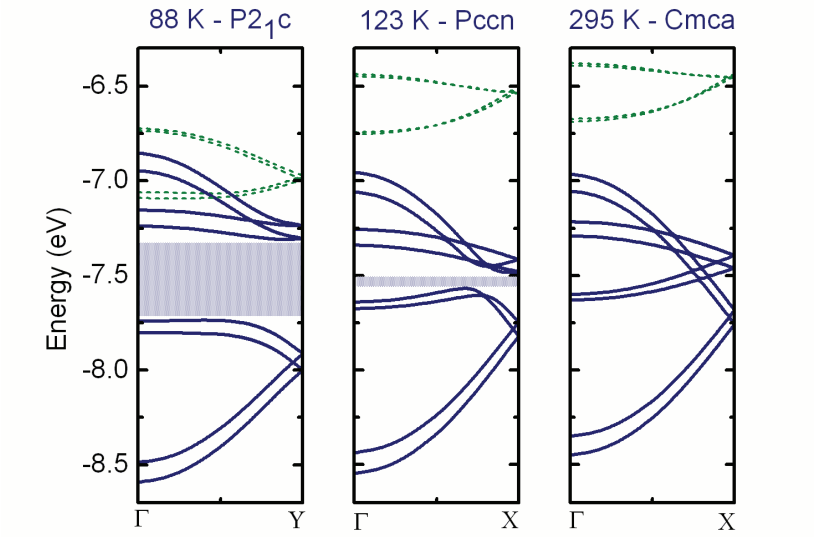

Figure 3.13 EHT dispersion curves for the three crystal structures of **3-2** (R = Me), showing the emergence of a band gap at lower temperatures. The solid blue lines are the COs arising from the radical SOMOs. Higher-lying orbitals (green, dashed lines) overlap in the $P2_1/c$ structure.

3.5.6 Discussion of the Transport Properties

Our design strategy in preparing the pyrazine-bridged bisdithiazolyls **3-2** was to obtain superimposed π-stacks in the solid state, so as to maximize orbital overlap between radical SOMOs and achieve a bandwidth *W* sufficiently large to overcome the on-site Coulomb repulsion energy *U*. We were very excited then to find that at 295 K, **3-2** (R =Me) adopted the high symmetry *Cmca* space group consisting of radicals locked by glide planes into alternating, but apparently evenly spaced, π-stacked arrays. This is a hitherto unobserved packing pattern for a neutral radical (f = ½) conductor, although similar symmetric ABABAB π-stacking arrangements defined by glide planes have been observed in CT salts.[26] The strongly interconnected π-stacks in **3-2** (R = Me) suggest a well-developed 2-dimensional electronic structure, a view confirmed by the band structure calculations. Given the apparent convergence of the necessary energetic and structural features, it was at first surprising that its conductivity is activated, and not metallic.

So why is **3-2** (R = Me) not a metal at room temperature? One possible reason is the material is a Mott insulator.[26] The weak but increasing paramagnetism above 120 K could be interpreted in terms of evenly spaced (undimerized) π-stacks consisting of strongly antiferromagnetically coupled radicals. The activated conductivity would then be a consequence of strong electron correlation, that is, *W* is insufficient to overcome *U*. Although the band calculations indicate a remarkably high bandwidth ($W \sim 1.5$ eV) for a molecular material, even this may not be sufficient to offset short range correlation.[27] The other possible explanation is that the material is a semiconductor. Indeed such a description would be the natural default if the diamagnetic π-dimer stacked structure identified at 88 K were also observed at room temperature. The band gap $E_g = 0.42$ eV value estimated from the EHT calculations would then be satisfyingly close to the threshold optical excitation found from near-IR measurements. It would also be about twice the value of the thermal activation energy $E_{act} = 0.19$ eV obtained from the variable temperature conductivity measurements, a result expected for an intrinsic semiconductor. The moderate response of the conductivity to pressure would also be in keeping with stacked π-dimer structures.[28] However, this simple explanation

is, by itself, insufficient, as it ignores the magnetic and structural changes that occur upon heating the material above 120 K. As noted earlier, previous work on diamagnetic π-stacked thiazyl dimers has shown that, with increasing temperature, an increase in the magnetic response is often observed.[22,23] This "spin breakout" can be rationalized in terms of a random uncoupling of dimers and the generation of radical defects. Figure 3.14 illustrates this process as it applies to the slightly tilted π-dimer stacks of the $P2_1/c$ structure of **3-2** (R = Me). In the absence of any residual defects (which are in reality present) the structure would be as shown in Figure 3.14A, with all radicals paired to afford a perfectly diamagnetic ground state. Heating the structure causes an opening of some of the dimers, to produce geminal (Figure 3.14B) and/or non-geminal (Figure 3.14C) radical defects. At the same time the previously regular tilt angle of the dimers is replaced by a random clockwise or counterclockwise rocking. Any of these structural modifications, or a combination thereof, will give rise to a gradual increase in magnetization and, at the same time, lead to a loss of crystallographic correlation in the orientation of the molecules along the stacking direction. This loss of correlation creates the illusion of higher symmetry. The observation of C-centering and assignment of the *Cmca* space group is thus not a result of perfect ordering of uncoupled radicals, as depicted in Figure 3.14D, but rather a consequence of thermally induced disorder along the π-stacks of the $P2_1/c$ cell, with the *Pccn* cell representing an intermediate phase in this process. The elongated thermal ellipsoids for the sulfur atoms in the *Cmca* structure (Figure 3.8) attest to the fact that the high symmetry space group is an artifact of the diffraction experiment, and that over the entire temperature range studied the transport properties of the material are best rationalized in terms of a structure consisting of defect-contaminated π-dimer stacks.

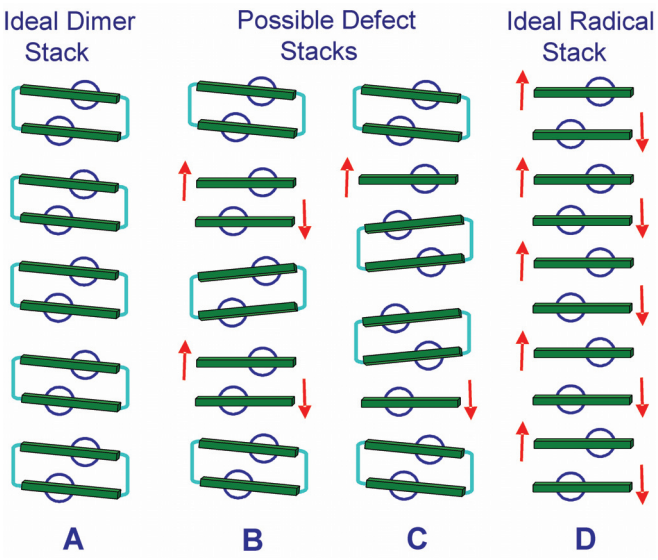

Figure 3.14 Radical defects (B, C) generated upon heating perfectly ordered π-dimer stacks (A). A fully symmetric π-radical stack (D) is also shown.

Given the above structural description, we propose a hopping model[29] to account for the conductivity of **3-2** (R = Me) as a function of temperature. We have used this approach before to rationalize the transport properties of the dithiazolyl radical **3-9** (Figure 3.15),[23] the solid state structure of which possessed a head-over-tail π-dimer stacking motif similar to the ABABAB arrangement described here. In the present case, topological defects and lattice disorder give rise to a finite density of states (Figure 3.16) within the band gap of the ideal $P2_1/c$ structure (Figure 3.13), even at low temperatures (< 120 K). With increasing temperature the radical spins generated by uncoupling of the dimers increase the density of these defect states. These states are not localized, and contribute to the conductivity. They may, however, be split by Coulomb correlations into donor (D^0) and acceptor (D^-) Hubbard sub-bands.[29] The low temperature conductivity (< 120 K) may thus be viewed as arising from variable range hopping between these weakly metallic midgap states (Figure 3.16A). These processes can be collectively associated with a thermal activation energy E_{act} = 0.12 eV (Figure 3.10). At elevated temperatures (> 120 K) the conductivity stems from hopping that also involves excitations between the midgap states and the band edges of either the valence or conduction bands (Figure 3.16B), processes for which E_{act} = 0.19 eV,

a value in good agreement with the band gap estimated from the optical measurements and EHT calculations. The infrared spectrum can also be explained within this model. The poorly resolved background below 3000 cm^{-1} (Figure 3.12) can be ascribed to electronic excitations between the midgap states and the valence/conduction bands, while the strong broad band above 3000 cm^{-1} corresponds to valence to conduction band excitations.

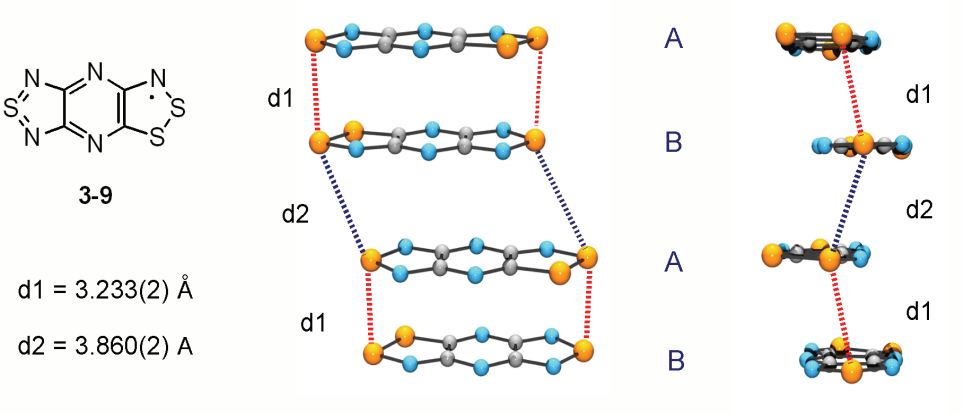

Figure 3.15 Head-over-tail ABAB π-dimer stacking in dithiazolyl radical **3-9**.

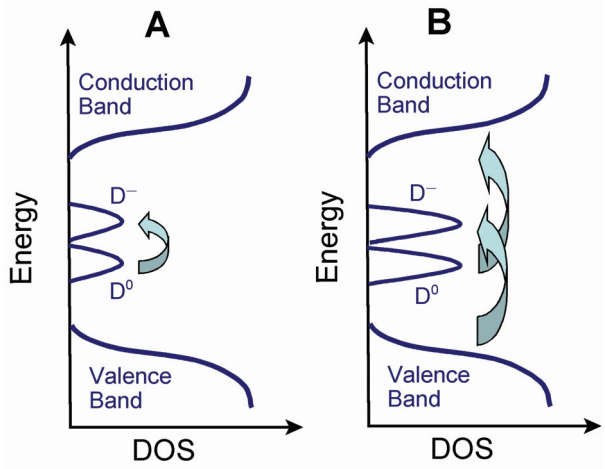

Figure 3.16 Schematic density of states (DOS) diagram showing donor (D°) and acceptor (D^{-}) Hubbard defect bands in **3-2** (R = Me), with low temperature excitations between these states (A) and high-temperature excitations from/to the valence/conduction bands (B).

3.6 Summary

In an exercise in crystal engineering and structural control, the pyrazine-bridged bisdithiazolyls **3-2** were pursued in order to obtain more nearly superimposed π-stacking in the solid state than the pyridine-bridged variants **3-1**. It was believed that this arrangement, if possible, would provide maximum orbital overlap between radicals, and afford a *W* that would surpass *U*. Two derivatives were investigated, and the CV and EPR studies demonstrated that the pyrazine-based framework **3-2** possessed a low *U* value and a delocalized spin distribution, features similar to those of **3-1** and necessary for use as neutral radical conductors. However, the ethyl-substituted compound formed two phases in the solid state, both consisting of diamagnetic σ-bonded dimers. It was found that with the removal of the steric protection afforded by the basal ligand, the radical becomes vulnerable to dimerization. The α-dimer represents the first heterocyclic thiazyl radical that dimerizes through a localized C-C σ-bond. Moreover, its conversion to the β-isomer provides a sobering caveat that, in the absence of lattice effects, ring-opening S-S σ-dimerization of bisdithiazolyl radicals is the thermodynamically preferred outcome.

By contrast the corresponding methyl derivative **3-2** (R = Me) crystallizes in alternating ABABAB π-stacked arrays, with rows of π-stacks dovetailed together by π-type interannular S---S′ interactions. The conductivity of this material is the highest ever seen for a neutral thiazyl radical, with a room temperature value $\sigma_{RT} \sim 0.001$ S cm^{-1}. The material is not, however, a metal, as the conductivity remains activated, even under an applied pressure of 5.5 GPa. The high symmetry space group *Cmca* observed crystallographically at ambient temperatures is nonetheless consistent with an $f = ½$ metallic state. Variable temperature magnetic measurements confirm diamagnetic behaviour below 120 K and low temperature crystallographic work establish a sequential lowering in space group symmetry from *Cmca* (295 K) to *Pccn* (123 K) to $P2_1/c$ (88 K), changes which give rise to an opening of a band gap at the Fermi level, and the formation of a semiconducting ground state. While the activated conductivity at room temperature could be ascribed to Mott insulating behaviour, we believe that the high symmetry *Cmca* space group is an artifact arising from the loss of long range correlation in the slightly tilted π-stacks of the $P2_1/c$ structure. As a result, at ambient

temperatures the material is still best described as a semiconductor, with conductivity arising from hopping within and to/from midgap states produced by radical defects present in the lattice.

Although the methyl-substitued radical avoided associating into σ-bonded dimers, and crystallized as vertically aligned π-stacks as designed, π-dimerization was not prevented. The work described here for the pyrazine-bridged bisdithiazolyls **3-2** suggests that superimposed π-stacking may be invariably unstable to dimerization, and that this packing arrangement may not be ideal for metallic conductivity after all.

3.7 Future Work

Selenium insertion is the obvious design modification for the pyrazine-bridged bisdithiazolyls **3-2** in the pursuit of a metallic conductor. Since these systems would be densely packed in the solid state, it would be interesting to see if a bandwidth large enough to afford metallic conductivity could be achieved. If so, what effect would selenium have on the packing arrangement? Would a selenium-containing variant be isostructural to **3-2** (R = Me) and adopt the alternating π-stacked structure, or would it form lateral σ-bonded dimers as seen for other 1,2,3-thiaselenazolyls?[15] Regardless, studying the effects of selenium incorporation on a new heterocyclic framework such as **3-2** would lead to a better understanding of the requirements necessary for high conductivity and strong magnetic exchange interactions in neutral radicals, and may lead to the discovery of very interesting functional materials.

Various attempts at selenium incorporation into the **3-2** system have been made, but have so far shown little success. Inserting selenium into the 2-position, as in [**3-10**]$^+$, by the reaction of [**3-2**]$^+$ with two or three equivalents of selenium dioxide in MeCN has shown partial completion by mass spectrometry. The reaction mixture gradually turns from blue to green, but before the two selenium atoms have been inserted the intermediates start to decompose. Currently, no material has been isolated by this method. As an alternative route, the reaction of the mono-substituted aminophosphiniminodithiol **3-7** with selenium tetrachloride has been tried, but has also been unsuccessful.

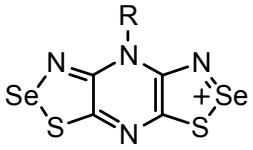

[**3-10**]$^+$

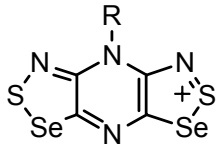

[**3-11**]$^+$

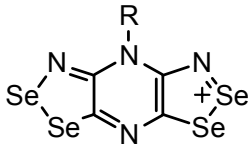

[**3-12**]$^+$

For selenium in the 1-position, as in [**3-11**]$^+$ and [**3-12**]$^+$, we have been able to make a variety of selenium-protected diaminopyrazine-diselenols, such as the selenocyanate **3-13**, the methylselenol **3-14**, and the cyanoethylselenol **3-15**, as potential starting materials. However, all reactions of these compounds with sulfur or selenium halides have failed. A variety of reaction conditions, such as the presence and amount of auxiliary base (such as triethylamine or pyridine) and changes in temperature and solvent, have been explored.

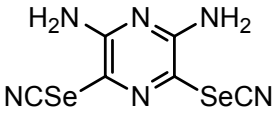

3-13

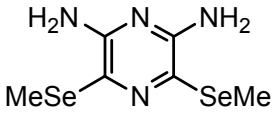

3-14

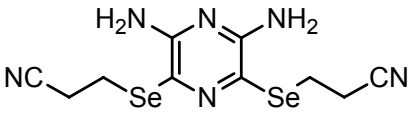

3-15

Although our previous efforts in isolating selenium-containing pyrazine frameworks have been unproductive, we have learned a great deal about selenium insertion reactions on the pyridine system **3-1** since that time. With this knowledge and experience in mind, future synthetic endeavours towards [**3-10**]$^+$, [**3-11**]$^+$ and [**3-12**]$^+$ should consider the insolubility of selenium-containing compounds, the counterion employed, the solvent used (MeCN or HOAc), as well as reaction time and temperature, as these variables tended to change considerably with each **3-1** framework studied.

3.8 Experimental Section

Preparation of 2,6-diaminopyrazine 3-5. Sodium azide (5.50 g, 84.6 mmol) was slowly added as a powdered solid to a stirred solution of dichloropyrazine **3-3** (6.00 g, 40.3 mmol) in 75 mL DMSO and the mixture heated to 70 °C in an oil bath for 1 h. The turbid orange solution was poured onto 1 L of ice/water,

and the resulting white fibrous precipitate of the diazide **3-4** filtered off on a Büchner funnel and washed with water (HAZARD). The crude (and still wet) diazide was transferred into a 500 mL flask, to which was added 200 mL water, 100 mL EtOH, 3 mL HOAc and iron filings (10.0 g). The mixture was heated to a gentle boil for 30 min, cooled and filtered. The filtrate was made alkaline (to pH > 12) with NaOH, and the resulting gelatinous precipitate filtered off. The aqueous filtrate was then flash evaporated and the residual solid extracted with 3 × 300 mL boiling DCE. The combined extracts were evaporated to afford crude 2,6-diaminopyrazine **3-5** as an off-white solid. Recrystallization from DCE afforded fibrous needles; yield 3.10 g (28.2 mmol, 70 % from **3-3**); mp 135-137 °C (lit. 136-137 °C).[3] IR: 3407 (w), 3312 (s), 3167 (s, br), 1632 (s), 1587 (m), 1537 (vs), 1293 (s), 1249 (m), 1137 (m), 1000 (m), 821 (m), 753 (w), 620 (w), 572 (w), 473 (w) cm^{-1}.

Preparation of 2,6-diamino-pyrazine-3,5-bisthiocyanate 3-6. A solution of bromine (29.0 g, 0.181 mol) in 100 mL cold MeOH was added dropwise to a cold (-78 °C) solution of NH_4SCN (27.6 g, 0.363 mol) in 500 mL MeOH over 1 h to afford a colorless slurry. After 10 min, a solution of **3-5** (10.0 g, 0.0908 mol) in 100 mL MeOH was added dropwise to the reaction mixture over 1 h, which was stirred for an additional hour at -78 °C. The mixture was warmed to room temperature and stirred for 16 h before being added to 2 L ice/water. After 1 h the yellow product **3-6** was filtered off and washed with water; yield 15.0 g (0.0669 mol, 74 %). IR: 3442 (w), 3339 (w), 3183 (w), 2168 (s), 2157 (s), 1626 (s), 1513 (s), 1430 (m), 1309 (m), 1254 (m), 1151 (w), 1036 (w), 764 (s), 676 (m), 480 (s), 454 (m), 409 (w) cm^{-1}. Anal. Calcd for $C_6H_4N_6S_2$: C, 32.13; H, 1.80; N, 37.47 %. Found: C, 32.17; H, 1.59; N, 37.20 %.

Preparation of 2-tributylphosphinimino-6-amino-pyrazine-3,5-dithiol 3-7. Tributylphosphine (27.0 mL, 0.108 mol) was added to a thick slurry of **3-6** (10.4 g, 0.0463 mol) in 250 mL MeCN to give a red solution. Upon brief stirring, a fine orange precipitate was formed. After 30 min, water (1.70 mL, 0.0943 mol) was added and the reaction mixture was stirred for an additional 30 min before filtration to afford an orange micro-crystalline powder. The product **3-7**, which crystallizes as a hydrate, was washed with 2 × 150 mL MeCN and 1 ×150 mL diethyl ether; yield 12.8 g (0.0326 mol, 70 %); dec 115 °C. IR: 3422 (w),

3276 (w), 3084 (w), 2252 (w), 1582 (m), 1553 (m), 1521 (m), 1421 (m), 1358 (m), 1292 (m), 1225 (m), 1209 (m), 1144 (m), 1113 (w), 1096 (w), 1044 (m), 937 (m), 906 (m), 891 (w), 833 (w), 780 (w), 459 (w) cm^{-1}. ^{31}P NMR (δ, $CDCl_3$): 54.6 (s, 1P). Anal. Calcd for $C_{16}H_{33}N_4OPS_2$: C, 48.95; H, 8.47; N, 14.27 %. Found: C, 48.22; H, 7.93; N, 13.91 %. The crude material was desolvated by heating it at 80 °C/10^{-3} Torr.

Preparation of 4H-bis[1,2,3]dithiazolo[4,5-b:5',4'-e]pyrazin-2-ium tetrachlorogallate [3-2][$GaCl_4$] (R = H). Pyridine (6.40 mL, 0.0791 mol) was added to a slurry of **3-7** (14.9 g, 0.0398 mol) in 400 mL MeCN. A solution of $SOCl_2$ (31.0 mL, 0.425 mol) in 30 mL MeCN was added dropwise to the slurry over 30 min to give a brown mixture (slight exotherm), which was set to reflux for 1 h. After cooling to room temperature, the brown solid [**3-2**][Cl] (R = H) was filtered off and washed with 200 mL MeCN and 200 mL DCE; yield 9.92 g (0.0369 mol, 93 %). IR: 1634 (w), 1562 (w), 1548 (w), 1535 (w), 1425 (s), 1319 (s), 1083 (m), 885 (w), 868 (w), 802 (w), 751 (w), 718 (m), 683 (w), 618 (m), 506 (m), 481 (m), 447 (m) cm^{-1}. Gallium trichloride (8.00 g, 0.0454 mol) was added to a slurry of crude [**3-2**][Cl] (R = H) (10.1 g, 0.0375 mol) in 150 mL MeCN to afford a dark violet-blue solution, which was stirred for 15 min before being filtered to remove any undissolved material. The solvent was removed from the filtrate by flash distillation to leave a purple-bronze residue that was triturated in 30 mL of a 1:1 HOAc:DCE solution. The gallate [**3-2**][$GaCl_4$] (R = H) was filtered and washed several times with HOAc/DCE mixtures, then neat HOAc, followed by diethyl ether; yield 10.3 g (0.0231 mol, 62 %). IR: 3194 (w), 1615 (w), 1559 (w), 1544 (w), 1427 (m), 1415 (m), 1330 (m), 1311 (m), 1088 (w), 880 (w), 847 (w), 723 (m), 635 (m), 505 (s), 479 (s) cm^{-1}.

Preparation of bis[1,2,3]dithiazolo[4,5-b:5',4'-e]pyrazine 3-8. A sample of [**3-2**][$GaCl_4$] (R = H) (8.19 g, 0.0184 mol) was dissolved in 150 mL MeCN to afford a blue solution that was filtered to remove any undissolved solid. A solution of Proton-Sponge (4.76 g, 0.0222 mol) in 150 mL MeCN was added dropwise to the filtrate over 15 min. After 20 min the blue-grey solid **3-8** was collected by filtration and washed with 3 × 100mL MeCN; yield 4.30 g (0.0180 mol, 100 %). IR: 1605 (w), 1412 (s), 1264 (s), 1124 (w), 1086 (m) cm^{-1}.

Preparation of 4-methyl-4H-bis[1,2,3]dithiazolo[4,5-b:5',4'-e]pyrazin-2-ium tetrafluoroborate [3-2][BF_4] (R = Me). Proton-sponge (2.03 g, 0.00945 mol) was added to a slurry of Me_3OBF_4 (5.58 g, 0.0377 mol) in 50 mL DCE to afford a yellow slurry. Zwitterion **3-8** (4.39 g, 0.0189 mol) was then added and the blue-green reaction mixture was stirred for 16 h at room temperature. The brown solid was filtered off and washed with 2 × 40 mL DCE. In order to remove protonated impurities the crude product was rapidly stirred in 200 mL warm (70 °C) HOAc for 40 min. The material so obtained was further purified by double recrystallization from MeCN to afford [**3-2**][BF_4] (R = Me) as lustrous red crystals; yield 1.64 g (0.00491 mol, 26 %); dec 273 °C. IR: 1614 (w), 1541 (m), 1503 (s), 1337 (s), 1198 (m), 1120 (m), 1085 (s), 1051 (s), 1019 (s), 951 (w), 891 (m), 877 (w), 720 (m), 663 (s), 526 (m), 513 (w), 488 (m), 477 (m) cm^{-1}. ^1H NMR (δ, CD_3CN): 3.49 (s, 3H, CH_3). UV-vis (MeCN) λ_{max}: 623 nm (log ε = 4.6). Anal. Calcd for $C_5H_3BF_4N_4S_4$: C, 17.97; H, 0.90; N, 16.77 %. Found: C, 18.08; H, 0.73; N, 17.00 %.

Preparation of 4-ethyl-4H-bis[1,2,3]dithiazolo[4,5-b:5',4'-e]pyrazin-2-ium tetrafluoroborate [3-2][BF_4] (R = Et). Proton-sponge (1.76 g, 0.00819 mol) was added to a colorless solution of Et_3OBF_4 (6.18 g, 0.0325mol) in 60 mL DCE to give a clear yellow solution. Zwitterion **3-8** (3.77 g, 0.0162 mol) was then added and the blue-green reaction mixture was stirred for 16 h at room temperature. The red-brown crude product was collected by filtration and washed 2 × 45 mL DCE. To remove protonated impurities the crude product was warmed at 70 °C in 200 mL HOAc for 40 min. This material was further purified by double recrystallization from MeCN to give [**3-2**][BF_4] (R = Et) as lustrous red crystals; yield 2.70 g (0.00775 mol, 48 %); dec 276 °C. IR: 1538 (m), 1503 (s), 1335 (s), 1198 (m), 1181 (m), 1069 (s), 1032 (s), 887 (m), 789 (m), 722 (m), 657 (m), 549 (w), 519 (m), 512 (m), 483 (m) cm^{-1}. ^1H NMR (δ, CD_3CN): 4.02 (q, 2H, N*CH*$_2$CH$_3$, *J* = 7.2 Hz), 1.27 (t, 3H, NCH$_2$*CH*$_3$, *J* = 7.2 Hz). UV-vis (MeCN) λ_{max}: 623 nm (log ε = 4.5). Anal. Calcd for $C_6H_5BF_4N_4S_4$: C, 20.70; H, 1.45; N, 16.09 %. Found: C, 20.86; H, 1.25; N, 16.31 %.

Preparation of 4-methyl-4H-bis[1,2,3]dithiazolo[4,5-b:5',4'-e]pyrazin-3-yl 3-2 (R = Me). A carefully degassed (4 freeze-pump-thaw cycles) solution of [**3-2**][BF_4] (R = Me) (0.250 g, 0.748 mmol) in 75 mL MeCN was added to an equally degassed solution of DMFc (0.256 g, 0.784 mmol) in 130 mL MeCN.

After 30 min, fine gold crystals of analytically pure **3-2** (R = Me) were collected by filtration and washed with 3 × 15 mL MeCN; yield 0.152 g (0.614 mmol, 84 %). IR: 1308 (w), 1212 (w), 1030 (m), 842 (w), 697 (w), 650 (w), 516 (m), 483 (w), 433 (w) cm^{-1}. Crystals suitable for crystallographic work and single crystal conductivity measurements were obtained by the slow diffusion of a degassed solution of [**3-2**][BF_4] (R = Me) (0.030 g, 0.0898 mmol) in 10 mL MeCN into a similarly degassed solution of DMFc (0.030 g, 0.0919 mmol) in 15 mL MeCN through a fine porosity frit. The fine copper needles were harvested after 16 h. Anal. Calcd for $C_5H_3N_4S_4$: C, 24.28; H, 1.22; N, 22.65 %. Found: C, 24.40; H, 1.20; N, 22.81 %.

Preparation of 4-ethyl-4H-bis[1,2,3]dithiazolo[4,5-b:5',4'-e]pyrazin-3-yl 3-2 (R = Et). A sample of [**3-2**][BF_4] (R = Et) (0.700 g, 0.00201 mol) and DMFc (0.689 g, 0.00211 mol) were combined in 30 mL degassed MeCN to give a fuschia colored solution. After 2 h the light brown solid was filtered off and washed with 3 × 10 mL MeCN; yield 0.393 g (0.00150 mol, 75 %). Vacuum sublimation of the isolated material at 10^{-4} Torr in a three-zone furnace along a temperature gradient of 100 °C to 50 °C gave a mixture of amber blocks of α-[**3-2**]$_2$ and black needles of β-[**3-2**]$_2$, which could be manually separated. Resublimation of the mixed material at 10^{-4} Torr along a temperature gradient of 110 °C to 50 °C afforded 100 % black needles of β-[**3-2**]$_2$. IR of α-[**3-2**]$_2$: 1606 (w), 1582 (w), 1562 (m), 1526 (w), 1496 (w), 1343 (w), 1262 (w), 1227 (w), 1179 (w), 1123 (w), 1067 (w), 1002 (w), 864 (w), 836 (w), 796 (w), 774 (w), 694 (m), 662 (w), 641 (m), 550 (w), 511 (w), 483 (w), 467 (w), 429 (w) cm^{-1}. IR of β-[**3-2**]$_2$: 1534 (m), 1434 (s), 1403 (w), 1353 (w), 1334 (s), 1262 (m), 1224 (s), 1183 (m), 1065 (m), 880 (s), 788 (w), 727 (m), 668 (w), 648 (w), 648 (w), 546 (w), 485 (w), 464 (w), 420 (w) cm^{-1}. Anal. Calcd for β-phase $C_6H_5N_4S_4$: C, 27.57; H, 1.93; N, 21.43 %. Found: C, 27.61; H, 2.00; N, 21.26 %.

Preparation of 2,6-diaminopyrazine-3,5-bis(selenocyanate) 3-13. A solution of bromine (8.69 g, 0.0543 mol) in 125 mL MeOH was added dropwise to a cold (-78 °C) solution of potassium selenocyanate (15.74 g, 0.109 mol) in 150 mL MeOH over 2 h. To this yellow slurry, a solution of **3-5** (3.02 g, 0.0275 mol) in 60 mL MeOH was added dropwise over 30 min. The reaction mixture was stirred for 1 h at -78 °C before the cold bath was removed and stirred for another hour. At this time the slurry was poured onto 1.4 L

ice/water. After 30 min the red-brown solid (of diselenide) was filtered off, and the resulting yellow filtrate was left to stand for 16 h. At this time, the yellow crystals of **3-13** were collected by filtration and washed with water; yield 5.96 g (0.0187 mol, 68 %), dec. > 176 °C. ^{1}H NMR (δ, d-DMSO): 6.75 (s, 2H, amine). IR: 3480 (w), 3428 (w), 3366 (w), 3313 (w), 2156 (w), 2145 (w), 1646 (s), 1626 (s), 1602 (s), 1506 (s), 1423 (m), 1246 (m), 1086 (w), 1036 (w), 760 (m), 731 (w), 500 (w), 444 (w) cm^{-1}.

Preparation of 2,6-diamino-3,5-bis(methylseleno)pyrazine 3-14. Sodium borohydride (0.67 g, 0.0177 mol) was added portionwise to a cold (0 °C) slurry of **3-13** (1.01 g, 0.0268 mol) in 50 mL MeOH to give a clear orange solution. After 20 min, methyl iodide (1.8 mL, 0.0289 mol) was added and the reaction mixture was stirred at 0 °C for 30 min before being poured onto 100 mL ice water. After 30 min, the orange precipitate of **3-14** was filtered off and washed with water; crude yield 2.13 g (7.22 mmol, 76 %), mp 121-124 °C. ^{1}H NMR (δ, d_6-DMSO): 5.66 (s, 2H, amine), 2.25 (s, 3H, methyl). IR: 3400 (w), 3299 (m), 3169 (m), 1364 (s), 1550 (m), 1460 (s), 1403 (s), 1233 (s), 1117 (w), 1048 (s), 911 (w), 754 (w), 721 (w), 622 (w), 463 (w) cm^{-1}.

Preparation of 2,6-diamino-3,5-bis(cyanoethylseleno)pyrazine 3-15. Sodium borohydride (0.85 g, 0.0225 mol) was added portionwise to a cold (0 °C) slurry of **3-13** (2.54 g, 7.99 mmol) in 30 mL MeOH to give a red solution with a fine red precipitate. The reaction mixture was stirred at 0 °C for 30 min and then at room temperature for 30 min before 3-bromopropionitrile (2.0 mL, 0.0242 mol) was added. After 1 h the reaction mixture was poured onto 200 mL ice/water and stirred for 30 min. The orange solid of crude **3-15** was filtered off, washed with water, dried and recrystallized from EtOH; yield 2.41 g (6.44 mmol, 81 %), mp 133-136 °C. ^{1}H NMR (δ, CD_3CN): 5.06 (s, 2H, amine), 3.10 (t, 2H, CH_2, J = 6.91 Hz), 2.80 (t, 2H, CH_2, J = 6.91 Hz). IR: 340 (w), 3425 (w), 3381 (w), 3295 (w), 3179 (w), 2242 (w), 1624 (s), 1598 (s), 1520 (s), 1497 (s), 1410 (s), 1265 (m), 1223 (s), 1189 (w), 1144 (w), 1036 (m), 936 (m), 886 (m), 767 (m), 730 (m), 477 cm^{-1}.

Chapter 4

The Synthetic Methodology to Selenium-Containing Bisdithiazolyls

4.1 Introduction

The development of the resonance stabilized bisdithiazolyl radicals **4-1** was a major advancement towards achieving a single component molecular conductor. These compounds resisted dimerization, possessed lower on-site Coulomb repulsion energies U, that is, smaller cell potentials E_{cell} and gas-phase disproportionation enthlapies ΔH_{disp}, than the monofunctional thiazyl radicals, and were thermally stable.[1,2] Unfortunately, the solid state packing motifs of these materials consisted of slipped π-stacks that did not allow for a bandwidth W large enough to overcome U, and these systems were Mott insulators. The necessary condition for high conductivity is a large W/U ratio, and since U is a maximum for systems with half-filled energy bands like those described here, W must be maximized in order to achieve metallic conductivity.

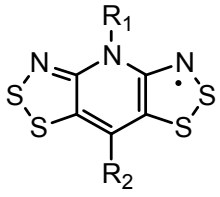

4-1

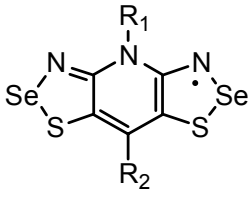

4-2

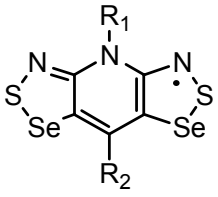

4-3

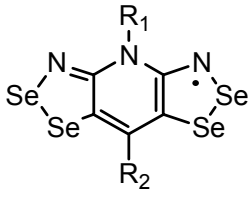

4-4

One approach towards improving bandwidth is to alter the packing arrangement so as to form more superimposed π-stacks in the solid state. This strategy was explored in Chapter 3 with the development of the pyrazine-bridged bisdithiazolyls, in which the pyridine ring in **4-1** was replaced by a pyrazine moiety.[3] This allowed for the removal of one of the bulky R substituents, a modification we hoped would

lessen the plate slippage along the stacks. It was found however, that removing the steric protection afforded by the basal ligand left the material vulnerable to dimerization. All examples of the pyrazine-bridged bisdithiazolyls formed spin-quenched dimers in the solid state, although high conductivity was still be observed.

An alternative approach to enhancing bandwidth in heterocyclic materials is the replacement of sulfur for its heavier, more spatially diffuse congener selenium, a design strategy used to increase *W,* and improve conductivity, in charge transfer salts.[4] We chose to incorporate selenium into the bisdithiazolyl framework **4-1**, a system with inherently beneficial features (as noted above), with a view of obtaining a bandwidth that would overcome *U*. There are three selenium-containing radicals possible, that is, the mixed S/Se compounds where selenium is in either the 2-position (**4-2**) or the 1-position (**4-3**) of the dithiazole rings, and the all-selenium framework **4-4**.

We have probed the energetic properties of the three new selenium-containing radicals using DFT methods, at the B3LYP/6-31G(d,p) level, using idealized models with $R_1 = R_2 = H$. The singly occupied molecular orbital (SOMO) of each selenazyl radical **4-2** to **4-4**, in addition to that of **4-1**, is shown in Figure 4.1. It is readily apparent that the SOMOs of all four radicals are essentially identical. Each SOMO is antibonding in nature with a_2 symmetry, and can be considered as an out-of-phase combination of the SOMOs of two monofunctional dithiazolyls. There is a nodal plane along the short axis of the molecule, suggesting, to a first approximation, that modifying the R substituents will have little effect on the energetic properties of the radical. The calculated spin densities of each framework are also presented in Figure 4.1 and again, there is very little difference between compounds. In general, there is strong, positive spin concentrations on the outer dithiazole rings, with relatively low, negative density along the center axis of each molecule. The computed gas-phase ionization potentials (*IP*) and electron affinities (*EA*) for all four radicals are listed in Table 4.1. There are very subtle changes in the values across the series, although there is a noticeable decrease in the gas-phase disproportionation enthalpies ΔH_{disp}, indicating a lowering of *U* with increasing selenium content. Overall, these theoretical investigations confirm that the delocalized spin

distributions and ion energetics of the selenium-containing radicals **4-2** to **4-4** are very similar to that of the parent compound **4-1**. However, these new systems should exhibit superior conductivity values as they are predicted to have higher bandwidths *W* due to better orbital overlap, and lower *U* values, features which result in more favourable *W*/*U* ratios.

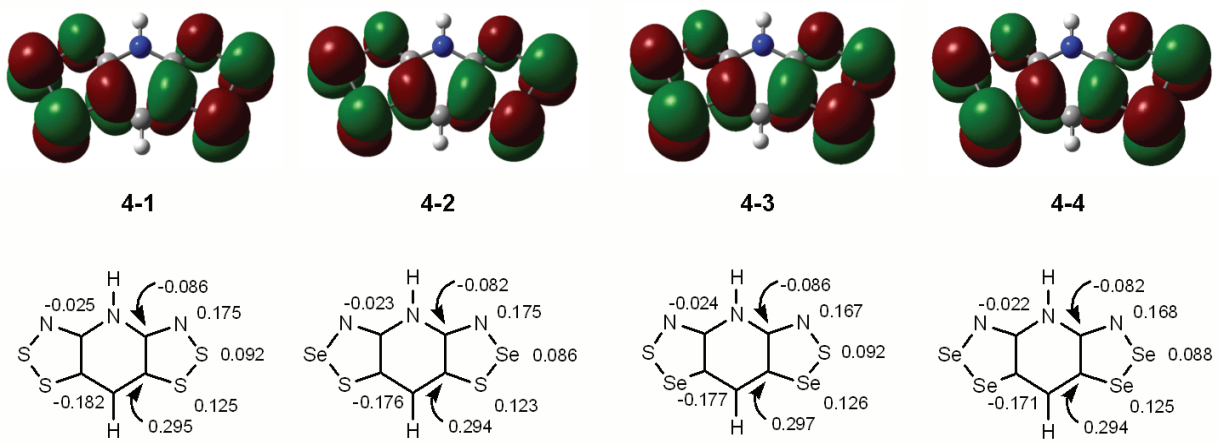

Figure 4.1 The B3LYP/6-31G(d,p) SOMOs for radicals **4-1** to **4-4** ($R_1 = R_2 = H$) above, with their respective spin densities below.

Table 4.1 Calculated Gas Phase Ion Energetics[a] of **4-1** to **4-4** ($R_1 = R_2 = H$)[b]

Compound	**4-1**	**4-2**	**4-3**	**4-4**
IP (eV)	6.16	6.07	6.08	5.99
EA (eV)	1.39	1.41	1.42	1.45
ΔH_{disp}[c] (eV)	4.77	4.65	4.66	4.54

[a] Adiabatic ΔSCF values from B3LYP/6-31G(d,p) calculations performed within a C_{2v} symmetry constraint. [b] Values generated using Gaussian 98W were reported in reference 11. The data listed here was calculated using Gaussian 03W. [c] ΔH_{disp} = IP - EA.

Given the favourable characteristics of the selenium-containing radicals **4-2** to **4-4**, they were pursued for use as neutral radical conductors. Their development however, was a major synthetic

endeavour, as very few preparative routes involving similar compounds had been reported, and a multi-step procedure was required. Accordingly, the synthetic methodologies and exploratory work involving the generation of these three systems has been allotted an entire chapter in this thesis. This section includes the preparation of each radical type **4-2** to **4-4**, as well as the R_1/R_2 substituent modifications made to each framework. Several reports have been published on these selenium-containing radicals, including their preparation, as they have very interesting solid state properties.[5,6,7]

4.2 Selenium in the 2-Position: The Type 2 Radicals

We have tried several methods for placing selenium in the 2-position of **4-1**, so as to achieve the mixed S/Se framework of **4-2**. Our first approach was to react a bifunctional aminothiol with selenium halides, as it has been reported that monofunctional 1,2,3-thiaselenazoles can be prepared by the condensation of aromatic *o*-aminothiols with $SeCl_4$.[8] For intractable aminothiols, the more workable S-acetylated compound has been used, which was condensed with $SeOCl_2$.[9] For the bifunctional 2,6-diamino-3,5-pyridinedithiol however, the reaction with $SeCl_4$ or $SeOCl_2$ failed to produce the desired tricyclic framework. The condensation was, however, successful when the thiols were protected with acetyl groups, as in **4-5**, and a mixture of $SeOCl_2$ and $SeCl_2$ was used as shown in Scheme 1.[10] By this route, the protonated chloride salt [**4-2**][Cl] (R_1 = H, R_2 = H) could be obtained. In order for this compound to be converted to the alkylated salt used in the final reduction step to the radical, a lengthy purification and metathesis procedure was required.[11]

Scheme 1

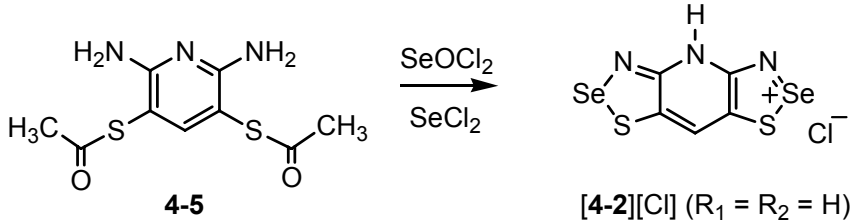

4-5 [**4-2**][Cl] (R_1 = R_2 = H)

The second approach to generating the mixed S/Se skeleton of [**4-2**]$^+$ involves the substitution of sulfur for selenium through the reaction of the all-sulfur cation [**4-1**]$^+$ with SeO_2. This route was first described for the insertion of selenium into monofunctional benzo-1,2,3-dithiazolium cations by Efros and coworkers,[12] and was later used by Rawson et. al. to incorporate selenium into the phenyl-1,2,3,5-dithiadiazolylium cation.[13] This reaction could be performed in either refluxing acetic acid (HOAc) or acetonitrile (MeCN), and selenium substitution was specific to the 2-position of the heterocycle. We have successfully used this procedure to achieve double insertion of selenium into the known all-sulfur framework [**4-1**]$^+$ by using 2 to 4 equivalents of SeO_2. By this method, we are able to obtain the desired cations [**4-2**]$^+$ in a single step,[5,14] allowing us to bypass the lengthy procedure previously used.[11]

Scheme 2

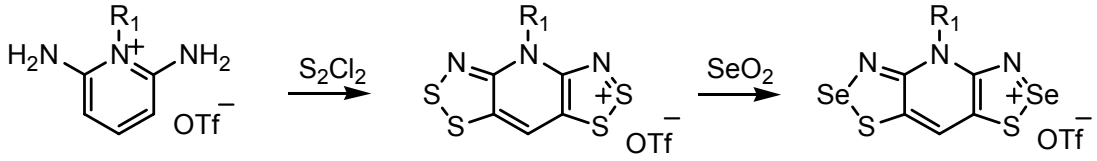

[**4-1**][OTf] [**4-2**][OTf]

For this route to be possible, the dithiazolium cations [**4-1**]$^+$ are required. The preparation of these compounds is well documented,[1,2,15] and involves the double Herz cyclization[16] of N-alkylated diaminopyridinium triflate (trifluoromethanesulfonate, OTf^-) salts with sulfur monochloride (Scheme 2). The double insertion of selenium into the 2-positions of particular derivatives of [**4-1**][OTf] to afford [**4-2**][OTf], could be accomplished by reaction with two equivalents of SeO_2 in refluxing HOAc for 1-2 hours. Unfortunately, for other variations of [**4-1**][OTf], Electrospray Ionization Mass Spectrometric (ESI-MS) analysis of the reaction mixture (Figure 4.2) revealed that the insertion was not completely regiospecific, as there were over 90% S_2Se_2 based cations, but also small amounts of S_3Se_1, S_1Se_3 and even Se_4 materials present. Our interpretation of these observations is outlined in Scheme 3, in that while the dominant reaction pathway involves selenium insertion into the 2-position of the heterocycle, to afford the desired cation [**4-2**]$^+$, replacement of sulfur in the 1-position can also take place. From this side-product single and double replacement at the two available 2-positions can then occur to give two different S_2Se_2 based isomers as well as S_1Se_3 materials.

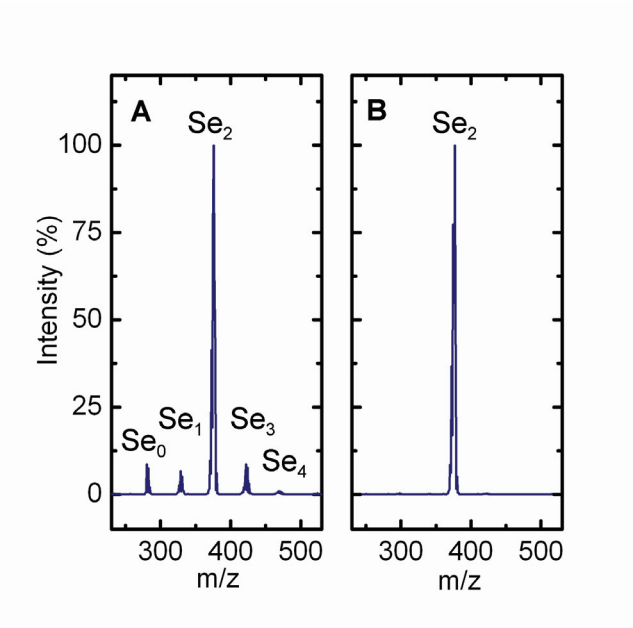

Figure 4.2 ESI mass spectra of the reaction mixture of SeO_2 with [**4-1**][OTf] (R_1 = Me, R_2 = Cl) in HOAc (A) and MeCN (B).

Scheme 3

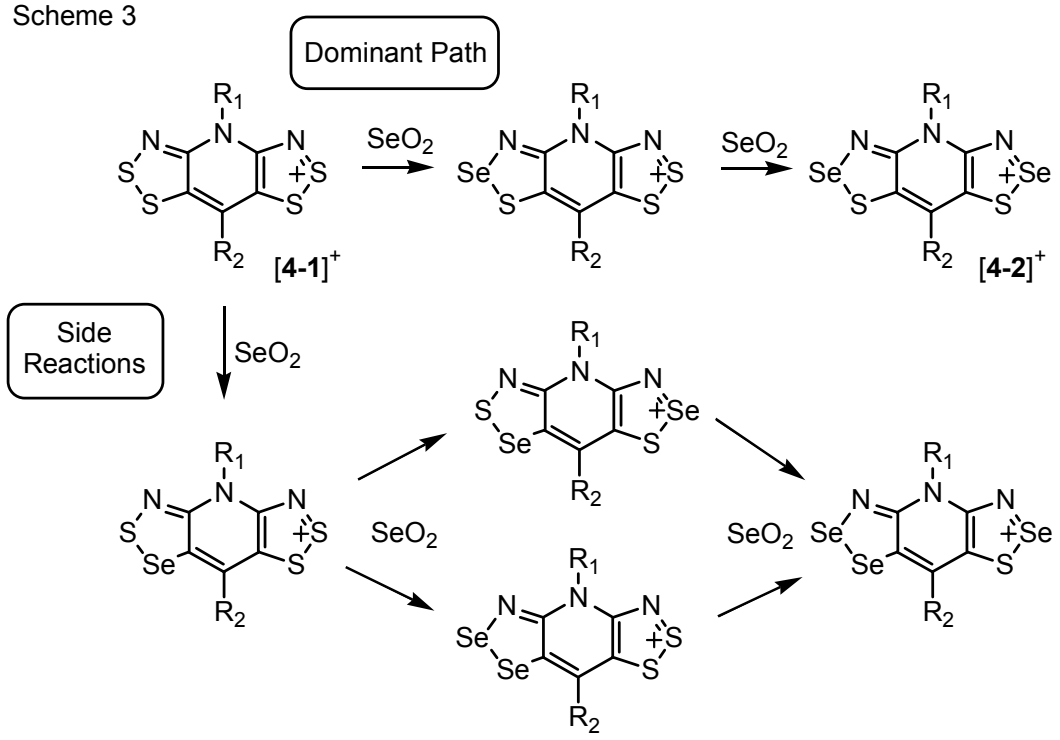

As an alternative to performing the selenium insertions in acetic acid, we have found that the reaction can also be carried out in acetonitrile at 110 °C in a pressure vessel. We now know that regiospecificity can be obtained for all derivatives of [**4-2**]$^+$ depending on the reaction conditions used (Figure 4.2), which are specific to the molecular framework, or more specifically, the R substituents present. In general, when R_2 = H, Me or Ph, the insertion is successful when performed in refluxing acetic acid with 4 equivalents of SeO_2, but for compounds with R_2 = F, Cl or Br, the reaction must be carried out in acetonitrile with a 3:1 ratio of selenium dioxide to [**4-1**][OTf]. The acetic acid route requires only 1.5 to 6 hours, and the crude product crystallizes upon cooling of the reaction mixture. Conversely, when the reaction is done in acetonitrile, completion is obtained after 48 to 72 hours, and product is isolated on evaporation of the reaction mixture. Progress of the reaction is monitored by ESI-MS and phase purity is established by both mass spectrometry and infrared analysis of the product. Typically, the triflate salts [**4-2**][OTf] are recrystallized from MeCN and/or HOAc as lustrous red crystals.

4.3 Selenium in the 1-Position: The Type 3 Radicals

In the preparation of the other mixed S/Se isomer [**4-3**]$^+$, as a first step, we needed to place selenium in the 3,5-positions of 2,6-diaminopyridine. A commonly used method for introducing a chalogen atom into an organic molecule is by thio- or selenocyanation.[17] This can be accomplished by the nucleophilic replacement of a halide by the chalcocyanate ion (NCE^-, E = S, Se) in an aryl halide with strong *ortho* or *para* electron-withdrawing substituents.[18] Alternatively, for aromatic compounds with electron-donating groups, the electrophilic substitution at the *para*-position will take place with the chalcocyanate ion in polar solvents.[19,20] Thiocyanogen and selenocyanogen are commonly used in this process.[17] However, these reagents are thermally unstable, as thiocyanogen polymerizes into an insoluble matrix above room temperature,[20,21] and selenocyanogen disproportionates to give a mixture of selenium dicyanide and selenium diselenocyanate.[22]

We were able to achieve selenium placement in the 3,5-positions of 2,6-diaminopyridine by selenocyanation. The bisselenocyanate **4-6** was prepared by the slow addition of diaminopyridine into a cold solution of a mixture of KSeCN[23] and bromine in methanol.[17] This process is analogous to that used for the preparation of the sulfur analogue, which is used in the synthetic route of [**4-1**][Cl],[24] although in this case, the reaction required much lower temperatures and was performed at -78 °C. After an aqueous work up, the di-substituted material **4-6** was isolated with 70 % overall yield. In order to facilitate ring closure, it was necessary to remove the cyanide moiety (CN^-) as it is a poor leaving group. However, the attempted formation of the selenol **4-7** by hydrolysis of the selenocyanate **4-6** ultimately led to the isolation of the insoluble diselenide **4-8**.[25] An alternative route to generating compound **4-8** is by treating **4-6** with tributylphosphine in wet MeCN. In the cases where there is a monofunctional diselenide formed, the oxidation products are often soluble and recrystallizable,[9] although when they are bifunctional, as in **4-8**, the resulting polymeric compounds can be insoluble and difficult to work with.[3,5] Although the dichalcogenides can be reduced back to the chalcogenates using $NaBH_4$, we were not successful in isolating reasonable quantities of **4-7** by this method. A common method used to by-pass this obstacle is to employ protecting groups to cap the chalcogenol during the construction of a molecular framework, and then removing them in the final stages of the synthetic sequence. Since the diselenide formed here was not reactive with sulfur halides, and we could not isolate the selenol **4-7**, a protecting group was required.

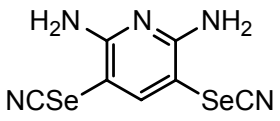

4-6

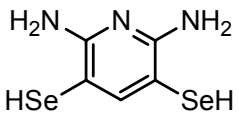

4-7

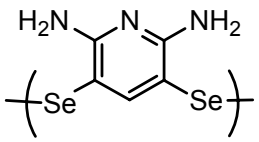

4-8

Several groups have been employed for the protection of chalcogenols.[26] Alkyl groups for example have been used for this purpose, as in the S-propyl substituted aromatic compounds used by Kazsynski et. al. in the preparation of thiadiazines,[27] and the methyl selenide used as an intermediate to an aromatic selenenyl chloride by Reich and Wollowitz.[28] In these reports, the propyl group was removed by the thermolysis of the intermediate sulfilimines, where as the methyl group was cleaved on reaction with

thionyl chloride. These alkyl-substituted aryl sulfides can be prepared by the reaction of an aryl thiocyanate with a primary alcohol and triphenylphosphine.[29] Alternatively, the 2-cyanoethyl group has been used in both nucleic acid chemistry[30,31] and in the generation of unsymmetrically substituted tetrachalocofulvalene derivatives,[32,33] to cap both thiols and selenols. This protecting group is stable in acidic conditions, but is easily removed with mild base, such as K_2CO_3, to afford the desired chalcogenol and presumably, acrylonitrile.

In the past, we have used acetyl groups for capping both thiols[11] and selenols.[9] These protected compounds are easily prepared by the hydrolysis of the chalcocyanate with disulfide ion to afford the chalcogenide, followed by reaction with acetic anhydride. The acetyl groups could be cleaved in the mild electrophillic conditions present in the subsequent condensation reaction with sulfur or selenium halides. Others have used selenocarbamates, selenocarbonates and selenoacetates as protected selenols, all of which can be deprotected by reaction with base.[34]

For our work in the development of the **4-3** framework, we initially used the 2-cyanoethyl group for the protection of the selenol. The cyanoethyl-substituted compound **4-9** was prepared by the reduction of the bisselenocyanate **4-6** with sodium borohydride in methanol, followed by the reaction with 3-bromopropionitrile.[31] Previous attempts at ring closure of the Se-protected diaminopyridine diselenol established that the selenium atoms in the 3,5-positions were extremely sensitive to C-Se bond cleavage, as the condensation reaction with S_2Cl_2, SCl_2 or $SeCl_4$ in refluxing MeCN failed, or produced a small quantity of the all-sulfur derivative [**4-1**][Cl].[25] Therefore, milder conditions were required for the ring closure reaction. After trying many reaction conditions, we found that the mixing of **4-9** with thionyl chloride in the presence of triethylamine, as in Scheme 4, was successful in forming the desired tricyclic framework of [**4-3**][Cl] (R_1 = H, R_2 = H) as a black insoluble powder.

Scheme 4

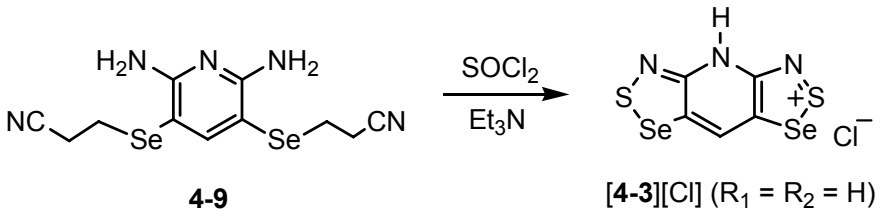

4-9 [**4-3**][Cl] (R_1 = R_2 = H)

The use of the auxiliary base (Et_3N) is three-fold: (i) it has been shown in the preparation of [**4-1**]$^+$ (R_1 = H, R_2 = H) to inhibit the replacement of the basal hydrogen with a chlorine atom,[35] (ii) it serves as a base to drive HCl elimination, and (iii) is used in the deprotection of the selenol, making it available for ring closure. Unfortunately, the 2-cyanoethyl substituent could not be completely removed under the described reaction conditions above, as there was evidence of the mono-condensed material in both the infrared and ESI mass spectra of the later, more soluble salts. We therefore switched protecting groups and used the methyl-substituted selenol as the starting material.

The methyl-capped selenol **4-10** was prepared by the reduction of the bisselenocyanate **4-6** with sodium borohydride, followed by reaction with methyl iodide.[28] This protected-selenol was more conducive to Se-CH_3 bond cleavage during the cyclocondensation step. Many different conditions were tried for the ring closure reaction, including variations in the stoichiometric ratios of reagents, the reaction temperature, and addition rates. Initially the reaction involved adding eight equivalents of triethylamine to an MeCN slurry of **4-10**, followed by the dropwise addition of six equivalents of thionyl chloride over a period of 30 to 60 minutes, while the reaction vessel was cooled at -40 °C. These relatively mild reaction conditions were successful in preventing the cleavage of the selenium atoms, and forming the desired Se/S heterocyclic framework of [**4-3**]$^+$ (R_1 = H, R_2 = H). Once the tricyclic skeleton was obtained, several steps were required to prepare and purify the desired alkylated triflate salts [**4-3**][OTf] (R_1 = Me, Et; R_2 = H). This reaction sequence is similar to that used in the work up of the related all-sulfur variants **4-1**, and is shown in Scheme 5.

Scheme 5

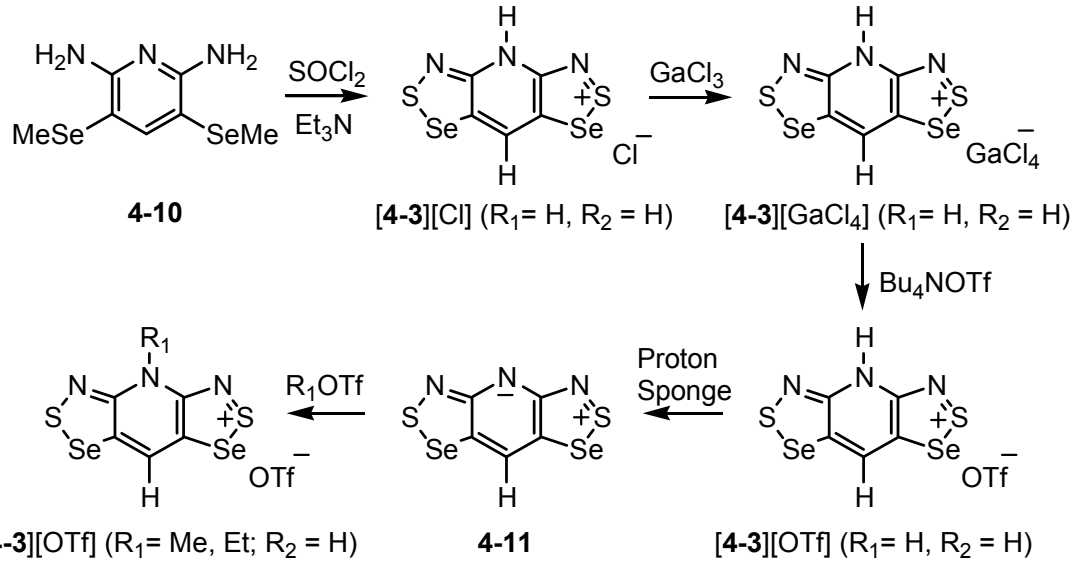

In order to clean up the impure chloride salt [**4-3**][Cl] (R_1 = H, R_2 = H), which was isolated as a black, insoluble powder, it was converted to the tetrachlorogallate salt [**4-3**][$GaCl_4$] (R_1 = H, R_2 = H) by reaction with gallium trichloride. For the related type 2 systems [**4-2**]$^+$, *via* the lengthy synthetic route,[11] purification was achieved by first filtering solutions of the tetrachlorogallate, to remove insoluble impurities, and then reprecipitating the chloride salt by reaction with pyridine. At this stage, the material was reacted with a silver salt to make either the protonated triflate or hexafluoroantimonate salt. This purification strategy was used initially for the type 3 compounds [**4-3**]$^+$, but in this case there was no improvement in purity. Instead, the isolated tetrachlorogallate [**4-3**][$GaCl_4$] (R_1 = H, R_2 = H) was dissolved in warm tetrahydrofuran (THF) and the solution was filtered to remove the insoluble materials. The filtrate was then reacted with tetrabutylammonium triflate to obtain directly the protonated triflate salt [**4-3**][OTf] (R_1 = H, R_2 = H).

Attempts at purifying [**4-3**][OTf] (R_1 = H, R_2 = H) by recrystallization from either MeCN or HOAc have failed. Large volumes and strong heat were necessary to dissolve the material, and yet on concentration only a small amount of silt-like material precipitated from solution. The addition of an anti-

solvent like diethyl ether succeeded in discharging solid from the solution, but it was invariably contaminated with impurities. With a view to increasing the solubility of this compound, the anion was switched to nonaflate (nonafluorobutanesulfonate), but this material did not behave any better. Eventually we concluded that the protonated cations [**4-3**]$^+$ (R_1 = H, R_2 = H) are thermally unstable, and tend to either scramble the S/Se atoms or break apart at high temperatures. Therefore, purification could not be performed at this step and the crude material was taken forward.

The next step in the synthetic sequence involved the deprotonation of crude [**4-3**][OTf] (R_1 = H, R_2 = H) with Proton Sponge, to afford the zwitterion **4-11**. This material was then treated with alkyl (methyl or ethyl) triflate, to give the triflate salts [**4-3**][OTf] (R_1 = Me, Et; R_2 = H). In practice, and in order to ensure complete reaction, the highly insoluble granular zwitterion was pulverized before use, and the reaction was carried out in the presence of Proton Sponge. The addition sequence was important in minimizing the generation of protonated impurities, which required the addition of **4-11** to a solution of alkyl triflate and Proton Sponge in dichloroethane (DCE).

The reaction times for the alkylation step varied with R_1 group. The methyl derivative was formed in less than 16 hours, where the ethyl compound took longer, usually requiring 48 hours for completion. Attempts to speed up the ethylation by using Et_3OPF_6 in DCE and warming overnight demonstrated that the material was particularly vulnerable to protonation, and the heating of the mixture of protonated and ethylated cations led to S/Se scrambling in the molecular framework. Therefore the alkyl triflates were used exclusively as the alkylating agents and the reactions were carried out at room temperature. The methyl and ethyl-substituted materials, [**4-3**][OTf] (R_1 = Me, Et; R_2 = H), were purified by recrystallization from both MeCN and HOAc and isolated as lustrous red crystals.

Throughout our work on making these compounds, we noticed that more and more frequently the reaction sequence in Scheme 5 would go very wrong, affording materials with high impurity concentrations and low yields. For example, in the work up of the tetrachlorogallate salt [**4-3**][$GaCl_4$] (R_1 = H, R_2 = H),

the product material was sometimes only partially soluble in MeCN and required large volumes of solvent or heat to fully dissolve. Yields would range from 30-70% depending on the reaction. In the next step, problems were encountered during the work up of the gallate solutions in THF in which a great deal of solid (>30%) would be removed on filtration, and on addition of Bu_4NOTf, soupy mixtures were formed affording a fine red precipitate of [**4-3**][OTf] (R_1 = H, R_2 = H) in low yield. Also, the zwitterion **4-11** would occasionally have a high concentration of protonated impurities, which could not be removed by repeated reactions with Proton Sponge. The purification of the alkylated triflate salts [**4-3**][OTf] (R_1 = Me, Et; R_2 = H) by recrystallization from MeCN were sometimes very troublesome, as the solutions would be thick and odorous, with low recovery. The material would be contaminated by the thermally unstable protonated material, as well as the difficult to remove S_3Se/SSe_3 compounds. Changing the recrystallization solvent to acetic acid did not improve matters.

We found that all of the problems associated with the reaction in Scheme 5 could be traced back to the condensation step and synthesis of the chloride salt [**4-3**][Cl] (R_1 = H, R_2 = H). If the ring closure reaction went well, all of the subsequent steps were straight forward and in good yield ($\geq$ 70 %). On the other hand, if the reaction was poor, the remaining steps would be difficult, proceeding in low yield, and would ultimately give contaminated product. We found that it was more time and cost efficient to start the reaction sequence over if the tetrachlorogallate [**4-3**][$GaCl_4$] (R_1 = H, R_2 = H) was not sufficiently pure. Infrared analysis was an effective tool in differentiating between pure and impure material, as demonstrated in Figure 4.3. The spectrum of a contaminated sample of the tetrachlorogallate possesses several extra bands, including a pair at ~1100 cm^{-1}.

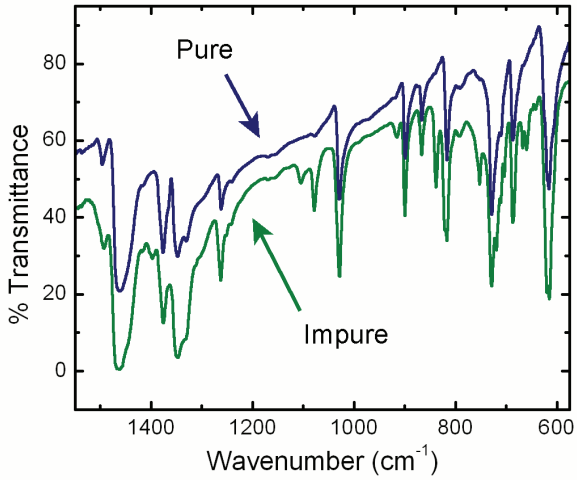

Figure 4.3 Infrared spectra of pure and impure samples of [**4-3**][$GaCl_4$] (R_1 = H, R_2 = H).

Various measures were taken to improve the cyclocondensation reaction: (i) the protected-selenol **4-10** was dried at 50 °C/10^{-2} Torr for at least 1 hour before use, (ii) the reaction temperature was increased to 0 °C, (iii) the solvent volume was increased by half and continuous stirring was ensured, (iv) the stoichiometric ratios of the reagents were modified to determine the optimum quantities,[‡] and (v) the addition rate of thionyl chloride to the reaction mixture was slowed to 60 - 90 minutes. Furthermore, we monitored the products of each subsequent step for impurities through infrared and ESI-MS analysis and could recognize contaminants. Through experience we became familiar with good product morphologies, reaction colours and overall yields. Unfortunately, this cyclocondensation step is still not perfect, as the success rate is only ~ 60 %. Methods to further improve this ring closure reaction, as well as alternative routes to the 1,2,3-selenathiazolylium framework [**4-3**]$^+$, are described in Section 4.8.

[‡] Many variations to the amounts of the reagents used in the cyclocondensation reaction were tried, ranging between 2-10 equivalents of both $SOCl_2$ and Et_3N. The best results were obtained when 4 $SOCl_2$ and 6 Et_3N were used.

4.4 Selenium in the 1- and 2-Positions: The Type 4 Radicals

The final derivative of the series is the **4-4** compound with selenium occupying all four positions of the framework. We found that the bisdiselenazolium cations [**4-4**]$^+$ could not be prepared by a cyclocondensation reaction of a protected diamino-diselenol with selenium halides. Instead, the desired cations were obtained by the double insertion of selenium into the bisselenathiazolium cations [**4-3**]$^+$ using SeO_2 as shown in Scheme 6, by the analogous reaction described for the placement of selenium in [**4-2**]$^+$ (Section 4.2). In this case, regiospecificity was not an issue, but reaction completion and molecular decomposition were a concern. Depending on the derivative of [**4-3**]$^+$, that is, the R_1/R_2 substituents, the SeO_2 reaction was performed by either the acetonitrile (pressure vessel at 110 °C) or acetic acid (ambient pressure at reflux) route. For some compounds, reactions performed in acetonitrile required long reaction times (> 48 h) and showed considerable decomposition by ESI-MS with low overall yields. For these derivatives, the selenium insertions were more successful when carried out in acetic acid, which were complete in approximately 2 hours.

Scheme 6

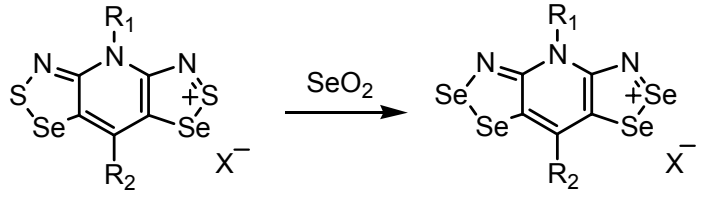

[**4-3**][X] X$^-$ = OTf$^-$, ONf$^-$ (R_1 = Me, Et; R_2 = H, Cl, Br)

[**4-4**][X] X$^-$ = OTf$^-$, ONf$^-$ (R_1 = Me, Et; R_2 = H, Cl, Br)

In the case of the R_1 = Me, R_2 = Cl derivative, solubility was a concern, as large volumes were necessary to dissolve the starting material, [**4-3**][OTf] (R_1 = Me, R_2 = Cl), for the selenium insertion reaction, as well as the product, [**4-4**][OTf] (R_1 = Me, R_2 = Cl), for its purification by recrystallization from either MeCN or HOAc. To improve solubility the anion was changed, and both the hexafluoroantimonate (SbF_6^-) and the nonaflate (ONf$^-$) counterions were explored. The anion switch (Scheme 7) could be carried out on either the [**4-3**]$^+$ or [**4-4**]$^+$ triflate salts, which were first converted to the chloride salts by

treatment with benzyltriethylammonium chloride, and then reacted with the appropriate silver salt. The initial exploratory work was performed on [**4-4**]$^+$ (R_1 = Me, R_2 = Cl), which established that the hexafluoroantimonate salt was impractical as it was too soluble in MeCN, and not at all soluble in HOAc. The nonaflate salt on the other hand, was much more manageable and could be recrystallized from both MeCN and HOAc. For subsequent reaction sequences, the methathesis was carried out on [**4-3**][OTf] (R_1 = Me, R_2 = Cl), and the selenium insertion was performed on [**4-3**][ONf] (R_1 = Me, R_2 = Cl). The resulting all-selenium salt [**4-4**][ONf] (R_1 = Me, R_2 = Cl) could easily be dissolved for purification and reduction steps.

Scheme 7

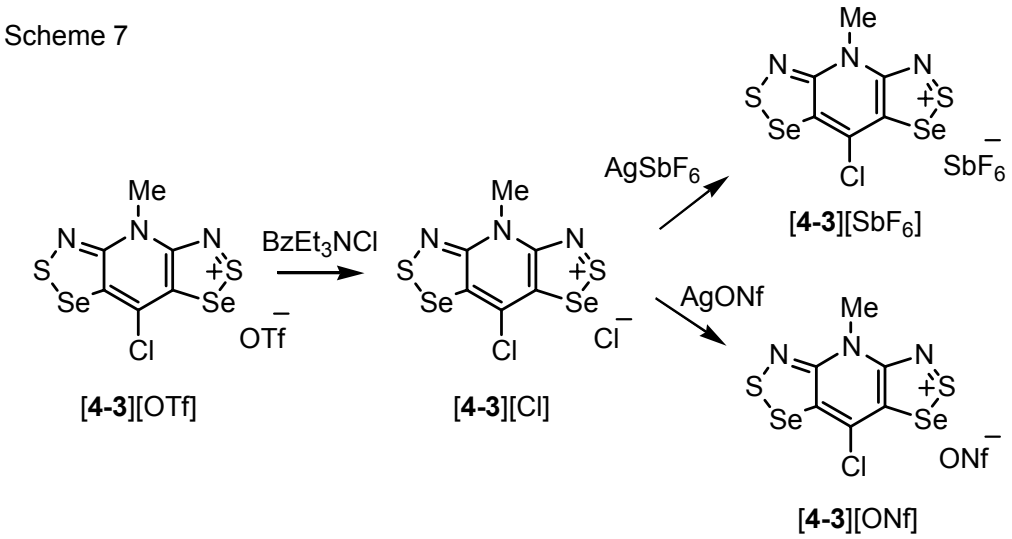

4.5 Modification of the R_2 Substituent

A variety of different R_2 substituents can be envisaged for radicals **4-1** to **4-4**, including alkyl groups,[15] amines, halogens, and even other heterocycles.[36] I will only present the work involving halogen substitution, as this is where I was directly involved. Of the four heterocycles, substituent modification was performed on the [**4-1**]$^+$ and [**4-3**]$^+$ cations, as the other derivatives, [**4-2**]$^+$ and [**4-4**]$^+$, are formed from these materials. Also, variation of the R_2 group could not be performed on the all-selenium cations [**4-4**]$^+$ as attempts at chlorination and bromination led to Se-Se bond breakage and decomposition of the molecular structure.

For the all-sulfur framework [**4-1**]$^+$, chlorine is situated on the basal position during the cyclocondensation reaction (Scheme 8), in which protonated-diaminopyridinium triflate [**4-12**][OTf] (R_1 = H, R_2 = H) is combined with S_2Cl_2 in refluxing MeCN to give [**4-1**][Cl] (R_1 = H, R_2 = Cl).[1] The hydrogen atom in the 4-position is invariably replaced by chlorine under these relatively harsh reaction conditions.‡ The analogous reaction with S_2Br_2‡‡ does not produce the brominated compound, but instead gives the protonated version [**4-1**]$^+$ (R_1 = H, R_2 = H). If bromine is introduced before cyclization, as in [**4-12**][OTf] (R_1 = Et, R_2 = Br), subsequent treatment with S_2Cl_2 leads to the electrophilic cleavage of the bromine atom and formation of the chlorinated cation [**4-1**]$^+$ (R_1= Et, R_2 = Cl). The bromination is however, successful when [**4-1**][OTf] (R_1= Me, Et; R_2 = H) is treated with either bromine or N-bromosuccinimide in refluxing MeCN. In making the iodine derivative (R_2 = I), past work has shown that the reaction of [**4-12**][OTf] (R_1 = Me, R_2 = I) with S_2Cl_2 at room temperature in the presence of triethylamine, affords mixtures of 4-chloro and 4-iodo materials.[36] More recent work however, has demonstrated that the iodine atom remains intact when the condensation reaction is performed at lower temperatures (−40 °C) and in the presence of Et_3N, yielding >99% of the R_2 = I material.

Scheme 8

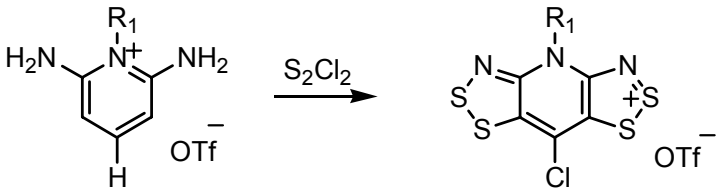

[**4-12**][OTf] [**4-1**][OTf]

The strong condensation conditions used for the ring closure of [**4-1**]$^+$ could not be used to chlorinate [**4-3**]$^+$ as the selenium atoms in the 3,5-positions would be severed. Instead, our approach was to chlorinate the triflate salt [**4-3**][OTf] (R_1 = Me, Et; R_2 = H) with a chlorinating agent. We avoided the

‡ Under milder conditions (25 °C, with Et_3N), the proton-substituted framework [**4-1**][OTf] (R_1 = H, R_2 = H) can be obtained. See reference 2.

‡‡ S_2Br_2 was formed in situ by the reaction of sulfur with bromine.

use of strong oxidizing agents such as chlorine and sulfuryl chloride, as we were worried about damaging the heterocycle. Instead, we tried N-chlorosuccinimide, but reactions with this compound either did not proceed, or went to partial completion with the isolation of a mixture of R_2 = H and Cl material. We were more successful with iodobenzene dichloride.[37] When $PhICl_2$ was reacted with [**4-3**][OTf] (R_1 = Me, Et; R_2 = H), in refluxing MeCN for 90 min, the desired product [**4-3**][OTf] (R_1 = Me, Et; R_2 = Cl) was obtained, as shown in Scheme 9.

Scheme 9

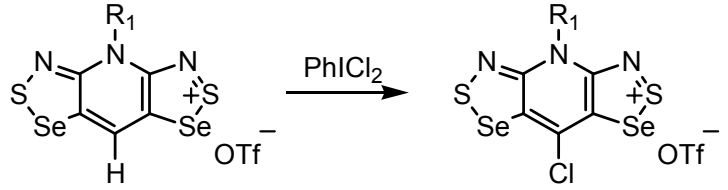

[**4-3**][OTf] (R_1= Me, Et; R_2 = H) [**4-3**][OTf] (R_1= Me, Et; R_2 = Cl)

The bromination of [**4-3**][OTf] (R_1 = Me, Et; R_2 = H) could be accomplished by two methods (Scheme 10). The first used bromine, which gave a mixture of the soluble triflate salt and a lustrous purple-black precipitate of what we believed to be the tribromide salt. This slurry was treated with bromide ion to give a mixture of $[Br_3]^-$ and $[Br]^-$ salts. The tribromide anion could be broken up with mild heating, or with a mild reducing agent such as triphenylantimony, but again, we were concerned about damaging the heterocycle in the process. Instead, the mixed salt was treated with silver triflate and the cation was isolated as a triflate salt [**4-3**][OTf] (R_1 = Me, Et; R_2 = Br). The second approach to the R_2 = Br material used N-bromosuccinimide (NBS) as the brominating agent. This procedure did not alter the counterion, as the isolated product was [**4-3**][OTf] (R_1 = Me, Et; R_2 = Br). Although this route required a single step, the yield was not as high as in the first method. Regardless of which pathway was used, the reaction went to completion with no evidence of protonated materials remaining.

Scheme 10

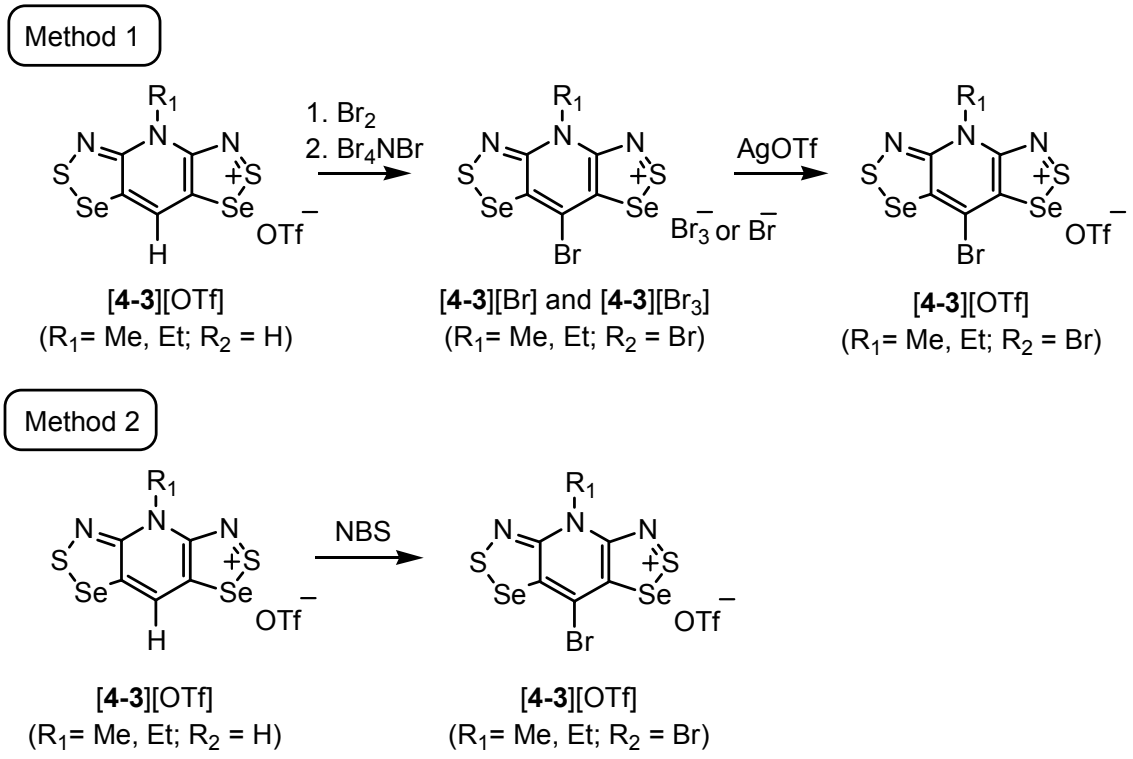

Placing iodine in the basal position has not yet been successful. We have tried treating [**4-3**][OTf] (R_1 = Me, R_2 = H) with iodine chloride, but instead of substituting an iodine atom for hydrogen, chlorine was placed in the R_2 position to give [**4-3**][OTf] (R_1 = Me, R_2 = Cl). A reaction of the R_2 = H salt with N-iodosuccinimide under the same conditions used for bromination, found that this agent was not strong enough to replace the hydrogen. Other iodine electrophiles, such as mixtures of iodine with an oxidizing agent (e.g., iodic acid,[38] dinitrogen dioxide[39]) or the triiodide ion,[40] may be more productive.

4.6 Reduction Chemistry

The final step of the synthetic sequence is the reduction of the purified cations with a reducing agent (Scheme 11). Several reducing agents have been used, chosen so that their reducing potential matches that of the reduction half-wave potential $E_{1/2}^{(+1/0)}$ for each individual cation. In general, when R_2

is a halogen atom (i.e. Cl, Br), hexamethylferrrocene was sufficient to reduce to the radical, where for alkylated compounds (R_2 = Me, H, Ph), a stronger agent was needed and either octa- or decamethylferrocene was used. When it was necessary for the product to be iron-free and not contaminated with ferrocinium by-products, as for materials that displayed interesting magnetic behaviour, tetrakisdimethylaminoethylene (TDAE) or *N,N,N′,N′*-tetramethyl-*p*-phenylenediamine (TMPDA) were employed. Table 4.2 lists the relative potentials for a variety of reducing agents.

Scheme 11

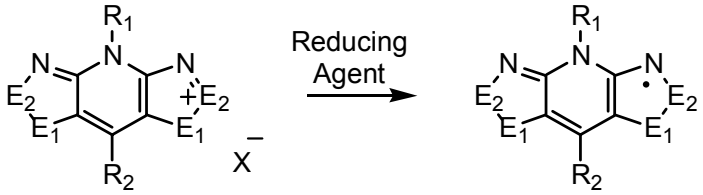

[**4-a**][X], a = 1-4
X = OTf^-, ONf^-
E_1, E_2 = S, Se

4-a, a = 1-4
E_1, E_2 = S, Se

For bulk measurements such as variable temperature conductivity and magnetism, the radicals were prepared by chemical reductions, which gave large quantities of microcrystalline material. Two methods were used, including the "bulb-to-bulb" reduction, in which degassed (by freeze-pump-thaw) solutions of reducing agent and salt were mixed, or by the "spin-out slurry" reduction, in which the reductant was added to a degassed (by bubbling of N_2) suspension of the salt. The spin-out reductions are more severe, particularly when a strong reducing agent such as TDAE is used. It was found through the magnetic studies performed on the radicals that display ferromagnetic behaviour that spin-out reductions using TDAE resulted in crystallites that were smaller and contained a greater number of structural defects within the crystal lattice, compared to material generated by gentler reducing conditions (bulb-to-bulb) and agents like TMPDA.[5] These defects caused the magnetic response of the material to be different than that of the same material reduced by TMPDA.

Table 4.2 Half-wave Potentials of Reducing Agents

Reducing Agent	$E_{½}^{(0/+1)}$, $E_{½}^{(+1/+2)}$	
	In house [a]	Literature [b]
Ferrocene	0.380	0.380 [c]
Dimethylferrocene	0.263	0.241, 0.30 [d]
Hexamethylferrocene	0.056	0.04 [e]
Octamethylferrocene	−0.038	0.01, −0.02 [f]
Decamethylferrocene	−0.131	−0.124 [g]
Tetramethyl-*p*-phenylenediamine	0.094, 0.692	0.10, 0.67 [h]
Tetrakisdimethylaminoethylene	−0.600 ($2e^-$)	−0.61, −0.78 [i]
		−0.62 ($2e^-$ DMF)

[a] Volts *vs* SCE, anhydrous CH_3CN, Pt electrodes, 0.1 *M* *n*-Bu_4N^+ PF_6^-, experiments performed by Dr. R. W. Reed. [b] See cited reference for experimental conditions, potentials have been normalized to SCE. [c] Boeré , R. T.; Roemmele, T. L. *Coord. Chem Rev*. **2000**, *210*, 369. [d] Hoh, G. L. J.; McEwen, W. E.; Kleinberg, J. *J. Am. Chem. Soc*. **1961**, *83*, 3949. Lemoine, P.; Gross, M.; Braunstein, P.; Mathey, F.; Deschamps, B.; Nelson, J. H. *Organometallics* **1984**, *3,* 1303. [e] Zürcher, S.; Petrig, J.; Perseghini, M.; Gramlich, V.; Wörle, M.; von Arx, D.; Togni, A. *Hel. Chim. Acta* **1999**, *82,* 1324. [f] Zou, C.; Wrighton, M. S. *J. Am. Chem. Soc.* **1990**, *112*, 7578. Hobi, M.; Ruppert, O.; Gramlich, V.; Togni, A.. *Organometallics* **1997**, *16*, 1384. [g] Noviandri, I.; Brown, K. N.; Flemming, D. S.; Gulyas, P. T.; Lay, P.A.; Masters, A. F.; Phillips, L. *J. Phys. Chem. B* **1999**, *103*, 6713. [h] Suzuki, T.; Tsuji, T.; Okubo, T.; Okada, A.; Obana, Y.; Fukushima, T.; Miyashi, T.; Yamashita, Y. *J. Org. Chem*. **2001**, *66,* 8954. [i] Burkholder, C.; Dolbier, W. R.; Medebielle, M.; *J. Org. Chem*. **1998**, *63*, 5385. Loss, S.; Magistrato, A.; Cataldo, L.; Hoffmann, S.; Geoffroy, M.; Roethlisberger, U.; Gruetzmacher, H. *Angew. Chem. Int. Ed.* **2001**, *40*, 723.

Unlike the all-sulfur compounds **4-1**, single crystals of the selenium-containing radicals could not be grown by recrystallization, as they were too insoluble. Instead, H-cell techniques were used to facilitate the slow diffusion of degassed (by freeze-pump-thaw) solutions of the salt with the reducing agent, to allow needle growth at the interface of the two solutions. Also, since the all-selenium radicals **4-4** have such high room temperature conductivity values, we had the opportunity for the first time to use electrocrystallization techniques to grow single crystals. By this method, single crystals were grown on a platinum electrode by passing current (1 - 10 μA) through a solution of the salt in the presence of supporting electrolyte (*n*-Bu_4NPF_6). Both of these techniques for single crystal growth are outlined in more detail in the Appendix.

In most cases the needles grown by the above methods were of suitable size and shape to allow structural determination by single crystal X-ray crystallography, although there have been a few instances when microcrystalline material was formed and powder diffraction methods were necessary for structure elucidation.

4.7 Summary

The replacement of sulfur for selenium is a well known strategy used to increase the bandwidth in charge transfer salts.[4] We have applied this concept to the bisdithiazolyl radicals **4-1** with the view of achieving a bandwidth *W* that would overcome the on-site Coulomb repulsion energy *U*. In this chapter, three selenium-containing radicals **4-2**, **4-3** and **4-4** were developed and the methodologies behind their preparation and modification were described. The synthetic challenges were also presented, as well as the techniques used to obtain bulk samples and single crystals of the radicals.

The materials made by these synthetic routes demonstrate very interesting physical behaviour. For some R_1/R_2 families of radicals, there is an isomorphous replacement of sulfur for selenium with sets of radicals crystallizing in the same space group.[5,6] This has allowed us to directly observe the effect of improved bandwidth on the transport properties of these compounds. We have been able to demonstrate that the incorporation of selenium does improve conductivity and lowers activation energy as desired. In addition, the stronger exchange interactions and the spin-orbit coupling effects occasioned by the heavy atom has afforded magnetic ordering for some derivatives, with the exhibition of either ferromagnetic or antiferromagnetic properties.[7,41] For other examples, σ-dimerization is observed in the solid state,[11] and these materials, as well as their response to applied pressure, are described in Chapter 5. Polymorphism is also found, in which multiple phases are formed in the solid state for a single compound, one exhibiting exceptionally high conductivity. This material, and its S/Se variations, are discussed in Chapter 6. With the discovery of such interesting solid state and behavioural properties for these heterocyclic compounds **4-1** to **4-4**, the development of other selenium-containing radicals is alluring. In the pursuit of the next

generation of neutral radicals for use as functional materials, the challenging synthetic work described here will be a definite asset when preparing these new systems.

4.8 Future Work

The biggest problem with the synthetic methodology for the selenium-containing radicals described above is the cyclocondensation reaction of the methyl-substituted selenol **4-10** with $SOCl_2$ and Et_3N to form [**4-3**][Cl] (R_1 = H, R_2 = H) as in Scheme 12. This reaction is the least reliable (~ 60% success rate) and the resulting product can cause difficulties in subsequent steps. It is difficult to suggest ways to improve this procedure, as many variations of the reaction conditions have been tried. Possible modifications however, include using more labile selenium-protecting groups such as acetyl or trimethylsilyl substitutents, or the use of a weaker (pyridine) or stronger (Hünig's base, Proton Sponge) auxiliary base.

Scheme 12

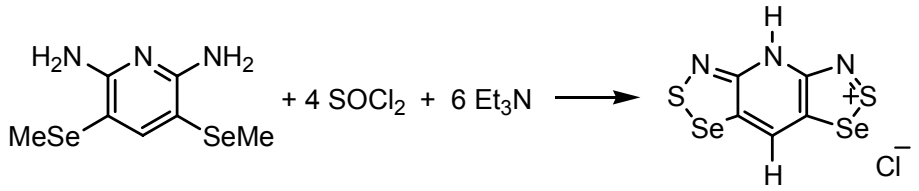

4-10 [**4-3**][Cl]

Alternatively, the synthetic sequence could be altered so as to decrease the number of overall steps. It has been shown that the Herz reaction of [**4-12**][OTf] (R_1 = Me, R_2 = H) with S_2Cl_2 affords the methylated triflate salt [**4-1**][OTf] (R_1 = Me, R_2 = H) in a single step.[2] We have tried applying this strategy to the related selenium-containing starting materials so as to reach [**4-3**][OTf] (R_1 = Me, Et; R_2 = H) in one reaction. Unfortunately, we have difficulty alkylating the methyl-protected selenol **4-10**. The treatment of methyl triflate on **4-10** affords a mixture of products with methylation occurring at the pyridine nitrogen, the amines and the selenium atoms. When the amines are blocked with acetyl groups, as in **4-13**, methylation takes place at the selenium sites to form the mono- and di-substituted compounds **4-14** and **4-15**. Akylation at the pyridine nitrogen may be more favourable if different protecting groups were used.

For example, the selenium sites could be capped with a bulkier substituent such as t-butyl, or a deactivating group like trifluoromethyl. Alternatively, the amines could be protected with a less deactivating substituent such as the trimethylsilyl group. Another option is to use a weaker alkylating agent, such as methyl iodide or ethyl triflate, that would preferentially react at the pyridine nitrogen.

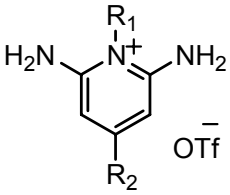

[**4-12**][OTf]

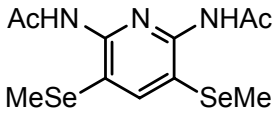

4-13

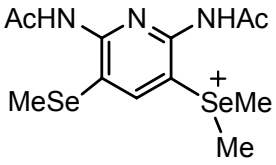

4-14

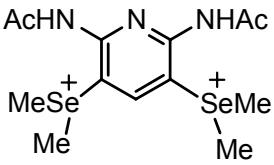

4-15

Given that the all-selenium radicals **4-4** have the most interesting conductive and magnetic properties, it would be worthwhile to formulate a reaction scheme that focused directly on making this framework. We have found in our laboratory that it is possible to do a Herz-type reaction on amino-naphthalene with $SeCl_2$ to give the diselenazolium compound [**4-16**][Cl]. It has been determined that this reaction does not work on the bifunctional material 2,6-diaminopyridine,[25] but could it be possible on a modified version of it? For example, preliminary work on treating the trimethylsilyl-protected diaminopyridinium triflate [**4-17**][OTf] with $SeCl_2$ has provided promising results. Further research in this area may be successful in forming $[\mathbf{4\text{-}4}]^+$ in a more timely and cost effective manner.

[**4-16**][Cl]

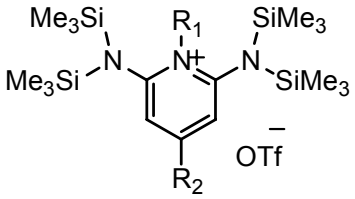

[**4-17**][OTf]

4.9 Experimental Section

4.9.1 Preparation of the Type 2 Salts

Preparation of 8-Chloro-4-methyl-4H-bis[1,2,3]thiaselenazolo[4,5-*b*:5',4'-*e*]pyridin-2-ium Triflate [4-2][OTf] (R_1 = Me, R_2 = Cl). Compound [**4-1**][OTf] (R_1 = Me, R_2 = Cl) (0.859 g, 2.00 mmol) and finely ground selenium dioxide (0.666 g, 6.00 mmol) were combined with 80 mL MeCN in a medium glass pressure vessel which was heated at 110 °C for 3 days in an oil bath. The reaction mixture was hot filtered on a glass Büchner funnel and the filtrate concentrated to 50 mL. After 16 h the red-brown solid of [**4-2**][OTf] (R_1 = Me, R_2 = Cl) was filtered off and washed with 10 mL MeCN; yield 0.740 g (1.41 mmol, 71%). Recrystallization from MeCN afforded red needles, dec. > 292 °C. IR: 1419 (s), 1397 (m), 1353 (m), 1341 (m), 1280 (s), 1230 (s), 1170 (s), 1152 (m), 1048 (w), 1022 (s), 977 (m), 855 (w), 749 (s), 636 (s), 594 (s), 584 (s), 543 (w), 514 (m), 478 (w) cm^{-1}. Anal. Calcd for $C_7H_3ClF_3N_3O_3S_3Se_2$: C, 16.05; H, 0.58; N, 8.02 %. Found: C, 16.27; H, 0.44; N, 8.19 %.

Preparation of 8-Bromo-4-methyl-4*H*-bis[1,2,3]dithiazolo[4,5-*b*:5',4'-*e*]pyridin-2-ium Triflate [4-1][OTf] (R_1 = Me, R_2 = Br). N-bromosuccinimide (0.549 g, 3.08 mmol) was added to a slurry of [**4-1**][OTf] (R_1 = Me, R_2 = H) (1.01 g, 2.54 mmol) in 45 mL MeCN, which was then heated at reflux for 1 h. At this time the reaction mixture was filtered hot through a fine (E porosity) frit, cooled slowly to room temperature, and then at -20 °C for 16 h. The red solid of crude [**4-1**][OTf] (R_1 = Me, R_2 = Br) was filtered off and rinsed with 25 mL DCE, yield 0.894 g (1.88 mmol, 74 %). The recrystallization from MeCN afforded a lustrous red microcrystalline solid, dec. > 271 °C. IR: 1517 (m), 1429 (s), 1355 (s), 1282 (s), 1269 (s), 1241 (s), 1207 (m), 1172 (s), 1157 (m), 1029 (s), 1024 (s), 966 (m), 916 (w), 876 (w), 810 (s), 763 (s), 716 (m), 673 (s), 637 (s), 587 (m), 573 (w), 515 (s), 480 (s) cm^{-1}. Anal. Calcd for $C_7H_3BrF_3N_3O_3S_5$: C, 17.72; H, 0.64; N, 8.86 %. Found: C, 17.54; H, 0.88; N, 8.69 %.

Preparation of 8-Bromo-4-ethyl-4*H*-bis[1,2,3]dithiazolo[4,5-*b*:5',4'-*e*]pyridin-2-ium Triflate [4-1][OTf] (R_1 = Et, R_2 = Br). *Method 1*: A solution of bromine (0.92 mL, 17.9 mmol) in 7 mL MeCN was added to a solution of [**4-1**][$GaCl_4$] (R_1 = Et, R_2 = H) (4.24 g, 8.98 mmol) in 250 mL MeCN and the reaction mixture was heated at reflux. After 1 h, tetrabutylammonium bromide (3.23g, 10.0 mmol) was added to give a green precipitate that was warmed at about 60°C for 30 min and then cooled to room temperature. The green solid of [**4-1**][Br] (R_1 = Et, R_2 = Br) was filtered and washed 3 x 100 mL MeCN, yield 3.76 g (8.97 mmol, 99 %). IR: 1505 (w), 1482 (m), 1449 (s), 1428 (m), 1354 (s), 1187 (w), 1181 (w), 1005 (w), 887 (w), 796 (m), 759 (s), 713 (w), 665 (w), 558 (w), 535 (w), 528 (w), 478 (w) cm^{-1}. Silver triflate (2.86 g, 11.1 mmol) was added to a slurry of [**4-1**][Br] (R_1 = Et, R_2 = Br) (3.76g, 8.97 mmol) in 200 mL MeCN to give a blue solution that was heated at about 60 °C for 45 min, before being filtered hot through paper to remove some of the white solid of AgBr. The filtrate was concentrated to 75 mL and upon cooling, the red solid of [**4-1**][OTf] (R_1 = Et, R_2 = Br) crystallized. This crude material was filtered and rinsed with DCM, yield 2.30 g (4.71 mmol, 52 %). *Method 2*: A slurry of [**4-1**][OTf] (R_1 = Et, R_2 = H) (1.96 g, 4.78 mmol) and N-bromosuccinimide (1.02 g, 5.73 mmol) in 80 mL MeCN was heated at reflux for 1 h before being filtered hot through a fine (E porosity) frit. The filtrate was cooled slowly to room temperature, and then at -20 °C for 16 h. Red flakes of [**4-1**][OTf] (R_1 = Et, R_2 = Br) were filtered on a glass Büchner funnel and washed with 25 mL DCM, yield 1.39 g (2.84 mmol, 59 %). The product was purified by recrystallization from MeCN and isolated as red needles, dec. > 280 °C. IR: 1515 (m), 1486 (s), 1434 (s), 1356 (s), 1271 (s), 1242 (s), 1227 (s), 1189 (m), 1168 (m), 1182 (m), 1126 (s), 1007 (w), 889 (w), 878 (w), 803 (m), 792 (m), 758 (s), 669 (s), 638 (s), 592 (w), 574 (w), 544 (w), 515 (m), 475 (s) cm^{-1}. Anal. Calcd for $C_8H_5BrF_3N_3O_3S_5$: C, 19.67; H, 1.03; N, 8.60 %. Found: C, 20.06; H, 0.75; N, 8.36 %.

Preparation of 8-Bromo-4-ethyl-4H-bis[1,2,3]thiaselenazolo[4,5-*b*:5',4'-*e*]pyridin-2-ium Triflate [4-2][OTf] (R_1 = Et, R_2 = Br). In a large glass pressure vessel, finely ground selenium dioxide (1.17 g, 10.5 mmol) was added to a slurry of [**4-1**][OTf] (R_1 = Et, R_2 = Br) (1.68 g, 3.44 mmol) in 150 mL MeCN, and the mixture was stirred and heated at 110 °C for 4-5 days. The reaction was monitored by ESI mass spectrometry, and upon completion the reaction mixture was filtered hot through a glass Büchner funnel,

and the filtrate was evaporated to dryness. The residue was triturated with 50 mL HOAc and then filtered off and washed with 20 mL DCM, yield 1.197 g (20.6 mmol, 60 %). Recrystallization of [**4-2**][OTf] (R_1 = Et, R_2 = Br) from MeCN afforded red needles, dec. > 259 °C. IR: 1505 (m), 1428 (s), 1358 (s), 1200 (s), 1183 (s), 1159 (s), 1085 (w), 1059 (s), 1004 (m), 908 (w), 853 (s), 738 (s), 589 (s), 537 (m), 475 (m) cm^{-1}. Anal. Calcd for $C_8H_5BrF_3N_3O_3S_3Se_2$: C, 16.50; H, 0.87; N, 7.22 %. Found: C, 16.30; H, 0.78; N, 7.14 %.

4.9.2 Preparation of the Type 3 Salts

Preparation of 2,6-Diaminopyridine-3,5-bis(selenocyanate) 4-6. A solution of bromine (8.90 mL, 0.173 mol) in 100 mL MeOH was added dropwise over a 1 h period to a cold (-78 °C) solution of potassium selenocyanate (50.0 g, 0.347 mol) in 200 mL MeOH. A solution of 2,6-diaminopyridine (9.45 g, 0.0866 mol) in 150 mL MeOH was then added dropwise over 90 min to afford an orange mixture that was stirred for 1 h at -78 °C. The reaction mixture was poured onto 1.5 L ice/water and left to stand at room temperature for 20 h. The resulting grey solid was filtered off and warmed in 1.5 L 10% aq. HCl for 2 h. Upon filtration, the yellow filtrate was cooled to 0 °C, and a yellow microcrystalline solid was formed upon the addition of concentrated ammonium hydroxide to reach a pH 8-9. After 2 h, the solid was collected by filtration and washed with water. The acid/base extraction was repeated several times; yield 19.6 g (0.0619 mol, 71 %); dec. > 200 °C. IR: 3490 (m), 3427 (s), 3382 (s), 3325 (w), 3151 (m, br), 3047 (w), 2145 (s), 1655 (s), 1627 (s), 1603 (s), 1555 (m), 1532 (s), 1460 (s), 1377 (s), 1311 (vw), 1260 (w), 1077 (vw), 1022 (vw), 952 (w), 800 (vw), 755 (m), 722 (vw), 619 (vw), 566 (vw), 502 (w), 458 (w) cm^{-1}. Anal. Calcd for $C_7H_5N_5Se_2$: C, 26.52; H, 1.59; N, 22.09 %. Found: C, 26.70; H, 1.39; N, 22.06 %.

Preparation of 2,6-Diaminopyridine-3,5-bis(ethylcyanoselenolate) 4-9. A slurry of **4-6** (5.0 g, 0.0158 mol) in 80 mL MeOH was cooled on an ice bath, and sodium borohydride (2.23 g, 0.0588 mol) was added portionwise to give an orange solution that was stirred for 30 min at 0 °C. At this time, 3-bromopropionitrile (4.0 mL, 0.0484 mol) was added. After 30 min the reaction mixture was poured onto 150 mL ice/water. The precipitate was filtered on a Büchner funnel after 1 h and rinsed with water. The

crude product of **4-9** was recrystallized from EtOH to afford yellow needles, yield 5.88 g (0.0158 mol, 98 %). IR: 3486 (m), 3427 (m), 3382 (m), 3299 (m), 3156 (m), 2245 (m), 1627 (s), 1601 (s), 1538 (s), 1435 (s), 1309 (w), 1262 (m), 1243 (m), 1205 (m), 1186 (w), 924 (m), 891 (m), 758 (s), 728 (w), 685 (w), 665 (w), 617 (w) cm^{-1}.

Preparation of 2,6-Diaminopyridine-3,5-bis(methylselenolate) 4-10. A slurry of **4-6** (13.0 g, 0.0410 mol) in 225 mL MeOH was cooled to 0 °C and sodium borohydride (5.10 g, 0.135 mol) was added slowly to give a clear yellow solution. After 30 min, methyl iodide (8.40 mL, 0.135 mol) was added and the reaction mixture was stirred for 1 h at 0 °C before being poured onto 1 L ice/water. After 2 h the yellow product was filtered off and washed with water, yield 11.1 g (0.0419 mol, 92 %). Recrystallization from 60 mL ethyl acetate afforded colourless needles of **4-10**; yield 9.89 g (0.0335 mol, 89 % from crude); mp 120 - 122 °C. IR: 3408 (m), 3282 (m, br), 3177 (vw), 1599 (s), 1544 (s), 1463 (vs), 1425 (vs), 1377 (vs), 1300 (w), 1266 (m), 1237 (w), 1153 (w), 1031 (w), 937 (m), 907 (s), 765 (s), 720 (m), 688 (vw), 634 (m, br), 584 (m), 449 (m) cm^{-1}. ^1H NMR (δ, $CDCl_3$): 7.81 (s, 1H, aromatic), 5.01 (s, 4H, amino), 2.10 (s, 6H, methyl). Anal. Calcd for $C_7H_{11}N_3Se_2$: C, 28.49; H, 3.76; N, 14.24 %. Found: C, 28.69; H, 3.87; N, 14.40 %.

Preparation of 4H-Bis[1,2,3]selenathiazolo[4,5-*b*:5',4'-*e*]pyridin-2-ium Chloride, [4-3][Cl] ($R_1 = R_2$ = H). Triethylamine (21.4 mL, 0.154 mol) was added to a slurry of **4-10** (11.3 g, 0.0382 mol) in 500 mL MeCN, and the mixture was cooled to 0 °C. A solution of thionyl chloride (16.8 mL, 0.230 mol) in 100 mL MeCN was then added over a period of 90 min to afford a dark brown precipitate. The slurry mixture was stirred for 16 h at room temperature, during which time the precipitate slowly turned black. This black precipitate of [**4-3**][Cl] ($R_1 = R_2$ = H) was filtered off and washed 3 × 200 mL MeCN and 2 × 200 mL DCM; yield 11.2 g (0.0309 mol, 81 %). IR: 1344 (s), 1261 (w), 1073 (w), 1031 (s), 885 (m), 806 (m), 735 (s), 711 (m), 691 (m), 609 (s), 496 (w), 446 (m) cm^{-1}.

Preparation of 4H-Bis[1,2,3]selenathiazolo[4,5-*b*:5',4'-*e*]pyridin-2-ium Triflate, [4-3][OTf] ($R_1 = R_2$ = H). Gallium trichloride (6.25 g, 0.0355 mol) was added to a slurry of [**4-3**][Cl] ($R_1 = R_2$ = H) (11.2 g, 0.0309 mol) in 400 mL MeCN. After 30 min, the solution was filtered through a fine (E porosity) frit, and the solvent was removed by flash distillation. The copper-red residue of crude [**4-3**][$GaCl_4$] ($R_1 = R_2$ = H) was triturated with 200 mL HOAc and filtered off, washed with 4 × 150 mL HOAc and 2 × 100 mL DCM; yield 12.2 g (0.0226 mol, 73 %). IR: 1497 (w), 1347 (s), 1262 (w), 1029 (s), 899 (m), 867 (w), 838 (w), 817 (m), 729 (s), 687 (m), 615 (s), 445 (w) cm^{-1}. Crude [**4-3**][$GaCl_4$] ($R_1 = R_2$ = H) (12.2 g, 0.0226 mol) was dissolved in 100 mL hot anhydrous THF and the reaction mixture was hot filtered through a fine (E porosity) frit. Tetrabutylammonium triflate (10.7 g, 0.0272 mol) dissolved in 60 mL DCE was added to the filtrate. After 1h, the resulting red precipitate of [**4-3**][OTf] ($R_1 = R_2$ = H) was collected by filtration and washed with 4 × 60 mL DCE, yield 6.46 g (0.0136 mol, 60 %), dec. > 227 °C. IR: 3197 (w), 1328 (s), 1257 (s), 1230 (s), 1166 (m), 1022 (s), 895 (w), 812 (m), 760 (w), 731 (m), 715 (s), 689 (m), 638 (m), 607 (s), 577 (w), 572 (w), 519 (w), 511 (m), 446 (s) cm^{-1}. Anal. Calcd for $C_6H_2F_3N_3O_3S_3Se_2$: C, 15.16; H, 0.42; N, 8.84 %. Found: C, 15.56; H, 0.50; N, 9.08 %.

Preparation of Bis[1,2,3]selenathiazolo[4,5-*b*:5',4'-*e*]pyridin-2-ium-4-ide, 4-11. Proton sponge (3.51g, 0.0164 mol) was added as a dry solid to a slurry of [**4-3**][OTf] ($R_1 = R_2$ = H) (6.46 g, 0.0136 mol) in 250 mL MeCN. After 16 h the green precipitate of **4-11** was filtered off and washed with 4 × 100 mL MeCN; yield 4.49 g (0.0138 mol, 99 %). IR: 1414 (m), 1345 (m), 1257 (w), 1047 (w), 1018 (m), 900 (s), 814 (w), 729 (m), 720 (s), 674 (w), 619 (m) cm^{-1}.

Preparation of 4-Methyl-4H-bis[1,2,3]selenathiazolo[4,5-*b*:5',4'-*e*]pyridin-2-ium Triflate, [4-3][OTf] (R_1 = Me, R_2 = H). Methyl triflate (3.40 mL, 30.0 mmol) was added to a solution of Proton Sponge (1.31 g, 6.11 mmol) dissolved in 200 mL DCE. Compound **4-11** (3.95 g, 12.1 mmol) was added and after 16 h the red solid of [**4-3**][OTf] (R_1 = Me, R_2 = H) was filtered and washed with 3 x 80 mL DCE, yield 5.48 g (11.2 mmol, 92%). The product was purified by double recrystallization from MeCN and isolated as red needles, dec. > 233 °C. UV-vis (MeCN) λ_{max} 700 nm (log ε = 4.6). IR: 1497 (w), 1352 (m), 1269 (m),

1243 (s), 1225 (m), 1156 (m), 1032 (s), 1016 (m), 904 (s), 858 (w), 831 (w), 758 (w), 730 (m), 713 (m), 684 (m), 653 (m), 639 (s), 575 (w), 519 (w), 473 (w) cm^{-1}. ^1H NMR (δ, *d*-DMSO): 8.45 (s, 1H, aromatic), 3.60 (s, 3H, methyl). Anal. Calcd for $C_7H_4F_3N_3O_3S_3Se_2$: C, 17.18; H, 0.82; N, 8.59 %. Found: C, 17.28; H, 1.08; N, 8.70 %.

Preparation of 4-Ethyl-4H-bis[1,2,3]selenathiazolo[4,5-*b*:5',4'-*e*]pyridin-2-ium Triflate, [4-3][OTf] (R_1 = Et, R_2 = H). Ethyl triflate (4.5 mL, 0.0348 mol) was added to a solution of Proton Sponge (1.48 g, 6.89 mmol) in 200 mL DCE. Compound **4-11** (4.49 g, 0.0138 mol) was added and the mixture stirred for 3-4 days. The fine red precipitate of crude [**4-3**][OTf] (R_1 = Et, R_2 = H) was filtered off, washed with 3 x 80 mL DCE, and dried in vacuo; yield 5.81 g (0.0115 mol, 84 %). The product was recrystallized from MeCN and HOAc and isolated as lustrous red needles; dec. > 235 °C. IR: 3088 (w), 1353 (s), 1263 (s), 1250 (m), 1238 (m), 1223 (m), 1175 (m), 1156 (m), 1146 (m), 1085 (w), 1035 (w), 1027 (m), 989 (w), 904 (w), 830 (m), 792 (s), 759 (w), 729 (s), 650 (m), 638 (s), 574 (m), 516 (s), 465 (m) cm^{-1}. Anal. Calcd for $C_8H_6F_3N_3O_3S_3Se_2$: C, 19.09; H, 1.20; N, 8.35 %. Found: C, 19.06; H, 1.26; N, 8.42 %.

4.9.3 Modification of the R_2 Substituent of Type 3 Salts

Preparation of 8-Chloro-4-methyl-4H-bis[1,2,3]selenathiazolo[4,5-*b*:5',4'-*e*]pyridin-2-ium Triflate, [4-3][OTf] (R_1 = Me, R_2 = Cl). Freshly prepared iodobenzene dichloride (2.52 g, 9.18 mmol) was added to a green slurry of [**4-3**][OTf] (R_1 = Me, R_2 = H) (3.76 g, 7.68 mmol) in 400 mL MeCN and the reaction mixture was heated at reflux for 90 min. The solution was filtered hot through a fine (D porosity) frit, and the filtrate was concentrated to 250 mL. After standing for 16 h, the red precipitate of [**4-3**][OTf] (R_1 = Me, R_2 = Cl) was filtered and washed with 30 mL DCM, yield 3.10 g (5.91 mmol, 77%). The solid was recrystallized from MeCN, dec. > 255 °C. IR: 1413 (m), 1352 (m), 1271 (m), 1237 (s), 1226 (s), 1198 (m), 1169 (m), 1153 (m), 1030 (s), 971 (w), 914 (w), 840 (m), 825 (m), 713 (s), 707 (m), 669 (m), 657 (s), 641 (s), 599 (w), 572 (w), 541 (w), 517 (m) cm^{-1}. Anal. Calcd for $C_7H_3ClF_3N_3O_3S_3Se_2$: C, 16.05; H, 0.58; N, 8.02%. Found: C, 16.32; H, 0.62; N, 8.20%.

Preparation of 8-Chloro-4-methyl-4H-bis[1,2,3]selenathiazolo[4,5-*b*:5',4'-*e*]pyridin-2-ium Nonaflate, [4-3][ONf] (R_1 = Me, R_2 = Cl). A solution of tetra-n-butylammonium bromide (1.96 g, 6.08 mmol) dissolved in 20 mL MeCN was added to a hot solution of [**4-3**][OTf] (R_1 = Me, R_2 = Cl) (2.12 g, 4.05 mmol) in 450 mL MeCN. After 30 min the resulting green precipitate of [**4-3**][Br] (R_1 = Me, R_2 = Cl) was filtered and washed 3 x 100 mL MeCN, yield 1.80 g (3.96 mmol, 98%). IR: 1501 (w), 1415 (s), 1403 (s), 1340 (s), 1201 (m), 1044 (m), 958 (w), 899 (w), 831 (m), 818 (m), 710 (m), 646 (s), 594 (w), 537 (w), 507 (m) cm^{-1}. Silver nonafluorobutanesulfonate[42] (1.94 g, 4.76 mmol) was added to a slurry of [**4-3**][Br] (R_1 = Me, R_2 = Cl) (1.80 g, 3.96 mmol) in 200 mL MeCN to give a green solution that was warmed at about 60 °C for 1 h. The white solid of AgBr was removed by double filtration through paper and the filtrate was concentrated to 125 mL. After 2 h, the reaction mixture was cooled at -20 °C for 3 h, and the product [**4-3**][ONf] (R_1 = Me, R_2 = Cl) filtered off and rinsed with 20 mL DCM, yield 2.47 g (3.66 mmol, 92%), dec. >238 °C. IR: 1413 (m), 1351 (m), 1268 (m), 1234 (s), 1201 (m), 1179 (m), 1132 (m), 1059 (m), 1044 (m), 1018 (w), 1005 (w), 969 (w), 911 (w), 839 (m), 825 (m), 802 (w), 739 (w), 715 (s), 668 (m), 655 (s), 619 (w), 599 (w), 565 (w), 538 (w), 521 (w) cm^{-1}. Anal. Calcd for $C_{10}H_3ClF_9N_3O_3S_3Se_2$: C, 17.83; H, 0.45; N, 6.24%. Found: C, 18.08; H, 0.30; N, 6.52%.

Preparation of 8-Bromo-4-methyl-4H-bis[1,2,3]selenathiazolo[4,5-*b*:5',4'-*e*]pyridin-2-ium Triflate, [4-3][OTf] (R_1 = Me, R_2 = Br). N-bromosuccinimide (0.816 g, 4.58 mmol) was added to a slurry of [**4-3**][OTf] (R_1 = Me, R_2 = H) (1.50 g, 3.07 mmol) in 240 mL MeCN and the reaction mixture was slowly heated to the boil. After 90 min at gentle reflux, the solution was filtered hot through a fine (E porosity) frit, cooled to room temperature, and then at -20 °C for 16 h. The red solid of crude [**4-3**][OTf] (R_1 = Me, R_2 = Br) was filtered off and rinsed with 25 mL DCM, yield, 0.81 g (1.43 mmol, 47 %). Recrystallization from HOAc afforded red crystals. IR: 1410 (s), 1345 (s), 1273 (s), 1239 (s), 1170 (m), 1028 (s), 911 (w), 838 (m), 802 (w), 735 (w), 709 (s), 658 (s), 639 (s), 573 (m), 516 cm^{-1}.

Preparation of 8-Bromo-4-ethyl-4H-bis[1,2,3]selenathiazolo[4,5-*b*:5',4'-*e*]pyridin-2-ium Triflate, [4-3][OTf] (R_1 = Et, R_2 = Br). *Method 1*: Bromine (0.35 mL, 6.81 mmol) was added to a slurry of [**4-3**][OTf] (R_1 = Et, R_2 = H) (2.50 g, 4.97 mmol) in 250 mL MeCN and the reaction mixture was slowly heated to reflux. After 3 h the slurry was cooled slightly and the precipitate of [**4-3**][Br] (R_1 = Et, R_2 = Br) was filtered in vacuo and washed 2 x 60 mL MeCN, yield 1.49 g (2.90 mmol, 58 %). IR: 1490 (m), 1448 (s), 1423 (s), 1346 (s), 1184 (m), 1086 (w), 1069 (w), 987 (w), 871 (m), 830 (m), 797 (m), 786 (m), 700 (s), 647 (s), 578 (m), 531 (s), 499 (s) cm^{-1}. Silver triflate (0.82 g, 3.19 mmol) was added to a slurry of [**4-3**][Br] (R_1 = Et, R_2 = Br) (1.49 g, 2.90 mmol) in 200 mL MeCN to give a green slurry that was warmed at about 60 °C for 1 h. The reaction mixture was filtered hot through paper to remove some of the white solid of AgBr. The filtrate was concentrated to 100 mL and then cooled slowly to room temperature. The red solid of [**4-3**][OTf] (R_1 = Et, R_2 = Br) was filtered and washed with 40 mL DCM, yield 1.32 g (2.26 mmol, 78 %). *Method 2*: A slurry of [**4-3**][OTf] (R_1 = Et, R_2 = H) (1.85 g, 3.67 mmol) and N-bromosuccinimide (0.850 g, 4.78 mmol) in 150 mL MeCN was heated slowly to reflux and after boiling for 90 min the resulting solution was filtered hot through a fine (E porosity) frit. The filtrate was cooled slowly to room temperature and then at -20 °C for 16 h. The red solid of [**4-3**][OTf] (R_1 = Et, R_2 = Br) was filtered and washed with 30 mL DCM, yield 1.00 g (1.72 mmol, 47 %). Recrystallization from HOAc afforded a lustrous powder, dec. > 265 °C. IR: 1498 (m), 1447 (s), 1434 (s), 1430 (s), 1350 (s), 1273 (s), 1237 (s), 1171 (m), 1075 (w), 1027 (s), 990 (w), 874 (m), 838 (m), 793 (m), 759 (w), 735 (w), 707 (s), 655 (s), 638 (s), 583 (w), 573 (w), 534 (w), 516 (m) cm^{-1}. Anal. Calcd for $C_8H_5BrF_3N_3O_3S_3Se_2$: C, 16.50; H, 0.87; N, 7.22 %. Found: C, 16.40; H, 1.00; N, 7.34 %.

4.9.4 Preparation of the Type 4 Salts

Preparation of 4-Methyl-4H-bis[1,2,3]diselenazolo[4,5-*b*:5',4'-*e*]pyridin-2-ium Triflate, [4-4][OTf] (R_1 = Me, R_2 = H). A green slurry of [**4-3**][OTf] (R_1 = Me, R_2 = H) (1.38 g, 2.83 mmol) and selenium dioxide (1.59 g, 14.3 mmol) in 650 mL HOAc was set to reflux and after 2 h the heat was removed and the reaction mixture was slowly cooled to room temperature. The red needles of [**4-4**][OTf] (R_1 = Me, R_2 =

H) were collected and washed with 1 × 100 mL HOAc and 1 × 100 mL DCE, yield 1.36 g (2.33 mmol, 82 %). The product was recrystallized in MeCN and isolated as red flakes, dec. > 240 °C. UV-vis (MeCN) λ_{max} 736 nm (log ε = 4.7). IR: 1423 (m), 1344 (s), 1269 (m), 1236 (s), 1224 (m), 1158 (m), 1136 (s), 1030 (s), 1002 (w), 864 (w), 759 (w), 717 (m), 695 (m), 672 (m), 640 (s), 569 (s), 515 (m) cm^{-1}. ^1H NMR (δ, *d*-DMSO): 8.50 (s, 1H, aromatic), 3.69 (s, 3H, methyl). Anal. Calcd for $C_7H_4F_3N_3O_3S_1Se_4$: C, 14.42; H, 0.69; N, 7.21 %. Found: C, 14.51; H, 0.90; N, 7.26 %.

Preparation of 4-Ethyl-4H-bis[1,2,3]diselenazolo[4,5-*b*:5',4'-*e*]pyridin-2-ium Triflate, [4-4][OTf] (R_1 = Et, R_2 = H). A 75 mL solution of [**4-3**][OTf] (R_1 = Et, R_2 = H) (0.504 g, 1.00 mmol) in HOAc was heated to the boil and ground selenium dioxide (0.333 g, 3.00 mmol) was added. The reaction mixture was heated at reflux for 90 min and then cooled slowly without stirring. The resulting red precipitate was filtered off and washed with DCE. The crude material was recrystallized from MeCN as purple-red needles, yield 0.500 g. (0.837 mmol, 83 %), dec. > 219 °C. IR: 1431 (w), 1350 (m), 1259 (s), 1235 (s), 1222 (m), 1177 (m), 1157 (m), 1140 (m), 1024 (s), 720 (m), 692 (m), 670 (s), 637 (s), 570 (s), 516 (m) cm^{-1}. Anal. Calcd for $C_8H_6F_3N_3O_3SSe_4$: C, 16.09; H, 1.01; N, 7.04 %. Found: C, 16.21; H, 1.15; N, 6.91 %.

Preparation of 8-Chloro-4-methyl-4H-bis[1,2,3]diselenazolo[4,5-*b*:5',4'-*e*]pyridin-2-ium Nonaflate, [4-4][ONf] (R_1 = Me, R_2 = Cl). Compound [**4-3**][ONf] (R_1 = Me, R_2 = Cl) (0.675 g, 1.00 mmol) and finely ground selenium dioxide (0.340 g, 3.00 mmol) were combined with 80 mL MeCN in a medium glass pressure vessel, which was then sealed and heated at 110 °C for 4 days. The heat was removed and after 16 h the red solid of [**4-4**][ONf] (R_1 = Me, R_2 = Cl) was filtered and washed with 30 mL DCM, yield 0.584 g (0.761 mmol, 76%). Recrystallization from MeCN afforded red needles, dec. > 254 °C. IR: 1410 (m), 1343 (m), 1264 (m), 1230 (s), 1185 (m), 1147 (w), 1133 (m), 1058 (m), 1044 (w), 1027 (w), 1015 (w), 1002 (w), 959 (w), 847 (w), 804 (w), 756 (w), 738 (w), 705 (s), 659 (m), 638 (w), 619 (w), 579 (s), 534 (w), 522 (w) cm^{-1}. Anal. Calcd for $C_{10}H_3ClF_9N_3O_3SSe_4$: C, 15.65; H, 0.39; N, 5.47 %. Found: C, 15.79; H, 0.28; N, 5.60 %.

Preparation of 8-Bromo-4-ethyl-4H-bis[1,2,3]diselenazolo[4,5-*b*:5',4'-*e*]pyridin-2-ium Triflate, [4-4][OTf] (R_1 = Et, R_2 = Br). Finely ground selenium dioxide (0.700 g, 6.31 mmol) was added to a hot solution of [**4-3**][OTf] (R_1 = Et, R_2 = Br) (1.22 g, 2.10 mmol) in 220 mL HOAc, and the reaction mixture was heated at reflux for 2 h. The heat was removed and the brown solution was cooled slowly to room temperature. After 16 h the red solid of [**4-4**][OTf] (R_1 = Et, R_2 = Br) was filtered and washed with 20 mL DCM, yield 0.902 g (1.33 mmol, 64 %). The product was recrystallized from HOAc and isolated as purple needles, dec. > 258 °C. IR: 2251 (w, MeCN), 1483 (w), 1417 (s), 1353 (s), 1318 (w), 1280 (s), 1244 (s), 1221 (s), 1176 (w), 1152 (s), 1085 (w), 1058 (w), 1026 (s), 985 (w), 894 (w), 774 (w), 759 (w), 735 (m), 712 (m), 699 (s), 637 (s), 581 (s), 572 (m), 566 (m), 532 (m), 516 (m) cm^{-1}. Anal. Calcd for $C_8H_5BrF_3N_3O_3S_1Se_4$: C, 14.21; H, 0.75; N, 6.22 %. Found: C, 14.10; H, 0.63; N, 6.21 %.

4.9.5 Preparation of the Radicals

Method 1: H-cells (diffusion or electrochemical) for single crystal growth.

Method 2: Large scale for bulk measurements.

Preparation of 4-Methyl-3H,4H-bis[1,2,3]selenathiazolo[4,5-*b*:5',4'-*e*]pyridin-3-yl, 4-3 (R_1 = Me, R_2 = H). *Method 1*: Crystals suitable for X-ray analysis were grown by slow diffusion of a degassed (4 freeze-pump-thaw cycles) solution of [**4-3**][OTf] (R_1 = Me, R_2 = H) (30 mg, 0.0613 mmol) in 15 mL MeCN into an equally degassed solution of octamethylferrocene (20 mg, 0.0671 mmol) in 10 mL MeCN. The golden needles of **4-3** (R_1 = Me, R_2 = H) were harvested after 16 h. *Method 2*: A degassed (4 freeze-pump-thaw cycles) solution of [**4-3**][OTf] (R_1 = Me, R_2 = H) (0.500 g, 1.02 mmol) in 90 mL MeCN was added to an equally degassed solution of decamethylferrocene (0.365 g, 1.19 mmol) in 210 mL MeCN. After 1 h the gold needles of **4-3** (R_1 = Me, R_2 = H) were collected by filtration in vacuo on a fine frit and washed 3 x 10 mL MeCN, yield 0.330 g (0.970 mmol, 95 %), dec. > 120 °C. IR: 1209 (m), 1003 (w), 860 (m), 719 (m), 682 (m), 670 (m), 634 (s), 514 (w) cm^{-1}. Anal. Calcd for $C_6H_4N_3S_2Se_2$: C, 21.18; H, 1.19; N, 12.35 %. Found: C, 21.50; H, 1.40; N, 12.20 %.

Preparation of 4-Methyl-3H,4H-bis[1,2,3]diselenazolo[4,5-*b*:5',4'-*e*]pyridin-3-yl, 4-4 (R_1 = Me, R_2 = H). *Method 1*: The slow diffusion of a degassed (4 freeze-pump-thaw cycles) solution of [**4-4**][OTf] (R_1 = Me, R_2 = H) (15 mg, 0.0257 mmol) in 17 mL MeCN into an equally degassed solution of octamethylferrocene (10 mg, 0.0335 mmol) in 5 mL MeCN afforded golden needles of **4-4** (R_1 = Me, R_2 = H) which were harvested after 3 h. *Method 2*: A degassed (4 freeze-pump-thaw cycles) solution of [**4-4**][OTf] (R_1 = Me, R_2 = H) (0.253 g, 0.434 mmol) in 200 mL MeCN was added to an equally degassed solution of octamethylferrocene (0.152 g, 0.510 mmol) in 90 mL MeCN. After 30 min the gold-brown precipitate of **4-4** (R_1 = Me, R_2 = H) was collected by filtration in vacuo on a fine frit and washed 3 × 10 mL MeCN, yield 0.160 g (0.369 mmol, 85 %), dec. > 120 °C. IR: 1291 (w), 1227 (s), 995 (w), 871 (m), 721 (w), 687 (s), 671 (m), 661 (m), 503 (m) cm^{-1}. Anal. Calcd for $C_6H_4N_3Se_4$: C, 16.61; H, 0.93; N, 9.68 %. Found: C, 16.54; H, 1.10; N, 9.48 %.

Preparation of 4-Ethyl-3H,4H-bis[1,2,3]selenathiazolo[4,5-*b*:5',4'-*e*]pyridin-3-yl, 4-3 (R_1 = Et, R_2 = H). *Method 1*: Degassed solutions (3 freeze-pump-thaw cycles) of decamethylferrocene (20 mg, 0.0613 mmol) in 15 mL MeCN and [**4-3**][OTf] (R_1 = Et, R_2 = H) (26 mg, 0.0517 mmol) in 10 mL MeCN were allowed to diffuse together slowly at room temperature over a period of 16 h. At this time the solvent was decanted to leave gold needles of **4-3** (R_1 = Et, R_2 = H) suitable for X-ray work. *Method 2*: A degassed (4 freeze-pump-thaw cycles) solution of [**4-3**][OTf] (R_1 = Et, R_2 = H) (0.299 g, 0.594 mmol) was added to an equally degassed solution of decamethylferrocene (0.233 g, 0.714 mmol) to afford the lustrous grey solid of **4-3** (R_1 = Et, R_2 = H). After standing for 90 min, the slurry was cooled on an ice bath for 30 min before being filtered on a fine (E porosity) frit. The microcrystalline solid was washed 3 x 25 mL MeCN, yield 0.136 g (0.384 mmol, 65 %), dec. > 120 °C. IR: 1420 (w), 1366 (w), 1312 (m), 1201 (s), 1084 (w), 1027 (m), 877 (w), 778 (w), 713 (s), 685 (s), 679 (s), 629 (s), 543 (m), 454 (m) cm^{-1}. Anal. Calcd for $C_7H_6N_3S_2Se_2$: C, 23.74; H, 1.71; N, 11.86 %. Found: C, 23.70; H, 1.62; N, 11.74 %.

Preparation of 4-Ethyl-3H,4H-bis[1,2,3]diselenazolo[4,5-*b*:5',4'-*e*]pyridin-3-yl, 4-4 (R_1 = Et, R_2 = H). *Method 1*: Degassed solutions (3 freeze-pump-thaw cycles) of decamethylferrocene (15 mg, 0.0460 mol) in 12 mL MeCN and [**4-4**][OTf] (R_1 = Et, R_2 = H) (21 mg, 0.0352mmol) in 12 mL MeCN were allowed to diffuse together slowly at room temperature over a period of 20 h. At this time the solvent was decanted to leave gold needles of **4-4** (R_1 = Et, R_2 = H) suitable for X-ray work. *Method 2*: Degassed (3 freeze-pump-thaw cycles) solutions of [**4-4**][OTf] (R_1 = Et, R_2 = H) (0.250 g, 0.419 mmol) in 130 mL MeCN and decamethylferrocene (0.178 g, 0.545 mmol) in 150 mL MeCN were combined to afford the lustrous grey precipitate of **4-4** (R_1 = Et, R_2 = H). After 1h the solid was filtered off and washed with 6 x 20 mL MeCN, yield 0.167 g (0.373 mmol, 89 %), dec. > 120 °C. IR: 1320 (m), 1204 (s), 1145 (w), 1085 (w), 1021 (m), 894 (w), 798 (m), 722 (w), 690 (s), 673 (s), 660 (s), 650 (m), 555 (m), 539 (w) cm^{-1}. Anal. Calcd for $C_7H_6N_3Se_4$: C, 18.77; H, 1.35; N, 9.38 %. Found: C, 19.00; H, 1.50; N, 9.51 %.

Preparation of 8-Chloro-4-methyl-4H-bis[1,2,3]thiaselenazolo[4,5-*b*:5',4'-*e*]pyridin-3-yl, 4-2 (R_1 = Me, R_2 = Cl). *Method 1*: The slow diffusion of a carefully degassed (4 freeze-pump-thaw cycles) solution of [**4-2**][OTf] (R_1 = Me, R_2 = Cl) (19 mg, 0.0363 mmol) in 15 mL MeCN into an equally degassed solution of hexamethylferrocene (12 mg, 0.0444 mmol) in 8 mL MeCN at room temperature, afforded **4-2** (R_1 = Me, R_2 = Cl). The resulting needles were harvested after 16 h. *Method 2*: Degassed solutions (3 freeze-pump-thaw cycles) of [**4-2**][OTf] (R_1 = Me, R_2 = Cl) (0.200 g, 0.382 mmol) in 180 mL MeCN and TMPDA (0.083 g, 0.505 mmol) in 40 mL MeCN were combined and after 30 min the gold-brown precipitate of **4-2** (R_1 = Me, R_2 = Cl) was filtered, washed with 5 x 30 mL MeCN and dried in vacuo, yield 0.125 g (0.334 mmol, 87 %), dec. > 120 °C. IR: 1251 (m), 1184 (w), 1043 (m), 958 (m), 823 (w), 736 (m), 691 (m), 578 (m), 525 (m), 463 (w) cm^{-1}. Anal. Calcd for $C_6H_3ClN_3S_2Se_2$: C, 19.24; H, 0.81; N, 11.22 %. Found: C, 19.40; H, 0.90; N, 11.25 %.

Preparation of 8-Chloro-4-methyl-4H-bis[1,2,3]selenathiazolo[4,5-*b*:5',4'-*e*]pyridin-3-yl, 4-3 (R_1 = Me, R_2 = Cl). *Method 1*: Carefully degassed solutions of [**4-3**][OTf] (R_1 = Me, R_2 = Cl) (19 mg, 0.0363 mmol) in 15 mL MeCN and hexamethylferrocene (12 mg, 0.0444 mmol) in 8 mL MeCN were allowed to diffuse

together slowly at room temperature. The silver needles of **4-3** (R_1 = Me, R_2 = Cl) were harvested after 16 h. *Method 2*: Degassed solutions (3 freeze-pump-thaw cycles) of [**4-3**][ONf] (R_1 = Me, R_2 = Cl) (0.200 g, 0.382 mmol) in 180 mL MeCN and TMPDA (0.083 g, 0.505 mmol) in 40 mL MeCN were combined and after 30 min the gold-brown precipitate of **4-3** (R_1 = Me, R_2 = Cl) was filtered, washed with 5 x 30 mL MeCN and dried in vacuo, yield 0.125 g (0.334 mmol, 87 %), dec. > 120 °C. IR: 1251 (m), 1184 (w), 1043 (m), 958 (m), 823 (w), 736 (m), 691 (m), 578 (m), 525 (m), 463 (w) cm^{-1}. Anal. Calcd for $C_6H_3ClN_3S_2Se_2$: C, 19.24; H, 0.81; N, 11.22 %. Found: C, 19.40; H, 0.90; N, 11.25 %.

Preparation of 8-Chloro-4-methyl-4H-bis[1,2,3]diselenazolo[4,5-*b*:5',4'-*e*]pyridin-3-yl, 4-4 (R_1 = Me, R_2 = Cl). *Method 1*: The electrocrystallization work that was used employed standard electrochemical H-cell techniques,[43] with samples of [**4-4**][ONf] (R_1 = Me, R_2 = Cl) (20 mg) dissolved under nitrogen in 20 mL of MeCN containing 0.008 M [*n*-Bu_4N][PF_6] as supporting electrolyte. Currents ranged from 5 to 10 μA, with growth periods of 2 - 4 days. *Method 2*: The bulk reductions of [**4-4**][ONf] (R_1 = Me, R_2 = Cl) with a variety of reducing agents (decamethylferrocene, hexamethylferrocene, TMPDA, TDAE) gave material that consisted of mixtures of at least two phases. A single phase could only be generated by electrocrystallization techniques, and it was this material that was used for bulk measurements. Dec. > 120 °C. IR: 1247 (m), 1178 (m), 1029 (w), 934 (m), 692 (m), 684 (m), 567 (m), 557 (m), 526 (w), 435 (w) cm^{-1}. Anal. Calcd for $C_6H_3ClN_3Se_4$: C, 15.39; H, 0.65; N, 8.97 %. Found: C, 15.13; H, 0.81; N, 8.96 %.

Preparation of 8-Bromo-4-methyl-4H-bis[1,2,3]dithiazolo[4,5-*b*:5',4'-*e*]pyridin-3-yl, 4-1 (R_1 = Me, R_2 = Br). *Method 1*: The slow diffusion of a carefully degassed (4 freeze-pump-thaw cycles) solution of [**4-1**][OTf] (R_1 = Me, R_2 = Br) (32 mg, 0.0675 mmol) in 13 mL MeCN into an equally degassed solution of decamethylferrocene (23 mg, 0.0705 mmol) in 15 mL MeCN at room temperature, afforded **4-1** (R_1 = Me, R_2 = Br). The resulting gold needles were harvested after 24 h. *Method 2*: Compound [**4-1**][OTf] (R_1 = Me, R_2 = Br) (0.437 g, 0.921 mmol) was added to a degassed slurry of decamethylferrocence (0.314 g, 0.962 mmol) in 15 mL MeCN to afford the gold-brown precipitate of **4-1** (R_1 = Me, R_2 = Br). After 90 min, the solid was filtered, washed with 5 x 15 mL MeCN and dried in vacuo, yield 0.290 g (0.892 mmol, 97

%). Golden needles were afforded by recrystallization from DCE, dec. > 120 °C. IR: 1241 (s), 1189 (m), 1043 (m), 952 (m), 779 (s), 738 (s), 679 (s), 653 (m), 572 (s), 504 (s), 495 (w), 455 (w) cm^{-1}. Anal. Calcd for $C_6H_3BrN_3S_4$: C, 22.15; H, 0.93; N, 12.92 %. Found: C, 22.30; H, 1.06; N, 12.93 %.

Preparation of 8-Bromo-4-methyl-4H-bis[1,2,3]selenathiazolo[4,5-*b*:5',4'-*e*]pyridin-3-yl, 4-3 (R_1 = Me, R_2 = Br). *Method 1*: Degassed (3 freeze-pump-thaw cycles) solutions of hexamethylferrocene (9 mg, 0.0333 mmol) in 8 mL MeCN and [**4-3**][OTf] (R_1 = Me, R_2 = Br) (15 mg, 0.0264 mmol) in 15 mL MeCN were allowed to diffuse together slowly at room temperature over a period of 20 h. At this time the solvent was decanted to leave gold needles of **4-3** (R_1 = Me, R_2 = Br). *Method 2*: Degassed (3 freeze-pump-thaw cycles) solutions of TMPDA (0.101g, 0.615 mmol) in 40 mL MeCN and [**4-3**][OTf] (R_1 = Me, R_2 = Br) (0.270 g, 0.475 mmol) in 250 mL MeCN were combined and after 30 min the gold-brown precipitate of **4-3** (R_1 = Me, R_2 = Br) was filtered off and washed with 4 x 20 mL MeCN, yield 0.155 g (0.370 mmol, 78 %), dec. > 120 °C. IR: 1238 (s), 1187 (w), 1032 (w), 927 (w), 772 (m), 722 (w), 693 (m), 673 (s), 635 (s), 562 (m), 498 (m), 482 (w) cm^{-1}. Anal. Calcd for $C_6H_3BrN_3S_2Se_2$: C, 17.20; H, 0.72; N, 10.03 %. Found: C, 17.42; H, 0.87; N, 10.14 %.

Preparation of 8-Bromo-4-ethyl-4H-bis[1,2,3]thiaselenazolo[4,5-*b*:5',4'-*e*]pyridin-3-yl, 4-2 (R_1 = Et, R_2 = Br). *Method 1*: Degassed (3 freeze-pump-thaw cycles) solutions of hexamethylferrocene (15 mg, 0.0555 mmol) in 10 mL MeCN and [**4-2**][OTf] (R_1 = Et, R_2 = Br) (30 mg, 0.0515 mmol) in 15 mL MeCN were allowed to diffuse together slowly at room temperature over a period of 16 h. At this time the solvent was decanted to leave gold needles of **4-2** (R_1 = Et, R_2 = Br) suitable for X-ray work. *Method 2*: Degassed (3 freeze-pump-thaw cycles) solutions of TMPDA (0.098g, 0.597 mmol) in 40 mL MeCN and [**4-2**][OTf] (R_1 = Et, R_2 = Br) (0.250 g, 0.429 mmol) in 150 mL MeCN were combined and after 30 min the gold-brown precipitate of **4-2** (R_1 = Et, R_2 = Br) was filtered off and washed with 4 x 20 mL MeCN, yield 0.172 g (0.397 mmol, 93 %), dec. > 120 °C. IR: 1442 (s), 1402 (w), 1352 (w), 1322 (m), 1230 (m), 1171 (w), 1085 (w), 1062 (w), 997 (w), 889 (w), 838 (m), 709 (w), 692 (m), 570 (w), 518 (w), 453 (w) cm^{-1}. Anal. Calcd for $C_7H_5BrN_3S_2Se_2$: C, 19.41; H, 1.16; N, 9.70 %. Found: C, 19.67; H, 1.36; N, 9.76 %.

Preparation of 8-Bromo-4-ethyl-4H-bis[1,2,3]selenathiazolo[4,5-*b*:5',4'-*e*]pyridin-3-yl, 4-3 (R_1 =Et, R_2 = Br). *Method 1*: Degassed (3 freeze-pump-thaw cycles) solutions of octamethylferrocene (13 mg, 0.0436 mmol) in 8 mL MeCN and [**4-3**][OTf] (R_1 = Et, R_2 = Br) (20 mg, 0.0344 mmol) in 15 mL MeCN were allowed to diffuse together slowly at room temperature over a period of 16 h. The solvent was decanted to leave bronze needles of **4-3** (R_1 = Et, R_2 = Br) suitable for X-ray work. *Method 2*: Degassed (3 freeze-pump-thaw cycles) solutions of TMPDA (0.095 g, 0.578 mmol) in 40 mL MeCN and [**4-3**][OTf] (R_1 = Et, R_2 = Br) (0.255 g, 0.438 mmol) in 180 mL MeCN were combined and after 30 min the gold-brown precipitate of **4-3** (R_1 = Et, R_2 = Br) was filtered off and washed with 5 x 20 mL MeCN, yield 0.147 g (0.339 mmol, 77 %), dec. > 120 °C. IR: 1440 (s), 1412 (m), 1350 (w), 1306 (m), 1215 (s), 1175 (m), 1082 (w), 1055 (w), 986 (w), 856 (w), 782 (w), 767 (s), 692 (m), 679 (s), 649 (w), 632 (w), 575 (m), 510 (w), 481 (w) cm^{-1}. Anal. Calcd for $C_7H_5BrN_3S_2Se_2$: C, 19.41; H, 1.16; N, 9.70 %. Found: C, 19.68; H, 1.33; N, 9.59 %.

Preparation of 8-Bromo-4-ethyl-4H-bis[1,2,3]diselenazolo[4,5-*b*:5',4'-*e*]pyridin-3-yl, 4-4 (R_1 = Et, R_2 = Br). *Method 1*: The electrocrystallization work that was used employed standard electrochemical H cell techniques,[43] with samples of [**4-4**][OTf] (R_1 = Et, R_2 = Br) (25 mg) dissolved under nitrogen in 20 mL MeCN containing 0.008 M [*n*-Bu_4N][PF_6] as supporting electrolyte. Currents ranged from 5 to 10 μA, with growth periods of 2 - 4 days. *Method 2*: Degassed (3 freeze-pump-thaw cycles) solutions of TMPDA (0.069g, 0.420 mmol) in 50 mL MeCN and [**4-4**][OTf] (R_1 = Et, R_2 = Br) (0.200 g, 0.296 mmol) in 200 mL MeCN were combined and after 30 min the gold-brown precipitate of **4-4** (R_1 = Et, R_2 = Br) was filtered off and washed with 4 x 20 mL MeCN, yield 0.143 g (0.271 mmol, 92 %), dec. > 120 °C. IR: 1448 (s), 1397 (m), 1366 (m), 1349 (w), 1315 (m), 1223 (s), 1167 (m), 1079 (w), 1053 (w), 988 (m), 875 (w), 811 (w), 703 (w), 687 (s), 563 (m), 517 (w), 422 (w) cm^{-1}. Anal. Calcd for $C_7H_5BrN_3Se_4$: C, 15.96; H, 0.96; N, 7.98 %. Found: C, 16.12; H, 1.09; N, 8.07 %.

Chapter 5

Pressure Response of Selenium σ-Dimers

5.1 Introduction

Obtaining a bandwidth *W* large enough to overcome the high on-site Coulomb repulsion energy *U* has been an on-going challenge in the design of neutral radical materials. The development of the resonance-stabilized bisdithiazolyls **5-1** was a major advancement in the pursuit of a single-component molecular conductor, as these systems did not dimerize in the solid state and possessed lower *U* values than monofunctional dithiazolyls.[1,2,3] However, as previously described in Chapter 1, the bandwidth afforded by the close intermolecular interactions along the slipped π-stacks was insufficient to offset *U*, and these materials were Mott insulators. To improve *W* in **5-1**, we developed the selenium-containing variants **5-2** to **5-4**, in hopes of increasing the *W*/*U* ratio and obtaining a metallic ground state.

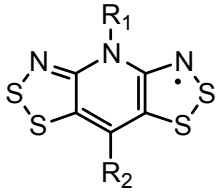

5-1

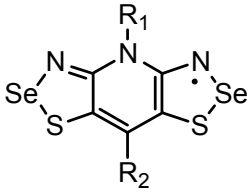

5-2

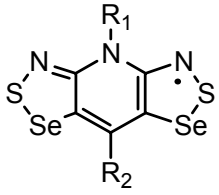

5-3

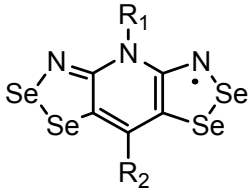

5-4

Our first successful attempt at selenium incorporation involved the generation of the **5-2** framework, which has selenium in the 2-position. Upon isolation of the early derivatives of this compound we found that the radicals associated to form σ-bonded dimers [**5-2**]$_2$ in the solid state (Figure 5.1).[4,5] This dimerization mode is unique in that the radicals fuse together laterally and form a covalent bond between two selenium atoms. Concomitant with the formation of the Se-Se′ σ-bond is the rupture of the endocyclic

Se-S bond and the generation of a thione unit. In addition, there is a rearrangement of the bond lengths, the pattern of distances being consistent with the closed shell valence bond formulation of [**5-2**]$_2$ shown in Figure 5.1.

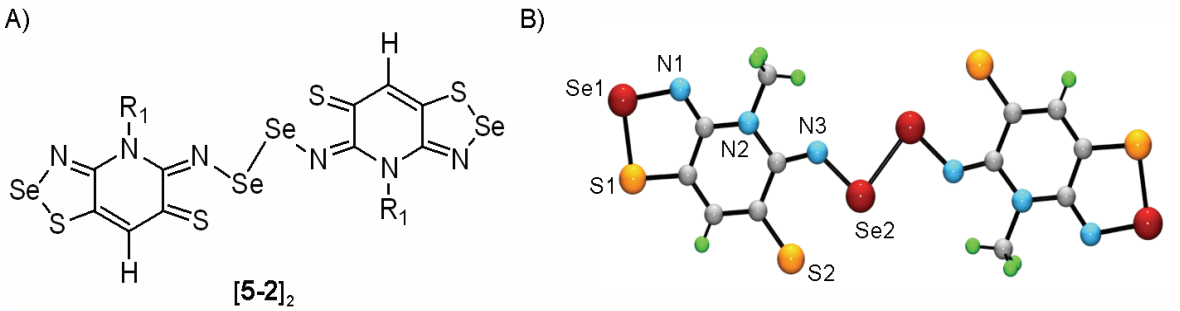

Figure 5.1 Valence bond formulation of [**5-2**]$_2$ (R_1 = Me, Et; R_2 = H) (A) and molecular structure of [**5-2**]$_2$ (R_1 = Me, R_2 = H) with atom numbering (B).

The σ-bonded dimerization mode had never been observed before the isolation of these dimers, and we were concerned that association of this type would be the inevitable fate of all of the proposed selenium-containing radicals **5-2** to **5-4**. In order to understand the energy requirements associated with σ-dimerization, and the possibility of its appearance elsewhere, we performed a series of DFT calculations (at the B3LYP/6-31G(d,p) level) on four model radicals **5-1** to **5-4** (R_1 = R_2 = H) and their respective σ-bonded dimers.[5] The resulting bond dissociation enthalpies ΔH_{diss} are presented in Table 5.1, which correspond to the reaction shown in Scheme 1. The calculated ΔH_{diss} values indicate that σ-dimerization is favoured for all of the radicals except **5-3**, and most especially for **5-2**. It appears that for maximum dimer stability, the preferred S/Se combination is when there is a bridging Se-Se′ bond with a terminal thione group. This can be rationalized in terms of the greater preference for sulfur (over selenium) to form a double bond to carbon, and the ability of selenium to form a more hypervalent arrangement, as in the E_1---E_2–E_2′---E_1′ conformation of the σ-dimer.

Table 5.1 B3LYP/6-31G(d,p) Bond Dissociation Enthalpies, ΔH_{diss}, for $[\mathbf{5\text{-}1}]_2$ to $[\mathbf{5\text{-}4}]_2$ (R_1 = H, R_2 = H)[a]

Compound	$[\mathbf{5\text{-}1}]_2$	$[\mathbf{5\text{-}2}]_2$	$[\mathbf{5\text{-}3}]_2$	$[\mathbf{5\text{-}4}]_2$
ΔH_{diss} [b] (kcal mol^{-1})	11.12	18.19	-1.12	8.87

[a] The ΔH_{diss} values reported in Reference 5 were obtained using Gaussian-98. The values listed here were recalculated using Gaussian-03. [b] For the reaction presented in Scheme 1.

Scheme 1

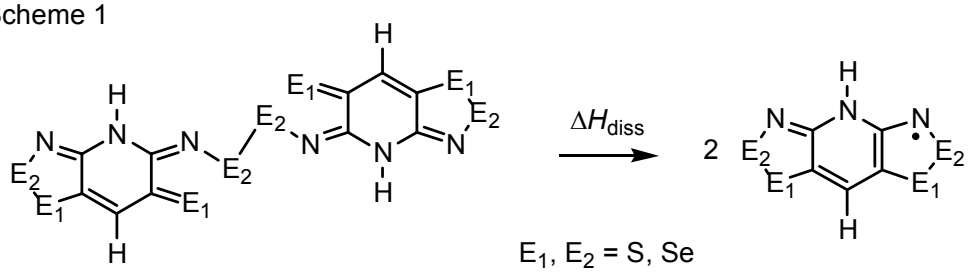

The calculated ΔH_{diss} value of **5-1** is comparable to that of **5-2** and suggests that this compound is also likely to form σ-dimers in the solid state. However, all investigated examples of **5-1** did not associate, and instead their crystal structures consisted of discrete radicals. Apparently, for these compounds, lattice energies are sufficient to overcome their tendency to dimerize. For **5-4**, we reasoned that since the calculated ΔH_{diss} value was lower than that for **5-1**, there was a chance that these radicals would also not undergo dimerization in the solid state. We therefore concluded that discrete radicals should be possible for compounds **5-3** and **5-4**, and potentially for **5-2**, and so we continued to pursue the three selenazyl radicals. We have found, as will be described in Chapter 6, that for particular R_1/R_2 substituents σ-dimerization can be avoided, and discrete radicals of **5-2**, **5-3** and **5-4** can be obtained.[6]

Although the early systems of **5-2** formed σ-dimers, and thus possessed diamagnetic ground states, both compounds $[\mathbf{5\text{-}2}]_2$ (R_1 = Me, Et; R_2 = H) were small band gap semiconductors with σ(295 K) values of ~10^{-6} S cm^{-1} and thermal activation energies E_{act} below 0.4 eV.[5] However, what was particularly impressive about these compounds was their behaviour under relatively mild applied pressure. The R_1 = Me derivative for example, now referred to as $[\mathbf{5\text{-}2a}]_2$, exhibited an increase in conductivity by five orders of magnitude reaching σ(295 K) of ~ 0.1 S cm^{-1} under 4 GPa of pressure, with E_{act} dropping below 0.05 eV

with only 5 GPa of applied pressure. The question immediately arises as to the cause of the dramatic pressure response, that is, the near metallization of a molecular material, with 5 GPa of pressure. Is it a result of the decomposition and/or rearrangement of the molecular framework, or is it the closure of the electronic band gap?

A search of the literature reveals that full metallization in single component, closed shell organic materials has only rarely been observed, typically in condensed ring aromatics. For example, the activation energy E_{act} of single crystals of pentacene can be reduced to zero near 27 GPa, although for powdered samples higher pressures are required.[7] Metallization has also been observed in iodine-substituted aromatics, for example, *p*-diiodobenzene,[8] hexaiodobenzene,[9] and iodanil,[10] but the onset of the metallic state for these systems typically requires pressures in excess of 30 GPa. The possibility of band edge overlap has been suggested as the source of metallization for these systems, but bond dissociation to afford domains of metallic iodine has also been proposed.[11] Selenium- and tellurium-substituted tetracenes have been shown to display enhanced conductivity under pressure, but little is known of the effect of pressure on the structure of these chalcogen-based materials.[12] However, for the elemental chalcogens, it is well-known that bond dissociation and structural rearrangements can occur under pressure.[13] In the case of sulfur, for example, increasing compression from 0 - 11 GPa at elevated temperature leads to opening of S_8 rings of the orthorhombic phase to produce a helical (trigonal) chain structure which, in turn, recyclizes to afford a rhombohedral structure based on S_6 rings.[14] Analogous trigonal[15] and rhombohedral[16] phases have been observed for selenium.

As for the present dimer [**5-2a**]$_2$, we have examined the sample by infrared analysis following the pressurization experiment to ensure that the pressure response was not a result of decomposition and/or rearrangement of the molecular framework. The results showed no indication of deterioration, suggesting that the structure remains intact upon application of 5 GPa of pressure. Furthermore, if the structure was damaged, the most likely decomposition products, sulfur and selenium, do not display appreciable conductivity values under these pressure conditions.[17,18] In order to gain some insight into the structure-

property relationship for these types of systems, and to determine if the pressure response is due to the closure of the band gap, we have prepared two isostructural σ-bonded dimers [**5-2b**]$_2$ (R = Me) and [**5-2c**]$_2$ (R = F), and compared the effects of applied pressure on the transport properties of the three compounds [**5-2a,b,c**]$_2$.

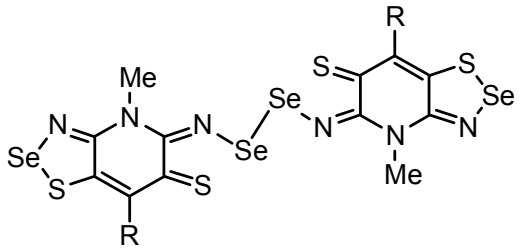

[**5-2a,b,c**]$_2$ (R = H, Me, F)

This chapter describes the synthesis, ambient pressure crystallography and high pressure conductivity measurements of the σ-dimers [**5-2a,b,c**]$_2$. We have found that all three compounds are isomorphous with the same general packing arrangement. The high pressure conductivity experiments show that for all three systems conductivity improves, and activation energies decline, with increasing applied pressure. There is a variation of the overall response across the series, with [**5-2a**]$_2$ exhibiting the largest change with pressure, and [**5-2b**]$_2$ displaying the least. Preliminary high pressure crystallography experiments on [**5-2a**]$_2$ have revealed a compression of the intermolecular contacts within the crystal structure with increasing pressure, suggesting that the differences in pressure response of the three derivatives is related to the compressibility of their respective structures. This has led to a closer examination of the ambient pressure crystal structures of the three dimers in order to gain some insight into the structure-property relationship of these compounds under pressure. Other than the early work of the first σ-dimers reported in 2005,[5] the work described here has not yet been published.

5.2 Synthesis

The preparation of the [**5-2a,b,c**]$_2$ compounds is shown in Scheme 2, and relies on the N-methyl diaminopyridinium salts [**5-5a,b,c**][OTf] as key precursors for all three derivatives. Double Herz chemistry of these salts with sulfur monochloride affords the all-sulfur frameworks [**5-1a,b,c**][OTf] in a single step.

Selenium insertion into the 2-position of these compounds to afford [**5-2a,b,c**][OTf] was achieved using selenium dioxide in refluxing acetic acid, a method reported some years ago for the incorporation of selenium into1,2,3-benzodithiazolium salts.[19] The preparative routes to the starting materials for the R_1 = H and Me derivatives, [**5-5a,b**][OTf], have been reported previously.[2,3] The remaining salt [**5-5c**][OTf] was obtained by first methylating 2,4,6-trifluoropyridine with methyl triflate, followed by amination of the isolated material with anhydrous ammonia at 70 °C in acetonitrile. The radical species **5-2a,b,c** were prepared by the reduction of the corresponding cations [**5-2a,b,c**]$^+$ with octamethylferrocene in acetonitrile, and crystallized out of solution as the σ-dimers [**5-2a,b,c**]$_2$.

Scheme 2

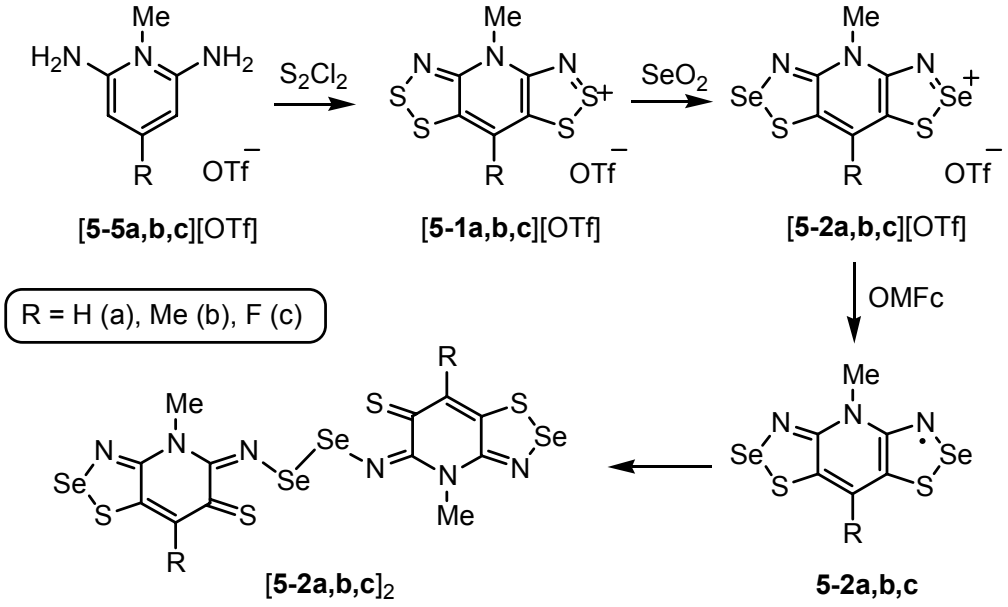

5.3 Crystal Structures

In our early work on the preparation and characterization of [**5-2a**]$_2$ we were able to obtain crystals of sufficient size and quality to allow its structural determination using single crystal X-ray methods.[5] However, in the case of [**5-2b**]$_2$ and [**5-2c**]$_2$, the size and morphology of the crystals were not suitable for single crystal studies, and instead the structures were solved and refined using powder diffraction methods. From these studies it was found that all three dimers [**5-2a,b,c**]$_2$ are isomorphous and crystallize in the

monoclinic space group $P2_1/c$. A representative unit cell drawing for [**5-2c**]$_2$ (R = F), viewed down the stacking direction, is shown in Figure 5.2. The crystallographic data for the three compounds is listed in Table 5.2, and selected intra- and intermolecular metrics are presented in Table 5.3.

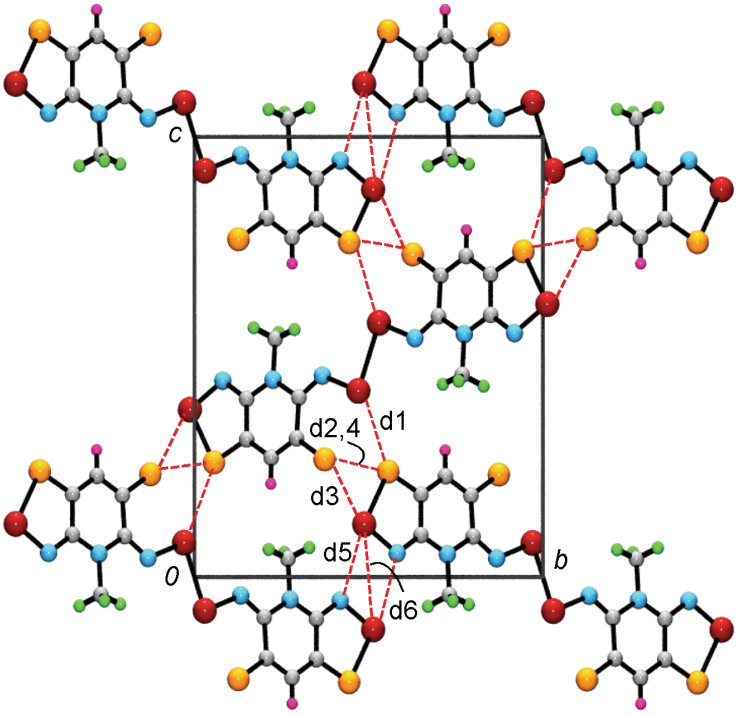

Figure 5.2 Unit cell drawing of [**5-2c**]$_2$, with close intermolecular contacts d1 to d6.

The three structures consist of interpenetrating slipped π-stacks, as shown in Figure 5.3, with the ends of each molecule directed towards the centers of neighbouring dimers. This arrangement allows for a web of close inter-dimer S---S′ and S---Se′ interactions d1 to d4. The molecules are also linked laterally into ribbons *via* Se---N′ and Se---Se′ contacts d5 and d6, which connect the dimers along the *b* direction. Neighbouring stacks along the *c* axis are tilted in opposite directions so as to give the interpenetrating stacks illustrated in Figure 5.3, and to produce the cross-braced arrangement shown in Figure 5.4.

Table 5.2 Crystallographic Data of [**5-2a,b,c**]$_2$

Compound	[**5-2a**]$_2$ (R = H)[b]	[**5-2b**]$_2$ (R = Me)	[**5-2c**]$_2$ (R = F)
formula	$C_{12}H_8N_6S_4Se_4$	$C_{14}H_{12}N_6S_4Se_4$	$C_{12}H_6F_2N_6S_4Se_4$
M, g mol^{-1}	680.32	708.38	716.30
a, Å	4.924(4)	4.2797(5)	4.3792(8)
b, Å	12.616(11)	13.4739(17)	13.3357(31)
c, Å	15.086(13)	17.6545(17)	16.081(4)
β, deg	94.563(14)	100.772(16)	101.854(22)
V, Å^3	934.1(14)	1000.10(12)	919.10(25)
ρ(calcd), g cm^{-1}	2.419	2.352	2.588
space group	$P2_1/c$	$P2_1/c$	$P2_1/c$
Z	2	2	2
Temp, K	295(2)	293(2)	293(2)
λ, Å	0.71073	1.54056	1.54056
θ_{full}, deg	26.99	-	-
data/restraints/parameters	2027/0/119	-	-
solution method	direct methods	powder data	powder data
R, R_w (on F^2)	0.0439, 0.0939	0.0601, 0.0886 [a]	0.0493, 0.0585 [a]

[a] R_p and R_{wp} respectively from the Rietveld refinement. [b] From reference 5.

Table 5.3 Selected Intra- and Intermolecular Distances[a] and Inclination Angles[b] of [**5-2a,b,c**]$_2$.[c]

	[**5-2a**]$_2$ (R = H)	[**5-2b**]$_2$ (R = Me)	[**5-2c**]$_2$ (R = F)
Se2-Se2′	2.460(2)	2.530(1)	2.565(1)
Se2---S2	2.785(3)	2.782(1)	2.790(1)
S2-C4	1.694(6)	1.690(1)	1.694(1)
Se2-N3	1.816(5)	1.812(1)	1.817(1)
N3-C3	1.298(7)	1.298(1)	1.300(1)
d1, Se2---S1′	3.663(3)	4.337(1)	3.651(1)
d2, S2---S1′	3.616(3)	3.549(1)	3.362(1)
d3, S2---Se1′	3.177(2)	3.618(1)	3.086(1)
d4, S2---S1′	3.268(3)	3.289(1)	3.246(1)
d5, N1---Se1′	2.892(5)	2.983(1)	2.963(1)
d6, Se1---Se1′	3.702(3)	3.844(1)	3.769(1)
δ[d]	3.535(2)	3.546(2)	3.509(2)
τ[e]	45.89(5)	55.94(3)	53.24(2)
θ[f]	174.4(5)	179.49(3)	172.76(2)
2τ	91.78	111.88	106.48

[a] Distance in Å. [b] Angle in degrees. [c] For atom numbering, see Figure 5.1. [d] δ is the interplanar separation between molecules. [e] τ is the tilt angle between the mean molecular plane and the *x* axis. [f] θ is the C3-N3-Se2-Se2′ torsion angle within a dimer.

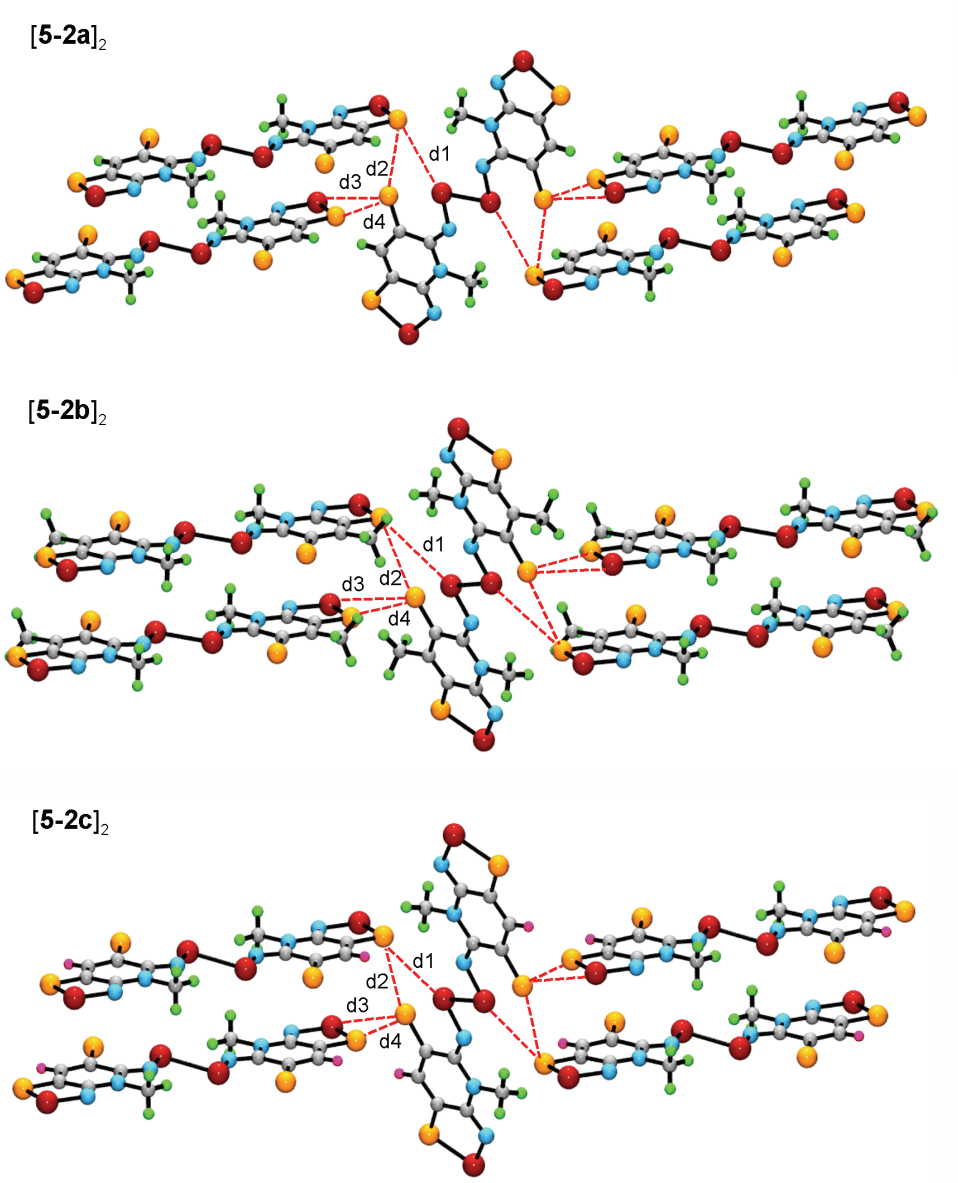

Figure 5.3 Interpenetrating slipped π-stacks of [**5-2a,b,c**]$_2$.

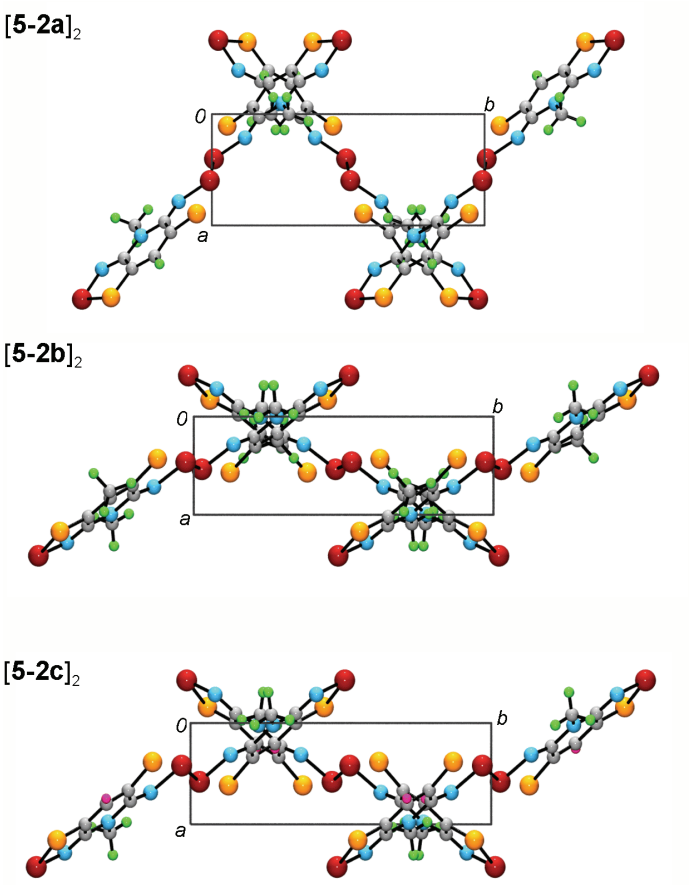

Figure 5.4 Unit cell drawings of [**5-2a,b,c**]$_2$ showing the cross-braced architecture.

From Figure 5.3, it is apparent that there are subtle differences between the three structures. The tilt angle between neighbouring dimers along the *c* direction varies with compound, as does the degree of plate slippage along the π-stacks. The differences in the tilt angle are more easily recognized in the criss-cross arrangement in Figure 5.4. These two structural features are a function of the slippage angle τ, which we define as the angle of inclination between the mean molecular plane of the dimer and the stacking axis. The angle at which neighbouring dimers intersect is twice this value (2τ), and both parameters are listed in Table 5.4, along with the dimer-to-dimer separation along the π-stacks, δ. Although δ is fairly consistent across the series (at about 3.5 Å), τ varies over a range of 10°. The degree of plate slippage (τ) is

noticeably smaller for [**5-2a**]$_2$ (R = H), and accordingly this structure has the steepest tilt angle (2τ) between dimers, as demonstrated in Figure 5.4. This orientation results in slightly different unit cell dimensions with respect to the other two variants. The remaining two compounds, [**5-2b,c**]$_2$, are more closely related, with similar τ angles and hence packing arrangements. The methyl derivative [**5-2b**]$_2$, however, has the most severely slipped π-stacks, affording the widest tilt angle between neighbouring dimers within the series.

5.4 High Pressure Conductivity

In order to explore the effect of pressure on the transport properties of compounds [**5-2a,b,c**]$_2$ we have carried out a series of high pressure conductivity measurements.[‡] Although this measurement has already been reported for [**5-2a**]$_2$, we have re-measured this compound, as we have developed improved methods for its preparation. The results are shown in Figure 5.5 as plots of conductivity σ and activation energy E_{act} as a function of pressure. Overall, under 5 GPa of pressure these compounds exhibit an increase in conductivity by at least five orders of magnitude, with an accompanying drop in E_{act}, which in the case of [**5-2c**]$_2$, decreases to 0.1 eV. In both plots, [**5-2b**]$_2$ displays a substantially lower pressure response than the other two derivatives. Compounds [**5-2a**]$_2$ and [**5-2c**]$_2$ appear to behave similarly with pressure, although [**5-2a**]$_2$ reaches a higher conductivity at the limit of the experiment. The sample of [**5-2a**]$_2$ measured in this study displayed a greater pressure response than that previously reported,[5] presumably due to the use of higher purity material.[‡‡]

[‡] These measurements were performed on a cubic anvil press by X. Yu and R. A. Secco at the University of Western Ontario. A summary of the experimental procedure is described in the Appendix.

[‡‡] In the earlier report, a conductivity value of 0.1 S cm^{-1} was reached under 4 GPa. In the present results a value of 1 S cm^{-1} is obtained at the same pressure.

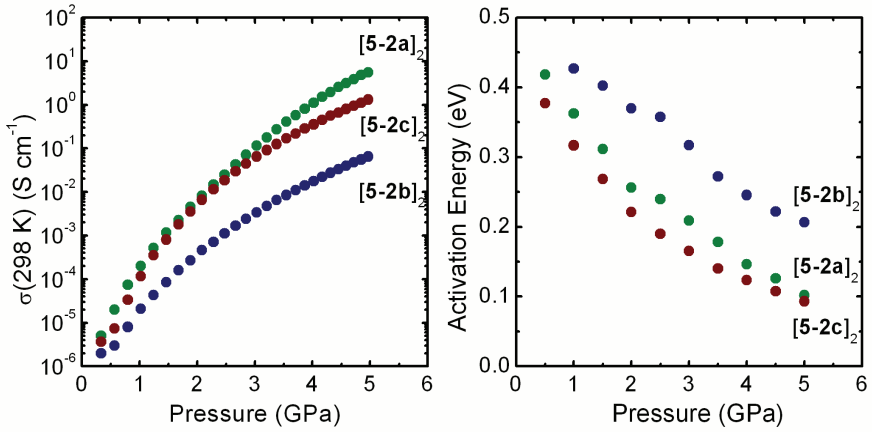

Figure 5.5 Plots of conductivity σ and activation energy E_{act} as a function of pressure for [**5-2a,b,c**]$_2$.

5.5 Preliminary High Pressure Crystallography

To gain some insight into the effects of applied pressure on the crystal structure of these materials, and to ensure that the molecular framework is undamaged as indicated by post-pressurization infrared analysis, we have obtained a series of variable pressure powder diffraction experiments on [**5-2a**]$_2$.[‡] The results are preliminary and must be viewed with caution, as the structures have not been fully refined. This early data suggests that the molecular framework remains intact and the crystal packing is maintained, even at 13 GPa, the limit of the experiment. Provided the model used in the structure determination is correct, the results reveal that while the molecular geometry is essentially unaltered when pressurized, there is a dramatic compression of the intermolecular contacts throughout the structure. This is demonstrated in Figure 5.6, which shows a portion of the crystal structure of [**5-2a**]$_2$, focused around the diselenide linkage, with intra- and intermolecular contacts r1 - r5 at both ambient pressure (0 GPa) and 8 GPa of pressure. A dramatic shortening of the *inter*molecular contacts by 0.5 - 0.8 Å is achieved when the structure is subjected to 8 GPa of pressure.

[‡] These measurements were performed by J. Tse at the Canadian Light Source.

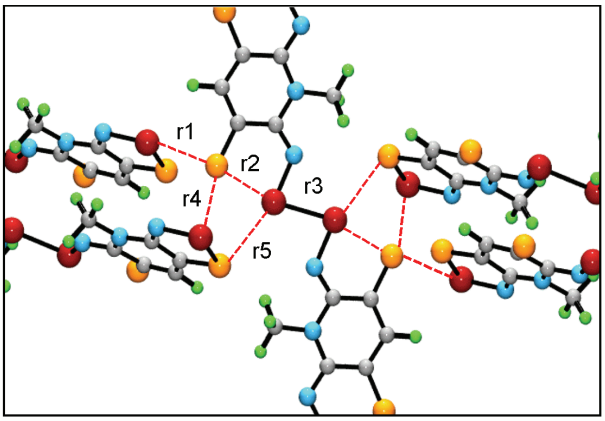

	r1	r2	r3	r4	r5
0 GPa	3.177	2.785	2.460	3.824	3.663
8 GPa	2.746	2.637	2.434	3.211	3.141

Figure 5.6 Crystal packing of [**5-2a**]$_2$ at 0 and 8 GPa, with intra- and intermolecular contacts r1 - r5 (in Å).

The structural investigations of [**5-2a**]$_2$, and the determination of crystallographic coordinates at a variety of pressures, has allowed for DFT band structure calculations and the estimation of the electronic band gap with increasing applied pressure.‡ A plot of the calculated band gap as a function of pressure is shown in Figure 5.7. Keeping in mind that the high pressure structural work is not complete, the results suggest an almost linear decrease in the band gap with increasing pressure, reaching approximately 0.05 eV at 13 GPa. Although the complete closure of the band gap has not been achieved, it does not seem far removed. It may be possible to obtain full metallization of the material with only slightly higher (> 13 GPa) applied pressures.

‡ These calculations were performed by J. Tse.

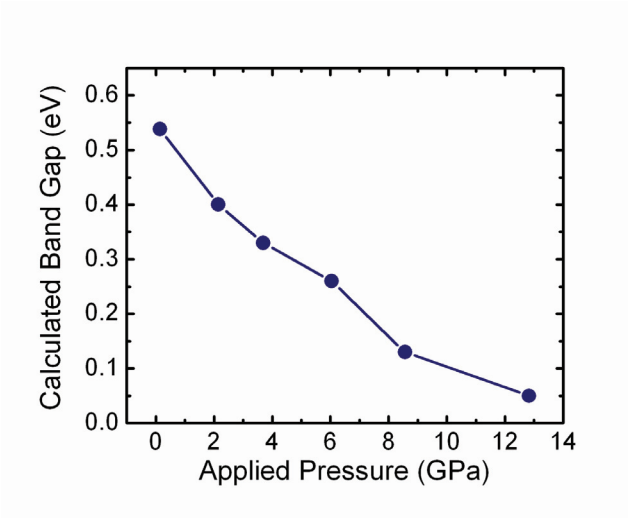

Figure 5.7 A plot of the calculated band gap as a function of pressure for [**5-2a**]$_2$, using preliminary structural data.

If we assume that the preliminary structural investigations are correct, then the molecular structure of the σ-dimer [**5-2a**]$_2$ is preserved with the application of pressure and the packing arrangement is compressed with the shortening of the intermolecular interactions. Consequently, pressurization of the material is accompanied by the closure of the band gap and an increase in conductivity. We suspect that these conclusions also pertain to the σ-dimers [**5-2b,c**]$_2$, which are isostructural to [**5-2a**]$_2$ and exhibit similar changes in conductive behaviour with increasing applied pressure. The variation in the pressure response of the three compounds can be attributed to the relative compressibility of their crystal structures, with the structure of the [**5-2b**]$_2$ dimer being the least responsive. A close examination of the central core of all three compounds (Figure 5.8) reveals that the limiting feature of the packing arrangement is the buffering interactions between the R substituents on neighbouring molecules. For the [**5-2b**]$_2$ dimer, the Me---Me′ contacts are already well within the van der Waals separation (4.0 Å)[20,21] at ambient pressure, and this close interaction would inhibit a compression. By contrast, the Me---H′ interaction in [**5-2a**]$_2$ is well outside the van der Waals separation (3.2 Å),[20] which allows for the dramatic compression of the structure, and increase in conductivity, with pressure. The H---F′ contact in [**5-2c**]$_2$ on the other hand, is on the boundary of the van der Waals separation (3.5 Å).[20] This may account for the drop off in

conductivity for this compound at higher pressures, in that the close contact between the R groups may be reaching the limit to how far they can be compressed, at a rate faster than that of [**5-2a**]$_2$. By this reasoning, the size of the R substituents, and how compressible their non-bonding interactions are, plays a major role in how the dimers respond to applied pressure. High pressure crystallography on all three compounds [**5-2a,b,c**]$_2$ would confirm this theory, and give a clearer understanding of the nature of the compression. Measurements of this kind are currently underway.

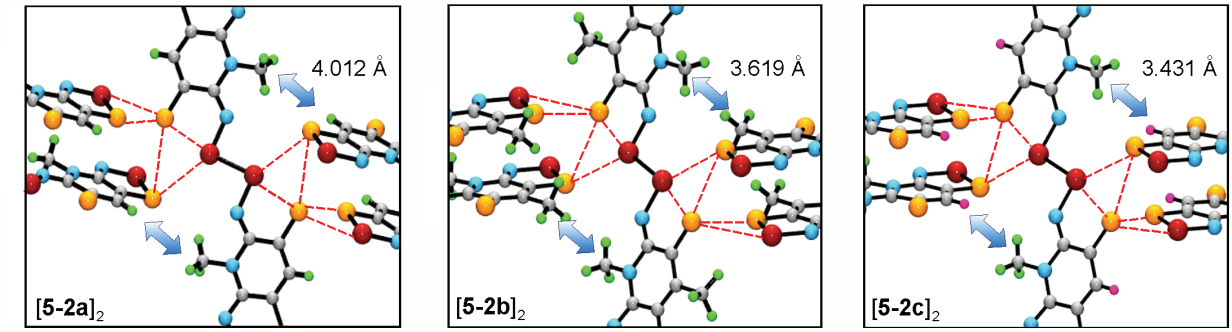

Figure 5.8 An expanded view of the crystal structures of [**5-2a,b,c**]$_2$ at ambient pressure, illustrating the approximate distance between neighbouring R substituents.

5.6 Discussion

Of the four heterocyclic radicals **5-1** to **5-4**, DFT calculations (Section 5.1) have predicted that σ-dimerization is most favourable for compound **5-2**, which has selenium located in the 2-position and sulfur in the remaining site. We have prepared several examples of compounds **5-1** to **5-4**, and found that σ-dimerization is observed exclusively for the **5-2** framework, although discrete radicals of this type have also been found. A list of these compounds is presented in Table 5.4, which specifies whether σ-dimers or discrete radicals are present in the crystal structure, as well as the space group to which they belong. The table includes the original σ-dimers [**5-2**]$_2$ (R_1 = Me, Et; R_2 = H) reported in 2005,[5] as well as those described above, with R_1 = Me; R_2 = H, Me and F. In addition to these, our preliminary work of **5-2** (R_1 = Et, R_2 = F) suggest that on precipitation, a mixture of radicals and σ-dimers are formed for this

compound. The remaining derivatives (R_1 = Me, R_2 = Cl and R_1 = Et, R_2 = Me, Cl, Br) in Table 5.4 do not form σ-dimers in the solid state, and instead remain as unassociated radicals.[22,23]

Table 5.4 The Space Groups and Association Preferences of Known Derivatives of **5-2**

	R_2					
R_1	H	F	Me	Cl	Br	C_6H_5
Me	σ-dimers	σ-dimers	σ-dimers	radicals	unknown	radicals
	$P2_1/c$[a]	$P2_1/c$[b]	$P2_1/c$[b]	$P2_1/n$[f]		$P3_121$[e]
Et	σ-dimers	mixture[b,c]	radicals	radicals	radicals	radicals
	$P2_1/c$[a]		$P\bar{4}2_1m$[d]	$P\bar{4}2_1m$[d]	$P\bar{4}2_1m$[d]	$P3_221$[e]

[a] Reference 5. [b] Unpublished work. [c] This material consists of radicals in the $P\bar{4}2_1m$ space group, and is contaminated with a diamagnetic impurity we believe to be the σ-dimer. [d] From reference 22a. [e] From reference 22b. [f] From reference 23.

For the σ-dimers to form, a pair of radicals must arrange laterally in a side-to-side fashion, so as to link *via* a Se---N′ four center contact, as illustrated in Figure 5.9. Once this pattern is achieved, the intra- and intermolecular contacts can rearrange to form the closed-shell dimer. If the packing influence of the R substituents is negligible, as presumed in the above calculations, all of the **5-2** radicals would likely associate in this way. However, in the solid state, this is not necessarily the case, as illustrated in Table 5.4. The preference for radicals of **5-2** to form σ-dimers diminishes from left to right across the table. As the molecular framework of the radical remains the same throughout, the cause of this structural dichotomy must involve the R substituents. The boundary between a crystal structure consisting of paired or unpaired radicals lies near the middle of the list around the methyl or chloro groups. It is possible that once the radius of the substituent reaches a particular value, for example, greater than 2.0 Å as for R_2 = Me,[21] its packing requirements override the tendency for radicals to align as in Figure 5.9. In fact, the compounds that remain undimerized in the solid state, and have the larger R_2 groups, do not exhibit packing motifs that have radicals arranged as in Figure 5.9.

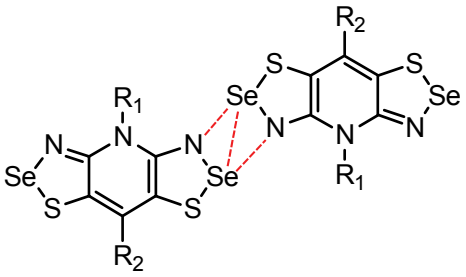

Figure 5.9 Potential packing arrangement for **5-2**, showing Se---N′ four centered contacts.

Dimerization through a lateral σ-bond has also been observed in a bisdithiazolyl radical. As described in Chapter 3, the structure of the β-phase of the pyrazine-bridged radical **5-6** consists of σ-bonded dimers [**5-6**]$_2$ in the solid state.[24] Unlike the derivatives of [**5-2**]$_2$, the σ-bond in [**5-6**]$_2$ involves two sulfur atoms. This compound behaves as a diamagnetic semiconductor similar to the [**5-2a,b,c**]$_2$ compounds reported above, although it displays a lower σ(298 K) value (~ 10^{-7} S cm^{-1}) and does not exhibit the same surge in conductivity with applied pressure. The differences in pressure response in these two compounds can be rationalized in terms of their contrasting crystal structures, which are illustrated in Figure 5.10.

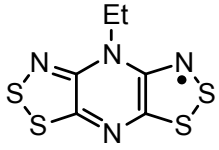

5-6

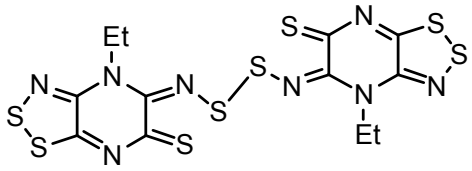

[**5-6**]$_2$

In the structure of [**5-2a**]$_2$, the dimers are arranged so that the ends of each molecule are directed towards the center of a neighbouring dimer, allowing for a series of close S---Se′ and S---S′ intermolecular interactions. By contrast, the structure of [**5-6**]$_2$ consists of dimers oriented in an end-to-end fashion, with no contact near the inner core of the dimers. In addition, the intermolecular contacts that are present, around the periphery of the molecule, involve only sulfur and nitrogen atoms. The higher conductivity observed for [**5-2a**]$_2$ can be attributed to its more compact structure and its complex network of strong chalcogen-chalcogen interactions. The compression of these contacts, and concomitant improvement in bandwidth, allows for the increase in conductivity with applied pressure for this compound.

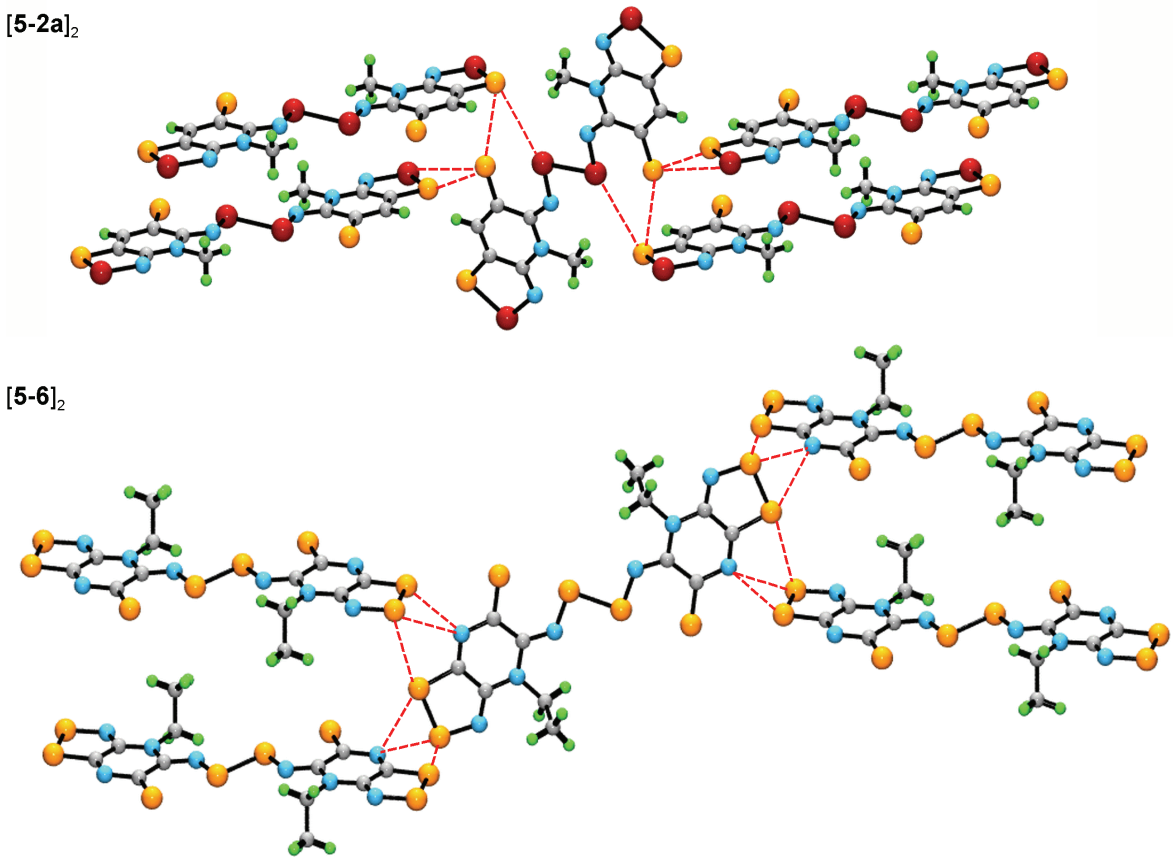

Figure 5.10 Packing arrangements of [**5-2a**]$_2$ (above) and [**5-6**]$_2$ (below).

5.7 Conclusions

In order to improve the bandwidth in the bisdithiazolyl **5-1**, and obtain a neutral radical conductor, we have been incorporating selenium into the framework by developing the derivatives **5-2** to **5-4**. Much to our chagrin, the first selenium-containing radical **5-2** crystalized as σ-bonded dimers in the solid state, with its charge carriers invariably quenched. Yet, even though the σ-dimers were diamagnetic semiconductors, they exhibited dramatic enhancements in conductivity with applied pressure, as conductivity increased by five orders of magnitude and activation energies dropped below 0.05 eV under a pressure of 5 GPa.[5] This incredible response to pressure prompted us to investigate the cause of the

behaviour, and the effects of pressure on the crystal structure. To gain some insight into this structure-property relationship, we have prepared two new σ-bonded dimers that are isomorphous to the compound previously reported, and probed the effects of applied pressure on the transport properties within the series [**5-2a,b,c**]$_2$.

We have found that the application of pressure to samples of [**5-2a,b,c**]$_2$ induces an improvement in the conductive behaviour of all three compounds, although to varying degrees, with [**5-2a**]$_2$ exhibiting the largest response and [**5-2b**]$_2$ displaying the least. Preliminary high pressure crystallography measurements on [**5-2a**]$_2$ suggest that pressurization of the material compresses the crystal structure, shortening the intermolecular contacts while leaving the molecular geometry comparatively unchanged. The variations in pressure response of [**5-2a,b,c**]$_2$ is attributed to the relative compressibility of their crystal structures, the limiting feature of which could be the buffering interactions between neighbouring R groups. The band calculations performed on the early high pressure crystal structures revealed an attenuation of the band gap with increasing pressure, although overlap of the band edges was not reached with an applied pressure of 13 GPa. Full metallization may be possible at only slightly higher pressures, and further experiments on all three compounds [**5-2a,b,c**]$_2$ are ongoing. In time, we hope to observe a transition to a metallic state for these heterocyclic dimers, and reveal the structural changes that accompany it.

5.8 Future Work

In this chapter, the improvement in conductivity displayed by the [**5-2a,b,c**]$_2$ compounds with applied pressure has been ascribed to the closure of the electronic band gap, a conclusion drawn from preliminary, and incomplete, crystal structure determinations. More definitive results may establish this hypothesis with more certainty, and as previously stated, work in this area is in progress. However, there is an alternative theory to consider. The behaviour can also be rationalized in terms of the generation of discrete radicals, and charge carriers, upon dissociation of the dimers under pressure. At a particular pressure, metallic behaviour in a radical-based system may be observed. This hypothesis is difficult to

confirm using pressure crystallography as the structural changes would be small. However, it can be tested using variable pressure, or possibly variable temperature, magnetic susceptibility measurements. If the dimers do uncouple, the experiment would reveal an increase in susceptibility on generation of unpaired spins. These experiments would quickly establish whether or not the increase in conductivity for these dimer systems with pressure is caused by a gradual transition to a radical (and conducting) state, and this avenue should therefore be pursued.

5.9 Experimental Section

Preparation N-methyl-2,4,6-trifluoropyridinium triflate. Methyl triflate (1.80 g, 11.0 mmol) and 2,4,6-trifluoropyridine (1.33 g, 10.0 mmol) were charged into a Schlenk tube and the mixture was stirred and heated in an oil bath at 60 °C. After a few minutes crystals were present, and after 2 hours the mixture was completely solid. The mixture was cooled and 5 mL DCE was added to break up the solid, which was filtered off and washed with 20 mL Et_2O. The crude product, N-methyl-2,4,6-trifluoropyridinium triflate, yield 2.70 g (9.1 mmol, 91%), was used without purification, but for analytical purposes it could be recrystallized from MeCN/DCE, mp 114-117 °C. IR: 3060(m), 1682 (s), 1646 (m), 1604 (s), 1539 (m), 1505 (m), 1265 (s, br), 1226 (m), 1149 (s), 1028 (s), 1012 (m), 889 (s), 874 (s), 758 (m), 713 (m), 638 (s), 574 (m), 517 (s), 459 (m) cm^{-1}. ^1H NMR (CD_3CN): 7.64 (*dd*, 2H, aromatic, J_F = 6.98, 2.13 Hz), 4.01 (*t*, 3H, methyl, J_F = 2.78 Hz). Anal. Calcd for $C_7H_5F_6NO_3S$: C, 28.29; H, 1.70; N, 4.71%. Found: C, 28.28; H, 1.75; N, 4.75%.

Preparation of N-methyl-2,6-diamino-4-fluoropyridinium triflate [5-5c][OTf]. Anhydrous ammonia was passed over a stirred solution of N-methyl-2,4,6-trifluoropyridinium triflate (4.49 g, 15.1 mmol) in 50 mL dry MeCN held at 0 °C in an ice bath. After 10 min, the ammonia flow was ceased and the ice bath removed. The solution warmed (heat of reaction) to about 40°C, turned very slightly yellow, and a gelatinous white precipitate of NH_4F formed. After 30 min the mixture was boiled briefly to expel excess ammonia, cooled to room temperature and the white ppt was filtered off. Evaporation of the solvent from

the filtrate afforded a sticky solid that was recrystallized from MeCN/DCE (1:10) to give white flakes of [**5-5c**][OTf] which were collected by filtration. Yield 3.47 g (11.9 mmol, 79%), mp 126-130 °C. IR: 3428 (m), 3359 (m), 3242 (m), 1686 (m), 1649 (m), 1593 (m), 1518 (w), 1331 (w), 1277 (s), 1225 (s), 1162 (s), 1027 (s), 809 (m), 706 (m), 722 (m), 634 (s), 575 (w), 518 (m), 456 (m) cm^{-1}. ^1H NMR (CD_3CN): 6.35 (*s*, 2H, amine), 6.00 (*d*, 1H, aromatic, J_F = 9.56 Hz), 3.40 (*s*, 3H, methyl). Anal. Calcd for $C_7H_9F_4N_3O_3S$: C, 28.87; H, 3.11; N, 14.43 %. Found: C, 28.69; H, 3.22; N, 14.17%.

Preparation of 8-Fluoro-4-methyl-4H-bis[1,2,3]dithiazolo[4,5-b:5',4'-e]pyridin-2-ium Triflate [5-1c][OTf]. A solution of S_2Cl_2 (2.16 g, 16.0 mmol) in 5 mL MeCN was added dropwise to a solution of [**5-5c**][OTf] (1.16 g, 4.00 mmol) in 10 mL MeCN, and the mixture heated to a gentle reflux under an atmosphere of nitrogen. After 1.5 h the mixture was cooled to room temperature and the light brown microcrystalline precipitate of crude [**5-1c**][OTf] (0.68 g, 1.65 mmol, 41 %) filtered off, washed with 3 × 20 mL hot DCE, and dried in vacuo. Recrystallization from MeCN afforded deep red plates, dec. > 295 °C. IR: 1510 (s), 1352 (m), 1280 (m), 1238 (s), 1174 (m), 1161 (w), 1125 (m), 1059 (w), 1027 (s), 937 (w), 868 (m), 791 (s), 713 (m), 678 (s), 654 (w), 638 (m), 557 (w), 559 (w),516 (m), 500 (w), 479 (s), 472 (s) cm^{-1}. Anal. Calcd for $C_7H_3F_4N_3O_3S_5$: C, 20.34; H, 0.73; N, 10.16%. Found: C, 20.60; H, 0.85; N, 10.11%.

Preparation of 4-Methyl-4H-bis[1,2,3]thiaselenazolo[4,5-b:5',4'-e]pyridin-2-ium Triflate [5-2a][OTf]. Finely ground selenium dioxide (0.450g, 4.06 mmol) was added to a solution of [**5-1a**][OTf] (0.398g, 1.01 mmol) dissolved in 100 mL HOAc and the reaction mixture was set to reflux for 4 h, at which time the heat was removed and the solution allowed to cool slowly. After 16 h, the resulting red crystalline solid was filtered and washed with DCM, crude yield; 0.434g (0.887 mmol, 89 %). The crude material was recrystallized twice from HOAc to afford [**5-2a**][OTf] as red flakes. The product was identified by comparison to the IR spectrum of a known sample, previously reported.[5]

Preparation of 8-Methyl-4-methyl-4H-bis[1,2,3]thiaselenazolo[4,5-b:5',4'-e]pyridin-2-ium Triflate [5-2b][OTf]. Finely ground selenium dioxide (0.670 g, 6.04 mmol) was added to a solution of [**5-1b**][OTf] (0.820 g, 2.00 mmol) dissolved in 140 mL HOAc, and the reaction mixture was set to reflux for 7 h. At this time the heat was removed and the solution slowly cooled. After 16 h, the golden brown powder was filtered and rinsed with DCM, crude yield; 0.842 g (1.67 mmol, 84 %). Recrystallization from MeCN provided golden flakes, dec. > 260 °C. IR: 1407 (m), 1359 (s), 1267 (s), 1239 (s), 1164 (s), 1030 (s), 1009 (m), 777 (w), 723 (s), 641 (s), 594 (s), 540 (m), 517 (m), 481 (m) cm^{-1}. Anal. Calcd for $C_8H_6F_3N_3O_3S_3Se_2$: C, 19.09; H, 1.20; N, 8.35%. Found: C, 18.99; H, 1.11; N, 8.26%.

Preparation of 8-Fluoro-4-methyl-4H-bis[1,2,3]thiaselenazolo[4,5-b:5',4'-e]pyridin-2-ium Triflate [5-2c][OTf]. Compound [**5-1c**][OTf] (0.830 g, 2.01 mmol) and finely ground selenium dioxide (0.670 g, 6.04 mmol) were combined in a large glass pressure vessel along with 80 mL MeCN, and the mixture was stirred in an oil bath at 110 °C for 72 h. After cooling slightly, the warm slurry was filtered through a glass Büchner funnel to remove a small amount of black powder, and the filtrate was concentrated to 30 mL and allowed to stand for 16 h. The resulting red solid was collected by filtration and rinsed with DCM, crude yield; 0.542 g (1.07 mmol, 54 %). The crude material was recrystallized from MeCN to afford red needles, dec. > 265 °C. IR: 1501 (s), 1350 (m), 1283 (s), 1225 (s), 1175 (m), 1113 (m), 1050 (w), 1004 (s), 854 (w), 773 (s), 716 (m), 637 (s), 596 (s), 515 (m), 494 (w), 477 (w) cm^{-1}. Anal. Calcd for $C_7H_3F_4N_3O_3S_3Se_2$: C, 16.58; H, 0.60; N, 8.28%. Found: C, 16.76; H, 0.57; N, 8.31%.

Preparation of Dimers [5-2a,b,c]$_2$. Degassed solutions (3 freeze-pump-thaw cycles) of [**5-2a,b, c**][OTf] (0.596 - 0.690 mmol) in 210 - 225 mL MeCN and OMFc (0.657 - 0.758 mmol) in 108 - 125 mL MeCN were combined and after 30 min the gold-brown microcrystalline precipitate of [**5-2a,b,c**]$_2$ was filtered off, washed 5 × 30 mL MeCN and dried in vacuo. Analytical data: [**5-2a**]$_2$. Identified by comparison to the IR spectrum of a known sample, previously reported.[5] [**5-2b**]$_2$. IR: 1505 (s), 1382 (m), 1342 (s), 1306 (s), 1174 (w), 1062 (w), 1008 (s), 842 (m), 715 (s), 608 (m), 568 (s), 522 (m), 464 (w) cm^{-1}. Anal. Calcd for $C_7H_6N_3S_2Se_2$: C, 23.74; H, 1.71; N, 11.86%. Found: C, 24.00; H, 1.90; N, 11.83%. [**5-2c**]$_2$. IR: 1522 (s),

1488 (m), 1438 (s), 1360 (m), 1304 (s), 1200 (w), 1176 (m), 1093 (m), 1036 (m), 853 (s), 765 (s), 712 (w), 610 (s), 564 (s) cm^{-1}. Anal. Calcd for $C_6H_3FN_3S_2Se_2$: C, 20.12; H, 0.84; N, 11.73;%. Found: C, 20.37; H, 0.93; N, 11.81%.

Chapter 6

A Non-Isomorphous Set of S/Se Radicals:

The R_1 = Me, R_2 = Cl Family

6.1 Introduction

In our pursuit of neutral radical conductors we have developed the resonance stabilized bisdithiazolyl radicals **6-1**. These systems show major improvements over monofunctional dithiazolyls with respect to stability and energetic behaviour.[1,2,3] In order to improve the bandwidth *W* of these materials, we developed the series of selenium-containing radicals **6-2** to **6-4**. With the improved bandwidth afforded by the larger and more polarizable selenium atom, higher conductivity values are expected for these new systems. However, as described in Chapter 5, compounds of type **6-2**, with selenium in the 2-position of the molecular framework, are particularly vulnerable to σ-dimerization, which gives rise to materials displaying diamagnetic semiconducting ground states.[4] This problem notwithstanding, we have been able to obtain all four variations and avoid σ-dimerization with particular combinations of R_1 and R_2 substituents.

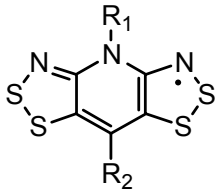

6-1

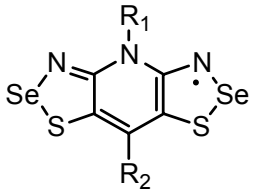

6-2

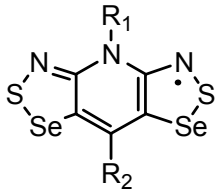

6-3

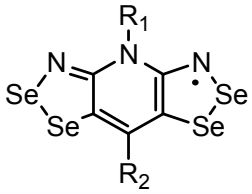

6-4

The sequential incorporation of selenium into **6-1**, and the generation of an entire family of radicals **6-1** to **6-4**, was pursued in hopes of achieving an isomorphous replacement of sulfur by selenium, as

depicted in Figure 6.1. With all four compounds having the same crystal structure, the effect of improved *W* on the transport properties could be directly observed. Several derivatives of **6-1** to **6-4** have been developed, and a selection of these is listed in Table 6.1, along with their respective space groups. We have found that, when σ-dimerization could be avoided, isomorphous mapping is possible, with families of radicals having the same packing motif. From this work we have been able to demonstrate that the presence of selenium has the desired effect, as conductivity values have improved and activation energies have diminished with an increase in selenium content.[5] Although metallic behaviour has yet to be achieved, the room temperature conductivity values have increased by 2-3 orders of magnitude by replacing sulfur for selenium, reaching σ_{RT} values of 10^{-4} S cm^{-1}.[6]

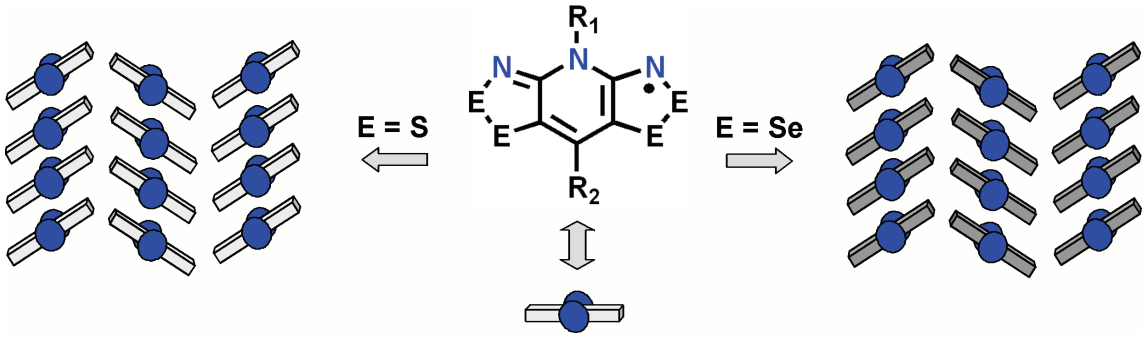

Figure 6.1 A representation of the isomorphous replacement of sulfur by selenium in bisdithiazolyls.

Table 6.1 Space Groups for a Selection of Characterized Radicals **6-1** to **6-4**

R_1, R_2	**6-1**	**6-2**	**6-3**	**6-4**
Et, H	$P2_1/c$[a]	σ-dimers[b]	$P2_1/c$[c]	$P2_1/c$[c]
Me, H	$P2_12_12_1$[a]	σ-dimers[b]	$P2_12_12_1$[d]	$P2_12_12_1$[d]
Et, Cl	$P\bar{4}2_1m$[e]	$P\bar{4}2_1m$[f]	$P\bar{4}2_1m$[f]	$P\bar{4}2_1m$[f]
Me, Cl	$P2_12_12_1$[e]	?	?	?

[a] Reference 2. [b] Reference 4. [c] Reference 7. [d] Reference 5. [e] Reference 1. [f] Reference 6.

Also emerging from the development of these selenazyl radicals were interesting magnetic properties. Compounds **6-3** (R_1 = Et; R_2 = H, Cl) and **6-4** (R_1 = Et, R_2 = H) for example, exhibit spin-canted antiferromagnetism with ordering temperatures T_N of 18, 14 and 27 K, respectively.[6,7] Other radicals, specifically **6-2** and **6-4** (R_1 = Et, R_2 = Cl) display ferromagnetic ordering,[6,8] with transition temperatures and coercivities that reach, or even surpass, those of the leading non-metal containing ferromagnets reported to date.[9] We attribute these new magnetic properties to a spin-orbit effect and consequent magnetic anisotropy associated with the heavy selenium atom within the framework.

As the incorporation of selenium into **6-1** has lead to enhancements in both the conductive and magnetic behaviour, other derivatives of **6-2** to **6-4** have been explored, including the family of radicals **6-1** to **6-4** (R_1 = Me, R_2 = Cl), hereafter referred to as **6-1a** to **6-4a**. The synthesis and characterization of the all-sulfur radical **6-1a** was reported some time ago,[1] and we wanted to observe any changes in its behaviour resulting from the presence of the heavy congener. Since isostructural mapping seemed to be straightforward for these types of compounds (Table 6.1), we expected the R_1 = Me, R_2 = Cl series to follow suit, with the three new radicals (**6-2a** to **6-4a**) crystallizing in the same arrangement as that of **6-1a**, with space group $P2_12_12_1$. Instead, the four compounds split into two groups, each having a different crystal structure and displaying considerably different transport properties. With this family of radicals we had the unique opportunity to not only examine the effects of the presence and position of selenium on the transport properties, but also the influence of the packing arrangement.

This chapter encompasses the work done on the **6-1a** to **6-4a** compounds, including synthesis, crystallography and transport property measurements. None of the radicals dimerize in the solid state, but instead form slipped π-stacks of discrete radicals. Compounds **6-1a** and **6-3a** form an isomorphous pair, having the orthorhombic space group $P2_12_12_1$, where **6-2a** and **6-4a**, themselves an isomorphous set, crystallize in the monoclinic space group $P2_1/n$. As a result of the differing packing arrangements, there is a substantial difference in the electronic behaviour of the two groups, with the monoclinic pair exhibiting higher conductivity values and stronger magnetic exchange interactions than their orthorhombic

counterparts. A computational investigation into the solid state packing requirements, that is, the degree and direction of plate slippage along the π-stacks, necessary for high conductivity and strong magnetic exchange in these types of radicals is described. This study involves both Extended Hückel Theory (EHT) band structure calculations and Density Functional Theory (DFT) broken symmetry methods to probe the exchange interactions within a series of model 1D π-stacks. The work described here has been published.[10]

6.2 Synthesis

A summary of the preparative sequences used to generate the cations [**6-1a**]$^+$ to [**6-4a**]$^+$ is illustrated in Scheme 1. The all-sulfur framework, [**6-1a**][OTf], was prepared by the reaction of N-methyl diaminopyridinium triflate [**6-5**][OTf] with sulfur monochloride (Scheme 1a), as previously reported.[1] For [**6-2a**][OTf], with selenium in the 2-position, the desired skeleton was achieved by the double insertion of selenium into [**6-1a**][OTf] by reaction with SeO_2 as shown in Scheme 1b. Complete regiospecificity could be obtained by performing the reaction in acetonitrile in a pressure vessel at 110 °C. The preparation of [**6-3a**][OTf], with selenium in the 1-position, followed the procedure used for the synthesis of the related compound [**6-3**][OTf] (R_1 = Et, R_2 = Cl),[6] and is outlined in Scheme 1c. The zwitterion **6-6** was first alklyated with methyl triflate to form [**6-3**][OTf] (R_1 = Me, R_2 = H), which was then chlorinated with iodobenzene dichloride to give [**6-3a**][OTf]. To prepare [**6-4a**]$^+$ it was necessary to change the anion to nonaflate (nonafluorobutanesulfonate, ONf^-) in order to obtain a more workable (soluble) salt. Therefore, as shown in Scheme 1d, [**6-3a**][OTf] was first converted to [**6-3a**][ONf] by reaction with bromide ion, followed by treatment of the subsequent bromide salt with silver nonaflate. Heating this compound with SeO_2 in acetonitrile gave the all-selenium salt [**6-4a**][ONf]. The full synthetic details of the preparation of these salts, as well as their reductions to the desired radicals, are described in Chapter 4.

Scheme 1

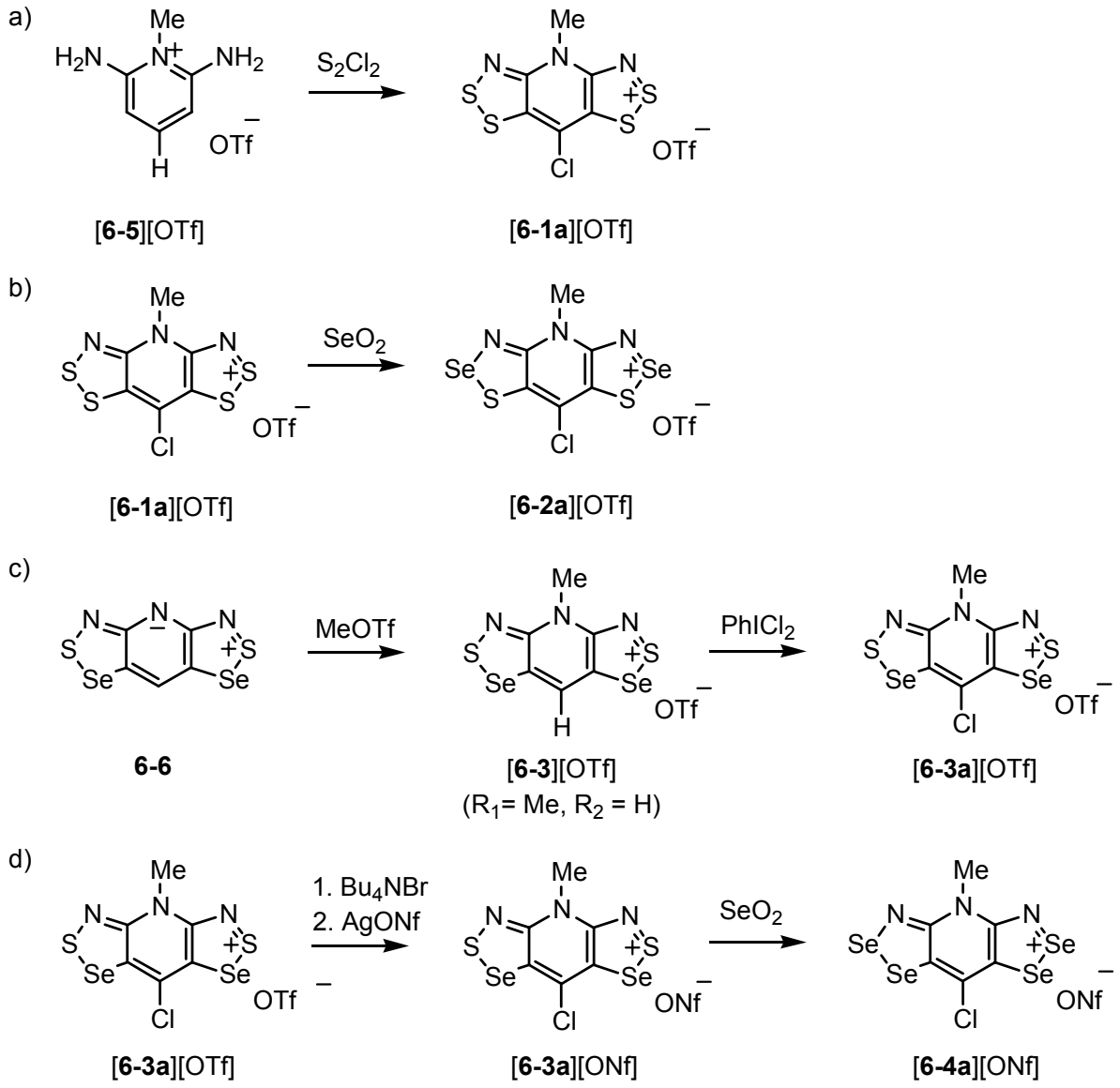

The purified salts [**6-2a**][OTf], [**6-3a**][OTf] and [**6-4a**][ONf] were reduced to afford the desired radicals. The choice of reductant was dictated in part by the reduction potentials of the cations, estimated from the known values of the N-Et series,[6] and partly by concerns about potential contamination of the resulting radicals by paramagnetic by-products, specifically ferrocinium salts. Therefore, the microcrystalline material used for bulk measurements of **6-2a** and **6-3a** was obtained by reaction with

TMPDA (*N,N,N′,N′*-tetramethyl-*p*-phenylenediamine), where HMFc (hexamethylferrocene) was used for single crystal growth.

The generation of **6-4a** however was not so straightforward, as all chemical reductions of [**6-4a**][ONf] afforded mixtures of at least two phases. A range of reducing agents were employed, including TDAE (tetrakisdimethylaminoethylene), OMFc (octamethylferrocene), and TMPDA, with all producing material consisting of multiple phases, in varying amounts. The polymorphism exhibited by **6-4a** was observed in both the powder diffraction pattern and the infrared spectrum of bulk samples. Fortunately, a single phase could be obtained by the electroreduction of [**6-4a**][ONf], which afforded crystals of what is termed the "α-phase", exclusively. A simulated powder diffraction pattern taken from the single crystal data of the α-phase of **6-4a** produced electrochemically is shown in Figure 6.2, along with the powder patterns of samples generated through bulk chemical reductions. It is evident from the large number of overlapping peaks in the low angle region that the material produced by chemical methods consists of multiple phases, including the α-phase. Likewise, infrared analysis of bulk samples of **6-4a** could assess the phase purity, as illustrated in Figure 6.3. The plot shows the fingerprint region of pure-phase material (the α-phase) grown by electrocrystallization (A), along with that of a sample obtained by chemical reduction with TMPDA (B). Although the latter material consists almost entirely of a different, unidentified phase, the powder pattern (Figure 6.2) reveals the presence of the α-phase. By electrochemical methods, only 5-10 mg of phase-pure **6-4a** could be produced in a 48 h period, although repeated experiments could generate enough material for bulk measurements and structural work. Material used for bulk property measurements was closely monitored for phase purity by infrared analysis.

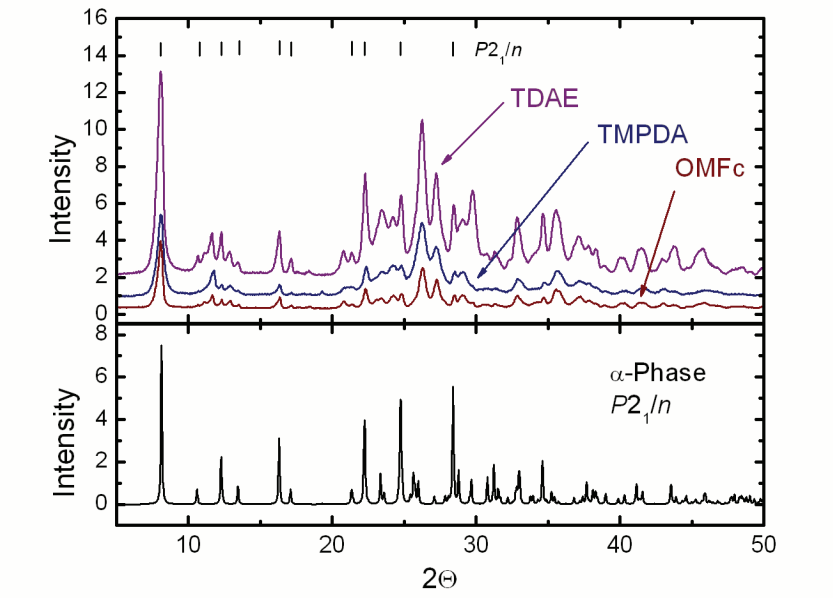

Figure 6.2 Powder diffraction patterns of **6-4a** prepared with a variety of reducing agents. The bottom plot is a simulated pattern of the α-phase in the $P2_1/n$ space group obtained from single crystal data.

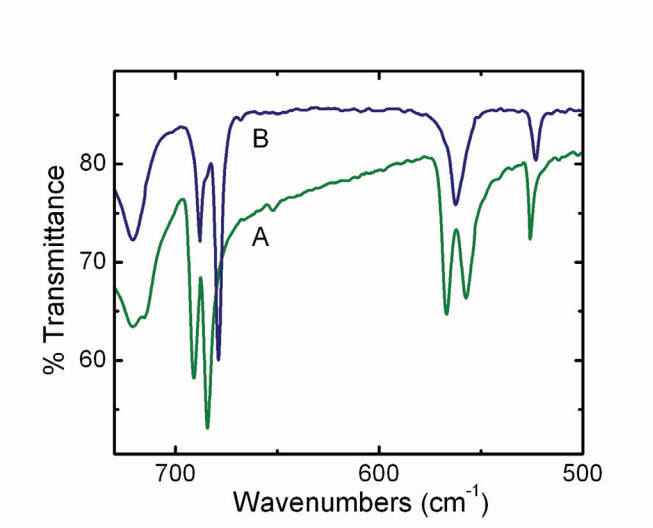

Figure 6.3 Infrared spectra of **6-4a** generated electrochemically (A) and by reduction with TMPDA (B).

Through single crystal X-ray crystallography, we found that radical **6-2a** was isostructural to the α-phase of **6-4a**, as both crystallized in the monoclinic space group $P2_1/n$. We were concerned that the polymorphism found for compound **6-4a** could also be present in **6-2a**, and we therefore analyzed the bulk microcrystalline material of **6-2a** by both powder diffraction and infrared measurements. Fortunately, we did not find any indication of multiple phases for this compound, and large quantities could be generated by bulk chemical reductions.

6.3 Crystal Structures

The crystal structure of the all-sulfur compound **6-1a** was reported previously,[1] and consisted of slipped π-stacks of undimerized radicals arranged in the orthorhombic space group $P2_12_12_1$. As accomplished for other R_1/R_2 series of radicals **6-1** to **6-4**, we wanted to achieve an isomorphous replacement of sulfur by selenium and obtain a complete set of four radicals, all crystallizing in the $P2_12_12_1$ space group as exhibited by **6-1a**. When selenium was situated in the 1-position, as for compound **6-3a**, the space group and packing arrangement were preserved, as radical **6-3a** crystallized in the $P2_12_12_1$ space group. However, when selenium occupied the 2-position, as in compounds **6-2a** and **6-4a**, a very different orientation was found. These radicals crystallized in the monoclinic space group $P2_1/n$ to form another isomorphous pair, which, like the orthorhombic set, consisted of slipped π-stacks of discrete radicals. All four systems showed no indication of formal dimerization in either a σ- or π-mode, a feature that had only been achieved once before.[6] ORTEP drawings of the four radicals are illustrated in Figure 6.4 and the crystallographic data is listed in Table 6.2.

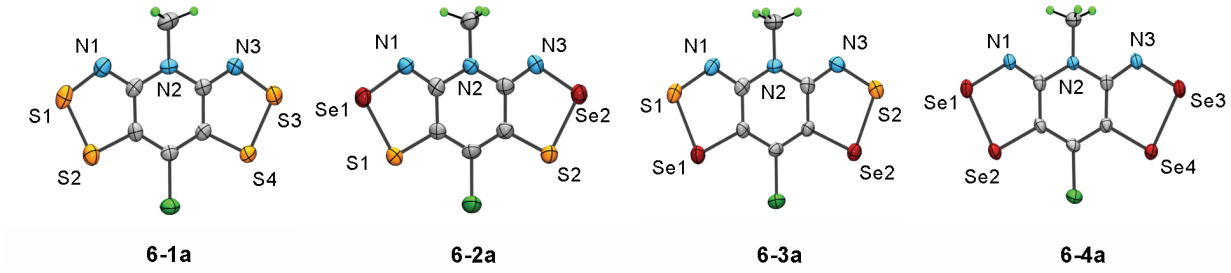

Figure 6.4 ORTEP drawings (50% thermal ellipsoids) of radicals **6-1a** to **6-4a**, with atom numbering.

Table 6.2 Crystallographic Data

Radical	**6-1a** [a]	**6-2a**	**6-3a**	**6-4a**
Formula	$C_6H_3ClN_3S_4$	$C_6H_3ClN_3S_2Se_2$	$C_6H_3ClN_3S_2Se_2$	$C_6H_3ClN_3Se_4$
M, g mol^{-1}	280.80	374.60	374.60	468.40
a, Å	4.2464(12)	4.1566(4)	4.1932(2)	4.1978(2)
b, Å	15.194(5)	14.0039(12)	15.1413(8)	14.3180(8)
c, Å	15.069(4)	16.4888(15)	16.1531(8)	16.7655(9)
β, deg	90	94.338(6)	90	96.2200(10)
V, Å^3	972.2(5)	957.04(15)	1025.57(9)	1001.74(9)
ρ_{calcd}, g cm^{-1}	1.918	2.600	2.426	3.106
space group	$P2_12_12_1$	$P2_1/n$	$P2_12_12_1$	$P2_1/n$
Z	4	4	4	4
temp, K	293(2)	295(2)	295(2)	296(2)
μ, mm^{-1}	1.208	15.983	7.836	14.873
λ, Å	0.7107	1.54178	0.71073	0.71073
θ_{full}, deg	26.01	67.49	29.13	26.37
data/restr./parameters	1915/0/128	1661/0/127	2760/0/127	2050/0/128
solution method	direct methods	direct methods	direct methods	direct methods
R, R_w (on F^2)	0.0314, 0.0544	0.0442, 0.1035	0.0268, 0.0499	0.0235, 0.0521

[a] From reference 1.

Selected intra- and intermolecular contacts are listed in Table 6.3 for **6-1a** and **6-3a**, and in Table 6.4 for **6-2a** and **6-4a**. Slippage along the π-stacks is defined in terms of τ, the angle of inclination between the mean molecular plane of the radical (excluding ligands) and the stacking axis, whereas δ is the mean plate-to-plate separation along the π-stacks. All four radicals are essentially planar with deviations from the mean plane being less than 0.05 Å in all cases. The distance between radicals along the stacks, δ, increases with selenium content as one might expect, although there is a larger plate separation when selenium is placed in the 2-position (as for **6-2a**) then when it occupies the 1-site (as for **6-3a**).

Table 6.3 Selected Metrics for **6-1a** and **6-3a**

Radical	**6-1a** [a] (E_1 = S)	**6-3a** (E_1 = Se)
N - S (Å)	1.657(3), 1.664(3)	1.652(3), 1.660(3)
S - E_1 (Å)	2.0981(15), 2.1046(15)	2.2381(9), 2.2462(9)
E_1 - C (Å)	1.727(4), 1.735(4)	1.860(3), 1.883(3)
C - C (Å)	1.437(5), 1.438(5)	1.427(4), 1.440(4)
C - N (Å)	1.300(5), 1.305(4)	1.311(4), 1.312(4)
d1 (Å)	3.541(2)	3.424(1)
d2 (Å)	3.324(2)	3.430(1)
d3 (Å)	3.369(2)	3.473(1)
d4 (Å)	3.546(2)	3.572(1)
d5 (Å)	3.861(2)	3.698(1)
δ (Å)	3.470(5)	3.500(1)
τ (deg)	54.81(13)	56.59(1)
deviation from plane (Å)	0.0252	0.0373

[a] From reference 1.

Table 6.4 Selected Metrics for **6-2a** and **6-4a**

Radical	**6-2a** (E_1 = S)	**6-4a** (E_1 = Se)
N - Se (Å)	1.839(6), 1.822(6)	1.826(3), 1.816(3)
Se - E_1 (Å)	2.241(2), 2.250(2)	2.3591(5), 2.3646(5)
E_1 - C (Å)	1.736(7), 1.743(7)	1.877(3), 1.874(3)
C - C (Å)	1.441(9), 1.454(9)	1.434(4), 1.438(4)
C - N (Å)	1.294(9), 1.298(8)	1.305(4), 1.311(4)
r1 (Å)	3.273(1)	3.313(1)
r2 (Å)	3.390(1)	3.449(1)
r3 (Å)	3.525(4)	3.509(1)
r4 (Å)	3.677(1)	3.700(1)
r5 (Å)	3.687(2)	3.746(1)
δ (Å)	3.517(1)	3.568(1)
τ (deg)	57.79(3)	58.22(1)
deviation from plane (Å)	0.0463	0.0445

Radicals **6-1a** and **6-3a**, which have sulfur in the 2-position, form the orthorhombic pair that crystallize in the $P2_12_12_1$ space group. A representative view of the unit cell and packing arrangement of **6-3a** is shown in Figure 6.5. The structure consists of slipped π-stacks that are connected by a complex network of close S/Se contacts d1 - d5, which are listed in Table 6.3, and are well within the expected van der Waals separation[11] for the appropriate combination of S and Se centers. Four columns are grouped around a 2-fold screw axis, with a pair linked by d3 and d4 contacts that zig zag down the stacking direction (Figure 6.5B). The remaining two radicals of the grouping are connected to the others *via* d1, d2 and d5 contacts, interactions that weave columns together along the *yz* plane. The π-stacks are tilted in such a way as to give a rippled appearance along the *yz* plane, and to distort a single layer of four radicals into a dome shape, as illustrated in Figure 6.6.

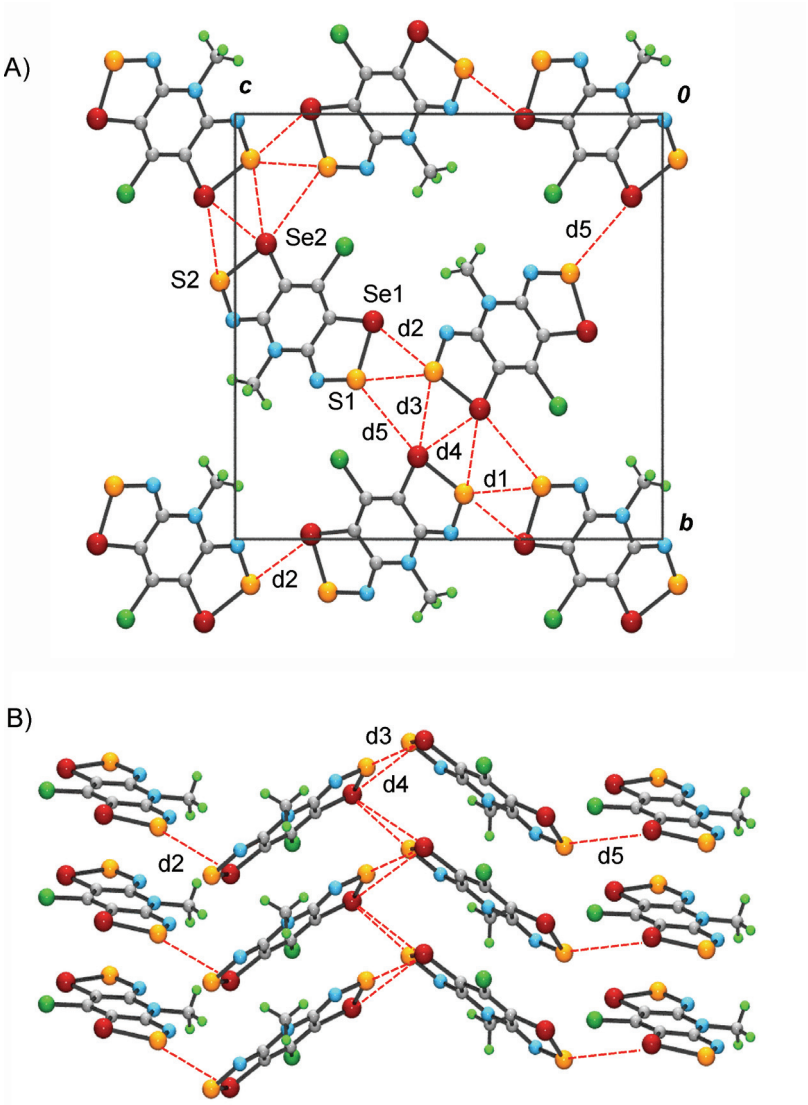

Figure 6.5 Unit cell drawing of **6-3a** viewed along *x* (A), as well as the slipped π-stack structure viewed perpendicular to *x* (B), with intermolecular contacts d1 - d5.

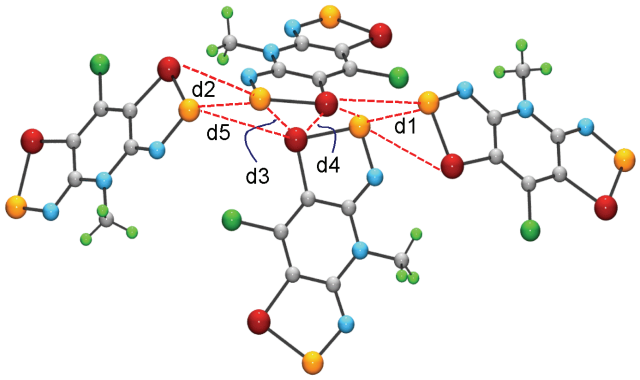

Figure 6.6 A layer of four radicals of **6-3a** tilted away from *x*, showing the dome shape.

By comparison, radicals **6-2a** and **6-4a** form the monoclinic set that arrange in the $P2_1/n$ space group. A representative view of the unit cell and packing arrangement of **6-2a** is illustrated in Figure 6.7. These compounds have selenium in the 2-position, and the radicals pack together so as to maximize the number and strength of close Se---Se′ interactions. Groups of four radicals cluster about an inversion center and are linked by the r1 - r4 contacts, which are listed in Table 6.4. The pair of molecules that are connected *via* r3 are coplanar, where the remaining pair, which are parallel but not coplanar, are twisted as shown in Figure 6.8. The structure consists of interpenetrating π-stacks (Figure 6.7B), with a degree of plate slippage (τ) that allows for a single close intracolumnar contact r5. This interaction is between a selenium atom on one molecule and a sulfur (**6-2a**) or selenium (**6-4a**) atom on a neighbouring molecule, the two atoms being almost directly aligned. This feature is exclusive to the monoclinic pair of radicals **6-2a** and **6-4a**, and its influence on the conductive and magnetic properties of these two compounds is evaluated below.

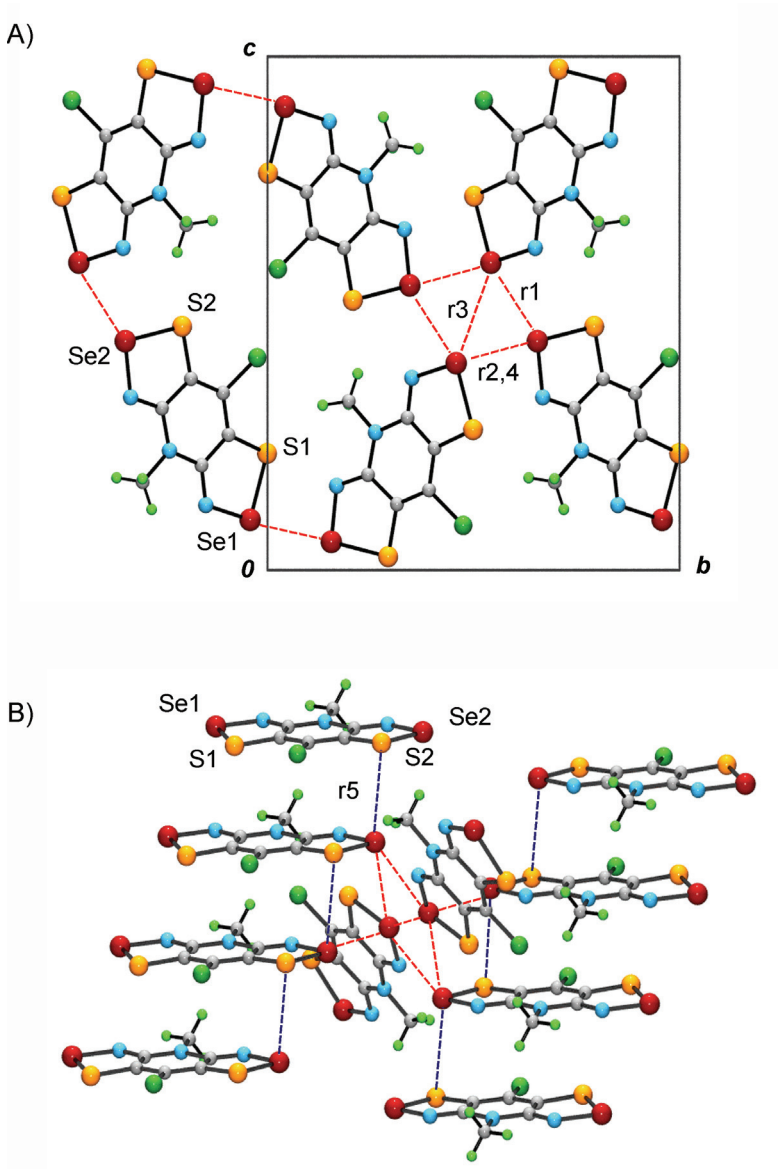

Figure 6.7 Unit cell drawing of **6-2a** viewed down *x*, showing close intermolecular contacts r1 - r4 (A), along with the interpenetrating slipped π-stacks, with plate-to-plate interaction r5 (B).

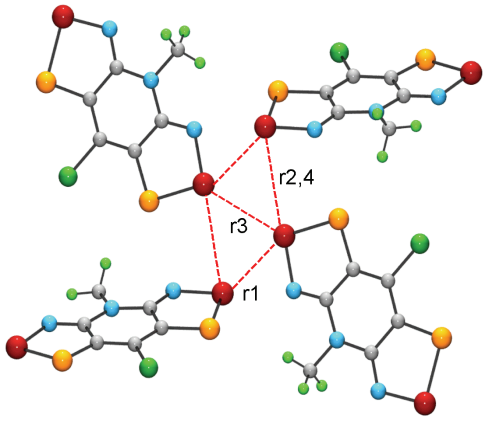

Figure 6.8 A layer of four radicals of **6-2a** tilted away from *x*, showing the twisted nature of the stacks.

6.4 Electronic Band Structures

In order to explore the electronic structures of radicals **6-1a** to **6-4a**, we have carried out a series of EHT band structure calculations using their crystallographic coordinates, at both 1D and 3D levels. The results must be viewed with caution, as the tight-binding approximation is unable to provide a proper description of the ground state of strongly correlated systems such as these. Nonetheless, the method does, within a series of closely related compounds, provide qualitative insight into the nature and extent of orbital interactions both within and between radical π-stacks across the series. The results are presented as dispersion curves of the crystal orbitals (COs) that arise from interactions between singly occupied molecular orbitals (SOMOs). The SOMOs of the four radicals **6-1a** to **6-4a** were presented in Chapter 4, which demonstrated that they are essentially identical across the series, regardless of the S/Se combination or the nature of the R_1 and R_2 groups. A representative view of the SOMO is shown in Figure 6.9, which illustrates its antibonding character and a_2 symmetry. As it is difficult to predict how the SOMOs overlap with one another in the crystal structures, the band diagrams provide some description of the interactions along the slipped π-stacks.

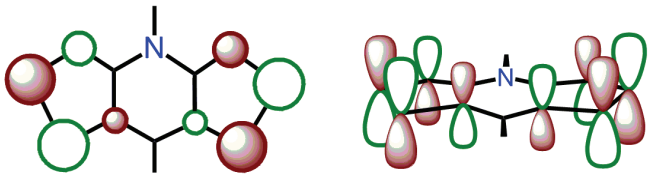

Figure 6.9 A representative SOMO of radicals **6-1a** to **6-4a**.

The results of both the 1D and 3D band calculations are presented as dispersion plots in Figure 6.10. When the calculations are limited to a single stack, only one CO is observed corresponding to the radical SOMO. When extended to three dimensions, four COs are present, arising from the four radical SOMOs in the respective unit cells. The plots are tracked along the direction in reciprocal space that can be associated precisely (for $P2_12_12_1$) and approximately (for $P2_1/n$) with orbital interactions along the stacking axis in real space. The bandwidth W, is expressed in terms of the dispersion $\Delta E_k = [E(k = \pi/a) - E(k = 0)]$, or energetic spread, of the crystal orbitals, where $W = |\Delta E_k|$.

It is readily apparent from Figure 6.10 that there is a large difference in band structure with respect to the space group, and the results of the 1D and 3D structures give essentially the same conclusions. For **6-1a**/**6-3a,** space group $P2_12_12_1$, the energy goes down with increasing k-vector, that is, the slope dE/dk is negative and $\Delta E_k < 0$. On the other hand, for **6-2a**/**6-4a** with space group $P2_1/n$, the energy goes up with increasing k-vector and dE/dk is positive. For these compounds, $\Delta E_k > 0$. While a rigorous explanation of these trends is not possible, the differences can be understood with a closer look at the plate slippage in each of the different space groups, as shown in Figure 6.11. For the $P2_12_12_1$ group, radicals slip laterally along the long axis of the molecule (or x direction), whereas radicals in the $P2_1/n$ group slip diagonally, so that radicals not only slip along the long axis of the molecule, but also along the short axis (y axis).[‡] This gives rise to very different interactions between the SOMOs of neighbouring radicals along the π-stacks.

[‡] The x and y directions are arbitrarily set with respect to the stacking direction and are not related to the crystallographic axes.

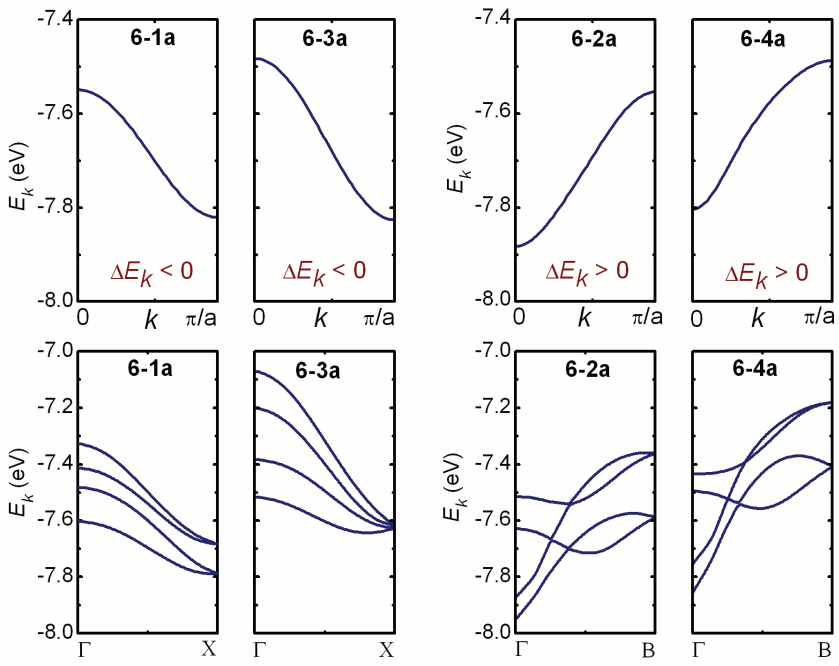

Figure 6.10 The 1D (above) and 3D (below) dispersion curves for **6-1a**/**6-3a** ($P2_12_12_1$) and **6-2a**/**6-4a** ($P2_1/n$).

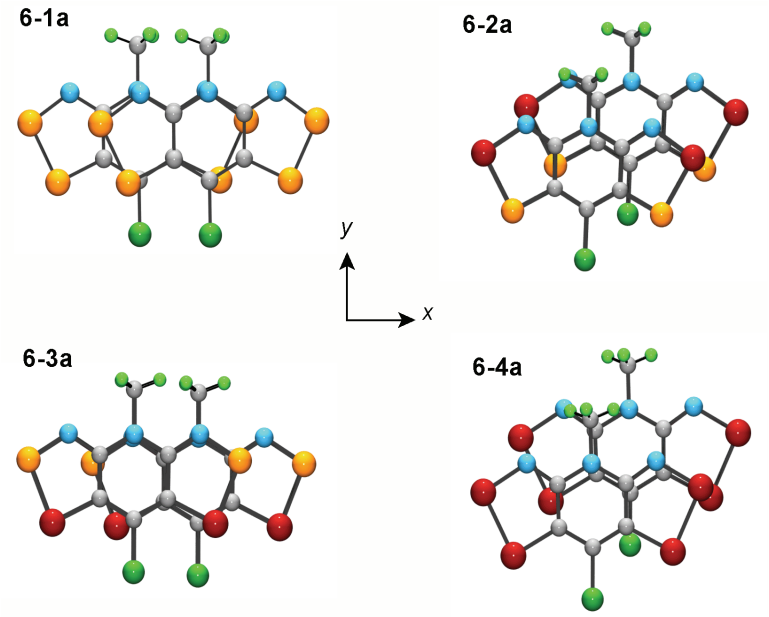

Figure 6.11 Plate slippage in **6-1a**/**6-3a** ($P2_12_12_1$) and **6-2a**/**6-4a** ($P2_1/n$) viewed from above.

Based on the behaviour of the dispersion curves in Figure 6.10 (and the sign of ΔE_k), the orbital overlap S at $k = 0$ for **6-1a**/**6-3a** is negative and antibonding in nature ($\Delta E_k < 0$), where for **6-2a**/**6-4a** S (*at* $k = 0$) is positive and the net interaction has bonding characteristics ($\Delta E_k > 0$). The latter case can be rationalized in terms of the short intermolecular contact r5 found in the $P2_1/n$ structure (Figure 6.6), and the bonding interaction that would arise between the pπ-orbitals of the nearly aligned S/Se (for **6-2a**) or Se/Se (for **6-4a**) atoms of neighbouring radicals along the π-stacks, as shown in Figure 6.12.

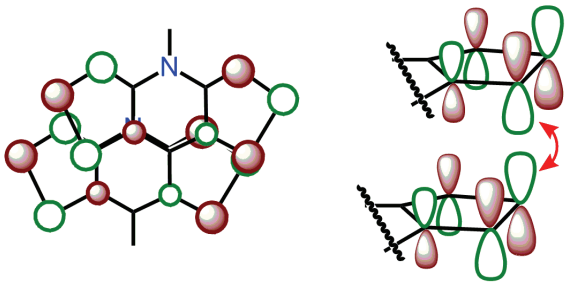

Figure 6.12 An illustration of the pπ-pπ orbital overlap between radical SOMOs of **6-2a** and **6-4a**.

Comparison of the 1D and 3D band structures in Figure 6.10, reveals that the overall dispersion, or energetic spread, of the COs in three dimensions relies heavily on lateral interactions. Not only are the 1D dispersion energies, which are associated exclusively with interactions along the π-stacks, smaller and relatively constant across the series, there is a strong divergence between the bands in the 3D structures. This feature reflects the extensive networks of close intermolecular interactions in the crystal structures of these four compounds. With respect to the 3D plots, there is a gradual increase in overall bandwidth W (or $|\Delta E_k|$) from **6-1a** to **6-4a**, as shown in Table 6.5. Within the mixed S/Se radicals **6-2a** and **6-3a**, the placement of the selenium atom and packing arrangement appears to have little affect on overall bandwidth as W is calculated to be about the same for these two compounds.

Table 6.5 Bandwidth, Conductivity and Magnetic Parameters

Radical	**6-1a**	**6-2a**	**6-3a**	**6-4a**
3D W (eV)[a]	0.46	0.58	0.59	0.68
σ(298 K) (S cm^{-1})[b]	5.3 ×10^{-6} [c]	2.1 × 10^{-3}	3.5 ×10^{-5}	4.3 × 10^{-3}
E_{act} (eV)[b]	0.395 [c]	0.20	0.30	0.17
C (emu K mol^{-1})	0.357 [c]	---	0.378	---
θ (K)	−13 [c]	---	−28	---
J (cm^{-1}) [d]	---	−101	---	−64
zJ (cm^{-1}) [d]	---	−17	---	−49

[a] $W = |\Delta E_k|$. [b] Data from ambient pressure measurements. [c] Data from reference 1. [d] From a fit to the Bonner-Fisher 1D S = ½ chain model.

6.5 Conductivity Measurements

The conductive properties of the three new selenium-containing radicals **6-2a** to **6-4a** have been measured by means of 4-probe variable temperature conductivity measurements on pressed pellet samples. The results are illustrated in Figure 6.13 as a log plot of conductivity (σ) as a function of inverse temperature, along with that of the previously reported all-sulfur compound **6-1a**.[1] The σ(298 K) values and derived activation energies E_{act} are listed in Table 6.5. As we have seen for other R_1/R_2 series of radicals **6-1** to **6-4**, increasing the selenium content within the heterocyclic framework improves conductivity and decreases activation energy. However, it is also apparent from Figure 6.13 that there is a marked difference in conductivity between the monoclinic pair (**6-2a**/**6-4a**) and the orthorhombic set (**6-1a**/**6-3a**) of radicals, with the former being much more conductive. In fact, the **6-2a**/**6-4a** radicals exhibit the highest conductivity values (σ(298 K) > 10^{-3} S/cm) ever observed for a heterocyclic neutral radical material. It appears that the packing arrangement achieved in the monoclinic space group, and the placement of selenium in the 2-position of the molecular framework, is much better suited for high conductivity.

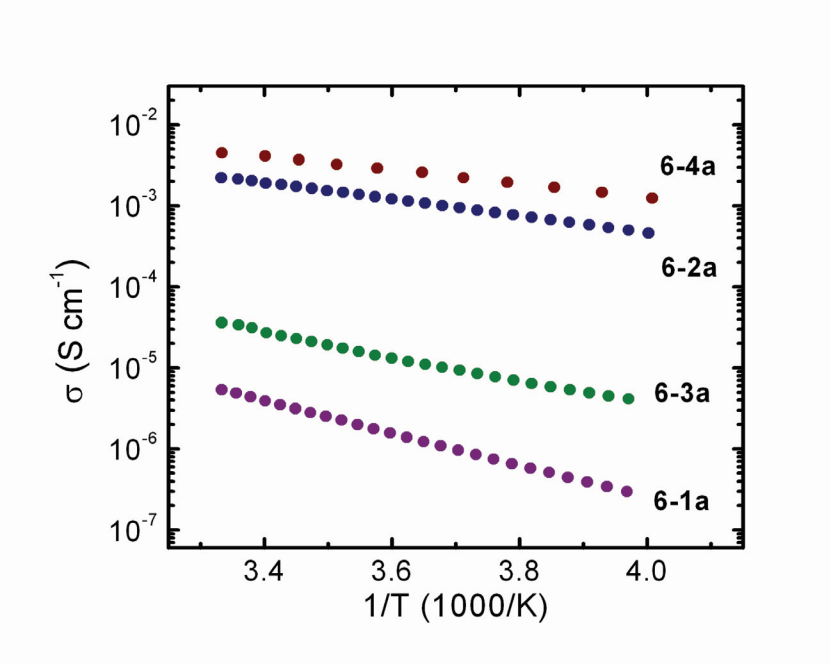

Figure 6.13 A log plot of σ versus 1/T for **6-1a**/**6-3a** ($P2_12_12_1$) and **6-2a**/**6-4a** ($P2_1/n$).

Since the conductivity of the monoclinic radicals **6-2a** and **6-4a** was so high, we probed their conductive behaviour under applied pressure using a cubic anvil press.[‡] The results are shown in Figure 6.14 as plots of σ(298 K) and E_{act} as a function of pressure. We have studied other thiazyl[12] and selenazyl[13] materials under applied pressure and have found, as we do for the present systems, that with the compression of the structure and shortening of the intermolecular contacts, comes a satisfying increase in conductivity and drop in activation energy. Both **6-2a** and **6-4a** show an increase in conductivity by about two orders of magnitude under 5 GPa of pressure, with the greatest response exhibited by the all-selenium radical **6-4a**, which reaches 2 S cm^{-1} at the limit of the experiment. With applied pressure the activation energy drops almost linearly for **6-2a** to approximately 0.08 eV at 5 GPa, while for **6-4a** the decrease appears to level off at a plateau value near 0.10 eV.

[‡] These measurements were performed by X. Yu and R. A. Secco at the University of Western Ontario. A summary of the experimental procedure is described in the Appendix.

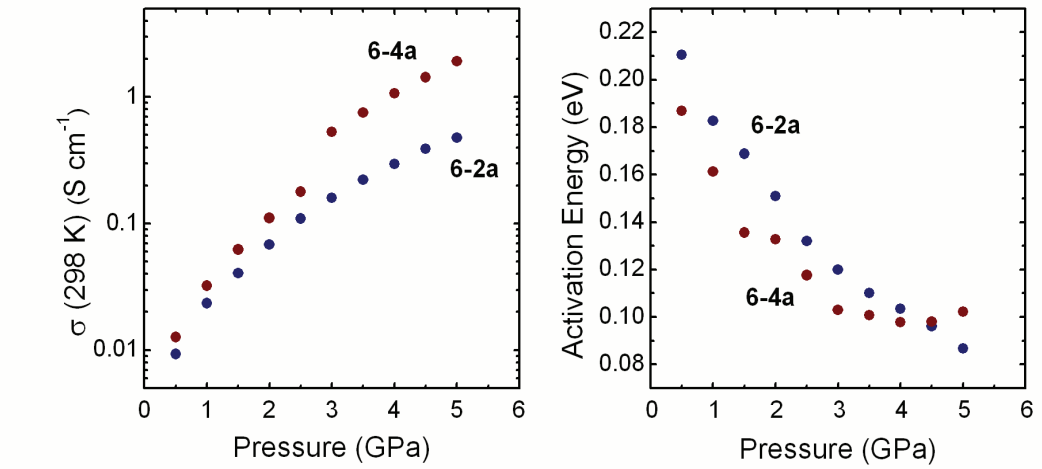

Figure 6.14 Plots of σ(298 K) and activation energy E_{act} versus applied pressure for **6-2a** and **6-4a**.

The differences in the pressure dependence of the activation energy of the two compounds was at first surprising, as we had expected **6-4a**, with its higher selenium content, to behave more dramatically than **6-2a** under applied pressure. While E_{act} continually decreases over the entire pressure range for **6-2a**, the activation energy for **6-4a** reaches a limit at around 3 GPa, with no further reductions with increasing pressure. This apparent discrepancy can be rationalized in terms of the relative compressibility of their crystal structures, that is, the ability of their intermolecular interactions, those that do not contribute to overall bandwidth, to be compressed. A portion of the crystal structure of **6-2a** is presented in Figure 6.15, which shows a cluster of four radicals and the non-bonding intermolecular contacts, S---Me′ (b1, b2), S---Cl′ (b3) and Cl---Cl′ (b4), that separate them. Specific distances, along with those corresponding to the analogous interactions in **6-4a**, are also listed. All of these contacts are close to or within the respective van der Waals separations,[11,14] and the compression of the crystal structure must overcome the combined buffering effects of these interactions.[‡] In the case of **6-4a**, where Se---Me′ and Se---Cl′contacts (with larger van der Waals separations) are involved, compression energies are likely to be larger, resulting in

[‡] The van der Waals separations were complied from references 11 and 14, and are listed here; 3.80 Å for S---Me′, 3.90 Å for Se---Me′, 3.55 Å for S---Cl′, 3.65 Å for Se---Cl′, and 3.50 Å for Cl---Cl′.

a lower overall response to applied pressure. These issues notwithstanding it is apparent that at 5 GPa the metallic state is not far removed for either compound, and may be accessible by increased physical pressure.

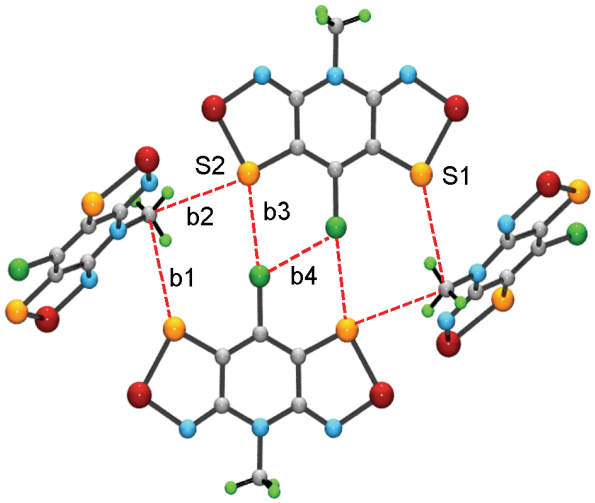

	6-2a	6-4a
b1	3.534(7)	3.550(4)
b2	3.824(8)	3.797(4)
b3	3.738(3)	3.741(1)
b4	3.383(4)	3.403(2)

Figure 6.15 Buffering interactions b1-b4 (in Å) for **6-2a** (and **6-4a**).

6.6 Magnetic Susceptibility Measurements

We have performed magnetic susceptibility χ measurements on the three selenium-containing radicals **6-2a** to **6-4a**. The magnetic data for the all-sulfur radical **6-1a** was previously reported,[1] and a plot of χT versus temperature, shown in Figure 6.16, established that the material behaves as a Curie-Weiss paramagnet above 100 K. At 300 K, χT reaches a value close to that expected (0.375 emu K mol^{-1}) for an S = ½ system of undimerized radicals. The *C* and θ values from the Curie-Weiss fit to the data above 100 K are listed in Table 6.5. Below 100 K, the material undergoes a phase transition in which there is a small but abrupt change in the slippage angle (τ) along the π-stacks. With this structural conversion is a slightly hysteretic increase in χT with decreasing temperature, a feature that signals the onset of weak ferromagnetic (FM) exchange. At temperatures below 20 K however, the χT value drops as the susceptibility is overcome by weaker antiferromagnetic (AFM) interactions. The magnetic behaviour of compound **6-3a**, the other member of the orthorhombic pair, is also shown in Figure 6.16. The susceptibility χ has been corrected for

diamagnetic contributions using Pascal's constants,[15] and the plot of χT as a function of temperature demonstrates that the material does not undergo a phase change as that seen for **6-1a**. Instead the material behaves as an antiferromagnetically coupled Curie-Weiss paramagnet between 7 - 300 K. Below 7 K there is a slight discontinuity in the χ versus T plot (at 100 Oe) as shown in Figure 6.16 (inset), which may indicate the onset of a spin canted AFM state, behaviour that has been observed for other radicals of type **6-3**.[6,7] A Curie-Weiss fit to the high temperature data (T > 100 K) gives a *C* value of 0.378 emu K mol^{-1} and Weiss constant of $\theta = -28$ K.

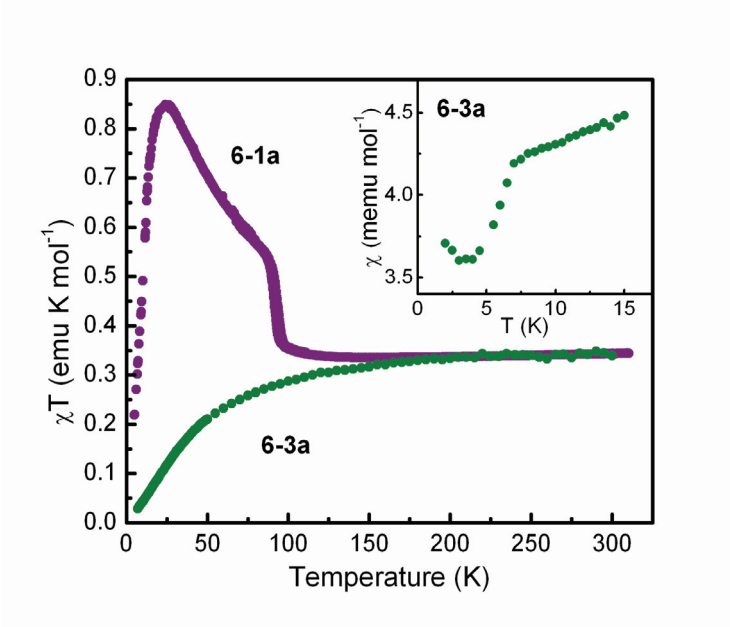

Figure 6.16 A plot of χT versus T for **6-1a** and **6-3a**. Inset shows χ versus T for **6-3a** (*H* = 100 Oe).

The radicals that make up the monoclinic pair, **6-2a** and **6-4a**, exhibit very different magnetic behaviour to that of their orthorhombic counterparts **6-1a** and **6-3a**. In Figure 6.17, plots of χ and χT as a function of temperature are shown for **6-2a** and **6-4a**, and demonstrate that there are much stronger AFM exchange interactions for this group. Even at 300 K, neither compound reaches a χT value expected for an S = ½ system (0.375 emu K mol^{-1}), and consequently no attempt was made to fit the data to the Curie-Weiss expression. Instead the Heisenberg model for a 1D chain of AFM coupled S = ½ centers was

employed. This approach was used since the crystal structure of the monoclinic compounds consist of π-stacks linked *via* a single intrastack contact r5 with strong orbital overlap between chalcogens, an alignment that might be expected to give rise to strong AFM exchange. Similar effects have been observed in the π-stacked bisthiadiazinyls described in Chapter 2.[16] The exchange parameters derived from fits based on a Bonner-Fisher approach[17] and Heisenberg Hamiltonian $H_{ex} = -2J\{S_1 \bullet S_2\}$ are listed in Table 6.5.[‡] While reasonable correlations were achieved in both cases, it is apparent from the large *zJ* values for **6-2a** and, more particularly, **6-4a**, that lateral magnetic interactions are strong, and that the molecular-field modified 1D chain model is at best a first approximation to the description of their magnetic structures.

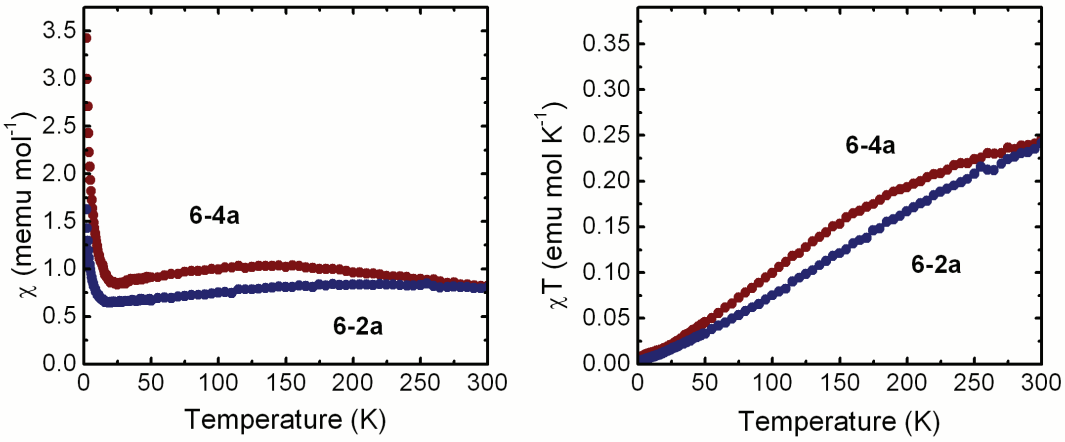

Figure 6.17 Plots of χ and χT as a function of temperature for **6-2a** and **6-4a**.

[‡] The derived fits of the experimental data of **6-2a** and **6-4a** required the following parameters, in addition to those listed in Table 6.5; **6-2a**: $g = 2.011$, $\theta = -12$ cm^{-1}, $\alpha = 0.01$, TIP = 0.00012 emu mol^{-1}, $R(\chi) = 2.1989$. **6-4a**: $g = 2.028$, $\theta = -19$ cm^{-1}, $\alpha = 0.024$, TIP = 0.000015 emu mol^{-1}, $R(\chi) = 2.6301$. $R(\chi) = [E(\chi_{obs}-\chi_{calc})^2/E(\chi_{obs})^2]^{½}$, α = fraction of monomeric paramagnetic impurity, TIP = temperature independent paramagnetism.

In order to explore the origin of the strong antiferromagnetic exchange interactions in **6-2a** and **6-4a**, and the appropriateness of a 1D chain model to fit the magnetic data, we have explored the local magnetic exchange interactions along the π-stacks. We have used a first principles approach,[18] within which bulk magnetic properties are represented as a composite of the individual exchange interactions arising from all pairwise combinations of a radical and its nearest neighbours in the lattice. The method, which has been successfully applied to a variety of nitrogen centered radicals,[19] heterocyclic thiazyls,[16,20,21] selenazyls[22] and phenalenyls,[23] employs exchange energies estimated from broken symmetry DFT methods developed by Noodleman.[24] Accordingly, and with reference to the Hamiltonian $H_{ex} = -2J\{S_1 \bullet S_2\}$, the exchange energy J for any pair of interacting radicals can be estimated from the total energies of the triplet (E_T) and broken symmetry singlet (E_{BSS}) states and the respective expectation values $< S^2 >$ of the two states, according to equation (**1**).

$$J = \frac{-(E_T - E_{BSS})}{<S^2>_T - <S^2>_{BSS}} \qquad (\mathbf{1})$$

There are many pairwise combinations possible between the radical π-stacks of **6-2a** and **6-4a**, and these are illustrated in Figure 6.18. In addition to exchange interactions along the π-stacks, denoted here as J_π, there are a total of seven lateral interstack interactions for every radical. However, six of these fall into symmetry related pairs J_1, J_2 and J_4, while the seventh, J_3, which links radicals in an end-to-end fashion across an inversion center, is unique. Single point total energies E_T and E_{BSS} were calculated for these five combinations (J_1 - J_4, J_π) using the hybrid exchange correlation functional B3LYP and a series of polarized, split-valence basis sets with double-zeta (6-31G(d,p)) and triple-zeta (6-311G(d,p)) functions.

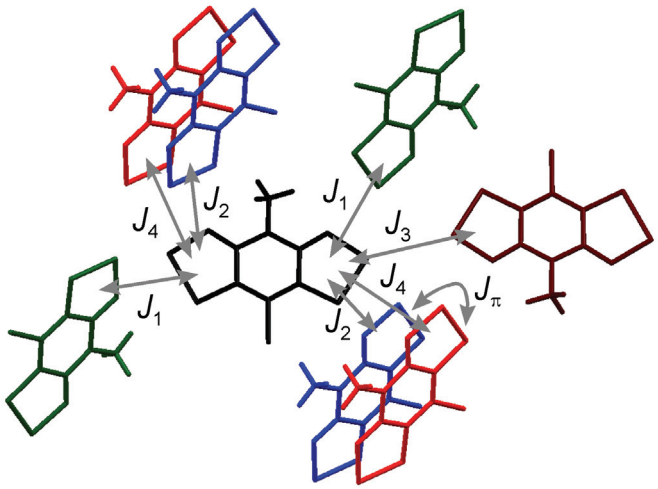

Figure 6.18 Pairwise exchange interactions J_1 - J_4 and J_π for radicals **6-2a** and **6-4a**.

Calculated values for the exchange energies J_1 - J_4 and J_π for **6-2a** and **6-4a** are listed in Table 6.6. While there are minor differences between the two basis sets, it is clear that the large AFM (negative) intrastack exchange energy J_π dominates. The lateral interstack interactions are, by comparison, smaller, with the effects of the FM set J_1, J_2 and J_4 being offset by the single larger AFM term J_3. Collectively the results provide qualitative support for interpreting the magnetic data in terms of a molecular-field modified 1D Heisenberg chain model, although they do not preclude other, more elaborate interpretations.[25]

Table 6.6 Calculated Exchange Energies[a] for **6-2a** and **6-4a**

	6-2a		**6-4a**	
	6-31G(d,p)	6-311G(d,p)	6-31G(d,p)	6-311G(d,p)
J_1	3.62	3.73	5.33	5.35
J_2	5.13	5.20	4.39	4.37
J_3	-13.77	-15.4	-14.24	-16.03
J_4	3.20	2.83	5.14	5.05
J_π	-100.18	-97.5	-68.94	-65.78

[a] J-values in cm^{-1} calculated from equation (**1**) using single point electronic energies.

It is apparent from the above measurements that the magnetic behaviour of the two structural groups are quite different. Although the entire family displays magnetic exchange that is antiferromagnetic in nature, it is evident that the interactions are weaker for the orthorhombic pair **6-1a**/**6-3a** as they behave as Curie-Weiss paramagnets at ambient temperature. By contrast, the monoclinic set **6-2a**/**6-4a** show much stronger magnetic exchange interactions and can be modeled as 1D chains of AFM coupled S = ½ centers. This model provided very large J_π energies along the π-stacks, suggesting that the r5 contact present in the $P2_1/n$ space group is an essential feature in generating the magnetic behaviour.

6.7 Discussion

Radicals **6-1a** to **6-4a** have been developed as a new family of resonance stabilized radicals based on the bisdithiazolyl framework for use as molecular conductors. These radicals were the first to form a non-isomorphous group, a feature which afforded the unique opportunity to examine the effects of the packing arrangement on the transport properties. But before the relationship between crystal structure and electronic behaviour is discussed, it would be prudent to comment on the preferred packing orientation with respect to the molecular framework. Why, for example, does **6-1a** and **6-3a** crystallize in the orthorhombic space group $P2_12_12_1$, where **6-2a** and **6-4a**, of the same approximate size and shape, break away from the usual trends and crystallize in a different orientation with space group $P2_1/n$? It seems that the location of selenium within the molecule, that is, whether it occupies the 1- or 2-position, affects the way in which the radicals align themselves in the solid state. In essence, the selenazyl radicals assume packing arrangements that maximize the number and strength of close Se---Se′ intermolecular interactions. In the $P2_1/n$ structure, radicals cluster together with the ends of four radicals pointing towards one another. This allows **6-2a** and **6-4a**, with selenium in the 2-position, to form four close Se---Se′ contacts (r1-r4) at each end of every molecule. By comparison, when selenium is positioned in the bottom site, as for **6-3a**, no short Se---Se′ interactions are possible if the radicals are arranged in this way. Instead, **6-3a** (like **6-1a**) packs in the $P2_12_12_1$ space group with the sides of molecules coming together, albeit at intersecting angles. When **6-3a** is arranged in this manner, a single short Se---Se′ contact (d4) is possible for each molecule.

Although the bandwidths W for the four structures change only slightly across the series **6-1a** to **6-4a**, and are calculated to be the same for the mixed S/Se radicals **6-2a** and **6-3a**, the conductive and magnetic properties between the two groups are very different. The degrees of plate slippage along the π-stacks (τ) of the two structure types ($P2_12_12_1$ versus $P2_1/n$), though similar in magnitude (Table 6.2), are dissimilar in direction (Figure 6.11), a feature which must effect the electronic communication between radicals along the stacks. The monoclinic pair (**6-2a**/**6-4a**) display a much stronger interaction between radicals than the orthorhombic set (**6-1a**/**6-3a**), as the former exhibits higher conductivity values and larger magnetic exchange interactions. The packing arrangement, and the degree of plate slippage, found in the $P2_1/n$ structures must play an important role on the transport properties of this group of radicals.

In order to gain some insight into the effects of plate slippage on the conductive and magnetic properties of these materials, we have performed a series of calculations on a 1D π-stack of model radicals **6-1** to **6-4** ($R_1 = R_2 = H$). Two types of calculations were performed and these include (i) EHT band structure calculations to determine the dispersion energies ΔE_k, and hence conductive capabilities as $W = |\Delta E_k|$, and (ii) DFT calculations using a first principles approach to obtain the magnetic exchange energy J_π, and therefore the strength and sign of the magnetic interactions. These calculations were introduced in Chapter 1 for compounds **6-1** and **6-4** ($R_1 = R_2 = H$), although here the investigation is extended to include all four S/Se combinations. The molecular geometries of the model compounds **6-1** to **6-4** ($R_1 = R_2 = H$) were taken from C_{2v} optimized B3LYP/6-31G(d,p) calculations, and radicals were separated (δ) by 3.5 Å along the π-stack. The dispersion energies ΔE_k and magnetic exchange interactions J_π were calculated as a function of plate slippage over a range of 3.0 Å along both the long axis (x axis) and short axis (y axis) of the molecule. A selection of special degrees of translation are shown in Figure 6.19, which include that of direct superposition [0.0, 0.0], and maximum slippage along x [3.0, 0.0], along y [0.0, 3.0], and diagonally at coordinates [3.0, 3.0]. For these model systems, with $R_1 = R_2 = H$, only the positive coordinates (+x,+y) were calculated as all other variations (±x, ±y) are equivalent by symmetry.

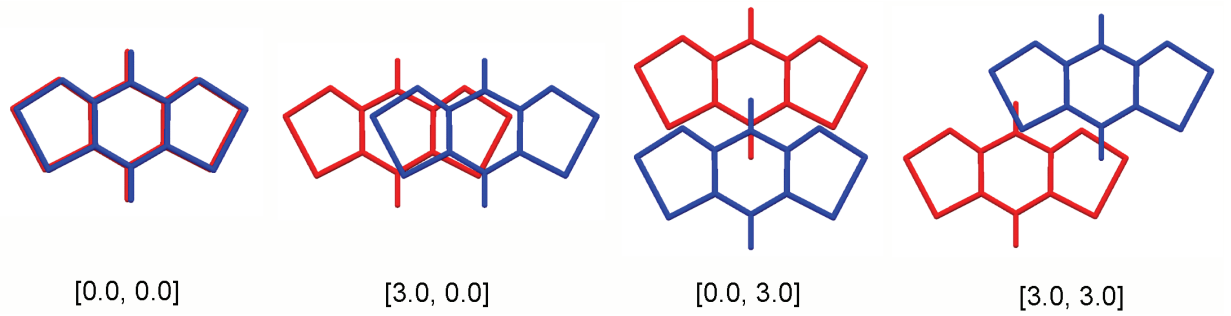

Figure 6.19 Slippage of π-stacks of **6-1** to **6-4** ($R_1 = R_2 = H$) as a function of *x* and *y*.

The results from the calculations are presented as contour maps for each parameter as a function of plate slippage along *x* and *y*. The 1D dispersion energy (ΔE_k) plots for the four model compounds are illustrated in Figure 6.20, and the corresponding magnetic exchange energy (J_π) maps are shown in Figure 6.21. With respect to the dispersion energy plots, there is little difference between the four derivatives **6-1** to **6-4** except for the relative minimum and maximum values, which become more extreme with selenium content. In general, when the radicals are nearly superimposed [0.0, 0.0], ΔE_k is very large and negative, indicating strong antibonding character between radical SOMOs (at $k = 0$). As the radicals slip along either the *x* or *y* direction, ΔE_k steadily decreases and becomes less negative. Along the *x* direction (with $y = 0$) the ΔE_k value plateaus around [2.5, 0.0] for all four compounds and never crosses over into the positive (bonding) regime. Along this axis, **6-1** and **6-3** do however reach a maximum and begin descending again to more negative values of ΔE_k. By contrast, slippage along *y* (with $x = 0$) eventually reaches a null point where ΔE_k is zero at approximately [0.0, 1.8]. With continuing translation along *y*, the sign of ΔE_k changes to positive and the magnitude climbs to a maximum at about [0.0, 2.6] for all compounds. A region of zero bandwidth (red line) meanders across the plot from about [0.0, 1.8] to [3.0, 3.0] for **6-1** and [3.0, 2.0] for **6-4**. In all four plots, there is a local maximum in dispersion energy near [1.4, 2.6] where, for example, ΔE_k reaches ~ 1.0 eV for **6-4**.

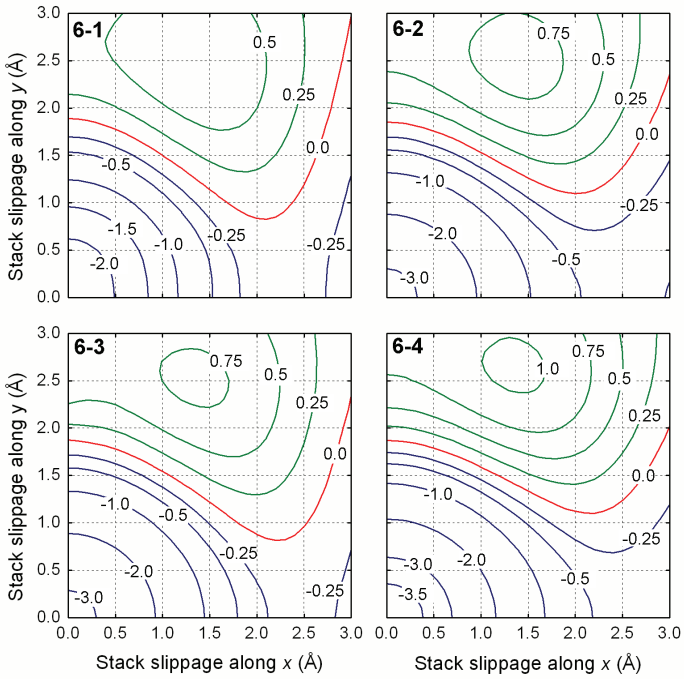

Figure 6.20 Dispersion energy ΔE_k (in eV) as a function of x and y for **6-1** to **6-4** ($R_1 = R_2 = H$).

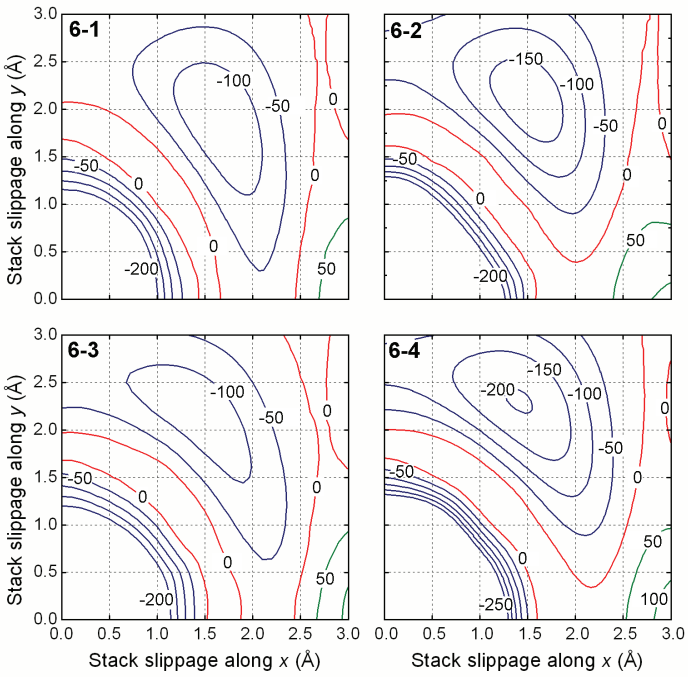

Figure 6.21 Exchange energy J_π (in cm^{-1}) as a function of x and y for **6-1** to **6-4** ($R_1 = R_2 = H$).

The contour plots of the magnetic exchange energies J_π as a function of plate slippage (Figure 6.21) are visually very similar to that of the 1D dispersion energy plots. Like the $\Delta E_k(x,y)$ plot, the maximum and minimum energies are more dramatic with increasing selenium content. Although the values of J_π around direct superposition [0.0, 0.0] could not be calculated,[‡] the energies obtained on moving away from the origin rapidly increase to zero, indicating a region of large negative J_π around the origin, suggestive of strong AFM interactions. With slippage along the x direction (with $y = 0$), J_π abruptly reaches zero at approximately [1.5, 0.0] for all four compounds. For **6-2**/**6-4**, J_π steadily increases with continuing slippage along x, but for **6-1**/**6-3** the value dips once again below zero before ascending onto a region of ferromagnetic exchange ($J_\pi > 0$) near [3.0, 0.0]. As all four radicals slip along the y direction, J_π crosses a null point into a small domain of low positive J_π values between $1.7 < y < 2.0$ Å that suggest a region of FM exchange. With continuing translation, J_π drops back into AFM territory and continues to more negative values until reaching a minimum around [0.0, 2.6]. There is a local minimum in the $J_\pi(x,y)$ plots at approximately [1.5, 2.3] for all compounds, signaling strong AFM exchange interactions at this degree of π-stack slippage.

From these calculations, it is evident that the DFT magnetic exchange energies J_π provide an appealing complement to the EHT 1D dispersion energies, especially when considered in the light of well established relationships between overlap and magnetic exchange, which were described in Chapter 1.[26] An analysis of the contour plots shows that for regions of strong overlap, expressed here in terms of large $|\Delta E_k|$, antiferromagnetic ($J_\pi < 0$) interactions are expected. Conversely, ferromagnetic ($J_\pi > 0$) exchange is predicted when $|\Delta E_k|$ is small. The highest values on the $\Delta E_k(x,y)$ map are seen around direct superposition at [0.0, 0.0], where $|\Delta E_k|$ reaches values greater than 3.5 eV for **6-4**. However, the very large, negative J_π values calculated for this position suggests strong AFM interactions, potentially leading to bond formation, that is, dimerization. The other region of strong dispersion energy on the $\Delta E_k(x,y)$ map, at translation coordinates [1.4, 2.6], may be more conducive to high conductivity, as the J_π values for this region of the

[‡] We were unable to achieve convergence on a broken symmetry singlet state ($<S^2> = 1$) for slippage coordinates close to the origin [0.0, 0.0]. Attempts to do so resulted in a closed shell singlet state ($<S^2> = 0$).

$J_\pi(x,y)$ plot are not as severe. By contrast, the band of low ΔE_k that meanders across the $\Delta E_k(x,y)$ map approximately overlaps onto the region of positive J_π and FM exchange, highlighting slippage coordinates, and thus crystal structures, that may exhibit ferromagnetic behaviour in the solid state.

Table 6.7 π-Stack Slippage of **6-1a** to **6-4a** as a Function of *x* and *y*

Radical	*x* coordinate (Å)	*y* coordinate (Å)
6-1a	2.45	0.07
6-2a	1.60	1.54
6-3a	2.31	0.11
6-4a	1.49	1.64

As for the four radicals **6-1a** to **6-4a** described in this chapter, the degrees of plate slippage in the crystal structures are illustrated in Figure 6.11 and the coordinates are listed in Table 6.7. When comparing the real structures to the contour maps, some caution is required as the calculations were performed on model compounds **6-1** to **6-4** ($R_1 = R_2 = H$), set at a specific interplanar separation ($\delta = 3.5$ Å). For the orthorhombic set **6-1a**/**6-3a**, the slippage coordinates place them in an area of low dispersion energy on the $\Delta E_k(x,y)$ map, and a fairly flat region in the $J_\pi(x,y)$ plot with weakly negative J_π values. These theoretical findings are consistent with the experimental properties of these two compounds, as they exhibit moderate conductivity values (10^{-6} - 10^{-5} S cm^{-1}) and small, negative Weiss constants (Table 6.5). The FM behaviour demonstrated by the low temperature structure of **6-1a** can be rationalized by its more extreme plate slippage [2.99, 0.03], which pushes the arrangement into the FM region of the $J_\pi(x,y)$ map. By contrast, the monoclinic radicals **6-2a**/**6-4a** have degrees of slippage that place them near the center of the contour maps. The ΔE_k values calculated for these positions are much higher than those observed for the other derivatives, and this would account for their higher conductivity values (> 10^{-3} S cm^{-1}). On the $J_\pi(x,y)$ map, **6-2a** and **6-4a** lie in a region of large negative J_π values, which is also consistent with experiment (Table 6.5). In addition, they are situated in an area with a steep slope, a feature which explains the difference in the modeled experimental *J* values between these two radicals.

It appears that the experimental behaviour of **6-1a** to **6-4a** corresponds quite well to that predicted by the calculated dispersion energy ΔE_k and magnetic exchange energy J_π plots. Both the conductive and magnetic properties of all four compounds can be rationalized in terms of the interactions that arise along the π-stacks as a result of their respective degrees of plate slippage in their crystal structures. This suggests that the contour maps can be used to predict the behaviour for these types of compounds, and also highlight desirable structures that provide either strong intrastack overlap, and hence conductivity, or specific magnetic interactions including FM or AFM exchange. For example, according to the $\Delta E_k(x,y)$ plot, radicals **6-2a**/**6-4a** have not reached the local maximum at [1.4, 2.6], suggesting that minor modifications in plate slippage could afford larger $|\Delta E_k|$ values. It is possible that small variations in size and/or shape of the R_1 and R_2 groups would be enough to increase plate slippage along the stacks, while maintaining the space group, and induce even higher conductivity values than those exhibited here.

6.8 Conclusions

The sequential incorporation of selenium into the bisdithiazolyl framework **6-1a** has provided the selenazyl radicals **6-2a** to **6-4a**. The entire family has been characterized and all four derivatives have structures that consist of slipped π-stacks, with no evidence of dimerization. Unlike the previously studied R_1/R_2 families of **6-1** to **6-4**, this group does not display an isomorphous mapping of selenium for sulfur, and instead the structures break into two isostructural pairs. One set, those that have sulfur occupying the 2-position of the heterocycle (**6-1a** and **6-3a**), crystallize in the orthorhombic space group $P2_12_12_1$, while the other pair, with selenium in the 2-position (**6-2a** and **6-4a**), crystallize in the monoclinic space group $P2_1/n$. This structural dichotomy has enabled us, for the first time, to study the effects of the packing arrangement on the transport properties. It is clear from the conductivity and magnetic measurements on these systems that the structure obtained in the monoclinic space group is much more conducive to strong communication between radicals.

The **6-2a**/**6-4a** compounds exhibit some of the highest conductivity values we have ever observed, with the all-selenium radical **6-4a** displaying a σ_{RT} value of 4.3 x 10^{-3} S cm^{-1} and an E_{act} of 0.17 eV. By applying a pressure of 5 GPa, these properties are improved for both compounds, with the behaviour of **6-4a** being most impressive, as a conductivity of 2 S cm^{-1} and activation energy of 0.10 eV is reached. Although the metallic state has not been obtained, the low E_{act} values at 5 GPa suggests that it may be achieved under slightly higher pressures. The magnetic measurements also show a difference between the two structural groups, with the **6-2a**/**6-4a** compounds exhibiting much stronger AFM interactions. The differences between the two structure types, that is, the orthorhombic and monoclinic arrangements, can be rationalized in terms of the position of the compounds on the calculated EHT bandwidth and DFT magnetic exchange energy contour plots. The degree of plate slippage in the monoclinic structures affords much stronger orbital overlap, and therefore larger bandwidth (and conductivity) and stronger magnetic exchange interactions are observed. With the structure-property correlations provided by these energy maps, we are now in a much better position to predict and potentially design molecular radicals with specific conductive and magnetic properties.

6.9 Future Work

It is clear that the calculated EHT bandwidth and DFT magnetic exchange energy plots will be a valuable tool in designing bisdithiazolyl radicals with specific properties. The qualitative correspondence between the degree of plate slippage along the radical π-stacks with experimental property has been observed, not only in the structures described above for **6-1a** to **6-4a**, but also for many other R_1/R_2 derivatives. One example involves the pyrazine-bridged radicals described in Chapter 3,[12] which formed superimposed π-stacks with slippage coordinates [0.0, 0.0]. Instead of obtaining a high bandwidth conductor as suggested by the $\Delta E_k(x,y)$ map, the structure consists of spin-quenched dimers, a result predicted by the $J_\pi(x,y)$ plot where $J_\pi << 0$ at this degree of plate slippage. This strong AFM behaviour suggests potential bond formation, and this is what occurs. High bandwidth systems based on discrete radicals are more likely to be found for structures with slippage coordinates [1.4, 2.6], a region close to

where the highly conductive **6-2a**/**6-4a** compounds are positioned. It may be possible that the replacement of the chlorine atom in these compounds with a bromine or iodine atom will be enough to maintain the space group while pushing the degree of slippage into the high bandwidth region.

The magnetic properties observed for a series of **6-2** radicals can also be rationalized by their slippage coordinates and position on the energy plots. A group of five radicals, **6-2** (R_1 = Et, Pr, CH_2CF_3; R_2 = Cl, and R_1 = Et; R_2 = Me, Br) have been developed, all being isostructural and crystallizing in the tetragonal space group $P\bar{4}2_1m$.[22] Ferromagnetic ordering is observed in only three of the five derivatives, and this discrepancy can be readily explained using the energy plots. The π-stacked structures of all five compounds slip exclusively along the *y* direction, but to varying degrees. Ferromagnetic behaviour is expected for systems with orthogonal overlap ($|\Delta E_k| \sim 0$) and $J_\pi > 0$, and the comparison of the EHT bandwidth and DFT magnetic exchange energy plots along the *y* direction reveals an area of FM exchange for $1.7 < y < 2.0$ Å. The calculated J_π values for slippage along *y* is shown in Figure 6.22. The slippage coordinates of the ferromagnetic materials sit in or near this region, where the remaining two are more severely slipped and lie beyond this area.

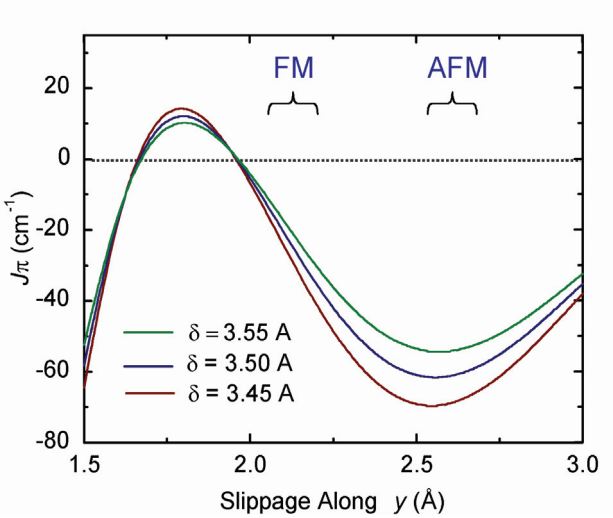

Figure 6.22 Calculated J_π values for **6-2** (R_1 = R_2 = H) as a function of plate slippage along *y*. The interplanar separation along the π-stack is δ. The areas enclosed in the brackets represent the slippage coordinates of the ferromagnetic (FM) and antiferromagnetic (AFM) derivatives.

Although the J_π calculations for these compounds were previously reported and demonstrated the importance of the packing arrangement on the magnetic interaction, the bandwidth calculations described here demonstrate that orthogonal orbital overlap is also obtained for the ferromagnetic materials. Since the FM compounds lie around the boundary of the FM region of the map, it may be possible to improve the magnetic properties by achieving slippage coordinates that correspond to the maximum in J_π along y. One possible way to achieve this is through substituent modification. The trend observed for the five compounds above suggests that an R_2 group larger than bromine, such as iodine, may be sufficient to preserve the space group while causing a small change in the degree of slippage, to put the structure into the high J_π position.

Another area of potential interest highlighted on the $J_\pi(x,y)$ map is a region of large positive J_π at [3.0, 0.0], where strong FM exchange is suggested. For example, J_π values reaching 100 cm^{-1} are predicted for the all-selenium derivative **6-4**. Structures with this degree of plate slippage may exhibit interesting ferromagnetic behaviour, as observed for the low temperature structure of **6-1a**. In order to achieve the severe translation exclusively along the long axis of the molecule, one may envision using bulky substituents that would force stack slippage due to steric repulsion while hindering slippage along the short axis of the molecule. Of course the molecules still need to communicate along the stacking direction, so the R groups can not be too large. Substituents such as dimethylamino, methoxy, *t*-butyl or isopropyl in the R_1 and R_2 positions may afford the desired degree of slippage, and if so, it may lead to the observation of strongly FM-coupled neutral radicals.

Appendix A

General Experimental and Computational Methods

A.1 Procedures

A.1.1 General Procedures

Many of the reactions and manipulations were performed under an inert atmosphere of nitrogen. Those reactions carried out in solution were handled by standard or modified Schlenk techniques using a double-manifold glass vacuum line (nitrogen / vacuum) with an Edwards E2M series rotary vacuum pump. Air sensitive solids were handled and stored in a nitrogen-filled Braun MB-150M drybox.

A.1.2 H-Cell Crystallizations

For materials that are highly insoluble and involatile, *i.e.*, recrystallization and sublimation are not viable options for crystal growth, H-cell techniques are often used to afford crystals of analytical purity. Commonly, diffusion H-Cells are used to grow single crystals of the radicals, although more recently, electrochemical H-Cell methods have been employed for the more conductive materials.

A.1.2.1 Diffusion H-Cells

Diffusion H-cell experiments are especially useful for the preparation of air and/or moisture sensitive materials such as neutral radicals, as a thorough degassing of the solvent is possible. A diffusion H-cell apparatus is illustrated in Figure A.1, and a typical experiment proceeds as follows; two solutions containing each reactant are placed in each of the round bottom flasks and the cell is oriented as shown in Figure A.1A. The solutions are put through five freeze-pump-thaw cycles to ensure all the oxygen has been removed from the vessel. The apparatus may be kept under vacuum or flooded with an inert gas (argon or nitrogen). The H-Cell is then inverted and tipped slightly askew as depicted in Figure A.1B, to allow the two solutions to combine slowly. One solution flows through the glass frit into the other resulting in crystal growth of the product at the interface of the two solutions.

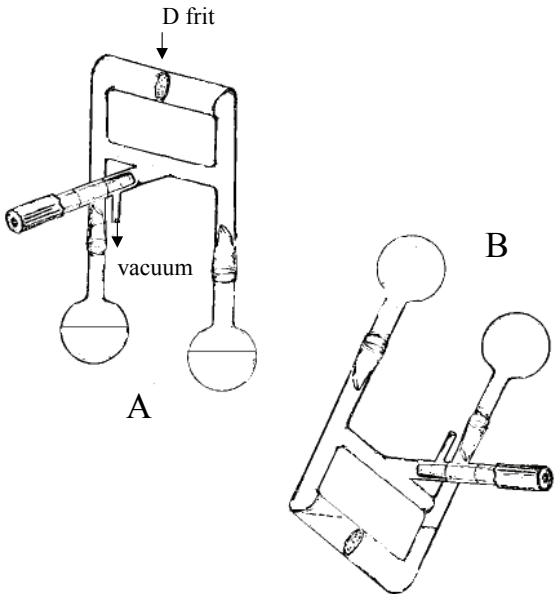

Figure A.1 Diffusion H-Cell apparatus for single crystal growth.

A.1.2.2 Electrochemical H-Cells

The electrocrystallization method of single crystal growth requires that the product be fairly conductive, typically with a σ_{RT} value of at least 10^{-4} S cm^{-1}. A schematic diagram of an electrochemical H-cell apparatus is shown in Figure A.2 and the procedure used follows standard electrochemical techniques.[1] In general, the sample is dissolved in degassed acetonitrile containing 0.025 M [*n*-Bu_4N][PF_6] as supporting electrolyte, and placed in one side of the cell. The other side is filled with an equally degassed acetonitrile solution of 0.025 M [*n*-Bu_4N][PF_6], to a level equal to the adjacent compartment. Once the apparatus is assembled as in Figure A.2, current ranging from 1 to 10 μA is applied, allowing for the electrochemical reduction of the reactant and crystallization of the product on the electrode. The experiment usually runs for a period of 2 to 7 days.

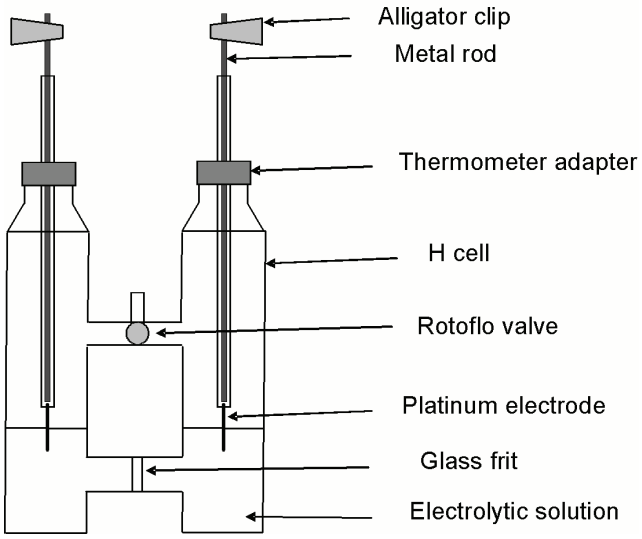

Figure A.2 Electrochemical H-cell apparatus for single crystal growth.

A.2 Techniques

A.2.1 Density Functional Theory Calculations

DFT calculations were run on PC workstations using the UB3LYP method[2] available in the Gaussian 98W[3] and Gaussian 03W[4] suite of programs.

A.2.1.1 Ion Energetics

Adiabatic (ΔSCF) ionization potential and electron affinity estimates were obtained from total electronic energy calculations using a 6-31G(d,p) basis set within the constraints of C_{2v} symmetry. Full vibrational frequency calculations on the final geometries of the radical and cation confirmed that they were stationary points. In the case of the anions, there was sometimes one negative frequency, which may be interpreted in terms of an incipient cleavage of one of the E-E[5] or E-N[6] (E = S, Se) bonds upon reduction of the radical.

A.2.1.2 Radical Association Enthalpies

Radical association energies were estimated in terms of the total electronic energy (B3LYP/6-31G(d,p)) difference between the radicals and their dimers. Dimer geometries were optimized within a C_{2h} symmetry constraint and were confirmed to be stationary points by frequency calculations.

A.2.1.3 Exchange Energy Calculations

The exchange energy J for any pair of interacting radicals was estimated in terms of the energy difference between the triplet (E_T) and broken symmetry singlet (E_{BSS}) states derived from the phenomenological Heisenberg Hamiltonian $H_{ex} = -2J\{S_1 \bullet S_2\}$ (Figure A.3).[7] Single point energies of the triplet (E_T) and broken symmetry singlet (E_{BSS}) states were calculated using the hybrid exchange correlation functional UB3LYP and a series of polarized, split-valence basis sets with double-zeta (6-31G(d,p)) and triple-zeta (6-311G(d,p)) functions. Exchange energies were then derived from Equation (**1**), using the calculated values of E_T and E_{BSS} and the respective $<S^2>$ expectation values. Tight convergence criteria were employed, and atomic coordinates were taken from crystallographic data.

$$\psi_{BSS} = \frac{1}{\sqrt{2}}\left(\psi_T \pm \psi_S\right)$$

$$\begin{aligned}\left\langle S^2 \right\rangle_{BSS} &= \frac{1}{2}\left\langle \psi_T + \psi_S \middle| S^2 \middle| \psi_T + \psi_S \right\rangle \\ &= \frac{1}{2}\left[\left\langle \psi_T \middle| S^2 \middle| \psi_T \right\rangle + \left\langle \psi_S \middle| S^2 \middle| \psi_S \right\rangle\right] \\ &= \frac{1}{2}\left[\left\langle S^2 \right\rangle_T + \left\langle S^2 \right\rangle_S\right] \\ &= \frac{1}{2}\left[2 + 0\right] \\ &= 1\end{aligned}$$

$$H_{ex} = -2J\{S_1 \cdot S_2\}$$

where $\left\langle S^2 \right\rangle = S(S+1)$ and $S = S_1 + S_2$

$$\langle H \rangle = \left\langle -J\left(S^2 - S_1^2 - S_2^2\right)\right\rangle$$

$$E = -J\left(\left\langle S^2 \right\rangle - \left\langle S_1^2 \right\rangle - \left\langle S_2^2 \right\rangle\right)$$

$$E = -J\left[(S(S+1)) - (S_1(S_1+1)) - (S_2(S_2+1))\right]$$

$$J = \frac{-\left(E_T - E_{BSS}\right)}{\left\langle S^2 \right\rangle_T - \left\langle S^2 \right\rangle_{BSS}} \qquad \textbf{(1)}$$

Figure A.3 Derivation of $<S^2>_{BSS}$ value and the expansion of the Heisenberg Hamiltonian to obtain the energies of any particular spin state. Also shown is the exchange energy J equation (**1**).

The relationship between the triplet E_T, singlet E_S and broken symmetry singlet E_{BSS} energy states and the exchange energy J is presented in Figure A.4.

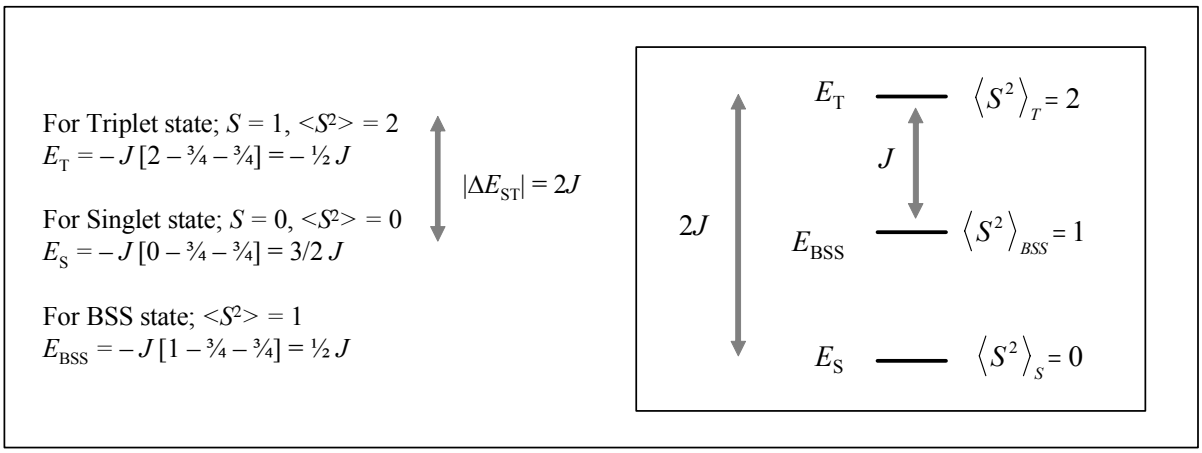

Figure A.4 Calculated energies of the triplet E_T , singlet E_S and broken symmetry singlet E_{BSS} states.

Coordinates for the model 1D calculations of J_π as a function of the π-stack slippage (x, y) were performed using coordinates for model compounds (with R = H) taken from UB3LYP/6-31G(d,p) calculations optimized in C_{2v} symmetry; the interplanar separation along the model π-stack was set at 3.5 Å. The smoothed energy surface was plotted from a grid consisting of at least 121 points.

A.2.2 NMR Spectra

^{1}H NMR spectra were collected on a Bruker Avance 300 MHz NMR spectrometer.

A.2.3 Infrared Spectral Analysis

Infrared spectra were recorded (at 2 cm^{-1} resolution) as Nujol mulls or neat liquids on KBr plates, on a Nicolet Avatar 320 FT infrared spectrometer.

A.2.4 Mass Spectrometry

Low resolution mass spectra (70 eV, EI, DEI and CI, DCI) were run on either a Micromass Q-TOF Ultima Global LC/MS/MS system or a JEOL HX110 double focusing mass spectrometer at the WATSPEC Mass Spectrometry Facility.

A.2.5 Cyclic Voltammetry

Cyclic voltammetry experiments were performed using a PINE Bipotentiostat, Model AFCCIBPI, on dry acetonitrile solutions containing 0.1 M tetra-*n*-butylammonium hexafluorophosphate. Scan rates of 50 - 100 mV s^{-1} were employed. Potentials were scanned from -2.5 to 2.0 V with respect to the quasi-

reference electrode in a single compartment cell fitted with Pt electrodes. The potentials were referenced to the ferrocenium/ferrocene couple at 0.38 V *vs* SCE and are cited relative to SCE in CH_3CN.[8]

A.2.6 UV-Visible Spectra

UV-visible spectra were recorded on a Perkin-Elmer Lambda 6 spectrometer in acetonitrile.

A.2.7 EPR Spectra

The X-band EPR spectra were recorded on methylene chloride or toluene solutions of the radical at ambient temperature using a Bruker EMX spectrometer. Hyperfine coupling constants were obtained by spectral simulation using Simfonia[9] and WinSim.

A.2.8 Elemental Analysis

Elemental analyses were performed by MHW Laboratories, Phoenix, AZ.

A.2.9 Magnetic Susceptibility Measurements

Magnetic susceptibilities were measured on a George Associates Faraday balance operating at 0.5 T (University of California, Riverside), DC magnetic susceptibility measurements were performed on a Quantum Design MPMS SQUID magnetometers (University of Victoria, Memorial University of Newfoundland and McMaster University). AC susceptibility measurements were performed on an Oxford Instruments MagLab EXA (McMaster). The results were corrected for diamagnetic contributions using Pascal's constants.[10]

For several compounds discussed in this thesis, the observed magnetic susceptibility data was fitted to a Bonner-Fisher 1D S = ½ AFM chain model[11] (Equation **2**) modified to include a molecular field parameter (zJ) to account for interchain interactions (Equation **3**).[12] Contributions from Temperature Independent Paramagnetism (TIP) and Curie-Weiss impurities (α) were also included (Equation **4**). In these equations, N is the Avogadro constant, k is the Boltzmann constant, g is the g-factor, S is the total spin angular momentum quantum number, θ is the Weiss constant and β is the Bohr magneton.

$$\chi_{BF} = \frac{Ng^2\beta^2}{k(T-\theta)}\left[\frac{0.25+0.14995X+0.30094X^2}{1.0+1.9862X+0.68885X^2+6.0626X^3}\right] \quad where\, X = \frac{|J|}{kT} \qquad (\mathbf{2})$$

$$\chi_{chain} = \frac{\chi_{BF}}{1 - \frac{2(zJ)\chi_{BF}}{Ng^2\beta^2}} \quad (3)$$

$$\chi_{obsd} = \left\{ \frac{\alpha\left[Ng^2\beta^2 S(S+1)\right]}{3kT} + TIP + \left[1-\alpha\right]\chi_{chain} \right\} \quad (4)$$

These equations were incorporated into software provided by Prof. Laurence Thompson (Memorial University) and compiled to run in TurboBasic. More recent versions of the fitting routines were developed by Randle Taylor (randle.taylor@gmail.com) and were built using Python version 2.5 and included the following packages: Numpy v1.2.1, Scipy v0.7.0 rc2 and wxpython v2.8.9.1 (msw-unicode). The GUI was built using wxGlade v0.6.3 and the Windows executable was created using py2exe v0.6.6.

A.2.10 Ambient Pressure Conductivity Measurements

Ambient pressure single-crystal (needle axis) conductivity measurements were made using a four-probe configuration, with in-line contacts made using silver paint. Conductivity was measured in a custom-made helium variable-temperature probe using a Lake Shore 340 temperature controller. A Keithley 236 unit was used as a voltage source and current meter, and two 6517A Keithley electrometers were used to measure the voltage drop between the potential leads in the four-probe configuration.

For pressed pellet samples, four-probe temperature dependent conductivity measurements were performed using either a Quantum Design PPMS instrument or a home-made device, to measure the voltage drop under dynamic vacuum. Silver paint was used to apply the electrical contacts.

A.2.11 Applied Pressure Conductivity Measurements

The high-pressure conductivity measurements were carried out in a cubic anvil press[13] using pyrophyllite ($Al_4Si_8O_{20}(OH)_4$) as the pressure-transmitting medium. Sample pressure was determined from previous calibrations of the applied hydraulic load against pressures of structure transformations in standards at room temperature (Hg L ↔I at 0.75 GPa, Bi I ↔ II at 2.46 GPa, Tl 1 ↔ III at 3.70 GPa, and Ba 1 ↔ III at 5.5 GPa).[14] Temperature was applied by Joulean heating of a cylindrical Nb foil (0.127 mm thick) furnace and monitored with a Pt/(Pt + 10% Rh) thermocouple, using a pressure-corrected emf. Two Pt electrodes, each constructed from a single length of wire, contacted the disk-shaped (~ 6.1 mm diameter and ~ 0.35 mm thick), pre-compacted, powder sample which was contained in a boron nitride ($\sigma_{BN} = 10^{-11}$

S cm^{-1}) cup. Both two-wire dc (Solartron 7061 Systems voltmeter) and four-wire ac (1 Hz and 1 kHz – Solartron 1260 impedence analyzer) resistance measurements were made. Separate experiments were performed at room temperature *vs* pressure (0.3 - 5.5 GPa) and at fixed pressures *vs* temperature (22 - 100 °C). In the constant room-temperature experiments, resistance was measured on increasing/decreasing pressure over 5 - 6 hours. In the variable temperature experiments, resistance was measured at fixed temperature intervals of 10 °C on heating/cooling at constant pressure. Pressure was increased and temperature was cycled again. The contiguous disk-shaped sample was extracted from the recovered pressure cell, and the sample geometry was measured to convert resistance to conductivity.

A.2.12 X-ray Crystallography

Single crystal X-ray data were collected at ambient temperature (and 100 K when stated) using phi and omega scans with a (i) Bruker APEX I CCD detector on a D8 3-circle goniometer (University of Waterloo), (ii) Bruker P4/CCD diffractometer (McMaster University, University of Louisville) and (iii) Bruker APEX II CCD detector on a D8 3-circle goniometer (McMaster University) with Mo Kα (λ = 0.71073 Å) radiation. Single crystal data were also collected on a Bruker SMART 6000 CCD on a D8 3-circle goniometer and a parallel focus Cu Kα (λ = 1.54178 Å) with a rotating anode generator. All data were scanned using Bruker's SMART program and integrated using Bruker's SAINT software[15] or by the APEX II software package. The structure was solved by direct methods using SHELXS-90[16] and refined by least-squares methods on F^2 using SHELXL-97[17] incorporated in the SHELXTL suite of programs.[18] Agreement indices are calculated as followed:

$R = [\Sigma||F_o| - |F_c||] / [\Sigma|F_o|]$ for $I > 2\sigma(I)$; $R_w = \{[\Sigma w(|F_o| - |F_c|)^2] / [\Sigma w|F_o|^2]\}^{½}$.

Powder data were collected on a X-ray powder diffractometer with a position sensitive detector (INEL) at ambient temperature using Cu Kα radiation (λ = 1.5406 Å). The structures were obtained using Crysfire to index the unit cell, simulated annealing methods (FOX) to solve the structures and GSAS to refine the solutions. Agreement indices are calculated as followed:

$R_p = [\Sigma (I_o - I_c)] / [\Sigma(I_o)]$; $R_{wp} = \{[\Sigma w(I_o - I_c)^2] / [\Sigma w(I_o)^2]\}^{½}$.

A.2.13 Band Structure Calculations

Electronic band structure calculations were performed with either the EHMACC suite of programs[19] or the Caesar suite of programs,[20] using the Coulomb parameters of Basch, Viste and Gray[21] and a quasi-split valence basis set adapted from Clementi and Roetti;[22] numerical values are tabulated elsewhere.[23] The off-diagonal elements of the Hamiltonian matrix were calculated with the standard

weighting formula.[24] Atomic positions for the full 3D calculations were taken from crystallographic data.

Coordinates for the model 1D-calculations of $\Delta E_k = [E(k = \pi/a) - E(k = 0)]$ as a function of the stack slippage were performed using coordinates for model compounds (with $R_1 = R_2 = H$) taken from UB3LYP/6-31G(d,p) calculations optimized in C_{2v} symmetry; the interplanar separation along the π-stack was set at 3.5 Å. The smoothed energy surface was plotted from a grid consisting of at least 121 points.

A.3 Source of Starting Materials

A.3.1 Purchased Chemicals that were Used as Received

2,6-diaminopyridine	(Aldrich)
acetic acid, glacial	(Fisher)
acetic anhydride, reagent grade	(Fisher)
aluminum trichloride	(Aldrich)
ammonia gas	(Matheson)
ammonium hydroxide (aqueous)	(Fisher)
ammonium thiocyanate	(Fisher)
argon gas	(Praxair)
benzene	(Fisher)
benzyltriethylammonium chloride	(Aldrich)
bromine	(Fisher)
n-butyllithium, 1.6 M in hexane	(Aldrich)
calcium hydride	(Fisher)
chlorine gas	(Matheson)
chlorobenzene	(Fisher)
chloroform-*d*	(Isotec)
chlorotrimethylsilane, 98%	(Aldrich)
decamethylferrocene	(Aldrich/Alfa Aesar)
diethyl ether	(Fisher)
dimethylsulfoxide-*d*	(Isotec)
ethanol, 95 %	(Fisher)

ethyl acetate	(Fisher)
ethyl triflate, 99 %	(Aldrich, Synquest)
ferrocene	(Aldrich)
gallium trichloride, anhydrous, beads, -10 mesh, 99.99 %	(Aldrich)
hexane	(Fisher)
hydrochloric acid, 12 M	(Fisher)
hydrogen peroxide, 30%	(EM Science)
magnesium sulfate	(EMD)
methanol	(Fisher)
methyl triflate, 99 %	(Aldrich)
nitric acid	(Fisher)
nitrogen gas	(In-house supply)
octamethylferrocene	(Aldrich)
phosphorous oxychloride	(Aldrich)
phosphorous pentoxide	(Fisher)
potassium carbonate	(BDH Laboratories)
potassium hydroxide, pellets, 99.99 %	(Aldrich)
potassium iodide	(Fisher)
Proton Sponge (1,8-bis(dimethylamino)napthalene)	(Aldrich)
pyridine	(Fisher)
selenium powder, -100 mesh, 99.5+ %	(Aldrich)
selenium dioxide	(Aldrich)
selenium oxychloride	(Aldrich)
silver hexafluoroantimonate	(Aldrich)
silver triflate	(Aldrich)
sodium	(BDH Laboratories)
sodium azide	(Aldrich)
sodium borohydride	(Aldrich)
sodium dithionite	(Aldrich)
sodium hydroxide, pellets, 97.0 %	(Aldrich)
sodium nitrite	(EM Science)
sodium sulfide nonahydrate	(Aldrich)
sulfur dioxide, anhydrous gas	(Matheson)

sulfur monochloride	(Aldrich)
tetra-*n*-butylammonium bromide	(Aldrich)
tetra-*n*–butylammonium fluoride, 1.0 M in THF	(Aldrich)
tetra-*n*-butylammonium tetrafluoroborate	(Aldrich)
tetra-*n*-butylammonium triflate	(Alfa Aesar)
tetrahydrofuran, anhydrous	(Aldrich)
thionyl chloride	(Acros)
triethylamine, 99%	(Aldrich)
triethyloxonium hexafluorophosphate	(Aldrich)
triflic acid	(Aldrich)
trifluoroacetic acid	(Aldrich)

A.3.2 Solvents Purified Prior to Use

acetonitrile (Caledon) - distilled from P_2O_5 or CaH_2

chlorobenzene (Fisher) - distilled from P_2O_5

dichloroethane, 1,2- (Fisher) - distilled from P_2O_5

methylene chloride (Fisher) - distilled from P_2O_5

tetrahydrofuran (Caledon) - distilled from lithium aluminum hydride

toluene (Fisher) - distilled from sodium

A.3.3 Chemicals Prepared "In-House"

A.3.3.1 Preparation of silver nonafluorobutanesulfonate.[25] A suspension of silver carbonate (5.00 g, 0.0181 mol) in 100 mL diethyl ether was cooled on an ice bath and nonafluorobutane-1-sulfonic acid (6 mL, 0.0370 mol) was added. After 3 h at 0 °C, the resulting slurry was filtered twice through celite to give a clear yellow solution. Hexane was added to precipitate the white gel-like solid of product, which was filtered on a Büchner funnel and rinsed with 20 mL hexane. The white solid of silver nonaflate was dried in vacuo and stored in a cool dark place (product is light and moisture sensitive).

A.3.3.2 Preparation of iodobenzene dichloride.[26] A solution of iodobenzene (6.57 g, 0.322 mol) in 50 mL DCM was cooled to 0 C, and chlorine gas was passed over for approximately 20 min to give a canary yellow precipitate. After stirring for another 20 min the cold bath was removed and the vessel

was vented to remove excess gas. After 25 min, iodobenzene dichloride was filtered off and rinsed with cold DCM, yield 6.24 g (0.0227 mol, 71 %).

A.4 Conductive Behaviour of Elemental and Synthetic Compounds

Table A.1 Conductive Behaviour of Selected Elemental and Synthetic Compounds

Compound	**σ_{RT} (S cm^{-1})**	**Type**
Cu[a]	10^{6}	Metal
Na[a]	10^{5}	Metal
$(SN)_x$[b]	10^{3}	Metal
[TTF][TCNQ][b]	10^{2}	Metal
Ge[c]	10^{-2}	Semiconductor
GaAs[d]	10^{-4}	Semiconductor
Se[a]	10^{-6}	Semiconductor
perylene[b]	10^{-14}	Insulator
diamond[c]	10^{-16}	Insulator
S[a]	10^{-18}	Insulator

[a] Weast, R. C. *CRC Handbook of Chemistry and Physics, 64th Ed.* CRC Press, Inc.; Boca Raton, Florida, **1982**. [b] Ferraro, J. R.; Williams, J. M. *Introduction to Synthetic Electrical Conductors*. Academic Press Inc.; California, U.S., **1987**. [c] Hugheey, J. E.; Keiter, E. A.; Keiter, R. L. *Inorganic Chemistry, Principles of Structure and Reactivity, 4th Ed.* HarperCollins College Publishers; New York, U. S., **1993**. [d] Patanè, A.; Allison, G.; Eaves, L.; Hopkinson, M.; Hill, G.; Ignatov, A. *J. Phys.: Condens. Matter* **2009**, *21*, 174209.

References for Chapter 1

1. Forrester, A. R.; Hay, J. M.; Thomson, R. H. *Organic Chemistry of Stable Free Radicals*; Academic Press: London, 1968.

2. Herzberg, G. *The Spectra and Structures of Simple Free Radicals*; Cornell University Press: Ithaca, 1971.

3. Griller, D.; Ingold, K. U. *Acc. Chem. Res*. **1979**, *9*, 13.

4. (a) Hicks, R. G. *Org. Biomol. Chem*. **2007**, *5*, 1321. (b) Preuss, K. E. *Dalton Trans*. **2007**, 2357.

5. Power, P. P. *Chem. Rev*. **2003**, *103*, 789.

6. Coulson, C. A. *Valence, 2nd Ed.;* Oxford University Press: London, 1961.

7. March, J. *Advanced Organic Chemistry: Reactions, Mechanisms, and Structure*; McGraw-Hill, Inc.: New York, 1977.

8. Gomberg, M. *J. Am. Chem. Soc*. **1900**, *22*, 757.

9. McBride, J. M. *Tetrahedron*, **1974**, *30*, 2009.

10. Neumann, W. P.; Uzick, W.; Zarkadis, A. K. *J. Am. Chem. Soc*. **1986**, *108*, 3762.

11. (a) Dunnebacke, D.; Neumann, W. P., Penenory, A.; Stewen, U. *Chem. Ber.* **1989**, *122*, 533. (b) Rajca, A.; Utamapanya, S. *J. Am. Chem. Soc*. **1993**, *115*, 2396. (c) Schlenk, W. *Liebigs Ann*. **1910**, *372*, 1. (d) Gomberg, M. *Ber. dt. Chem. Ges*. **1904**, *37*, 1640.

12. (a) Ballester, M. *Acc. Chem. Res*. **1985**, *18*, 380. (b) Ballester, M.; Riera-Figueras, J.; Castaner, J.; Badfa, C.; Monso, J. M. *J. Am. Chem. Soc*. **1971**, *93*, 2215.

13. Culshaw, P. N.; Walton, J. C.; Hughes, L.; Ingold, K. U. *J. Chem. Soc. Perkin Trans. 2* **1993**, 879.

14. Sitzmann, H.; Bock, H.; Boese, R.; Dezember, T.; Havlas, Z.; Kaim, W.; Moscherosch, M.; Zanathy, L. *J. Am. Chem. Soc*. **1993**, *115*, 12003.

15. Reid, D. H. *Quart. Rev.* **1965**, *19*, 274.

16. Goto, K.; Kubo, T.; Yamamoto, K.; Nakasuji, K.; Sato, K.; Shiomi, D.; Takui, T.; Kubota, M.; Kobayashi, T.; Yakusi, K.; Ouyang, J. *J. Am. Chem. Soc*. **1999**, *121*, 1619.

17. Koutentis, P. A.; Chen, Y.; Cao, Y.; Best, T. P.; Itkis, M. E.; Beer, L.; Oakley, R. T.; Cordes, A. W.; Brock, C. P.; Haddon, R. C. *J. Am. Chem. Soc*. **2001**, *123*, 3864.

18. Zheng, S.; Lan, J.; Khan, S. I.; Rubin, Y. *J. Am. Chem. Soc*. **2003**, *125*, 5786.

19. Beer, L.; Mandal, S. K.; Reed, R. W.; Oakley, R. T.; Tham, F. S.; Donnadieu, B.; Haddon, R. C. *Cryst. Growth Des*. **2007**, *7*, 802.

20. Altwicker, E. R. *Chem. Rev*. **1967**, *67*, 475.

21. (a) Wright, J. S.; Johnson, E. R.; Dilabio, G. A. *J. Am. Chem. Soc*. **2001**, *123*, 1173. (b) Wright, J. S.; Carpenter, D. J.; McKay, D. J.; Ingold, K. U. *J. Am. Chem. Soc*. **1997**, *119*, 4245.

22. Coppinger, G. M. *J. Am. Chem. Soc*. **1957**, *79*, 501.

23. Novak, I.; Kovač, B. *Chem. Phys. Lett.* **2005**, *413*, 351.

24. Ballester, M.; Castañer, J.; Olivella, S. *Tetrahedran Lett*. **1974**, *7*, 615.

25. (a) Poirier, R. H.; Kahler, E. J.; Benington, F. *J. Org. Chem*. **1952**, *17*, 1437. (b) Chen, M. M.; Sane, K. V.; Walter, R. I.; Weil, J. A. *J. Phys. Chem*. **1961**, *65*, 713. (c) Ionita, P. *Chem. Pap*. **2005**, *59*, 11.

26. (a) Kuhn, R.; Trischmann, H. *Angew. Chem., Int. Ed. Engl.* **1963**, *3*, 155. (b) Kuhn, R.; Trischmann, H. *Monatshefte fuer Chemie* **1964**, *95*, 457.

27. (a) Neugebauer, F. A.; Fischer, H. *Angew. Chem. Int. Ed. Engl*. **1980**, *19*, 724. (b) Neugebauer, F. A.; Fischer, H.; Siegel, R. *Chem. Ber*. **1988**, *121*, 815.

28. (a) Keana, J. F. W. *Chem. Rev*. **1978**, *78*, 37. (b) Yao, M.; Asakura, S.; Abe, M.; Inoue, H.; Yoshioka, N. *Cryst. Growth Des.* **2005**, *5*, 413.

29. Griffith, O. H.; Waggoner, A. S. *Acc. Chem. Res*. **1969**, *2*, 17.

30. (a) Ullman, E. F.; Osiecki, J. H.; Boocock, D. G. B.; Darcy, R. *J. Am. Chem. Soc*. **1972**, *94*, 7049. (b) Osiecki, J. H.; Ullman, E. F. *J. Am. Chem. Soc*. **1968**, *90*, 1078. (c) Brough, P.; Chiarelli, R.; Pécaut, J.; Rassat, A.; Rey, P. *Chem. Commun*. **2003**, 2722.

31. Pauling, L. *The Nature of the Chemical Bond, 3rd Ed.;* Cornell University, Ithaca, NY, 1960.

32. (a) Miura, Y.; Katsura, Y.; Kinoshita, M. *Chem. Lett*. **1977**, 409. (b) Miura, Y.; Asada, H.; Kinoshita, M. *Chem. Lett*. **1978**, 1085. (c) Miura, Y.; Tanaka, A. *J. Chem. Soc., Chem. Commun*. **1990**, 441.

33. Oakley, R. T. *Prog. Inorg. Chem*. **1988**, *36*, 299.

34. (a) Vegas, A.; Pérez-Salazar, A.; Banister, A. J.; Hey, R. G. *J. Chem. Soc., Dalton Trans*. **1980**, 1812. (b) Cordes, A. W.; Haddon, R. C.; Hicks, R. G.; Oakley, R. T.; Palstra, T. T. M. *Inorg. Chem*. **1992**, *31*, 1802. (c) Cordes, A. W.; Bryan, C. D.; Davis, W. M.; Delaat, R. H.; Glarum, S. H.; Goddard, J. D.; Haddon, R. C.; Hicks, R. G.; Kennepohl, D. K.; Oakley, R. T.; Scott, S. R.; Westwood, N. P. C. *J. Am. Chem. Soc*. **1993**, *115*, 7232. (d) Cordes, A. W.; Haddon, R. C.; Hicks,

R. G.; Kennepohl, D. K.; Oakley, R. T.; Palstra, T. T. M.; Schneemeyer, L. F.; Scott, S. R.; Waszczak, J. V. *Chem. Mater*. **1993**, *5*, 820. (e) Cordes, A. W.; Haddon, R. C.; Hicks, R. G.; Kennepohl, D. K.; Oakley, R. T.; Schneemeyer, L. F.; Waszczak, J. V. *Inorg. Chem*. **1993**, *32*, 1554. (f) Bryan, C. D.; Cordes, A. W.; Haddon, R. C.; Hicks, R. G.; Oakley, R. T.; Palstra, T. T. M; Perel, A. J. *J. Chem. Soc., Chem. Commun*. **1994**, 1447. (g) Clarke, C. S.; Haynes, D. A.; Rawson, J. M.; Bond, A. D. *Chem. Commun*. **2003**, 2774. (h) Hofs, H. U.; Bats, J. W.; Gleiter, R.; Hartmann, G.; Mews, R.; Eckertmaksic, M.; Oberhammer, H.; Sheldrick, G. M. *Chem. Ber*. **1985**, *118*, 3781. (i) Banister, A. J.; Hansford, M. I.; Hauptman, Z. V.; Wait, S. T.; Clegg, W. *J. Chem. Soc., Dalton Trans*. **1989**, 1705. (j) Cordes, A. W.; Goddard, J. D.; Oakley, R. T.; Westwood, N. P. C. *J. Am. Chem. Soc*. **1989**, *111*, 6147. (k) Barclay, T. M.; Cordes, A. W.; George, N. A.; Haddon, R. C.; Itkis, M. E.; Oakley, R. T. *Chem. Commun*. **1999**, 2269.

35. Rawson, J. M.; Alberola, A.; Whalley, A. *J. Mater. Chem*. **2006**, *16*, 2560.

36. (a) Banister, A. J.; Bricklebank, N.; Clegg, W.; Elsegood, M. R. J.; Gregory, C. I.; Lavender, I.; Rawson, J. M.; Tanner, B. K. *J. Chem. Soc., Chem. Commun*. **1995**, 679. (b) Banister, A. J.; Bricklebank, N.; Lavender, I.; Rawson, J. M.; Gregory, C. I.; Tanner, B. K.; Clegg, W.; Elsegood, M. R. J.; Palacio, F. *Angew. Chem., Int. Ed. Engl*. **1996**, *35*, 2533. (c) Banister, A. J.; Batsanov, A. S.; Dawe, O. G.; Herbertson, P. L.; Howard, J. A. K.; Lynn, S.; May, I.; Smith, J. N. B.; Rawson, J. M.; Rogers, T. E.; Tanner, B. K.; Antorrena, G.; Palacio, F. *J. Chem. Soc., Dalton Trans*. **1997**, 2539. (d) Antorrena, G.; Davies, J. E.; Hartley, M.; Palacio, F.; Rawson, J. M.; Smith, J. N. B.; Steiner, A. *Chem. Commun*. **1999**, 1393.

37. Burford, N.; Passmore, J.; Schriver, M. J. *J. Chem. Soc., Chem. Commun*. **1986**, 140. (b) Passmore, J.; Sun, X. P.; Parsons, S. *Can. J. Chem*. **1992**, *70*, 2972. (c) Aherne, C.; Banister, A. J.; Luke, A. W.; Rawson, J. M.; Whitehead, R. J. *J. Chem. Soc., Dalton Trans*. **1992**, 1277.

38. (a) Wolmershäuser, G.; Kraft, G. *Chem. Ber*. **1990**, *123*, 881. (b) Brownridge, S.; Du, S. B.; Fairhurst, S. A.; Haddon, R. C.; Oberhammer, H.; Parsons, S.; Passmore, J.; Schriver, M. J.; Sutcliffe, L. H.; Westwood, N. P. C. *J. Chem. Soc., Dalton Trans*. **2000**, 3365. (c) Awere, E. G.; Burford, N.; Mailer, C.; Passmore, J.; Schriver, M. J.; White, P. S.; Banister, A. J.; Oberhammer H.; Sutcliffe, L. H. *J. Chem. Soc., Chem. Commun*. **1987**, 66. (d) Awere, E. G.; Burford, N.; Haddon, R. C.; Parsons, S.; Passmore, J.; Waszczak, J. V.; White, P. S. *Inorg. Chem*. **1990**, *29*, 4821.

39. Barclay, T. M.; Cordes, A. W.; George, N. A.; Haddon, R. C.; Oakley, R. T.; Palstra, T. T. M.; Patenaude, G. W.; Reed, R. W.; Richardson, J. F.; Zhang, H. *Chem. Commun*. **1997**, 873.

40. (a) Wolmershäuser, G.; Johann, R. *Angew. Chem., Int. Ed. Engl*. **1989**, *28*, 920. (c) Fujita, W.; Awaga, K. *Science* **1999**, *286*, 261. (d) McManus, C. D.; Rawson, J. M.; Feeder, N.; van Duijn, J.; McInnes, E. J. L.; Novoa, J. J.; Burriel, R.; Palacio, F.; Oliete, P. *J. Mater. Chem*. **2001**, *11*, 1992. (e) Heckmann, G.; Johann, R.; Kraft, G.; Wolmershäuser, G. *Synth. Met*. **1991**, *43*, 3287.

41. (a) Barclay, T. M.; Cordes, A. W.; George, N. A.; Haddon, R. C.; Itkis, M. E.; Mashuta, M. S.; Oakley, R. T.; Patenaude, G. W.; Reed, R. W.; Richardson, J. F.; Zhang, H. *J. Am. Chem. Soc*. **1998**, *120*, 352. (b) Brusso, J. L.; Clements, O. P.; Haddon, R. C.; Itkis, M. E.; Leitch, A. A.; Oakley, R. T.; Reed, R. W.; Richardson, J. F. *J. Am. Chem. Soc*. **2004**, *126*, 8256.

42. Matsuzaki, H.; Fujita, W.; Awaga, K.; Okamoto, H. *Phys. Rev. Lett*. **2003**, 91, 017403.

43. (a) Oakley, R. T.; Reed, R. W.; Robertson, C. M.; Richardson, J. F. *Inorg. Chem*. **2005**, *44*, 1837. (b) Barclay, T. M.; Cordes, A. W.; Haddon, R. C.; Itkis, M. E.; Oakley, R. T.; Reed, R. W.; Zhang, H. *J. Am. Chem. Soc*. **1999**, *121*, 969. (c) Barclay, T. M.; Beer, L.; Cordes, A. W.; Oakley, R. T.; Preuss, K. E.; Taylor, N. J.; Reed, R. W. *Chem. Commun*. **1999**, 531.

44. Beer, L.; Cordes, A. W.; Haddon, R. C.; Itkis, M. E.; Oakley, R. T.; Reed, R. W.; Robertson, C. M. *Chem. Commun*. **2002**, 1872.

45. (a) Beer, L.; Britten, J. F.; Brusso, J. L.; Cordes, A. W.; Haddon, R. C.; Itkis, M. E.; MacGregor, D. S.; Oakley, R. T.; Reed, R. W.; Robertson, C. M. *J. Am. Chem. Soc*. **2003**, *125*, 14394. (b) Beer, L.; Brusso, J. L.; Cordes, A. W.; Haddon, R. C.; Itkis, M. E.; Kirschbaum, K.; MacGregor, D. S.; Oakley, R. T.; Pinkerton, A. A.; Reed, R. W. *J. Am. Chem. Soc*. **2002**, *124*, 9498. (c) Beer, L.; Brusso, J. L.; Cordes, A. W.; Godde, E.; Haddon, R. C.; Itkis, M. E.; Oakley, R. T.; Reed, R. W. *Chem. Commun*. **2002**, 2562. (d) Beer, L.; Britten, J. F.; Clements, O. P.; Haddon, R. C.; Itkis, M. E.; Matkovich, K. M.; Oakley R. T. *Chem. Mater*. **2004**, *16*, 1564.

46. (a) Boeré, R. T.; Oakley, R. T.; Reed, R. W.; Westwood, N. P. C. *J. Am. Chem. Soc*. **1989**, *111*, 1180. (b) Boeré, R. T.; Roemmele, T. L. *Phosphorus, Sulfur, and Silicon* **2004**, *179*, 875.

47. (a) Cordes, A. W.; Hayes, P. J.; Josephy, P. D.; Koenig, H.; Oakley, R. T.; Pennington, W. P. *J. Chem. Soc., Chem. Commun*. **1984**, 1021. (b) Hayes, P. J.; Oakley, R. T.; Cordes, A. W.; Pennington, W. T. *J. Am. Chem. Soc*. **1985**, *107*, 1346.

48. (a) Cordes, A. W.; Haddon, R. C.; Hicks, R. G.; Oakley, R. T.; Palstra, T. T. M. *Inorg. Chem*. **1992**, *31*, 1802. (b) Belluz, P. D.; Cordes, A. W.; Kristof, E. M.; Kristof, P. V.; Liblong, S. W.; Oakleyl, R. T. *J. Am. Chem. Soc*. **1989**, *111*, 9276. (c) Cordes, A. W.; Glarum, S. H.; Haddon, R. C.; Hallford, R.; Hicks, R. G.; Kennepohl, D. K.; Oakley, R. T.; Palstra, T. T. M.; Scott, S. R. *J. Chem. Soc., Chem. Commun*. **1992**, 1265. (d) Cordes, A. W.; Haddon, R. C.; Hicks, R. G.; Oakley, R. T.; Palstra, T. T. M.; Schneemeyer, L. F.; Waszczak, J. V. *J. Am. Chem. Soc*. **1992**, *114*, 1729. (e) Davis, W. M.; Hicks, R. G.; Oakley, R. T.; Zhao, B. Y.; Taylor, N. J. *Can. J. Chem*. **1993**, *71*, 180.

49. Feeder, N.; Less, R. J.; Rawson, J. M.; Oliete, P.; Palacio, F. *Chem. Commun*. **2000**, 2449.

50. Oakley, R. T.; Reed, R. W.; Cordes, A. W.; Craig, S. L.; Graham, J. B. *J. Am. Chem. Soc*. **1987**, *109*, 7745.

51. Bestari, K.; Cordes, A. W.; Oakley, R. T.; Young, K. M. *J. Am. Chem. Soc*. **1990**, *112*, 2249.

52. Fleming, I. *Frontier Orbitals and Organic Chemical Reactions;* John Wiley & Sons: Great Britain, 1976.

53. (a) Zimmer, H.; Lankin, D. C.; Horgan, S. W. *Chem. Rev*. **1971**, *71*, 229. (b) de Nooy, A. E. J.; Besemer, A. C.; van Bekkum, H. *Synthesis* **1996**, 1153. (c) Sheldon, R. A.; Arends, I. W. C. E.; ten Brink, G.; Dijksman, A. *Acc. Chem. Res*. **2002**, *35*, 774.

54. (a) Wright, J. S.; Carpenter, D. J.; McKay, D. J.; Ingold, K. U. *J. Am. Chem. Soc*. **1997**, *119*, 4245. (b) Scaiano, J. C.; Martin, A.; Yap, G. P. A.; Ingold, K. U. *Org. Lett*. **2000**, *2*, 899. (c) Wright, J. S.; Johnson, E. R.; Dilabio, G. A. *J. Am. Chem. Soc*. **2001**, *123*, 1173. (d) Font-Sanchis, E.; Aliaga, C.; Focsaneanu, K. -S.; Scaiano, J. C. *Chem. Commun*. **2002**, 1576. (e) Watanabe, A.; Noguchi, N.; Fujisawa, A.; Kodama, T.; Tamura, K.; Cynshi, O.; Niki, E. *J. Am. Chem. Soc*. **2000**, *122*, 5438.

55. (a) Hawker, C. J.; Bosman, A. W.; Harth, E. *Chem. Rev*. **2001**, *101*, 3661. (b) Georges, M. K.; Veregin, R. P. N.; Kazmaier, P. M.; Hamer, G. K. *Macromolecules* **1993**, *26*, 2987. (c) Dollin, M.; Szkurhan, A. R.; Georges, M. K. *J. Polym. Sci., Part A: Polym. Chem*. **2007**, *45*, 5487.

56. (a) Stubbe, J.; van der Donk, W. A. *Chem. Rev*. **1998**, *98*, 705. (b) Stubbe, J. *Chem. Commun*. **2003**, 2511. (c) Zweier, J. L.; Kuppusamy, P. *Proc. Natl. Acad. Sci. USA* **1988**, *85*, 5703.

57. (a) Yokoyama, H.; Ono, T.; Yoshimura, T. *Appl. Magn. Reson*. **2007**, *32*, 283. (b) Yardanov, A. T.; Yamada, K.; Krishna, M. C.; Mitchell, J. B.; Woller, E.; Cloninger, M.; Brechbiel, M. W. *Angew. Chem. Int. Ed.* **2001**, *40*, 2690. (c) Reddy, T. J.; Iwama, T.; Halpern, H. J.; Rawal, V. H. *J. Org. Chem*. **2002**, *67*, 4635.

58. (a) Taylor, P.; Lahti, P. M.; Carroll, J. B.; Rotello, V. M. *Chem. Commun*. **2005**, 895. (b) Keana, J. F. W. *Chem. Rev*. **1978**, *78*, 37. (c) Stroh, C.; Mayor, M.; von Hänisch, C. *Tetrahedron Lett.* **2004**, *45*, 9623.

59. (a) Janzen, E. G. *Acc. Chem. Res*. **1971**, *4*, 31. (b) Konorev, E. A.; Tarpey, M. M.; Joseph, J.; Baker, J. E.; Kalyanaraman, B. *Free Radical Biology & Medicine* **1995**, *18*, 169. (c) Beckwith, A. L. J.; Bowry, V. W.; Ingold, K. U. *J. Am. Chem. Soc*. **1992**, *114*, 4983. (d) Rehorek, D. *Chem. Soc. Rev*. **1991**, *20*, 341.

60. (a) Zienkiewicz, J.; Fryszkowska, A.; Zienkiewicz, K.; Guo, F.; Kaszynski, P.; Januszko, A.; Jones, D. *J. Org. Chem*. **2007**, *72*, 3510. (b) Tamura, R.; Uchida, Y.; Ikuma, N. *J. Mater. Chem*. **2008**, *18*, 2872. (c) Uchida, Y.; Tamura, R.; Ikuma, N.; Shimono, S.; Yamauchi, J.; Shimbo, Y.; Takezoe, H.; Aoki, Y.; Nohira, H. *J. Mater. Chem*. **2009**, *19*, 415.

61. Hearns, N. G. R.; Preuss, K. E.; Richardson, J. F.; Bin-Salamon, S. *J. Am. Chem. Soc*. **2004**, *126*, 9942.

62. (a) Hicks, R. G.; Koivisto, B. D.; Lemaire, M. T. *Org. Lett*. **2004**, *6*, 1887. (b) Hicks, R. G. *Aust. J. Chem*. **2001**, *54*, 597.

63. Alberola, A.; Less, R. J.; Pask, C. M.; Rawson, J. M.; Palacio, F.; Oliete, P.; Paulsen, C.; Yamaguchi, A.; Farley, R. D.; Murphy, D. M. *Angew. Chem., Int. Ed.* **2003**, *42*, 4782.

64. (a) Robertson, C. M.; Myles, D. J. T.; Leitch, A. A.; Reed, R. W.; Dooley, B. M.; Frank, N. L.; Dube, P. A.; Thompson, L. K.; Oakley, R. T. *J. Am. Chem. Soc.* **2007**, *129*, 12688. (b) Robertson, C. M.; Leitch, A. A.; Cvrkalj, K.; Reed, R. W.; Myles, D. J. T.; Dube, P. A.; Oakley, R. T. *J. Am. Chem. Soc*. **2008**, *130*, 8414. (c) Robertson, C. M.; Leitch, A. A.; Cvrkalj, K.; Myles, D. J. T.; Reed, R. W.; Dube, P. A.; Oakley, R. T. *J. Am. Chem. Soc*. **2008**, *130*, 14791.

65. Banister, A. J.; Bricklebank, N.; Lavender, I.; Rawson, J. M.; Gregory, C. I.; Tanner, B. K.; Clegg, W.; Elsegood, M. R. J.; Palacio, F. *Angew. Chem., Int. Ed.* **1996**, *35*, 2533.

66. Mito, M.; Nakano, H.; Kawae, T.; Hitaka, M.; Takagi, S.; Deguchi, H.; Suzuki, K.; Mukai, K.; Takeda, K. *J. Phys. Soc. Jpn*. **1997**, *66*, 2147.

67. Leitch, A. A.; Brusso, J. L.; Cvrkalj, K.; Reed, R. W.; Robertson, C. M.; Dube, P. A.; Oakley, R. T. *Chem. Commun*. **2007**, 3368.

68. Kahn, O.; Matinez, C. J. *Science* **1998**, *279*, 44.

69. (a) Itkis, M. E.; Chi, X.; Cordes, A. W.; Haddon, R. C. *Science* **2002**, *296*, 1443. (b) Fujita, W.; Awaga, K. *Synth. Met.* **2001**, *121*, 1767.

70. Haddon, R. C. *Nature* **1975**, *256*, 394.

71. (a) Naber, W. J. M.; Faez, S.; van der Wiel, W. G. *J. Phys. D: Appl. Phys*. **2007**, *40*, R205. (b) Rocha, A. R.; Garcia-Suárez, V. M.; Bailey, S. W.; Lambert, C. J.; Ferrer, J.; Sanvito, S. *Nat. Mat.* **2005**, *4*, 335. (c) Wolf, S. A.; Awschalom, D. D.; Buhrman, R. A.; Daughton, J. M.; von Molnár, S.; Roukes, M. L.; Chtchelkanova, A. Y.; Treger, D. W. *Science* **2001**, *294*, 1488. (d) Prinz, G. A. *Science* **1998**, *282*, 1660. (e) Xiong, Z. H.; Wu, D.; Vardeny, V.; Shi, J. *Nature* **2004**, *427*, 821.

72. Jiles, D. *Introduction to Magnetism and Magnetic Materials*; Chapman and Hall: London, 1991.

73. (a) Miller, J. S.; Epstein, A. J. *Angew. Chem. Int. Ed. Engl*. **1994**, *33*, 385. (b) Miller, J. S. *Adv. Mater*. **2002**, *14*, 1105. (c) Blundell, S. J. *Contemporary Physics* **2007**, *48*, 275. (d) Blundell, S. J.; Pratt, F. L. *J. Phys.: Condens. Matter* **2004**, *16*, R771. (e) Itoh, K.; Kinoshita, M. *Molecular Magnetism: New Magnetic Materials*; Gordon and Breach Science Publishers: Japan, 2000.

74. (a) Murugesu, M.; Wernsdorfer, W.; Christou, G.; Brechin, E. K. *Polyhedron* **2007**, *26*, 1845. (b) Nihei, M.; Yoshida, A.; Koizumi, S.; Oshio, H. *Polyhedron* **2007**, *26*, 1997. (c) Stamatotos, T. C.; Abboud, K. A.; Wernsdorfer, W.; Christou, G. *Polyhedron* **2007**, *26*, 2042.

75. (a) Rahman, B.; Kanbara, K.; Akutsu, H.; Yamada, J.; Nakatsuji, S. *Polyhedron* **2007**, *26*, 2287. (b) Koizumi, K.; Shoji, M.; Kitagawa, Y.; Takeda, R.; Yamanaka, S.; Kawakami, T.; Okumura, M.; Yamaguchi, K. *Polyhedron* **2007**, *26*, 2135. (c) Harvey, M. D.; Pace, J. T.; Yee, G. T. *Polyhedron* **2007**, *26*, 2037.

76. (a) Kaneko, Y.; Kajiwara, T.; Yamane, H.; Yamashita, M. *Polyhedron* **2007**, *26*, 2074. (b) Hearns, N. G. R.; Hesp, K. D.; Jennings, M.; Korčok, J. L.; Preuss, K. E.; Smithson, C. S. *Polyhedron* **2007**, *26*, 2047. (c) Tanaka, K.; Furuichi, K.; Kozaki, M.; Suzuki, S.; Shiomi, D.; Sato, Z.; Takui, T.; Okada, K. *Polyhedron* **2007**, *26*, 2021. (d) Nihei, M.; Maeshima, T.; Kose, Y.; Oshio, H. *Polyhedron* **2007**, *26*, 1993. (e) Gatteschi, D.; Bogani, L.; Cornia, A.; Mannini, M.; Sorace, L.; Sessoli, R. *Solid State Sci.* **2008**, *10*, 1701.

77. (a) Sessoli, R.; Tsai, H. -L.; Schake, A. R.; Wang, S.; Vincent, J. B.; Folting, K.; Gatteschi, D.; Christou, G.; Hendrickson, D. N. *J. Am. Chem. Soc*. **1993**, *115*, 1804. (b) Sessoli, R.; Gatteschi, D.; Caneschi, A.; Novak, M. A. *Nature* **1993**, *365*, 141. (c) Lis, T. *Acta. Cryst*. **1980**, *B36*, 2042.

78. Caneschi, A.; Gatteschi, D.; Renard, J. P.; Rey, P.; Sessoli, R. *Inorg. Chem*. **1989**, *28*, 1976.

79. (a) Manriquez, J. M.; Yee, G. T.; McLean, R. S.; Epstein, A. J.; Miller, J. S. *Science* **1991**, *252*, 1415. (b) Miller, J. S.; Calabrese, J. C.; Epstein, A. J.; Bigelow, R. W.; Zhang, J. H.; Reiff, W. M. *J. Chem. Soc., Chem. Commun*. **1986**, 1026.

80. Rittenberg, D. K.; Sugiura, K.; Sakata, Y.; Mikami, S.; Epstein, A. J.; Miller, J. S. *Adv. Mater.* **2000**, *12*, 126.

81. Sugimoto, T.; Tsuji, M.; Suga, T.; Hosoito, N.; Ishikawa, M.; Takeda, N.; Shiro, M. *Mol. Cryst. Liq. Cryst*. **1995**, *272*, 183.

82. (a) Sakakibara, T.; Miyazaki, Y.; Ishida, T.; Nogami, N.; Sorai, M. *J. Phys. Chem. B* **2002**, *106*, 6390. (b) Mito, M.; Deguchi, H.; Tanimoto, T.; Kawae, T.; Nakatsuji, S.; Morimoto, H.; Anzai, H.; Nakao, H.; Murakami, Y.; Takeda, K. *Phys. Rev. B* **2003**, *67*, 024427. (c) Rajca, A.; Utamapanya, S. *J. Am. Chem. Soc*. **1993**, *115*, 2396. (d) Murata, H.; Miyazaki, Y.; Inaba, A.; Paduan-Filho, A.; Bindilatti, V.; Oliveira, N. F.; Delen, Z.; Lahti, P. M. *J. Am. Chem. Soc*. **2008**, *130*, 186.

83. Fujita, W.; Awaga, K. *Chem. Phys. Lett*. **2002**, *357*, 385.

84. Allemand, P.; Khemani, K. C.; Koch, A.; Wudl, F.; Holczer, K.; Donovan, S.; Grunner, G.; Thompson, J. D. *Science* **1991**, *253*, 301.

85. (a) Takahashi, M.; Turek, P.; Nakazawa, Y.; Tamura, M.; Nozawa, K.; Shiomi, D.; Ishikawa, M.; Kinoshita, M. *Phys. Rev. Lett*. **1991**, *67*, 746. (b) Tamura, T.; Nakazawa, Y.; Shiomi, D.; Nozawa, K.; Hosokoshi, Y.; Ishikawa, M.; Takahashi, M.; Kinoshita, M. *Chem. Phys. Lett*. **1991**, *186*, 401.

86. Chiarelli, R.; Novak, M. A.; Rassat, A.; Tholence, J. L. *Nature* **1993**, *363*, 147.

87. Alberola, A.; Less, R. J.; Pask, C. M.; Rawson, J. M.; Palacio, F.; Oliete, P.; Paulsen, C.; Yamaguchi, A.; Farley, R. D.; Murphy, D. M. *Angew. Chem. Int. Ed.* **2003**, *42*, 4782.

88. Mito, M.; Kawae, T.; Takeda, K.; Takagi, S.; Matsushita, Y.; Deguchi, H.; Rawson, J. M.; Palacio, F. *Polyhedron* **2001**, *20*, 1509.

89. (a) Kremer, R. K.; Kanellakobulos, B.; Bele, P.; Brunner, H.; Neugebauer, F. *Chem. Phys. Lett*. **1994**, *230*, 255. (b) Mukai, K., Nuwa, M.; Morishita, T.; Muramatsu, T.; Kobayashi, T. C.; Amaya, K. *Chem. Phys. Lett*. **1997**, *272*, 501.

90. McConnell, H. M. *J. Chem. Phys*. **1963**, *39*, 1910.

91. Salem, L. *Electrons in Chemical Reactions; First Principles*; John Wiley & Sons: New York, 1982.

92. (a) Kahn, O.; Briat, B. *J. Chem. Soc., Faraday Trans*. **1976**, *2*, 268. (b) Verdaguer, M. *Polyhedron* **2001**, *20*, 1115. (c) Kahn, O. *Molecular Magnetism*; Wiley-VCH: New York, 1993.

93. Murrell, J. N.; Kettle, S. F. A.; Tedder, J. M. *The Chemical Bond, 2nd Ed.*, John Wiley & Sons, Great Britian, 1985.

94. Atkins, P. W. *Molecular Quantum Mechanics, 2nd Ed.*; Oxford University Press: New York, 1983.

95. Deumal, M.; Robb, M. A.; Novoa, J. J. *Prog. Theo. Chem. Phys*. **2007**, *16*, 271.

96. (a) Noodleman, L.; Norman, J. G. *J. Chem. Phys*. **1979**, *70*, 4903. (b) Noodleman, L. *J. Chem. Phys*. **1981**, *74*, 5737.

97. Heisenberg, W. *Z. Phys*. **1926**, *38*, 411.

98. (a) Novoa, J. J.; Deumal, M. *Struct. Bonding* **2001**, *100*, 33. (b) Jornet, J.; Deumal, M.; Ribas-Ariño, J.; Bearpark, M. J.; Robb, M. A.; Hicks, R. G.; Novoa, J. J. *Chem. Eur. J*. **2006**, *12*, 3995.

99. (a) Rawson, J. M.; Luzon, J.; Palacio, F. *Coord. Chem. Rev*. **2005**, *249*, 2631. (b) Luzon, J.; Campo, J.; Palacio, F.; McIntyre, G. J.; Rawson, J. M. *Polyhedron* **2005**, *24*, 2579. (c) Deumal, M.; LeRoux, S.; Rawson, J. M.; Robb, M. A.; Novoa, J. J. *Polyhedron* **2007**, *26*, 1949.

100. (a) Decken, A.; Mattar, S. M.; Passmore, J.; Shuvaev, D. V.; Thompson, L. K. *Inorg. Chem*. **2006**, *45*, 3878. (b) Leitch, A. A.; Oakley, R. T.; Reed, R. W.; Thompson, L. K. *Inorg. Chem*. **2007**, *46*, 6261.

101. Robertson, C. M.; Leitch, A. A.; Cvrkalj, K.; Myles, D. J. T.; Reed, R. W.; Dube, P. A.; Oakley, R. T. *J. Am. Chem. Soc*. **2008**, *130*, 14791.

102. Takano, Y.; Taniguchi, T.; Isobe, H.; Kubo, T.; Morita, Y.; Yamamoto, K.; Nakasuji, K.; Takui, T.; Yamaguchi, K. *J. Am. Chem. Soc*. **2002**, *124*, 11122.

103. Melby, L. R.; Harder, R. J.; Hertler, W. R.; Mahler, W.; Benson, R. E.; Mochel, W. E. *J. Am. Chem. Soc*. **1962**, *84*, 3374.

104. Ferraro, J. R.; Williams, J. M. *Introduction to Synthetic Electrical Conductors*; Academic Press: Florida, 1987.

105. Torrance, J. B. *Acc. Chem. Res*. **1979**, *12*, 79.

106. Siemons, W. J.; Bierstedt, P. E.; Kepler, R. G. *J. Chem. Phys*. **1963**, *39*, 3523.

107. Melby, L. R. *Can. J. Chem*. **1965**, *43*, 1448.

108. Garito, A. F.; Heeger, A. J. *Acc. Chem. Res*. **1974**, *7*, 232.

109. Ferraris, J.; Cowan, D. O.; Walatka, V.; Peristein, J. H. *J. Am. Chem. Soc*. **1973**, *95*, 948.

110. (a) Bendikov, M.; Wudl, F.; Perepichka, D. F. *Chem. Rev*. **2004**, *104*, 4891. (b) Yamada, J.; Akutsu, H.; Nishikawa, H.; Kikuchi, K. *Chem. Rev*. **2004**, *104*, 5057.

111. Engler, E. M.; Patel, V. V. *J. Am. Chem. Soc*. **1974**, *96*, 7376.

112. (a) Geiser, U.; Schlueter, J. A. *Chem. Rev*. **2004**, *104*, 5203.(b) Kobayashi, H.; Cui, H.; Kobayashi, A. *Chem. Rev*. **2004**, *104*, 5265.

113. Bechgaard, K.; Jacobsen, C. S.; Mortensen, K.; Pedersen, H. J.; Thorup, N. *Solid State Commun*. **1980**, *33*, 1119.

114. (a) Williams, J. M.; Emge, T. J.; Wang, H. H.; Beno, M. A.; Copps, P. T.; Hall, L. N.; Carlson, K. D.; Crabtree, G. W. *Inorg. Chem*. **1984**, *23*, 2558. (b) Shibaeva, R. P.; Yagubskii, E. B. *Chem. Rev*. **2004**, *104*, 5347.

115. (a) Bechgaard, K.; Carneiro, K.; Rasmussen, F. B.; Rindorf, O. G.; Jacobsen, C. S.; Pedersen, H. J.; Scott, J. C. *J. Am. Chem. Soc*. **1981**, *103*, 2440. (b) Jérome, D.; Mazaud, A.; Ribault, M.; Bechgaard, K. *J. Physique Lett*. **1980**, *41*, 95.

116. Williams, J. M.; Wang, H. H.; Beno, M. A.; Emge, T. J.; Sowa, L. M.; Copps, P. T.; Behroozi, F.; Hall, L. N.; Carlson, K. D.; Crabtree, G. W. *Inorg. Chem*. **1984**, *23*, 3839.

117. (a) Tanaka, H.; Okano, Y.; Kobayashi, H.; Suzuki, W.; Kobayashi, A. *Science* **2001**, *291*, 285. (b) Tanaka, H.; Tokumoto, M.; Ishibashi, S.; Graf, D.; Choi, E.; Brooks, J. S.; Yasuzuka, S.; Okano, Y.; Kobayashi, H.; Kobayashi, A. *J. Am. Chem. Soc*. **2004**, *126*, 10518. (c) Kobayashi, A.; Sasa, M.; Suzuki, W.; Fujiwara, E.; Tanaka, H.; Tokumoto, M.; Okano, Y.; Fujiwara, H.; Kobayashi, H. *J. Am. Chem. Soc*. **2004**. *126*, 426.

118. Kobayashi, A.; Fujiwara, E.; Kobayashi, H. *Chem. Rev*. **2004**, *104*, 5243.

119. (a) Coronado, E.; Gmez-Garca, C. J. *Chem. Rev*. **1998**, *98*, 273. (b) Coronodo, E.; Day, P. *Chem. Rev*. **2004**, *104*, 5419.

120. Coronado, E.; Galán-Mascarós, J. R.; Gómez-Garcia, C. J.; Laukhin, V. *Nature* **2000**, *408*, 447.

121. Shirakawa, H.; Louis, E. J.; MacDiarmid, A. G.; Chiang, C. K.; Heeger, A. J. *J. C. S. Chem. Comm*. **1977**, 578.

122. Chiang, C. K.; Druy, M. A.; Gau, S. C.; Heeger, A. J.; Louis, E. J.; MacDiarmid, A. G.; Park, Y. W.; Shirakawa, H. *J. Am. Chem. Soc*. **1978**, *100*, 1013.

123. Chiang, C. K.; Fincher, C. R.; Park, Y. W.; Heeger, A. J.; Shirakawa, H.; Louis, E. J.; Gau, S. C.; MacDiarmid, A. G. *Phys. Rev. Lett*. **1977**, *39*, 1098.

124. Deits, W.; Cukor, P.; Rubner, M.; Jopson, H. *Ind. Eng. Chem. Prod. Res. Dev*. **1981**, *20*, 696.

125. (a) Kanazawa, K. K.; Diaz, A. F.; Geiss, R. H.; Gill, W. D.; Kwak, J. F.; Logan, J. A.; Rabolt, J. F.; Street, G. B. *J. C. S. Chem. Comm*. **1979**, 854. (b) Benincori, T.; Brenna, E.; Sannicol, F.; Zotti, G.; Zecchin, S.; Schiavon, G.; Gatti, C.; Frigerio, G. *Chem. Mater*. **2000**, *12*, 1480.

126. (a) Kobayashi, M.; Chen, J.; Chung, T. -C.; Moraes, F.; Heeger, A. J.; Wudl, F. *Synth. Met*. **1984**, *9*, 77. (b) Ballarin, B.; Seeber, R.; Tassi, L.; Tonelli, D. *Synth. Met*. **2000**, *114*, 279. (c) Harima, Y.; Kunugi, Y.; Tang, H.; Yamashita, K.; Shiotani, M.; Ohshita, J.; Kunai, A. *Synth. Met*. **2000**, *113*, 173.

127. (a) Bourahla, A.; Saiter, J. M.; Vautier, C. *Mat. Chem. Phys*. **2001**, *69*, 163. (b) Ng, S. C.; Chan, H. S. O.; Ong, T. T.; Kumura, K.; Mazaki, Y.; Kobayashi, K. *Macromolecules* **1998**, *31*, 1221.

128. Walatka, V. V.; Labes, M. M.; Perlstein, J. H. *Phys. Rev. Lett*. **1973**, *31*, 1139.

129. Green, R. L.; Street, G. B.; Suter, L. *J. Phys. Rev. Lett*. **1975**, *34*, 577.

130. Labes, M. M.; Love, P.; Nichols, L. F. *Chem. Rev*. **1979**, *79*, 1.

131. (a) Cohen, M. J.; Garito, A. F.; Heeger, A. J.; MacDiarmid, A. G.; Mikulski, C. M.; Saran, M. S.; Kleppinger, J. *J. Am. Chem. Soc*. **1976**, *98*, 3844. (b) Stejny, J.; Dlugosz, J.; Keller, A. *J. Mater. Sci*. **1979**, *14*, 1291.

132. Whangbo, M, -H.; Hoffman, R.; Woodward, R. B. *Proc. R. Soc. Lond. A* **1979**, *366*, 23.

133. Wolmershäuser, G.; Brulet, C. R.; Street, G. B. *Inorg. Chem*. **1978**, *17*, 3586.

134. Cordes, A. W.; Haddon, R. C.; Oakley, R. T. *Phosphorus, Sulfur, Silicon and Related Elements* **2004**, *179*, 673.

135. Peierls, R. E. *Quantum Theory of Solids*; Oxford Press: London, 1955.

136. (a) Huang, J.; Kertesz, M. *J. Phys. Chem. A* **2007**, *111*, 6304. (b) Whangbo, M. *J. Chem. Phys*. **1979**, *70*, 4963. (c) Friedel, J.; Noguera, C. *Int. J. Quantum Chem*. **1983**, *23*, 1209.

137. Cox, P. A. *The Electronic Structure and Chemistry of Solids*; Oxford University Press: New York, 1987.

138. (a) Kaszynski, P. *J. Phys. Chem. A*, **2001**, *105*, 7626. (b) Boeré, R. T.; Roemmele, T. L. *Coord. Chem. Rev.* **2000***, 210*, 369. (b) Parker, V. D. *J. Am. Chem. Soc*. **1976**, *98*, 98.

139. (a) Pal, S. K.; Itkis, M. E.; Reed, R. W.; Oakley, R. T.; Cordes, A. W.; Tham, F. S.; Siegrist, T.; Haddon, R. C. *J. Am. Chem. Soc*. **2004**, *126*, 1478. (b) Chi, X.; Itkis, M. E.; Tham, F. S.; Oakley, R. T.; Cordes, A. W.; Haddon, R. C. *Int. J. Quant. Chem*. **2003**, *95*, 853. (c) Chi, X.; Itkis, M. E.; Reed, R. W.; Oakley, R. T.; Cordes, A. W.; Haddon, R. C. *J. Phys. Chem. B* **2002**, *106*, 8278.

140. Chi, X.; Itkis, M. E.; Patrick, B. O.; Barclay, T. M.; Reed, R. W.; Oakley, R. T.; Cordes, A. W.; Haddon, R. C. *J. Am. Chem. Soc*. **1999**, *121*, 10395.

141. Chi, X.; Itkis, M. E.; Kirschbaum, K.; Pinkerton, A. A.; Oakley, R. T.; Cordes, A. W.; Haddon, R. C. *J. Am. Chem. Soc*. **2001**, *123*, 4041.

142. (a) Pal, S. K.; Itkis, M. E.; Tham, F. S.; Reed, R. W.; Oakley, R. T.; Donnadieu, B.; Haddon, R. C. *J. Am. Chem. Soc*. **2007**, *129*, 7163. (b) Mandal, S. K.; Samanta, S.; Itkis, M. E.; Jensen, D. W.; Reed, R. W.; Oakley, R. T.; Tham, F. S.; Donnadieu, B.; Haddon, R. C. *J. Am. Chem. Soc*. **2006**, *128*, 1982. (c) Pal, S. K.; Itkis, M. E.; Tham, F. S.; Reed, R. W.; Oakley, R. T.; Haddon, R. C. *Science* **2005**, *309*, 281.

143. Pal, S. K.; Itkis, M. E.; Tham, F. S.; Reed, R. W.; Oakley, R. T.; Haddon, R. C. *J. Am. Chem. Soc*. **2008**, *130*, 3942.

144. (a) Haddon, R. C.; Wudl, F.; Kaplan, M. L.; Marshall, J. H.; Cais, R. E.; Bramwell, F. B. *J. Am. Chem. Soc*. **1978**, *100*, 7629. (b) Haddon, R. C.; Wudl, F.; Kaplan, M. L.; Marshall, J. H. *J. C. S. Chem. Comm*. **1978**, 429.

145. Beer, L.; Reed, R. W.; Robertson, C. M.; Oakley, R. T.; Tham, F. S.; Haddon, R. C. *Org. Lett*. **2008**, *10*, 3121.

146. (a) Neilands, O. *Mol. Cryst. Liq. Cryst*. **2001**, *355*, 331. (b) Balodis, K.; Khasanov, S.; Chong, C.; Maesato, M.; Yamochi, H.; Saito, G.; Neilands, O. *Synth. Met*. **2003**, *133*, 353. (c) Murata, T.; Balodis, K.; Saito, G. *Synth. Met*. **2008**, *158*, 497.

147. Fairhurst, S. A.; Johnson, K. M.; Sutcliffe, L. H.; Preston, K. F.; Banister, A. J.; Hauptman, Z. V.; Passmore, J. *J. Chem. Soc. Dalton Trans*. **1986**, 1465.

148. (a) Barclay, T. M.; Cordes, A. W.; Oakley, R. T.; Preuss, K. E.; Reed, R. W. *Chem. Mater*. **1999**, *11*, 164. (b) Barclay, T. M.; Burgess, I. J.; Cordes, A. W.; Oakley, R. T.; Reed, R. W. *Chem. Commun*. **1998**, 1939. (c) Cordes, A. W.; George, N. A.; Haddon, R. C.; Kennepohl, D. K.; Oakley, R. T.; Palstra, T. T. M.; Reed, R. W. *Chem. Mater*. **1996**, *8*, 2774.

149. Boeré, R. T.; Moock, K. H. *J. Am. Chem. Soc*. **1995**, *117*, 4755.

150. Leitch, A. A.; Brusso, J. L.; Cvrkalj, K.; Reed, R. W.; Robertson, C. M.; Dube, P. A.; Oakley, R. T. *Chem. Commun*. **2007**, 3368.

151. (a) Robertson, C. M.; Myles, D. J. T.; Leitch, A. A.; Reed, R. W.; Dooley, B. M.; Frank, N. L.; Dube, P. A.; Thompson, L. K.; Oakley, R. T. *J. Am. Chem. Soc*. **2007**, *129*, 12688. (b) Robertson, C. M.; Leitch, A. A.; Cvrkalj, K.; Reed, R. W.; Myles, D. J. T.; Dube, P. A.; Oakley, R. T. *J. Am. Chem. Soc*. **2008**, *130*, 8414.

152. Robertson, C. M.; Leitch, A. A.; Cvrkalj, K.; Myles, D. J. T.; Reed, R. W.; Dube, P. A.; Oakley, R. T. *J. Am. Chem. Soc*. **2008**, *130*, 14791.

References for Chapter 2

1. (a) Ullman, E. F.; Osiecki, J. H.; Boocock, D. G. B.; Darcy, R. *J. Am. Chem. Soc*. **1972**, *94*, 7049. (b) Osiecki, J. H.; Ullman, E. F. *J. Am. Chem. Soc*. **1968**, *90*, 1078. (c) Brough, P.; Chiarelli, R.; Pécaut, J.; Rassat, A.; Rey, P. *Chem. Commun*. **2003**, 2722.

2. (a) Kuhn, R.; Trischmann, H. *Monatshefte fuer Chemie* **1964**, *95*, 457. (b) Neugebauer, F. A.; Fischer, H. *Angew. Chem. Int. Ed. Engl*. **1980**, *19*, 724. (c) Neugebauer, F. A.; Fischer, H.; Siegel, R. *Chem. Ber*. **1988**, *121*, 815.

3. (a) Beer, L.; Britten, J. F.; Brusso, J. L.; Cordes, A. W.; Haddon, R. C.; Itkis, M. E.; MacGregor, D. S.; Oakley, R. T.; Reed, R. W.; Robertson, C. M. *J. Am. Chem. Soc*. **2003**, *125*, 14394. (b) Beer, L.; Brusso, J. L.; Cordes, A. W.; Haddon, R. C.; Itkis, M. E.; Kirschbaum, K.; MacGregor, D. S.; Oakley, R. T.; Pinkerton, A. A.; Reed, R. W. *J. Am. Chem. Soc*. **2002**, *124*, 9498. (c) Beer, L.; Brusso, J. L.; Cordes, A. W.; Godde, E.; Haddon, R. C.; Itkis, M. E.; Oakley, R. T.; Reed, R. W. *Chem. Commun*. **2002**, 2562. (d) Beer, L.; Britten, J. F.; Clements, O. P.; Haddon, R. C.; Itkis, M. E.; Matkovich, K. M.; Oakley R. T. *Chem. Mater*. **2004**, *16*, 1564.

4. Cordes, A. W.; Mingie, J. R.; Oakley, R. T.; Reed, R. W.; Zhang, H. *Can. J. Chem*. **2001**, *79*, 1352.

5. (a) Boeré, R. T.; Oakley, R. T.; Reed, R. W.; Westwood, N. P. C. *J. Am. Chem. Soc*. **1989**, *111*, 1180. (b) Boeré, R. T.; Roemmele, T. L. *Phosphorus, Sulfur, and Silicon* **2004**, *179*, 875.

6. Hayes, P. J.; Oakley, R. T.; Cordes, A. W.; Pennington, W. T. *J. Am. Chem. Soc*. **1985**, *107*, 1346.

7. (a) Zienkiewicz, J.; Kaszynski, P.; Young, V. G., Jr. *J. Org. Chem*. **2004**, *69*, 7525. (b) Zienkiewicz, J.; Fryszkowska, A.; Zienkiewicz, K.; Guo, F.; Kaszynski, P.; Januszko, A.; Jones, D. *J. Org. Chem*. **2007**, *72*, 3510.

8. Beer, L.; Haddon, R. C.; Itkis, M. E.; Leitch, A. A.; Oakley, R. T.; Reed, R. W.; Richardson, J. F.; VanderVeer, D. G. *Chem. Commun*. **2005**, 1218.

9. Leitch, A. A.; Oakley, R. T.; Reed, R. W.; Thompson, L. K. *Inorg. Chem*. **2007**, *46*, 6261.

10. (a) Zienkiewicz, J.; Kaszynski, P.; Young, V. G., Jr. *J. Org. Chem*. **2004**, *69*, 2551. (b) Gilchrist, T. L.; Rees, C. W.; Vaughan, D. *J. Chem Soc., Perkin Trans*. **1983**, *1*, 55. (c) Levchenko, E. S.; Borovikova, G. S.; Borovik, E. I.; Kalinin,V. N. *Russ. J. Org. Chem*. **1984**, *20*, 176. (d) Shermolovich, Y. G.; Simonov, Y. A.; Dvorkin, A. A.; Polumbrik, O. M.; Borovikova, G. S.; Kaminskaya, E. I.; Levchenko, E. S.; Markovskii, L. N. *Russ. J. Org. Chem*. **1989**, *25*, 550. (e) Gilchrist, T. L.; Rees, C. W.; Vaughan, D. *J. Chem. Soc., Perkin Trans*. **1983**, *1*, 49. (f) Gilchrist, T. L.; Rees, C. W.; Vaughan, D. *J. Chem. Soc., Chem. Commun*. **1978**, 1049. (g) Markovskii, L. N.; Darmokhval, E. A.; Levchenko, E. S. *Russ. J. Org. Chem*. **1973**, *9*, 2055.

11. (a) Oxley, P.; Partridge, M. W.; Short, W. F. *J. Chem. Soc*. **1947**, 1110. (b) Finch, N.; Ricca, S. Jr.; Werner, L. H.; Rodebaugh, R. *J. Org. Chem*. **1980**, *45*, 3416.

12. Benko, V. P.; Pallos, L. *Journal für Praktische Chemie* **1971**, *313*, 179.

13. Abdelhamid, A. O.; Khalifa, F. A.; Ghabrial, S. S. *Phosphorus, Sulfur, Silicon and Related Elements* **1988**, *40*, 41.

14. (a) Hutchison, K.; Srdanov, G.; Hicks, R.; Yu, H.; Wudl, F.; Strassner, T.; Nendel, M.; Houk, K. N. *J. Am. Chem. Soc*. **1998**, *120*, 2989. (b) Langer, P.; Bodtke, A.; Saleh, N. N. R.; Görls, H.; Schreiner, P. R. *Angew. Chem. Int. Ed.* **2005**, *44*, 5255. (c) Prieto, J. B.; Arbeloa, F. L.; Martínez, V.M.; Arbeloa, I. L. *Chem. Phys*. **2004**, *296*, 13. (d) Wudl, F.; Koutentis, P. A.; Weitz, A.; Ma, B.; Strassner, T.; Houk, K. N.; Khan, S. I. *Pure & Appl. Chem*. **1999**, *71*, 295.

15. Bondi, A. *J. Phys. Chem*. **1964**, *68*, 41.

16. Bonner, J. C.; Fischer, M. E. *Phys. Rev*. **1964**, *135*, A640.

17. Heisenberg, W. *Z. Phys*. **1926**, *38*, 411.

18. (a) Noodleman, L.; Norman, J. G. *J. Chem. Phys*. **1979**, *70*, 4903. (b) Noodleman, L. *J. Chem. Phys*. **1981**, *74*, 5737.

19. (a) Novoa, J. J.; Deumal, M. *Struct. Bonding* **2001**, *100*, 33. (b) Jornet, J.; Deumal, M.; Ribas-Ariño, J.; Bearpark, M. J.; Robb, M.A.; Hicks, R. G.; Novoa, J. J. *Chem. Eur. J*. **2006**, *12*, 3995.

20. (a) Rawson, J. M.; Luzon, J.; Palacio, F. *Coord. Chem. Rev*. **2005**, *249*, 2631. (b) Luzon, J.; Campo, J.; Palacio, F.; McIntyre, G. J.; Rawson, J. M. *Polyhedron* **2005**, *24*, 2579.

21. Decken, A.; Mattar, S. M.; Passmore, J.; Shuvaev, K. V.; Thompson, L. K. *Inorg. Chem*. **2006**, *45*, 3878.

22. Itoh, K.; Kinoshita, M. *Molecular Magnetism, New Magnetic Materials*; Gordon and Breach Science Publishers: Japan, 2000, p 76.

23. (a) Beer, L.; Brusso, J. L.; Haddon, R. C.; Itkis, M. E.; Kleinke, H.; Leitch, A. A.; Oakley, R. T.; Reed, R. W.; Richardson, J. F.; Secco R. A.; Yu, X. *J. Am. Chem. Soc*. **2005**, *127*, 1815. (b) Beer, L.; Brusso, J. L.; Haddon, R. C.; Itkis, M. E.; Oakley, R. T.; Reed, R. W.; Richardson, J. F.; Secco, R. A.; Yu, X. *Chem. Commun*. **2005**, 5745. (c) Brusso, J. L.; Cvrkalj, K.; Leitch, A. A.; Oakley, R. T.; Reed, R. W.; Robertson, C. M. *J. Am. Chem. Soc*. **2006**, *128*, 15080. (d) Brusso, J. L.; Derakhshan, S.; Itkis, M. I.; Kleinke, H.; Haddon, R. C.; Oakley, R. T.; Reed, R. W.; Richardson, J. F.; Robertson, C. M.; Thompson, L. K. *Inorg. Chem*. **2006**, *45*, 10958.

24. (a) Di, C.; Li, J.; Yu, G.; Xiao, Y.; Guo, Y.; Liu, Y.; Qian, X.; Zhu, D. *Org. Lett*. **2008**, *10*, 3025. (b) Briseno, A. L.; Miao, Q.; Ling, M.; Reese, C.; Meng, H.; Bao, Z.; Wudl, F. *J. Am. Chem. Soc*. **2006**, *128*, 15576.

25. Riley, A. E.; Mitchell, G. W.; Koutentis, P. A.; Bendikov, M.; Kaszynski, P.; Wudl, F.; Tolbert, S. H. *Adv. Funct. Mater*. **2003**, *13*, 531.

26. (a) Bendikov, M.; Wudl, F.; Perepichka, D. *Chem. Rev*. **2004**, *104*, 4891. (b) Koch, N. *Chem. Phys. Chem*. **2007**, *8*, 1488.

27. (a) Klinga, M.; Polamo, M.; Leskela, M. *Acta. Cryst*. **1994**, *C50*, 2051. (b) Silva, G. A.; Costa, L. M. M.; Brito, F. C. F.; Miranda, A. L. P.; Barreiro, E. J.; Fraga, C. A. M. *Bioorg. Med. Chem*. **2004**, *12*, 3149. (c) Cheeseman, G. W. H.; Rishman, G. *Tetrahedron*, **1980**, *36*, 2681.

References for Chapter 3

1. Leitch, A. A.; McKenzie, C. E.; Oakley, R. T.; Reed, R. W.; Richardson, J. F.; Sawyer, L. D. *Chem. Commun*. **2006**, 1088.

2. Leitch, A. A.; Reed, R. W.; Robertson, C. M.; Britten, J. F.; Yu, X.; Secco, R. A.; Oakley, R. T. *J. Am. Chem. Soc*. **2007**, *129*, 7903.

3. Shaw, J. T.; Brotherton, C. E.; Moon, R. W.; Winland, M. D.; Anderson, M. D.; Kyler, K. S. *J. Heterocyclic Chem*. **17**, *11*, 1980.

4. Zienkiewicz, J.; Kaszynski, P.; Young, V. G., Jr. *J. Org. Chem*. **2004**, *69*, 2551.

5. Beer, L.; Brusso, J. L.; Cordes, A. W.; Haddon, R. C.; Itkis, M. E.; Kirschbaum, K.; MacGregor, D. S.; Oakley, R. T.; Pinkerton, A. A.; Reed, R. W. *J. Am. Chem. Soc.* **2002***, 124*, 9498.

6. (a) Beer, L.; Brusso, J. L.; Cordes, A. W.; Haddon, R. C.; Godde, E.; Itkis, M. E.; Oakley, R. T.; Reed, R. W. *Chem. Commun.* **2002**, 2562. (b) Beer, L.; Britten, J. F.; Brusso, J. L.; Cordes, A. W.; Haddon, R. C.; Itkis, M. E.; MacGregor, D. S.; Oakley, R. T.; Reed, R. W.; Robertson, C. M. *J. Am. Chem. Soc*. **2003**, *125*, 14394.

7. Beer, L.; Britten, J. F.; Clements, O. P.; Haddon, R. C.; Itkis, M. E.; Matkovich, K. M.; Oakley, R. T.; Reed, R. W. *Chem. Mat*. **2004**, *16*, 1564.

8. (a) Baker, A. J.; Hill, S. A. *J. Chem. Soc*. **1962**, 3464. (b) Lochon, P.; Méheux, P.; Néel, J. *Bull. Soc. Chim. Fr.* **1967**, *11*, 4387. (c) Okada M.; Marvel, C. S. *J. Polym. Sci., Part A-1* **1968**, *6*, 1259.

9. Flowers, W. T.; Holt, G.; Omogbal, F.; Poulos, C. P. *J. Chem. Soc., Perkin I* **1976**, 2394.

10. Antonello, S.; Benassi, R.; Gavioli, G.; Taddei, F.; Maran, F. *J. Am. Chem. Soc*. **2002**, *124*, 7529.

11. Barclay, T. M.; Cordes, A. W.; Goddard, J. D.; Mawhinney, R. C.; Oakley, R. T.; Preuss, K. E.; Reed, R. W. *J. Am. Chem. Soc.* **1997***, 119*, 12136.

12. (a) Cordes, A. W.; Mingie, J. R.; Oakley, R. T.; Reed, R. W.; Zhang, H. *Can. J. Chem.* **2001**, *79*, 1352. (b) Barclay, T. M.; Beer, L.; Cordes, A. W.; Oakley, R. T.; Preuss, K. E.; Taylor, N. J.; Reed, R. W. *Chem. Commun*. **1999**, 531. (c) Preston, K. F.; Sutcliffe, L. H. *Magn. Reson. Chem*. **1990**, *28*, 189.

13. Benson, S. W. *J. Chem. Educ*. **1965**, *42*, 502.

14. (a) Kahr, B.; Engen, D.V.; Mislow, K. J. *J. Am. Chem. Soc*. **1986**, *108*, 8305. (b) Kaupp, G.; Boy, J. *Angew. Chem., Int. Ed. Engl*. **1997**, *36*, 48.

15. (a) Beer, L.; Brusso, J. L.; Haddon, R. C.; Itkis, M. E.; Leitch, A. A.; Oakley, R. T.; Reed, R. W.; Richardson, J. F. *Chem. Commun*. **2005**, 1543. (b) Beer, L.; Brusso, J. L.; Haddon, R. C.; Itkis,

M. E.; Kleinke, H.; Leitch, A. A.; Oakley, R. T.; Reed, R. W.; Richardson, J. F.; Secco, R. A.; Yu, X. *J. Am. Chem. Soc*. **2005**, *127*, 18159.

16. Another example of a dimer bonded *via* a hypervalent disulfide linkage has been reported in a phenylenyl radical. Beer, L.; Reed, R. W.; Robertson, C. M.; Oakley, R. T.; Tham, F. S.; Haddon, R. C. *Org. Lett*. **2008**, *10*, 3121.

17. (a) Barclay, T. M.; Cordes, A. W.; Haddon, R. C.; Itkis, M. E.; Oakley, R. T.; Reed, R. W.; Zhang, H. *J. Am. Chem. Soc*. **1999**, *121*, 969. (b) Barclay, T. M.; Beer, L.; Cordes, A. W.; Oakley, R. T.; Preuss, K. E.; Taylor, N. J.; Reed, R. W. *Chem. Commun*. **1999**, 531.

18. Two modes of dimerization have been reported for spiro-biphenalenyls. Liao, P.; Itkis, M. E.; Oakley, R. T.; Tham, F. M.; Haddon, R. C. *J. Am. Chem. Soc*. **2004**, *126*, 14297.

19. Brooks, M. V. F.; Burford, N.; Passmore, J.; Schriver, M. J.; Sutcliffe, L. H. *J. Chem. Soc., Chem. Commun*. **1987**, 69.

20. Bondi, A. *J. Phys. Chem*. **1964**, *68*, 41.

21. Carlin, R. L. *Magnetochemistry*; Springer-Verlag: New York, 1986.

22. (a) Beekman, R. A.; Boeré, R. T.; Moock, K. H.; Parvez, M. *Can. J. Chem*. **1998**, *76*, 85. (b) Andrews, M. P.; Cordes, A. W.; Douglass, D. C.; Fleming, R. M.; Glarum, S. H.; Haddon, R. C.; Marsh, P.; Oakley, R. T.; Palstra, T. T. M.; Schneemeyer, L. F.; Trucks, G. W.; Tycko, R.; Waszczak, J. V.; Young, K. M.; Zimmerman, N. M. *J. Am. Chem. Soc.* **1991**, *113*, 3559. (c) Cordes, A. W.; Haddon, R. C.; Hicks, R. G.; Kennepohl, D. K.; Oakley, R. T.; Palstra, T. T. M.; Schneemeyer, L. F.; Scott S. R.; Waszczak, J. V. *Chem. Mater*. **1993**, *5*, 820.

23. Barclay, T. M.; Cordes, A. W.; Haddon, R. C.; Itkis, M. E.; Oakley, R. T.; Reed, R. W.; Zhang, H. *J. Am. Chem. Soc*. **1999**, *121*, 969.

24. Beer, L.; Brusso, J. L.; Haddon, R. C.; Itkis, M. E.; Oakley, R. T.; Reed, R. W.; Richardson, J. F.; Secco, R. A.; Yu, X. *Chem. Commun*. **2005**, 5745.

25. In perfectly superimposed π-stacked CT salts of dithiadiazolyl and diselenadiazoyl radicals, EHT bandwidths approaching 3.0 eV have been reported. Bryan, C.D.; Cordes, A. W.; George, N. A.; Haddon, R. C.; MacKinnon, C. D.; Oakley, R. T.; Palstra, T. T. M.; Perel, A. S. *Chem. Mater*. **1996**, *8*, 762.

26. Heuzé, K.; Fourmigué, M.A.; Batail, P.; Coulon, C.; Clérac, R.B.; Canadell, E.C.; Auban-Senzier, P.A.; Ravy, S.D.; Jérome, D. *Adv. Mat*. **2003**, *15*, 1251.

27. Ohno, K.; Noguchi, N.; Yokoi, T.; Ishii, S.; Takeda, J.; Furuya, M. *ChemPhysChem* **2006**, *7*, 1820.

28. Britten, J. F.; Clements, O. P.; Cordes, A. W.; Haddon, R. C.; Oakley, R. T.; Richardson, J. F. *Inorg. Chem*. **2001**, *40*, 6820.

29. Mott, N. F.; Davis, E. A. *Electronic Processes in Non-Crystalline Materials*, *2nd Ed.*; Oxford University Press: Oxford, 1993.

References for Chapter 4

1. Beer, L.; Brusso, J. L.; Cordes, A. W.; Haddon, R. C.; Itkis, M. E.; Kirschbaum, K.; MacGregor, D. S.; Oakley, R. T.; Pinkerton, A. A.; Reed, R. W. *J. Am. Chem. Soc*. **2002**, *124*, 9498.

2. Beer, L.; Britten, J. F.; Brusso, J. L.; Cordes, A. W.; Haddon, R. C.; Itkis, M. E.; MacGregor, D. S.; Oakley, R. T.; Reed, R. W.; Robertson, C. M. *J. Am. Chem. Soc*. **2003**, *125*, 14394.

3. (a) Leitch, A. A.; McKenzie, C. E.; Oakley, R. T.; Reed, R. W.; Richardson, J. F.; Sawyer, L. D. *Chem. Commun*. **2006**, 1088. (b) Leitch, A. A.; Reed, R. W.; Robertson, C. M.; Britten, J. F.; Yu, X.; Secco, R. A.; Oakley, R. T. *J. Am. Chem. Soc*. **2007**, *129*, 7903.

4. (a) Beechgaard, K.; Cowan, D. O.; Block, A. N. *J. Chem. Soc., Chem. Commun*. **1974**, 937. (b) Engler, E. M.; Patel, V. V. *J. Am. Chem. Soc*. **1974**, *96*, 7376.

5. Robertson, C. M.; Leitch, A. A.; Cvrkalj, K.; Reed, R. W.; Myles, D. J. T.; Dube, P. A.; Oakley. R. T. *J. Am. Chem. Soc*. **2008**, *130*, 8414.

6. Brusso, J. L.; Cvrkalj, K.; Leitch, A. A.; Oakley, R. T.; Reed, R. W.; Robertson, C. M. *J. Am. Chem. Soc*. **2006** *128*, 15080.

7. Leitch, A. A.; Brusso, J. L.; Cvrkalj, K.; Reed, R.; Robertson, C. M.; Dube, P. A.; Oakley, R. T. *Chem. Commun*. **2007**, 3368.

8. Barclay, T. M.; Cordes, A. W.; Goddard, J. D.; Mawhinney, R. C.; Oakley, R. T.; Preuss, K. E.; Reed, R. W. *J. Am. Chem. Soc*. **1997**, *119*, 12136.

9. Oakley, R. T.; Reed, R. W.; Robertson, C. M.; Richardson, J. F. *Inorg. Chem*. **2005**, *44*, 1837.

10. Beer, L.; Brusso, J. L.; Haddon, R. C.; Itkis, M. E.; Leitch, A. A.; Oakley, R. T.; Reed, R. W.; Richardson, J. F. *Chem. Commun*. **2005**, 1543.

11. Beer, L.; Brusso, J. L.; Haddon, R. C.; Itkis, M. E.; Kleinke, H.; Leitch, A. A.; Oakley, R. T.; Reed, R. W.; Richardson, J. F.; Secco, R. A.; Yu, X. *J. Am. Chem. Soc*. **2005**, *127*, 18159.

12. Akulin, Y. I.; Gel'mont, M. M.; Strelets, B. K.; Éfros, L. S. *Khim. Geterotsikl. Soedin*. **1978**, 912.

13. Less, R. J.; Rawson, J. M.; Jones, M. *Polyhderon* **2001**, *20*, 523.

14. Beer, L.; Brusso, J. L.; Haddon, R. C.; Itkis, M. E.; Oakley, R. T.; Reed, R. W.; Richardson, J. F.; Secco, R. A.; Yu, X. *Chem. Commun*. **2005**, 5745.

15. Beer, L.; Britten, J. F.; Clements, O. P.; Haddon, R. C.; Itkis, R. C.; Matkovich, K. M.; Oakley, R. T.; Reed, R. W. *Chem. Mat*. **2004**, *16*, 1564.

16. Warburton, W. K. *Chem. Rev*. **1957**, 1011.

17. Klayman, D. L.; Gunther, W. H. H. *Organic Selenium Compounds: Their Chemistry and Biology*; John Wiley & Sons: United States of America, **1973**.

18. Still, I. W. J.; Watson, I, D. G. *Synth. Commun*. **2001**, *31*, 1355.

19. Toste, F. D.; De Stefano, V.; Still, I. W. J. *Synth. Commun*. **1995**, *25*, 1277.

20. Bacon, R. G. R.; Guy, R. G. *J. Chem. Soc*. **1960**, 318.

21. Burchell, C. J.; Aucott, S. M.; Robertson, S. D.; Slawin, A. M. Z.; Woollins, J. D. *Phosphorus, Sulfur Silicon Relat. Elem.* **2004**, *179*, 865.

22. Burchell, C. J.; Kilian, P.; Slawin, A. M. Z.; Woollins, J. D.; Tersago, K.; Van Alsenoy, C.; Blockhuys, F. *Inorg. Chem*. **2006**, *45*, 710.

23. Waitkins, G. R.; Shutt, R. *Inorg. Synth*. **1946**, *2*, 186.

24. Beer, L.; Brusso, J. L.; Cordes, A. W.; Haddon, R. C.; Itkis, M. E.; Kirschbaum, K.; MacGregor, D. S.; Oakley, R. T.; Pinkerton, A. A.; Reed. R. W. *J. Am. Chem. Soc*. **2002**, *124*, 9498.

25. Beer, L. *Resonance Stabilized Heterocyclic Thiazyl Radicals*. Ph. D. Thesis. University of Waterloo, **2004**.

26. Patai, S. *The Chemistry of the Thiol Group. Part 2*; John Wiley & Sons, Ltd.: Great Britain, **1974**, p. 669.

27. Zienkiewicz, J.; Kaszynski, P. *J. Org. Chem*. **2004**, *69*, 2551.

28. Reich, H. J.; Wollowitz, S. *J. Am. Chem. Soc*. **1982**, *104*, 7051.

29. Flowers, W. T.; Holt, G.; Omogbai, F.; Paulos, C. P. *J. C. S. Perkin I* **1976**, 2394.

30. Coleman, R. S.; Arthur, J. C.; McCary, J. L. *Tetrahedron* **1997**, *53*, 11191.

31. Logan, G.; Igunbor, C.; Gen, G.; Davis, H.; Simon, A.; Salon, J.; Huang, Z. *Synlett* **2006**, *10*, 1554.

32. Binet, L.; Fabre, J. M.; Montiginoul, C.; Simonsen, K. B.; Becher, J. *J. Chem. Soc., Perkin Trans. 1* **1996**, 783.

33. Kumasaki, M.; Tanaka, H.; Kobayashi, A. *J. Mater. Chem*. **1998**, *8*, 301.

34. Reinerth, W. A.; Tour, J. M. *J. Org. Chem*. **1998**, *63*, 2397.

35. Beer, L.; Britten, J. F.; Brusso, J. L.; Cordes, A. W.; Haddon, R. C.; Itkis, M. E.; MacGregor, D. S.; Oakley, R. T.; Reed, R. W.; Robertson, C. M. *J. Am. Chem. Soc*. **2003**, *125*, 14394.

36. Brusso, J. L. *The Bandwidth Challenge in Thiazyl and Selenazyl Radical Conductors*. Ph. D. Thesis. University of Waterloo, **2006**.

37. Brauer, G. *Handbook of Preparative Inorganic Chemistry, Vol. 1*; Academic Press: New York, 1963, p 423.

38. Patil, B. R.; Bhusare, S. R.; Pawar, R. P.; Vibhute, Y. B. *Arkivoc* **2006**, 104.

39. Noda, Y.; Kashima, M. *Tetrahedron Lett*. **1997**, *38*, 6225.

40. (a) Arotsky, J.; Darby, A. C.; Hamilton, J. B. A. *J. Chem. Soc. B* **1968**, 739. (b) Arotsky, J.; Darby, A. C.; Hamilton, J. B. A. *J. Chem. Soc. Perkin Trans. 2* **1973**, 595.

41. Robertson, C. M.; Leitch, A. A.; Cvrkalj, K.; Myles, D. J. T.; Reed, R. W.; Dube, P. A.; Oakley, R. T. *J. Am. Chem. Soc*. **2008**, *130*, 14791.

42. Byers, J.; Patterson, K.; Cho, S.; McCallum, M.; Willson, C. G. *J. Photopolym. Sci. Technol*. **1998**, *11*, 465.

43. (a) Ferraro, J. R.; Williams, J. M. *Introduction to Synthetic Electrical Conductors*; Academic Press: New York, 1987, p 25. (b) Stephens, D. A.; Rehan, A. E.; Compton, S. J.; Barkhau, R. A.; Williams, J. M. *Inorg. Synth*. **1986**, *24*, 135.

References for Chapter 5

1. Beer, L.; Brusso, J. L.; Cordes, A. W.; Haddon, R. C.; Itkis, M. E.; Kirschbaum, K.; MacGregor, D. S.; Oakley, R. T.; Pinkerton, A. A.; Reed, R. W. *J. Am. Chem. Soc.* **2002**, *124*, 9498.

2. (a) Beer, L.; Brusso, J. L.; Cordes, A. W.; Haddon, R. C.; Godde, E.; Itkis, M. E.; Oakley, R. T.; Reed, R. W. *Chem. Commun.* **2002**, 2562. (b) Beer, L.; Britten, J. F.; Brusso, J. L.; Cordes, A. W.; Haddon, R. C.; Itkis, M. E.; MacGregor, D. S.; Oakley, R. T.; Reed, R. W.; Robertson, C. M. *J. Am. Chem. Soc*. **2003**, *125*, 14394.

3. Beer, L.; Britten, J. F.; Clements, O. P.; Haddon, R. C.; Itkis, M. E.; Matkovich, K. M.; Oakley, R. T.; Reed, R. W. *Chem. Mat*. **2004**, *16*, 1564.

4. Beer, L.; Brusso, J. L.; Haddon, R. C.; Itkis, M. E.; Leitch, A. A.; Oakley, R. T.; Reed, R. W.; Richardson, J. F. *Chem. Commun*. **2005**, 1543.

5. Beer, L.; Brusso, J. L.; Haddon, R. C.; Itkis, M. E.; Kleinke, H.; Leitch, A. A.; Oakley, R. T.; Reed, R. T.; Reed, R. W.; Richardson, J. F.; Secco, R. A.; Yu, X. *J. Am. Chem. Soc*. **2005**, *127*, 18159.

6. (a) Robertson, C. M.; Leitch, A. A.; Cvrkalj, K.; Reed, R. W.; Myles, D. J. T.; Dube, P. A.; Oakley, R. T. *J. Am. Chem. Soc*. **2008**, *130*, 8414. (b) Leitch, A. A.; Brusso, J. L.; Cvrkalj, K.; Reed, R. W.; Robertson, C. M.; Dube, P. A.; Oakley, R. T. *Chem. Commun.* **2007**, 3368. (c) Brusso, J. L.; Cvrkalj, K.; Leitch, A. A.; Oakley, R. T.; Reed, R. W.; Robertson, C. M. *J. Am. Chem. Soc*. **2006**, *128*, 15080.

7. Aust, R. B.; Bentley, W. H.; Drickamer, H. G. *J. Chem. Phys*. **1964**, *41*, 1856.

8. Brillante, A.; Della Valle, R. G.; Farina, L.; Venutti, E.; Cavazzoni, C.; Emerson, A. P. J.; Syassen, K. *J. Am. Chem. Soc*. **2005**, *127*, 3038.

9. (a) Nakayama, A.; Aoki, K.; Carlòn, R. P. *Phys. Rev. B: Condens. Matter* **2001**, *64*, 064104. (b) Nakayama, A.; Fujihisa, H.; Takemura, K.; Aoki, K.; Carlòn, R. P. *Synth. Met*. **2001**, *120*, 767. (c) Iwasaki, E.; Shimizu, K.; Amaya, K.; Nakayama, A.; Aoki, K.; Carlòn, R. P. *Synth. Met.* **2001**, *120*, 1003.

10. (a) Nakayama, A.; Fujihisa, H.; Aoki, K.; Shirotani, I. *Synth. Met*. **1999**, *103*, 1901. (b) Nakayama, A.; Aoki, K.; Matsushita, Y.; Shirotani, I. *Solid State Commun*. **1999**, *110*, 627. (c) Shirotani, I.; Hayashi, J.; Yakushi, K.; Takeda, K.; Yokota, T.; Shimizu, K.; Amaya, K.; Nakayama, A.; Aoki, K. *Physica B* **2001**, *304*, 6.

11. Tateyama, Y.; Ohno, T. *J. Phys.: Condens. Matter* **2002**, *14*, 10429.

12. (a) Saito, G.; Yoshida, Y. *Bull. Chem. Soc. Jpn*. **2007**, *80*, 1. (b) Onodera, A.; Shirotani, I.; Inokuchi, H.; Kawai, N. *Chem. Phys. Lett*. **1974**, *25*, 296. (c) Shirotani, I.; Kamura, Y.; Inokuchi, H.; Hirooka, T. *Chem. Phys. Lett*. **1976**, *40*, 257.

13. (a) Akahama, Y.; Kobayashi, M.; Kawamura, H. *Phys. Rev. B* **1993**, *48*, 6862. (b) Luo, H.; Greene, R. G.; Ruoff, A. L. *Phys. Rev. Lett*. **1993**, *71*, 2943. (c) Akahama, Y.; Kobayashi, M.; Kawamura, H.; *Phys. Rev. B* **1993**, *47*, 20.

14. Crapanzano, L.; Crichton, W. A.; Monaco, G.; Bellissent, R.; Meouar, M. *Nat. Mater.* **2005**, *4*, 550.

15. Cherin, P.; Unger, P. *Inorg. Chem*. **1967**, *6*, 1589.

16. Miyamoto, Y. *Jpn J. Appl. Phys*. **1980**, *19*, 1813.

17. Selenium enters a metallic phase near 25 GPa. (a) Riggleman, B. M.; Drickamer, H. G. *J. Chem. Phys*. **1962**, *37*, 446. (b) Bundy, F. P.; Dunn, K. J. *J. Chem. Phys*. **1979**, *71*, 1550.

18. Sulfur is converted into a metallic state at pressures above 40 GPa. (a) Chhabildas, L. C.; Ruoff, A. L. *J. Chem. Phys*. **1977**, *66*, 983. (b) Dunn, K. J.; Bundy, F. P. *J. Chem. Phys*. **1977**, *67*, 5048. (c) Peanasky, M. J.; Jurgensen, C.W.; Drickamer, H. G. *J. Chem. Phys*. **1984**, *81*, 6407.

19. Akulin, Y. I.; Gel'mont, M. M.; Strelets, B. K.; Éfros, L. S. *Khim. Geterotsikl. Soedin*. **1978**, 912.

20. Bondi, A. *J. Phys. Chem.* **1964**, *68*, 441.

21. (a) Dougill, M. W.; Paddock, N. L. *J. C. S. Dalton*, **1974**, 1022. (b) Brant, D. A.; Miller, W. G.; Flory, P. J. *J. Mol. Biol*. **1967**, *23*, 47. (c) Brant, D. A.; Flory, P. J. *J. Am. Chem. Soc*. **1965**, *87*, 2791.

22. (a) Robertson, C. M.; Leitch, A. A.; Cvrkalj, K.; Myles, D. J. T.; Reed, R. W.; Dube, P. A.; Oakley, R. T. *J. Am. Chem. Soc*. **2008**, *130*, 14791. (b) Brusso, J. L.; Derakhshan, S.; Itkis, M. E.; Kleinke, H.; Haddon, R. C.; Oakley, R. T.; Reed, R. W.; Richardson, J. F.; Robertson, C. M.; Thompson, L. K. *Inorg. Chem*. **2006**, *45*, 10958.

23. Leitch, A. A.; Yu, X.; Winter, S. M.; Secco, R. A.; Dube, P. A.; Oakley, R. T. *J. Am. Chem. Soc*. **2009**, *131*, 7112.

24. Leitch, A. A.; McKenzie, C. E.; Oakley, R. T.; Reed, R. W.; Richardson, J. F.; Sawyer, L. D. *Chem. Commun*. **2006**, 1088.

References for Chapter 6

1. Beer, L.; Brusso, J. L.; Cordes, A. W.; Haddon, R. C.; Itkis, M. E.; Kirschbaum, K.; MacGregor, D. S.; Oakley, R. T.; Pinkerton, A. A.; Reed, R. W. *J. Am. Chem. Soc*. **2002**, *124*, 9498.

2. Beer, L.; Britten, J. F.; Brusso, J. L.; Cordes, A. W.; Haddon, R. C.; Itkis, M. E.; MacGregor, D. S.; Oakley, R. T.; Reed, R. W.; Robertson, C. M. *J. Am. Chem. Soc*. **2003**, *125*, 14394.

3. Beer, L.; Britten, J. F.; Clements, O. P.; Haddon, R. C.; Itkis, M. E.; Matkovich, K. M.; Oakley, R. T.; Reed, R. W. *Chem. Mat*. **2004**, *16*, 1564.

4. (a) Beer, L.; Brusso, J. L.; Haddon, R. C.; Itkis, M. E.; Leitch, A. A.; Oakley, R. T.; Reed, R. W.; Richardson, J. F. *Chem. Commun*. **2005**, 1543. (b) Beer, L.; Brusso, J. L.; Haddon, R. C.; Itkis, M. E.; Kleinke, H.; Leitch, A. A.; Oakley, R. T.; Reed, R. W.; Richardson, J. F.; Secco, R. A.; Yu, X. *J. Am. Chem. Soc*. **2005**, *127*, 18159.

5. Brusso, J. L.; Cvrkalj, K.; Leitch, A. A.; Oakley, R. T.; Reed, R. W.; Robertson, C. M. *J. Am. Chem. Soc*. **2006**, *128*, 15080.

6. Robertson, C. M.; Leitch, A. A.; Cvrkalj, K.; Reed, R. W.; Myles, D. J. T.; Dube, P. A.; Oakley, R. T. *J. Am. Chem. Soc*. **2008**, *130*, 8414.

7. Leitch, A. A.; Brusso, J. L.; Cvrkalj, K.; Reed, R. W.; Robertson, C. M.; Dube, P. A.; Oakley, R. T. *Chem. Commun*. **2007**, 3368.

8. Robertson, C. M.; Myles, D. J. T.; Leitch, A. A.; Reed, R. W.; Dooley, B. M.; Frank, N. L.; Dube, P. A.; Thompson, L. K.; Oakley, R. T. *J. Am. Chem. Soc*. **2007**, *129*, 12688.

9. (a) Allemand, P. M.; Khemani, K. C.; Koch, A.; Wudl, F.; Holczer, K.; Donovan, S.; Gruner, G.; Thompson, J. D. *Science* **1991**, *253*, 301. (b) Fujita, W.; Awaga, K. *Chem. Phys. Lett*. **2004**, *388*, 186. (c) Kinoshita, M.; Turek, P.; Tamura, M.; Nozawa, K.; Shiomi, D.; Nakazawa, Y.; Ishikawa, M.; Takahashi, M.; Awaga, K.; Inabe, T.; Maruyama, Y. *Chem. Lett*. **1991**, 1225. (d) Alberola, A.; Less, R. J.; Pask, C. M.; Rawson, J. M.; Palacio, F.; Oliete, P.; Paulsen, C.; Yamaguchi, A.; Farley, R. D.; Murphy, D. M. *Angew. Chem., Int. Ed.* **2003**, *42*, 4782.

10. Leitch, A. A.; Yu, X.; Winter, S. M.; Secco, R. A.; Dube, P. A.; Oakley, R. T. *J. Am. Chem. Soc*. **2009**, *131*, 7112.

11. Bondi, A. *J. Phys. Chem.* **1964**, *68*, 441.

12. Leitch, A. A.; Reed, R. W.; Robertson, C. M.; Britten, J. F.; Yu, X.; Secco, R. A.; Oakley, R. T. *J. Am. Chem. Soc*. **2007**, *129*, 7903.

13. Beer, L.; Brusso, J. L.; Haddon, R. C.; Itkis, M.E.; Oakley, R. T.; Reed, R. W.; Richardson, J. F.; Secco, R. A.; Yu, X. *Chem. Commun.* **2005**, 5745.

14. (a) Dougill, M. W.; Paddock, N. L. *J. C. S. Dalton* **1974**, 1022. (b) Brant, D. A.; Miller, W. G.; Flory, P. J. *J. Mol. Biol*. **1967**, *23*, 47. (c) Brant, D. A.; Flory, P. J. *J. Am. Chem. Soc.* **1965**, *87*, 2791.

15. Carlin, R. L. *Magnetochemistry*; Springer-Verlag: New York, 1986.

16. Leitch, A. A.; Oakley, R. T.; Reed, R. W.; Thompson, L. K. *Inorg. Chem*. **2007**, *46*, 6261.

17. Bonner, J. C.; Fisher, M. E. *Phys. Rev*. **1964**, *135*, A640.

18. Deumal, M.; Robb, M. A.; Novoa, J. J. *Prog. Theo. Chem. Phys*. **2007**, *16*, 271.

19. (a) Novoa, J. J.; Deumal, M. *Struct. Bonding* **2001**, *100*, 33. (b) Jornet, J.; Deumal, M.; Ribas-Ariño, J.; Bearpark, M. J.; Robb, M.A.; Hicks, R. G.; Novoa, J. J. *Chem. Eur. J.* **2006**, *12*, 3995.

20. (a) Rawson, J. M.; Luzon, J.; Palacio, F. *Coord. Chem. Rev*. **2005**, *249*, 2631. (b) Luzon, J.; Campo, J.; Palacio, F.; McIntyre, G. J.; Rawson, J. M. *Polyhedron* **2005**, *24*, 2579. (c) Deumal, M.; LeRoux, S.; Rawson, J. M.; Robb, M. A.; Novoa, J. J. *Polyhedron* **2007**, *26*, 1949.

21. (a) Decken, A.; Mattar, S. M.; Passmore, J.; Shuvaev, K. V.; Thompson, L. K. *Inorg. Chem*. **2006**, *45*, 3878.

22. Robertson, C. M.; Leitch, A. A.; Cvrkalj, K.; Myles, D. J. T.; Reed, R. W.; Dube, P. A.; Oakley, R. T. *J. Am. Chem. Soc*. **2008**, *130*, 14791.

23. Takano, Y.; Taniguchi, T.; Isobe, H.; Kubo, T.; Morita, Y.; Yamamoto, K.; Nakasuji, K.; Takui, T.; Yamaguchi, K. *J. Am. Chem. Soc*. **2002**, *124*, 11122.

24. (a) Noodleman, L.; Norman, J. G. *J. Chem. Phys*. **1979**, *70*, 4903. (b) Noodleman, L. *J. Chem. Phys.* **1981**, *74*, 5737.

25. Rovira, C. *Struct. Bonding* **2001**, *100*, 164.

26. (a) Kahn, O. *Molecular Magnetism*: VCH: New York, 1993. (b) Kahn, O.; Galy, J.; Journaux, Y.; Jaud, J.; Morgenstern-Badarau, I. *J. Am. Chem. Soc.* **1982**, *104*, 2165. (c) Verdaguer, M. *Polyhedron* **2001**, *20*, 1115.

References for Appendix A

1. (a) Ferraro, J. R.; Williams, J. M. *Introduction to Synthetic Electrical Conductors*; Academic Press: New York, 1987, p 25. (b) Stephens, D. A.; Rehan, A. E.; Compton, S. J.; Barkhau, R. A.; Williams, J. M. *Inorg. Synth*. **1986**, *24*, 135.

2. (a) Beck, A. D. *J. Chem. Phys.*, **1993**, *98*, 5648. (b) Lee, C.; Yang, W.; Parr, R. C. *Phys. Chem. Rev. B*, **1988**, *37*, 785.

3. Frisch, M. J.; Trucks, G. W.; Schlegel, H. B.; Scuseria, G. E.; Robb, M. A.; Cheeseman, J. R.; Zakrzewski, V. G.; Montgomery Jr., J. A.; Stratmann, R. E.; Burant, J. C.; Dapprich, S.; Millam, J. M.; Daniels, A. D.; Kudin, K. N.; Strain, M. C.; Farkas, O.; Tomasi, J.; Barons, V.; Cossi, M.; Cammi, R.; Mennucci, B.; Pomelli, C.; Adamo, C.; Clifford, S.; Ochterski, J.; Petersson, G. A.; Ayala, P. Y.; Cui, Q.; Morokuma, K.; Malick, D. K.; Rabuck, A. D.; Raghavachari, K.; Foreman, J. B.; Cioslowski, J.; Ortiz, J. V.; Stefanov, B. B.; Liu, G.; Fox, D. J.; Keith, T.; Al-Laham, M. A.; Peng, C. Y.; Nanayakkara, A.; Wong, M. W.; Andres, J. L.; Gonzalez, C.; Head-Gordon, M.; Repogle, E. S.; Pople, J. A. *Gaussian 98*, Revision A:6. Gaussian, Inc.: Pittsburg, PA, **1998**.

4. Frisch, M. J.; Trucks, G. W.; Schlegel, H. B.; Scuseria, G. E.; Robb, M. A.; Cheeseman, J. R.; Montgomery, Jr., J. A.; Vreven, T.; Kudin, K. N.; Burant, J. C.; Millam, J. M.; Iyengar, S. S.; Tomasi, J.; Barone, V.; Mennucci, B.; Cossi, M.; Scalmani, G.; Rega, N.; Petersson, G. A.; Nakatsuji, H.; Hada, M.; Ehara, M.; Toyota, K.; Fukuda, R.; Hasegawa, J.; Ishida, M.; Nakajima, T.; Honda, Y.; Kitao, O.; Nakai, H.; Klene, M.; Li, X.; Knox, J. E.; Hratchian, H. P.; Cross, J. B.; Adamo, C.; Jaramillo, J.; Gomperts, R.; Stratmann, R. E.; Yazyev, O.; Austin, A. J.; Cammi, R.; Pomelli, C.; Ochterski, J. W.; Ayala, P. Y.; Morokuma, K.; Voth, G. A.; Salvador, P.; Dannenberg, J. J.; Zakrzewski, V. G.; Dapprich, S.; Daniels, A. D.; Strain, M. C.; Farkas, O.; Malick, D. K.; Rabuck, A. D.; Raghavachari, K.; Foresman, J. B.; Ortiz, J. V.; Cui, Q.; Baboul, A. G.; Clifford, S.; Cioslowski, J.; Stefanov, B. B.; Liu, G.; Liashenko, A.; Piskorz, P.; Komaromi, I.; Martin, R. L.; Fox, D. J.; Keith, T.; Al-Laham, M. A.; Peng, C. Y.; Nanayakkara, A.; Challacombe, M.; Gill, P. M. W.; Johnson, B.; Chen, W.; Wong, M. W.; Gonzalez, C.; Pople, J. A. *Gaussian 03*, Revision C.02. Gaussian Inc.: Wallingford, CT, **2004**.

5. Antonello, S.; Benassi, R.; Gavioli, G.; Taddei, F.; Maran, F. *J. Am. Chem. Soc*. **2002**, *124*, 7529.

6. Barclay, T. M.; Cordes, A. W.; Goddard, J. D.; Mawhinney, R. C.; Oakley, R. T.; Preuss, K. E.; Reed, R. W. *J. Am. Chem. Soc*. **1997**, *119*, 12136.

7. Heisenberg, W. *Z. Phys*. **1926**, *38*, 411.

8. Boeré, R. T.; Moock, K. H.; Parvez, M. Z. *Anorg. Allg. Chem.*, **1994**, *620*, 1589.

9. *WinEPR Simfonia, version 1.25*; Bruker Instruments, Inc.: Billerica, MA, **1966**.

10. Carlin, R. L. *Magnetochemistry*; Springer-Verlag: New York, **1986**.

11. Bonner, J. C.; Fisher, M. E. *Phys. Rev*. **1964**, *135*, A640.

12. Estes, W. E.; Gavel, D. P.; Hatfield, W. E.; Hodgson, D. J. *Inorg. Chem*. **1978**, *17*, 1415.

13. Secco, R. A. *Can. J. Phys.*, **1995**, *73*, 287.

14. Secco, R. A.; Schloessin, H. H. *J. Appl. Phys.*, **1986**, *60*, 1625.

15. *SAINT, version 6.22*; Bruker Advanced X-ray Solutions, Inc.: Madison, WI, **2001**.

16. Sheldrick, G. M. SHELXS-90. *Acta Crystallogr. A* **1990**, *46*, 467.

17. Sheldrick, G. M. SHELXL-97. *Program for the Refinement of Crystal Structures*; University of Göttingen, Göttingen, Germany, **1997**.

18. SHELXTL, VERSION 6.12 *Program Library for Structure Solution and Molecular Graphics*; Bruker Advanced X-ray Solutions, Inc.: Madison, WI, **2001**.

19. EHMACC, *Quantum Chemistry Program Exchange*, program number 571, Bloomington, IN, **1962**.

20. CAESAR, *Version 2 Program for Crystal and Electronic Structure Analysis*; PrimeColor Software, Inc.: Cary, NC **1998**.

21. Basch, H.; Viste, A.; Gray, H. B. *Theor. Chim. Acta* **1965**, *3*, 458.

22. Clementi, E.; Roetti, C. *At. Data. Nucl. Data Tables* **1974**, *14*, 177.

23. Cordes, A. W.; Haddon, R. C.; Oakley, R. T.; Schneemeyer, L. F.; Waszczak, J. V.; Young, K. M.; Zimmerman, N. M. *J. Am. Chem. Soc*. **1991**, *113*, 582. (b) Andrews, M. P., *et al.*; *J. Am. Chem. Soc*. **1991**, *113*, 3559.

24. Ammeter, J. H.; Bürgi, H. B.; Thibeault, J. C.; Hoffmann, R. *J. Am. Chem. Soc.* **1978**, *100*, 3686.

25. Byers, J.; Patterson, K.; Cho, S.; McCallum, M.; Willson, C. G. *J. Photopolym. Sci. Technol*. **1998**, *11*, 465.

26. Brauer, G. *Handbook of Preparative Inorganic Chemistry*; Academic: New York, **1963**; Vol. 1, p 423.